



Defense Threat Reduction Agency
8725 John J. Kingman Road, MS 6201
Fort Belvoir, VA 22060-6201



DTRA-TR-03-37

TECHNICAL REPORT

Investigation into the Feasibility of Highly Enriched Uranium Detection by External Neutron Stimulation (Expanded Study)

Approved for public release; distribution is unlimited.

May 2006

DTRA-MIPR-03-2207-M

Martin E. Nelson, et al.

Prepared by:
United States Naval Academy
Mechanical Engineering
Department
590 Holloway Rd.
Annapolis, MD 21402

DESTRUCTION NOTICE

FOR CLASSIFIED documents, follow the procedures in DoD 5550.22-M, National Industrial Security Program Operating Manual, Chapter 5, Section 7 (NISPOM) or DoD 5200.1-R, Information Security Program Regulation, Chapter 1X.

FOR UNCLASSIFIED limited documents, destroyed by any method that will prevent disclosure of contents or reconstruction of the document.

Retention of this document by DoD contractors is authorized in accordance with DoD 5220.22M, Industrial Security manual.

PLEASE NOTIFY THE DEFENSE THREAT REDUCTION AGENCY, ATTN: IMMI, 8725 JOHN J. KINGMAN ROAD, MS-6201, FT. BELVOIR, VA 22060-6201. IF YOUR ADDRESS IS INCORRECT, IF YOU WISH IT DELETED FROM THE DISTRIBUTION LIST, OR IF THE ADDRESSEE IS NO LONGER EMPLOYED BY YOUR ORGANIZATION.

DISTRIBUTION LIST UPDATE

This mailer is provided to enable DTRA to maintain current distribution lists for reports. (We would appreciate you providing the requested information.)

- ☐ Add the individual listed to your distribution list.
- ☐ Delete the cited organization/individual.
- ☐ Change of address.

Note:

Please return the mailing label from the document so that any additions, changes, corrections or deletions can be made easily. For distribution cancellation or more information call DTRA/BDMI (703) 767-4724.

NAME: _____

ORGANIZATION: _____

OLD ADDRESS

NEW ADDRESS

TELEPHONE NUMBER: () _____

DTRA PUBLICATION NUMBER/TITLE

CHANGES/DELETIONS/ADDITONS, etc.

(Attach Sheet if more Space is Required)

DTRA or other GOVERNMENT CONTRACT NUMBER: _____

CERTIFICATION of NEED-TO-KNOW BY GOVERNMENT SPONSOR (if other than DTRA):

SPONSORING ORGANIZATION: _____

CONTRACTING OFFICER or REPRESENTATIVE: _____

SIGNATURE: _____

DEFENSE THREAT REDUCTION AGENCY
ATTN: BDLMI
8725 John J Kingman Road, MS 6201
Fort Belvoir, VA 22060-6201

DEFENSE THREAT REDUCTION AGENCY
ATTN: BDLMI
8725 John J Kingman Road, MS 6201
Fort Belvoir, VA 22060-6201

REPORT DOCUMENTATION PAGE

Form Approved
OMB No. 0704-0188

Public reporting burden for this collection of information is estimated to average 1 hour per response, including the time for reviewing instructions, searching existing data sources, gathering and maintaining the data needed, and completing and reviewing this collection of information. Send comments regarding this burden estimate or any other aspect of this collection of information, including suggestions for reducing this burden to Department of Defense, Washington Headquarters Services, Directorate for Information Operations and Reports (0704-0188), 1215 Jefferson Davis Highway, Suite 1204, Arlington, VA 22202-4302. Respondents should be aware that notwithstanding any other provision of law, no person shall be subject to any penalty for failing to comply with a collection of information if it does not display a currently valid OMB control number. PLEASE DO NOT RETURN YOUR FORM TO THE ABOVE ADDRESS.

1. REPORT DATE (DD-MM-YYYY) 00-05-2006		2. REPORT TYPE Technical		3. DATES COVERED (From - To) 020301 - 031231	
4. TITLE AND SUBTITLE Investigation into the Feasibility of Highly Enriched Uranium Detection by External Neutron Stimulation (Expanded Study)				5a. CONTRACT NUMBER DTRA-MIPR-03-2207-M	
				5b. GRANT NUMBER	
				5c. PROGRAM ELEMENT NUMBER	
				5d. PROJECT NUMBER	
6. AUTHOR(S) Martin E. Nelson, James F. Ziegler, Harry F. Feigel, Crystine M. Good, Bryan N. Blackburn, Joseph S. St. John, Sean J. Locke, and Jeffrey D. Allen				5e. TASK NUMBER	
				5f. WORK UNIT NUMBER	
7. PERFORMING ORGANIZATION NAME(S) AND ADDRESS(ES) United States Naval Academy Mechanical Engineering Department 590 Holloway Rd. Annapolis, MD 21402				8. PERFORMING ORGANIZATION REPORT NUMBER	
9. SPONSORING / MONITORING AGENCY NAME(S) AND ADDRESS(ES) Defense Threat Reduction Agency 8725 John J. Kingman, STOP 6201 Ft. Belvoir, VA 22060-6201 CSC/ G. Sampoll-Ramirez				10. SPONSOR/MONITOR'S ACRONYM(S) DTRA-TR-03-37	
				11. SPONSOR/MONITOR'S REPORT NUMBER(S)	
12. DISTRIBUTION / AVAILABILITY STATEMENT Approved for public release; distribution is unlimited.					
13. SUPPLEMENTARY NOTES					
14. ABSTRACT This report studied the detect ability of 1kg of HEU in a cargo container, whose dimensions are 20'x8'x8', by stimulating the HEU with neutron source located external to the container and counting the neutrons that would be produced with a high sensitivity thermal neutron detector. This project examined a wide variety of different energy sources, counting options, and the effect of different cargo materials present within the container. The study considered solution approaches using both deterministic and Monte Carlo techniques. The major project conclusion is that this approach would be successful in all common environments except one, if a pulsed 14MeV neutron source with a strength of 10E12 neutrons/sec was used and the delayed fission neutrons are counted between pulses. The study also developed different facility designs, which included a shielding analysis, container activation and storage requirements, and overall concept economic feasibility using the Port of Baltimore as a benchmark.					
15. SUBJECT TERMS Neutron Detection HEU Fission Neutron Stimulation Cargo Activation Source Standoff Helium-3 Detectors Port of Baltimore Cargo Containers Monte Carlo					
16. SECURITY CLASSIFICATION OF:			17. LIMITATION OF ABSTRACT SAR	18. NUMBER OF PAGES 238	19a. NAME OF RESPONSIBLE PERSON
a. REPORT Unclassified	b. ABSTRACT Unclassified	c. THIS PAGE Unclassified			19b. TELEPHONE NUMBER (include area code)

SUMMARY

This investigation evaluates the feasibility requirements in the use of external neutron stimulation in order to detect the presence of 1 kg of highly enriched uranium (HEU) in a large shipping cargo container. After reviewing the neutron and gamma properties of special nuclear material, the existing container inspection process as developed by the container security initiative is described and several current portside inspection technologies were analyzed in order to determine their adequacy for this problem. It was concluded that vulnerabilities exist in each of these technologies and a supplemental technology could increase port security.

A benchmark container, whose dimensions are 20' x 8' x 8', was analyzed with several polyethylene moderated He^3 neutron detector(s) on one side and the neutron source on the other side for a wide variety of different energy sources, transmission and backscattered counting options, source distances from the container, prompt and delayed neutrons, and the effect of different cargo materials present with the container. The study considered solution approaches using both deterministic and Monte Carlo techniques of which the later solution approach was based on the MCNP4C2 transport code. The study also considered the detector response to the expected neutron background, interference reactions that could produce delayed neutrons, and counting statistics. The project concluded that the neutron stimulation approach would be successful in the presence of different cargo materials one if a pulsed 14 MeV source was used and only the delayed neutrons were counted. This could be accomplished by use of a gating technique that turned the neutron detector on when the neutron source was off and visa versa. It was calculated that the system would require a source strength of 10^{12} neutrons/sec and should be cycled on and off 48 times to obtain the maximum signal to noise response for a 5 minute examination time. The one cargo condition that would render this approach ineffective was the case where the cargo had a density of 1 gram/cm³ or greater and had a hydrogen atom density of 15% or greater.

The study also considered the effect of cargo activation and government regulations for release of activated material. The results showed that cargo hold times due to activation would be less than current practices at the port of Baltimore and thus should have little impact on the flow of commerce. A feasibility study was also performed using the Port of Baltimore as a baseliner. This study estimated that it would cost \$2 million to build and operate the facility for one year and less than half this amount for subsequent years. The facility would have more than sufficient capacity to meet the inspection needs at the port.

TABLE OF CONTENTS

Section	Page
SUMMARY.....	ii
FIGURES.....	vii
TABLES.....	xii
ACKNOWLEDGEMENTS.....	xv
1 BACKGROUND AND STATEMENT OF PROBLEM.....	1
1.1 SNM NUCLEAR PROPERTIES AND PASSIVE GAMMA DETECTION..	2
1.2 SNM NUCLEAR PROPERTIES AND PASSIVE NEUTRON DETECTION	3
1.3 SNM AND ACTIVE PHOTON DETECTION TECHNIQUES.....	4
1.4 SNM AND ACTIVE NEUTRON TECHNIQUES.....	5
1.5 SNM DETECTION AND WELL-LOGGING TECHNOLOGY.....	5
1.6 SNM DETECTION AND NON-DESTRUCTIVE NUCLEAR WASTE ASSAYING.....	6
1.7 CONTAINER SECURITY INITIATIVE.....	7
1.7.1 Container Security Initiative Background..	7
1.7.2 CSI Steps Prior to Containers Arriving in the United States.....	8
1.7.3 CSI Role Upon Container Arrival into the Port of Baltimore.....	10
1.8 VACIS (VEHICLE AND CARGO INSPECTION SYSTEM).....	14
1.8.1 VACIS Background.....	14
1.8.2 VACIS Operation.....	15
1.8.3 VACIS Source Exposure to Operators.....	17
1.8.4 VACIS Vulnerabilities.....	20
1.9 PORTAL MONITORING SYSTEM.....	22
1.9.1 Portal Monitoring System Operation.....	22
1.9.2 Portal Monitor Sensitivity to 1 kg HEU With and Without Iron Shielding.....	23
1.9.3 Portal Monitor Vulnerability Summary.....	26
1.10 RADIATION ISOTOPE DETECTOR.....	26
1.10.1 Radiation Isotope Detector Operation.....	27
1.10.2 HEU Counts in Radioisotope with 1 kg HEU..	27
1.10.3 Radiation Isotope Detector Vulnerabilities.....	33
1.10.4 Summary.....	34
1.11 FUNDAMENTAL PROJECT SCENARIO.....	34

TABLE OF CONTENTS (Continued)

Section	Page
1.12 METHOD OF APPROACH.....	35
2 BENCHMARK FACILITY DESCRIPTION AND MODEL DEVELOPMENT.....	36
2.1 BENCHMARK FACILITY DESCRIPTION.....	36
2.2 MCNP MODEL.....	38
2.3 MODEL PLOTTING SOFTWARE.....	41
2.4 ONDAC DETECTOR.....	42
3 STIMULATION USING A CONTINUOUS NEUTRON SOURCE WITH PROMPT NEUTRON COUNTING AND NO CARGO.....	46
3.1 PARAMETER STUDY.....	46
3.2 CONCLUSIONS.....	55
4 STIMULATION USING A PULSED 14 MEV NEUTRON SOURCE AND COUNTING DELAYED NEUTRONS IN A CONTAINER WITH NO PAYLOAD.....	56
4.1 DESCRIPTION OF THE TECHNIQUE.....	56
4.2 ADVANTAGES AND DISADVANTAGES OF PULSED 14 MEV NEUTRON SOURCES.....	57
4.3 AVAILABILITY OF PULSED 14 MEV NEUTRON SOURCES.....	59
4.4 DETERMINISTIC ANALYSIS.....	59
4.5 MCNP ANALYSIS.....	73
4.6 COMPARISON OF THE DETERMINISTIC AND MCNP METHODS....	77
4.7 RECOMMENDATIONS FOR OPERATING PARAMETERS AND MINIMUM PULSE RATE.....	77
4.8 CONCLUSIONS.....	80
5 EFFECT OF PAYLOAD WITHIN CONTAINER.....	81
5.1 DESCRIPTION OF ADDING CARGO TO MCNP MODEL.....	81
5.2 NUMERICAL MCNP CARGO RESULTS.....	82
5.3 GRAPHICAL ANALYSIS OF MCNP RESULTS.....	83
5.3.1 Neutrons Gained by Fissioning.....	84
5.3.2 Radiative Capture with 14 MeV Neutrons....	86
5.3.3 Delayed Neutron Production.....	91
5.3.4 Delayed Neutron ONDAC Interactions and Radiative Capture.....	91
5.3.5 ONDAC Interactions per 14 MeV Source Particle.....	94
5.3.6 Study of Detector Distance Effect from HEU	97
5.3.7 Maximum Payload.....	98

TABLE OF CONTENTS (Continued)

Section	Page
5.4 INTERFERENCE REACTION.....	99
5.5 EFFECT OF HYDROGEN ON ONDAC INTERACTIONS.....	101
5.6 CONCLUSIONS.....	104
6 SHIELDING ANALYSIS.....	105
6.1 SHIELDING REQUIREMENTS-EMPRICAL APPROACH.....	105
6.2 SHIELDING REQUIREMENTS-MCNP APPROACH.....	107
6.3 CONCLUSIONS.....	110
7 STUDY ON EFFECTS OF VARYING SOURCE DISTANCE TO THE CARGO CONTAINER.....	111
7.1 MOTIVATION FOR DISTANCE STUDY.....	111
7.2 MCNP MODEL TO STUDY SOURCE STANDOFF.....	111
7.3 EFFECT OF SOURCE STANDOFF ON NEUTRON PRODUCTION FROM HEU FOR DIFFERENT CARGO MATERIALS.....	112
7.4 INTERACTIONS IN CENTER ONDAC PER 14 MEV SOURCE PARTICLE.....	114
7.5 CONCLUSIONS.....	117
8 CARGO ACTIVATION.....	118
8.1 METHODOLOGY.....	118
8.1.1 Assumptions.....	118
8.1.2 Saturated Activity.....	119
8.1.3 Activity During Pulsing and Decay Phase of Each Cycle.....	125
8.1.4 Effect of Average Distance Assumption on Flux.....	126
8.2 ACTIVITY DURING EXAMINATION PERIOD FOR IRON, ALUMINUM, AND LEAD.....	128
8.3 TIME FOR IRON, ALUMINUM, AND LEAD ACTIVITY TO DECREASE BY TEN HALF-LIVES TO MEET GOVERNMENT RELEASE REGULATIONS.....	132
8.4 USNA IRADIATION EXPERIMENT TO DETERMINE TIME IRON, ALUMINUM, LEAD, AND OTHER MATERIALS DECAY TO BACKGROUND.....	135
8.5 CONCLUSIONS.....	142
9 PORT OF BALTIMORE AND FEASIBILITY STUDY OF NEUTRON STIMULATION FACILITY.....	144
9.1 PORT OF BALTIMORE.....	144

TABLE OF CONTENTS (Continued)

Section	Page
9.2 RULES AND REGULATIONS APPLICABLE TO A NEUTRON STIMULATION SPECIAL NUCLEAR MATERIAL MONITORING FACILITY.....	149
9.2.1 Exposure Dose Standards.....	149
9.2.2 Storage of Activated Cargo Material.....	150
9.2.3 High Radiation Area Requirements.....	151
9.3 COST ANALYSIS.....	151
9.3.1 Radiation Instrumentation Costs.....	152
9.3.2 Pulsed Neutron Generator Costs.....	152
9.3.3 Facility Construction and Operation.....	152
9.3.4 Staffing Costs.....	153
9.3.5 Dosimetry Costs.....	154
9.3.6 Summary of Annual Costs.....	156
9.4 SITE DESIGN AND LAYOUT.....	159
9.5 CONCLUSIONS.....	171
10 COMPARISON OF GAMMA SIGNATURES IN COMMON CARGO MATERIALS TO THAT OF HEU AND REACTOR GRADE PLUTONIUM.....	173
10.1 GAMMAS FROM HEU AND REACTOR GRADE PLUTONIUM.....	173
10.2 GAMMA EMITTING ISOTOPES IN CARGO MATERIAL.....	177
10.3 MCNP ANALYSIS OF GAMMA TRANSPORT FROM A PLUTONIUM SOURCE IN A SHIPPING CONTAINER TO AN EXTERNAL PORTAL MONITORING SYSTEM (ST. JOHN, 2003).....	179
10.4 CONCLUSIONS.....	184
11 CONCLUSIONS AND RECOMMENDATIONS.....	185
11.1 CONCLUSIONS.....	185
11.2 RECOMMENDATIONS FOR FUTURE WORK.....	187
12 REFERENCES.....	191
Appendix	
A SAMPLE MCNP INPUT FILES.....	A-1
B CALCULATION OF AVERAGE DISTANCE FROM THE SOURCE TO CARGO DRUMS.....	B-1
C PORT OF BALTIMORE AND MOBILE VACIS INFORMATION QUESTIONS AND ANSWERS.....	C-1

FIGURES

Figure	Page
1-1 Photon emissions for U^{235} (St. John, 2002).....	3
1-2 Container flowchart overview.....	12
1-3 Detailed CSI container path.....	13
1-4 Mobile VACIS in use, inspecting containers at a port (Americana Impex Consulting Co, 2003).....	14
1-5 Dose equivalent plot for source distance of 5 to 762 cm (2 inches to 25 feet) for 1 second exposure per container from Mobile VACIS.....	18
1-6 Dose equivalent plot for source distance of 100 to 762 cm for 1 second exposure per container from Mobile VACIS...	19
1-7 Plot of the effects of source distance on dose rate for a portal monitoring station with no shielding.....	24
1-8 Plot of effect of an iron shield on the dose rate measured by the portal monitoring system with 1 kg HEU at 304 cm.....	25
1-9 Example of a vehicle portal monitoring station.....	26
1-10 Picture of the hand-held radiation isotope detector, the Cryo3.....	27
1-11 Pictorial view of the area in which the HEU will self-absorb gammas, and the area in which the gammas will escape.....	30
1-12 Experimental set-up of the gamma spectroscopy experiment at USNA using a germanium detector.....	31
1-13 Counts in the radiation isotope detector versus counting time for 1 kg of HEU with Cryo3 and HEU located in worst-case scenario position.....	32
2-1 Benchmark facility: Dry freight container with dimensions 20' x 8' x 8' (Cronos, 2002).....	37
2-2 SABRINA representation of benchmark facility.....	38
2-3 MCNP model of cargo container as viewed in the x-y plane.	42
2-4 ONDAC detector cross sectional geometry.....	43
2-5 ONDAC system with composite case and Eberline E-600 survey meter.....	44
3-1 Effect of source energy on ONDAC efficiency.....	47
3-2 U^{235} fission cross section.....	48
3-3 Resonance study - Normalized detector distance from source vs. response ratio in central ONDAC.....	49
3-4 Interaction ratios in ONDAC detectors vs. source energy with HEU to source distance of 5 cm.....	50
3-5 Effect of HEU distance to source with a 14 MeV source....	51
3-6 SABRINA model of borated polyethylene rectangular parallelepiped surrounding neutron source.....	52

FIGURES (Continued)

Figure		Page
3-7	Effect of borated polyethylene shield volume on interaction rate in ONDAC using backscattered neutrons..	53
3-8	Effect of borated polyethylene shield volume on ratio of interactions (HEU present to no HEU present) in ONDAC with source in center of shield.....	54
3-9	Effect of cadmium on ratio of interactions in center ONDAC detector with HEU present to interactions with no HEU present with a 14 MeV source.....	55
4-1	Neutron die-away characterization for a 100 μ sec 14 MeV pulse (Gozani, 2002).....	57
4-2	Schematic representation of time intervals in a pulsed neutron system approach.....	60
4-3	Schematic representation of the major aspects of components in the deterministic model.....	61
4-4	Effect of varying detector count time with a 5 ms pulse width on counting delayed neutrons from a 14 MeV pulsed source with an ONDAC detector.....	65
4-5	Effect of varying detector count time with a 10 ms pulse width on counting delayed neutrons from a 14 MeV pulsed source with an ONDAC detector.....	66
4-6	Effect of varying detector count time with a 15 ms pulse width on counting delayed neutrons from a 14 MeV pulsed source with an ONDAC detector.....	67
4-7	Effect of varying detector count time with a 20 ms pulse width on counting delayed neutrons from a 14 MeV pulsed source with an ONDAC detector.....	68
4-8	Effect of varying detector pulse width with a 14 MeV source on an ONDAC detector.....	69
4-9	Effect of varying source neutron emission rate on counting delayed neutrons from a 14 MeV pulsed source with an ONDAC detector along with ONDAC background count rate.....	70
4-10	Effect of varying distance of source and detector to HEU on counting delayed neutrons from a 14 MeV pulsed source with an ONDAC detector.....	71
4-11	Effect on detector CPM of equal pulse widths and count times up to 35000 msec (35 seconds) on counting delayed neutrons from a 14 MeV source with an ONDAC detector....	72
4-12	Delayed neutron probability distribution over five energy bins by Batchelor and Bonner and by Burgy.....	74
4-13	Interactions per source particle in center ONDAC detector versus source energy for five energy spectra analyzed with shipping container filled with air.....	76

FIGURES (Continued)

Figure	Page
4-14 Effect of varying source neutron emission rate to detect HEU for worst case scenario in the benchmark facility when using three ONDAC detectors that are located at lengthwise coordinates -200 cm, 0 cm and +200 cm and using operational parameters given in table 4-3.....	80
5-1 Neutron gain by fissioning in HEU per 14 MeV source particle for various cargo materials.....	85
5-2 Neutron gain from (n,xn) reactions per 14 MeV source particle for various cargo materials.....	86
5-3 Radiative capture per 14 MeV neutron emitted to the center ONDAC detector for various cargo materials.....	88
5-4 Delayed fission neutrons produced per 14 MeV source particle in HEU for various cargo materials.....	91
5-5 Interactions per delayed neutron source particle (1E-04) in center ONDAC detector for various cargo materials....	93
5-6 Radiative capture per delayed neutron emitted for various cargo materials.....	94
5-7 Neutron interactions per 14 MeV source particle in the center ONDAC detector for various cargo materials.....	95
5-8 Cargo comparisons to air by the ratio of interactions in the center ONDAC detector per 14 MeV source particle in air to that of each cargo material.....	96
5-9 Interference ratio of oxygen in air versus decay using benchmark facility dimensions.....	101
5-10 Neutron interactions per 14 MeV source particle in center ONDAC detector for various amounts of hydrogen in a cargo material composed of hydrogen, oxygen, and carbon based molecules.....	103
6-1 Effect of concrete shield thickness on the neutron mrem/hr dose rate in air as a function of concrete shield thickness per 14 MeV neutron emitted per second by the source using equation (6.1) (Cloutier 1963).....	106
6-2 Effect of concrete shield thickness on the neutron mrem/hr dose rate in air as a function of concrete shield thickness per 14 MeV neutron emitted per second by the source (Boerse and Van Werven 1966).....	107
6-3 MCNP model to calculate dose behind concrete shield.....	108
6-4 MCNP dose rate per 14 MeV source neutron/sec emitted through concrete.....	109
7-1 Neutron gain by fissioning in HEU with cargo container material in air, iron, and lead versus distance of source from container side.....	114
7-2 Interactions in center ONDAC per 14 MeV source particle in air, iron, and lead versus distance of source from container side.....	116

FIGURES (Continued)

Figure		Page
7-3	Normalized interaction in the center ONDAC detector with source 1 foot outside container for cargo materials air, iron, and lead as a function of source distance from side of container.....	117
8-1	SABRINA representation of benchmark facility.....	122
8-2	Activity versus time during the examination process with iron designated as the cargo material.....	130
8-3	Activity versus time during the examination process with aluminum designated as the cargo material.....	131
8-4	Activity versus time during the examination process with lead designated as the cargo material.....	132
8-5	Activity versus holding time for iron cargo.....	133
8-6	Activity versus holding time for aluminum cargo.....	134
8-7	Activity in lead cargo versus holding time.....	135
8-8	Experimental set-up of the USNA irradiation experiment...	136
8-9	Sample of the iron, aluminum, and lead material irradiated in the USNA irradiation experiment.....	137
8-10	12 cm distance between the neutron generator and the material sample.....	138
8-11	Picture of the AN-PDQ-1 with DT-680 probe used to monitor the irradiation of iron, aluminum, and lead samples during the USNA irradiation experiment.....	139
8-12	Dose rate per kilogram of aluminum, iron, and lead after irradiation.....	140
9-1	One of many container shipping yards in Baltimore Port...	145
9-2	Container being moved at the Port of Baltimore.....	145
9-3	Container ship and container loading operations in port..	146
9-4	Layout of the Port of Baltimore.....	147
9-5	Standard radiation caution symbol.....	151
9-6	Site controlled area layout.....	161
9-7	Top view of design A (tunnel version 1).....	163
9-8	3-D view of design A (tunnel version 1).....	163
9-9	Top view of design B (tunnel version 2).....	165
9-10	End view of design B (tunnel version 2).....	166
9-11	Top view of design C (subterranean version 1).....	167
9-12	Side perspective of design C showing outer shape of the underground facility.....	168
9-13	Side perspective of design C showing relation to surface.	168
9-14	Side perspective of design C showing size of tunnel and location of neutron generator and ONDAC detectors.....	169
9-15	Top view of design D (subterranean version 2) (outer concrete walls not shown).....	170
9-16	Perspective view of design D showing relationship to surface and circular path of containers (subterranean version 2).....	171

FIGURES (Continued)

Figure	Page
10-1 U ²³⁵ gamma spectrum with HPGe detector and 2000 channel MCA (St. John, 2002).....	174
10-2 Pu ²³⁹ gamma spectrum with HPGe detector and 4500 channel MCA (channels 1-2000) (St. John, 2002).....	175
10-3 Pu ²³⁹ gamma spectrum with HPGe detector and 4500 channel MCA (channels 2000-4500) (St. John, 2002).....	176
10-4 Pu ²⁴⁰ gamma spectrum with HPGe detector and 4000 channel MCA (St. John, 2002).....	177
10-5 4 kg plutonium gamma spectrum for volume and surface source modeled as 10 bins between 100 and 1057 KeV.....	180
10-6 MCNP model of container with plutonium source and single PVT detector located at container midplane.....	181
10-7 PVT detector gamma interaction rate as a function of its distance from container midplane with no cargo.....	182

TABLES

Table		Page
1-1	Neutron production rate from cosmic rays and self-fissioning in HEU and reactor grade (RG) plutonium.	4
1-2	Example list of acceptable and not acceptable container cargo description (24-Hour Advance Vessel Manifest Rule, 2003).....	9
1-3	VACIS characteristics (SAIC, 2003).....	15
1-4	Mass attenuation coefficients for 1.25 MeV gamma in ten different materials.....	16
1-5	Thickness of materials that would appear as the same material density as 1 kg of HEU in VACIS.....	21
1-6	Typical portal monitor system characteristics (Exploranium, 2002).....	23
1-7	Number of gammas emitted for each energy in HEU between 143 KeV and 222 KeV per 100 decays.....	28
1-8	Summary of parameters to determine the number of counts from gamma spectroscopy for 1 kg of HEU.....	31
2-1	Types, physical dimensions, and general uses of maritime containers.....	36
4-1	Potential pulsed 14 MeV neutron generator procurement sources.....	59
4-2	Average energies for the Batchelor, Bonner, and Burgy energy spectra.....	75
4-3	Summary of five energy spectra MCNP computer run time and relative error.....	76
4-4	Recommendations for operational conditions to be applied when examining shipping container with pulsed 14 MeV neutron source and counting delayed neutrons.....	78
5-1	Numerical summary of MCNP cargo analysis.....	82
5-2	Summary of nuclear interactions and mean path lengths for different cargo materials.....	83
5-3	Calculation of 1 MeV and 14 MeV macroscopic radiative cross-sections for various cargo materials.....	89
5-4	Calculation of 1 MeV and 14 MeV slowing down powers for various cargo materials.....	90
5-5	Cartesian coordinates of the three ONDAC detectors and the HEU and the distances to the HEU for each ONDAC detector in MCNP model.....	97
5-6	Ratio of the center ONDAC interaction rate to the side ONDAC interaction rate compared to the mean free path length by source energy for each cargo material.....	98
5-7	Density and weight of cargo materials examined.....	99
5-8	Comparison of the delayed fission neutron interactions per 14 MeV source particle in the center ONDAC detector of carbon and alcohol under identical conditions with the MCNP facility model.....	102

TABLES (Continued)

Table	Page
7-1 Source position data.....	112
7-2 Numerical summary of neutron gain by fissioning in HEU per 14 MeV source particle with varied distances of the source to the side of container.....	113
7-3 Numerical Summary of delayed fission neutrons produced in HEU per 14 MeV source particle with varied distances of the source to the side of the container.....	114
7-4 Numerical summary of interactions in center ONDAC per delayed neutron source particle for air, iron, and lead.	115
7-5 Interactions in center ONDAC per 14 MeV source particle for air, iron, and lead for various distances between the source and side of cargo container.....	115
8-1 Recommended times during the examination period.....	118
8-2 Data table of natural isotopes of iron that shows their atom fractions, atomic numbers, neutron activated reactions, the reaction's half-life, decay constant, and the 14 MeV microscopic cross sections for absorption....	120
8-3 Data table for aluminum which shows the neutron activated reactions, the reaction's half-life, the decay constant, and the 14 MeV microscopic cross sections for absorption	121
8-4 Data table of natural isotopes of lead that shows their atom fractions, atomic numbers, neutron activated reactions, the reaction's half-life, decay constant, and the 14 MeV microscopic cross sections for absorption....	121
8-5 Parameters and values used to find the saturated activity	123
8-6 Saturated activity for each of iron's isotopes reactions.	124
8-7 Saturated activity for the neutron activated reactions of Al^{27}	124
8-8 Saturated activity for each of lead's isotopes reactions.	125
8-9 Data for estimating effect in average distance procedure between cargo drums and the source.....	127
8-10 Activity in Curies for iron during the first ten cycles of the examination period.....	129
8-11 Mass of each specimen used in the USNA irradiation experiment.....	139
8-12 Summary of theoretical and experimental 14 MeV neutron activation study for aluminum, iron, and lead.....	140
8-13 Summary of weight and time for irradiated material to reach background after 14 MeV exposure to a neutron flux of 1.68×10^7 n/cm ² sec for 139.2 sec.....	141
9-1 Information on shipping containers for Port of Baltimore in 2003 (Costello, 2003).....	148
9-2 Pay chart for U.S. Customs officials in Baltimore area (30% overhead), 2003.....	154
9-3 Annual investment per person, effective October 1, 2002, for monthly, bimonthly, or quarterly service.....	155

TABLES (Continued)

Table	Page
9-4 Annual dosimetry costs for necessary personnel/visitors..	156
9-5 Cost to build and operate a neutron stimulation facility for the first year.....	157
9-6 Cost for subsequent years of neutron stimulation operation.....	158
9-7 Comparison of costs per year between unloading containers and facility operation.....	158
9-8 Percentage of containers that will be inspected at the Port of Baltimore as a function of the hours the facility is open per week.....	159
10-1 Gamma energy and intensity for decay of U^{235} (ICRP, 1983).	173
10-2 Summary of key gamma energies emitted by HEU and reactor grade plutonium.....	177
10-3 Single naturally occurring radioisotopes present in cargo materials which are gamma emitters (Eisenbud, 1987).....	178
10-4 Gamma energies of radioisotopes in thorium series (Cember, 1983).....	178
10-5 Gamma interactions/sec with single mid-plane PVT detector and with entire container (243.8 cm x 605.8 cm x 259.1 cm) surrounded by PVT detector with 4 kg plutonium source in container center.....	183
10-6 Potassium-40 concentration in food.....	183
11-1 Comparison of basic parameters in both benchmark and scaled neutron stimulation facility assuming a pulsed source strength of 3×10^8 n/sec	189
B-1 Source location and width position of cargo drum rows used in the USNA MCNP cargo container model.....	B-1
B-2 X-position of each of the five container lengthwise distances.....	B-2
B-3 Twenty straight-line distances between the source and the cargo drums, used to calculate the average distance neutrons travel in the container.....	B-3
C-1 Penetration distance for Cs^{137} and Co^{60} in lead and platinum.....	C-4

ACKNOWLEDGEMENTS

The authors are deeply indebted to Mike Evenson, Derek Mahin, and Dr. Karen Hirsch at the Defense Threat Reduction Agency for their advice and guidance during the project. Without their support, this project would not have been possible.

At the US Naval Academy the authors are very grateful to Mr. Kelly Delikat, who provided substantial computer assistance throughout the project. Also the authors would like to thank CDR Matt Carr of the Mechanical Engineering Department for the mentorship he provided to midshipmen who worked on the project during the 2003-2004 academic year.

The authors would also like to acknowledge Eric Abkemeirer of the Naval Radiological Affairs Support Office in Yorktown, Virginia for the consultation he provided regarding regulatory matters on accelerator produced activation productions. From the Strategic Systems Program Office, LCDR Marshall Millett gave invaluable assistance in the development of the MCNP cargo container model used by the project. Next the authors would like to thank Dr. Matt Forsbacka, Defense Nuclear Safety Board, who provided reference information on highly enriched uranium. Also, the authors would like to thank both R. Costello of the Baltimore Port Authority and D.J. Austin of the US Customs Office for the cooperation in providing information concerning Baltimore port operations. Lastly, the authors are very appreciative of a number of individuals at different organizations such as Lawrence Berkeley National Laboratory, Sandia National Laboratory, Halliburton, MF Physics, and the Naval Research Laboratory who gave of their time and insights in discussions with project personnel.

SECTION 1

BACKGROUND AND STATEMENT OF PROBLEM

The illegal entry of special nuclear material (SNM) into the United States poses a significant security threat. This report studies the feasibility of one technique that potentially could be applied to detect SNM in a specific scenario. SNM consists primarily of fissile material such as highly enriched uranium (HEU) or reactor-grade plutonium. For the purposes of this study, HEU has been taken to be 93% U^{235} and 7% U^{238} . The major isotopes of reactor-grade (RG) plutonium are Pu^{239} and Pu^{240} . The International Atomic Energy Agency (IAEA) monitors the illicit trafficking of SNM. From January 1, 1993 to April 1, 2001, the IAEA recorded over 180 nuclear smuggling incidents involving more than 40 countries (Anzelon 2001). There is no treaty that requires countries to protect their weapons-usable material from being stolen (Bunn and Bunn 2001). This results in a global problem that leaves the illegal entry of SNM into the United States as a significant threat. A major concern is that SNM can cause significant damage if it is used as a crude nuclear device. Specific measures must be taken to monitor and interdict nuclear smuggling. Complicating this task is that the system(s) chosen for SNM detection must yield results in a relatively short period of time, produce a signal that can be readily interpreted by the operator, not be easily defeated by shielding materials, and be relatively inexpensive.

SNM can be detected by either active or passive techniques from their photon and neutron signatures. In an active technique, an external photon (i.e. x-ray or gamma) or neutron beam is applied to the container or package to be interrogated. In contrast, a passive technique involves the measurement of photons or neutrons from either the SNM isotopes or their decay products. There are two principal sources of neutron emissions from SNM. First, they can undergo fissioning or neutron producing reactions such as (n,2n) from cosmic-ray induced neutrons. Second, they can self-fission. However, the relative importance of these two reactions can vary significantly between different SNM isotopes.

SNM nuclear properties are briefly discussed for use in passive and active detection techniques from either photons (i.e. gammas or x-rays) or neutrons in sections 1.1 through 1.4. Well-logging and nondestructive nuclear waste assaying techniques are reviewed in sections 1.5 and 1.6 for their usefulness to detect SNM. Section 1.7 describes the Container Security Initiative (CSI) and how the U.S. Customs Service implements the program with respect to containers arriving at U.S. ports. Three non-intrusive technologies are reviewed in the next three sections that are either in use or under consideration for use at U.S. ports to determine their

vulnerabilities and whether there is a need for supplemental technologies such as external neutron stimulation. Section 1.8 reviews the Vehicle and Cargo Inspections System (VACIS). Next the Portal Monitoring System is examined in section 1.9. Finally section 1.10 discusses the Radiation Isotope Detector. Section 1.11 describes the basic SNM detection problem analyzed in this report, which is the use of active neutron stimulation to detect 1kg of HEU in a large shipping container. Finally, section 1.12 outlines the method of approach used to analyze this problem in this report.

1.1 SNM NUCLEAR PROPERTIES AND PASSIVE GAMMA DETECTION.

For passive gamma detection, U^{235} dominant gamma emission lines occur between 143 KeV and 222 KeV as shown in figure 1-1. When U^{235} undergoes alpha decay, Th^{231} is produced and this isotope has major gamma lines between 25 KeV and 163 KeV. Pu^{239} has its dominant gamma lines that extend between 38 KeV to 769 KeV, while Pu^{240} main gamma lines fall between 45 KeV and 160 KeV. When plutonium is produced in a reactor, nuclear transmutations occur which produce Am^{241} . However, the major gamma lines of Am^{241} have energies comparable to that of Pu^{239} (Sowby 1983). The intensity of the gamma emission from an isotope is directly proportional to the isotope's half-life. U^{235} has a half-life of approximately 704 million years, while Pu^{239} has a half-life of nearly 24 thousand years. Consequently, the gamma signature from U^{235} or HEU is much weaker than that from Pu^{239} or reactor grade plutonium. High atomic number materials are very effective at shielding gamma rays whose energies are less than 200 KeV (LaMarsh 2001). The above facts make the passive detection of HEU difficult to detect in a field environment, where time, cost, and simplicity are important factors. Still considerable effort has still gone into the detection of SNM using the passive gamma techniques. The portal monitoring system, which is discussed in section 1.9, and the Radiation Isotope Detector, which is discussed in section 1.10, are two systems that are based on this approach.

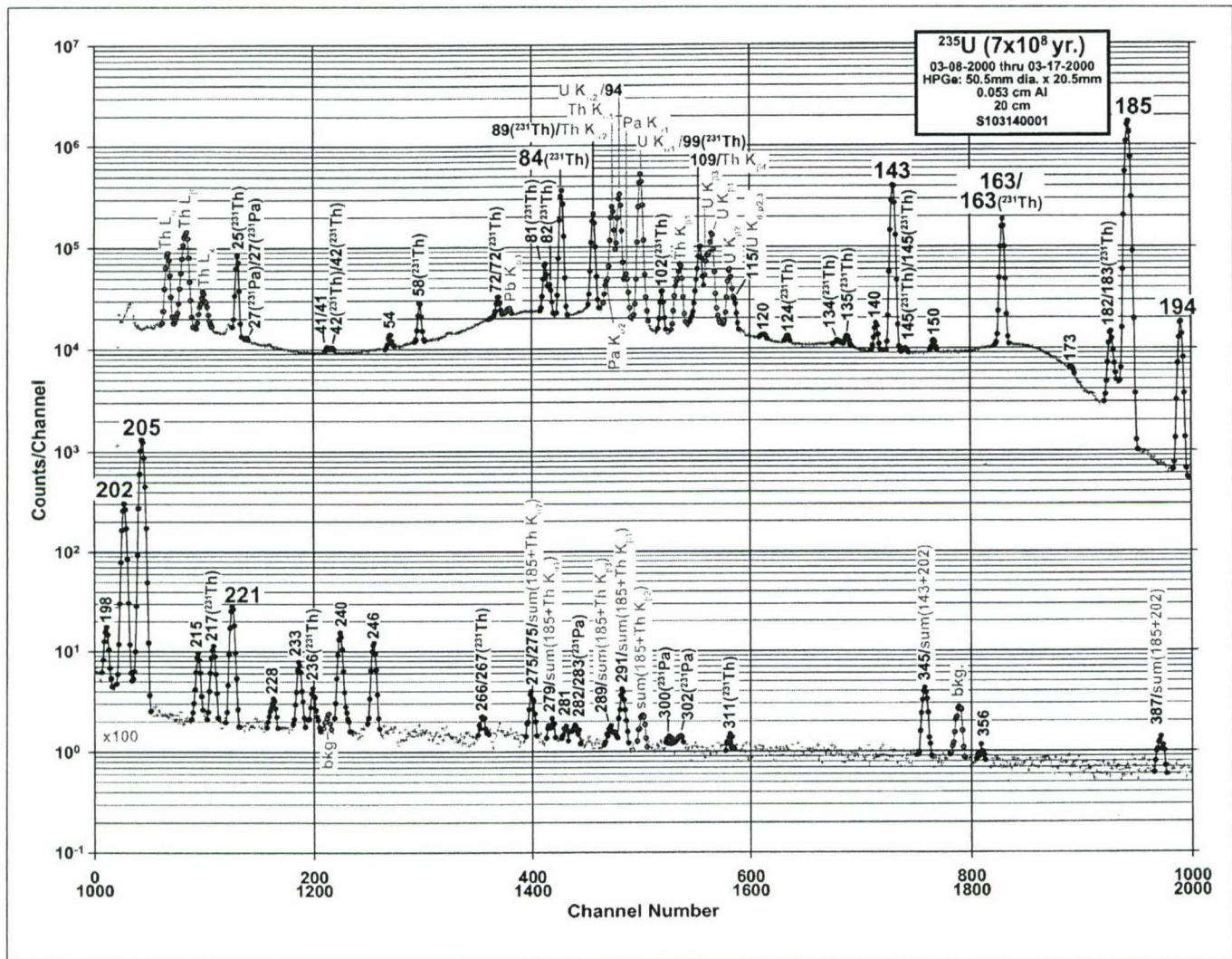


Figure 1-1. Photon emissions for U^{235} (St. John, 2002).

1.2 SNM NUCLEAR PROPERTIES AND PASSIVE NEUTRON DETECTION.

For passive neutron detection, cosmic ray neutron production potentially could be helpful. A recent USNA study has measured the cosmic ray thermal neutron flux in the Annapolis, Maryland area (Dirk 2000). This study concluded that the ambient thermal flux had a value of 6 neutrons/cm² hr within a factor of 2. Using this flux, the neutron emission rate (S) can be directly calculated using equation (1.1) below for either 1 kg of HEU or Pu²³⁹.

$$S = v \Sigma_f \phi V \quad (1.1)$$

where

- v = average number of neutrons released per fission, 2.42 for HEU and 2.87 for Pu²³⁹
- Σ_f = macroscopic fission cross section of HEU or Pu²³⁹, 27.8 cm⁻¹ for HEU and 36.7 cm⁻¹ for Pu²³⁹

ϕ = ambient thermal flux, 6 n/cm² hr
 V = volume of 1kg of either HEU or plutonium, 50 cm³

Equation (1.1) predicts a cosmic ray neutron production rate of approximately 2.0×10^4 n/hr kg for HEU and 3.2×10^4 n/hr kg for Pu²³⁹ or reactor grade plutonium. U²³⁸ and Pu²⁴⁰ can be neglected in this calculation as neither fission with thermal neutrons. In HEU, the self-fissioning half-lives of U²³⁵ and U²³⁸ are respectively 9.8×10^{18} years and 8.2×10^{15} years. Thus, 99% of the self-fission neutrons in HEU come from U²³⁸. In reactor- grade plutonium the self-fissioning half-lives of Pu²³⁹ and Pu²⁴⁰ are respectively 7.8×10^{15} years and 1.2×10^{11} years, which means that Pu²⁴⁰ dominates self-fissioning. Thus the self-fissioning neutron production rate in reactor grade plutonium is 1.3×10^9 neutrons/hr kg, while HEU would only yield 1.4×10^4 neutrons/hr kg (Millett 1997). These results are summarized in table 1-1.

Table 1-1. Neutron production rate from cosmic rays and self-fissioning in HEU and reactor grade (RG) plutonium.

Material	Cosmic ray neutrons neutrons/hr kg	Self-fissioning neutrons neutrons/hr kg	Total neutron production rate Neutrons/hr kg
HEU	2.0×10^4	1.4×10^4	3.4×10^4
RG Plutonium	3.2×10^4	1.3×10^9	1.3×10^9

The above results indicate that 1 kg of HEU will be much more difficult to detect compared to reactor grade plutonium by passive neutron methods as the source emission rate per kg is over four orders of magnitude smaller.

Considerable effort has been devoted by government agencies to developing systems which would detect neutrons from SNM by passive means. One of many examples that could be provided is that Los Alamos National Laboratory (LANL) has developed vehicle monitors using wide array plastic scintillators to detect neutron emissions from SNM (Fehlau 1987). These systems are very expensive and for reasons discussed above have much greater success in detecting plutonium than HEU.

1.3 SNM AND ACTIVE PHOTON DETECTION TECHNIQUES.

The US Customs Service (USCS) has reviewed a number of non-intrusive active technologies for seaport cargo inspection systems (Lindquist 2001) based on the use of x-rays and gamma rays. For example, radiographic inspections or low dose x-ray ($E_{xray} = 160$ KeV) methods as found at airports are popular, because of their relatively low cost and simplicity of use. Fixed truck x-ray systems (TXR) have been evaluated to inspect commercial vehicles entering the United States.

However, fixed systems are very susceptible to circumvention by smugglers. Recently, the USCS has been evaluating mobile truck x-ray systems coupled with increased power and size capacity. Two such systems that are now commercially available include the CX-450M (L-3 Communications, 2003) and the Mobile Search System (AS&E, 2003). Both of these systems use x-rays generated at approximately 450 kVp. The USCS has decided that the maximum energy of photon source should be 6 MeV. 6 MeV was chosen in order to provide a penetration, while keeping the integrity of the non-destructive testing techniques that could cause products to be altered. Additionally the USCS has been evaluating the uses of gamma ray sources such as Cs^{137} ($E_\gamma = 0.662$ MeV) and Co^{60} ($E_\gamma = 1.17$ and 1.33 MeV). The VACIS system which is described in section 1.8, is based on the use of this technique with either of these isotopes. Imaging is also very important in cargo inspection quality and substantial progress has been made in this area (Moore 2002). Low energy x-rays and gamma rays are significantly attenuated by high density materials, such as lead and SNM itself. This leads to the concern that a smuggler could shield the SNM and it would go undetected.

1.4 SNM AND ACTIVE NEUTRON TECHNIQUES.

Active neutron techniques have been proposed by several groups. Thermal neutron radiography has been suggested to image light elements, such as hydrogen, carbon, and nitrogen (Berger 1965). This technique has been modified by using fast neutrons at different energies and mathematically treating the different images created as a set of linear equations, which can then be solved for the container contents (Chen 2001). This detector has shown good potential for drug and explosives, but has not been applied to heavy elements, such as uranium. Two pulsed 14 MeV neutrons systems have been studied. First, the SeaVEDS system, which is currently under development, consists of a neutron generator, gamma ray detectors, and a data acquisition decision computer (Gonzani 2001 and Brown 2001). In this system, the container contents are determined by performing gamma spectrum analysis on the activated material. Second, Los Alamos National Laboratory has developed an active neutron interrogation package monitor (Rooney 2002). This system also consists of a pulsed 14 MeV neutron source and detector cells containing three He^3 tubes surrounded by polyethylene with a cadmium liner that is used to detect any neutrons that would be emitted by SNM within the container. Both these systems are designed to interrogate relatively small containers or packages. Also no lower limit of detection is given for these systems to detect a given mass of either HEU or RG plutonium.

1.5 SNM DETECTION AND WELL-LOGGING TECHNOLOGY.

Well-logging is an established technique used in the oil service industry for oil and natural gas exploration. In this technique,

fast neutrons are emitted from a source and enter a borehole. The resulting neutron interactions produce both gammas and neutrons. The spatial distribution, relative intensity, energy distribution, and/or time distribution of these neutron and gammas are directly related to the porosity and type of fluids in the borehole (Smith 1979). Many different tools have been developed for application of this technique, nearly all of which are patented and proprietary. The detectors used count either gammas, prompt fission neutrons (PFN), or delayed fission neutrons (DFN). However, the use of pulsed 14 MeV neutrons sources are widely used by commercial vendors when applying this technique (Halliburton 2002; Schlumberger 2002). The use of well-logging techniques with 14 MeV pulsed sources has been investigated to assay for uranium in the soil with success obtained for ore-grades of 0.22 weight % U_3O_8 (Givens 1976) and for 1.0 weight % uranium ores (Czubek 1972). These studies concluded that counting DFN was the best approach to this problem.

A major difference exists in concentration levels between well-logging applications and the SNM cargo detection problem. A large 20' x 8' x 8' cargo container typically would have a maximum payload of 30,000 kg. In the situation where the container possessed one kg of SNM, the weight percent of the SNM would be only 0.003%. Unfortunately this concentration is two or more orders of magnitude smaller than the uranium detected by either Givens or Czubek. Because of the proprietary nature of well-logging tools, no literature appears to exist on the lower limits of detection for this technology. It was concluded that the current commercially off-the-shelf (COTS) well-logging tools would not be applicable to the SNM problem. However, this approach did provide strong motivation for the technical solution developed by this study.

1.6 SNM DETECTION AND NON-DESTRUCTIVE NUCLEAR WASTE ASSAYING.

The Department of Energy (DOE) and its contractors have spent considerable effort developing assay technologies. The DOE has also sponsored a number of Nondestructive Waste Assay Conferences, which describe many different methods, techniques and instruments that have been developed to measure transuranics that have been stowed in thousands of 55 gallon drums. Presently the DOE uses the following technologies: (1) NaI gamma counting; (2) passive neutron coincidence counting (PNCC); (3) passive/active neutron counting (PAN); and (4) radiochemistry. The PAN instrument, which contains an external neutron source, was developed at LANL (Caldwell 1986) and has undergone numerous enhancements and variations. New instruments are under development such as the combined thermal/epithermal neutron system (CTEN). This instrument uses thermalized neutrons from a pulsed 14 MeV neutron generator to irradiate and then interrogate radioactive waste drums (Melton 1998). Depending on the drum contents, measurement times are 40 to 200 seconds, with Pu^{239} sensitivities ranging from one to fifty milligrams. Another new

development is combining modern imaging systems with the above technologies, such as the imaging passive/active neutron system (IPAN) employed at Hanford (Hanford 2002). While these systems have very low limits of detection, their success is contingent on placing the neutron source in close proximity to the SNM within the container. In the scenario described in the next subsection, such source positioning is not possible since the shipping container will be much larger in size than a 55 gallon waste drum.

1.7 CONTAINER SECURITY INITIATIVE.

In this section the Container Security Initiative (CSI) (US Customs Service, 2002) is discussed in detail. The CSI is a relatively new inspection program that encompasses container tracking, cargo declarations, and current non-intrusive inspection technologies. The program is controlled by the U.S. Customs Service, and is used to combat the smuggling of illegal materials into the U.S. The CSI background is presented in section 1.7.1, and the initial CSI steps and risk evaluations completed prior to the vessel arriving in the U.S. are detailed in section 1.7.2. Section 1.7.3 outlines the role of the CSI program once the vessel arrives in the U.S. and the containers are offloaded.

1.7.1 Container Security Initiative Background.

The Container Security Initiative is a new process, which was fully implemented in February, 2003. In the CSI process carriers must provide a cargo declaration, or a manifest, detailing information about the containers and the cargo being transported. The purpose of the CSI is to provide the means for the U.S. Customs to track and monitor all goods being imported into the United States. When a container is loaded with cargo, laden on a vessel at a foreign port, and brought into the United States, each container follows a similar path regardless of the port of entry. Figure 1-2 shows the basic container path outline, and figure 1-3 provides in great detail a typical path that a container takes while entering the United States, specifically at the Port of Baltimore. The importance of knowing a typical container path is necessary to determine where the neutron stimulation facility would have to be placed within this flow path. A logical position for the placement of the neutron stimulation facility is shown as a darkened box in figure 1-3.

The four goals of the CSI are: (1) using automated information to identify and target high-risk containers; (2) pre-screening those containers identified as high-risk before they arrive at U.S. ports; (3) using detection technology to quickly pre-screen high-risk containers; and (4) using smarter, tamper proof containers (U.S. Customs Service, 2002).

1.7.2 CSI Steps Prior To Containers Arriving in the United States.

In coordination with the CSI flow chart a detailed explanation of the process is necessary. The first step in the CSI process is the vendor, the owner of the cargo, will load the cargo into the cargo containers. The contents of the container are completely listed in detail. This list is referred to as the container manifest. Table 1-2 shows an example list of acceptable and not acceptable container cargo descriptions. A document titled "24-Hour Advance Vessel Manifest Rule" provides this list (US Customs Service, 2003). The container declarations are given to the carriers, and the carriers must submit the manifest 24 hours prior to loading the cargo onto a vessel. The manifest can be sent electronically to the U.S Customs Service through a program called the Sea Automated Manifest System (AMS) (US Customs Service, 2003). If the manifest is not submitted prior to the 24 hours required, then a "Do not load message" from the U.S. Customs will stop the carrier from loading the containers onto the vessel (US Customs Service, 2003).

Once the manifest is sent to the U.S. Customs Service, the container risks are evaluated. The cargo is determined to be a high or low risk. The level of risk is based on five criteria. The port location, cargo description, shippers name and address, consignee and to order bill, and the seals on the containers are the five areas that determine the level of risk. The port location must specify the name of the port where the cargo is destined. Familiar ports such as those from Japan and Europe would have a lower risk value associated with it as compared to a port that provides few exports destined for the U.S. The cargo description must be accurate and detailed. Information about the shipper must be accurate and in depth rather than providing broad information regarding the business of the shipper. The consignee and to order bill provides the name of the cargo owner or a representative for the owner. Like the ports, the more familiar the U.S. is in doing business with a particular owner, the greater the trust and security. This familiarity contributes to lowering the risk level. The seals on the containers must have seal numbers and there must be no evidence of any seal tampering. The cargo owners, in coordination with the shippers, put these seals in place or provide seal numbers, and the carriers are also responsible for checking the seal numbers (US Customs Service, 2003).

Each risk evaluation criteria is reviewed once the local U.S. Customs agents receive the manifest. If the risk level is high, the containers are inspected at the foreign ports. If any problems in the manifest or container inspection are identified, then a "Do no load message" will be created. The carrier must correct any discrepancies and the cargo declaration process then begins once again. Lower risk containers are still subjected to random searches

by U.S. Customs agents or by local authorities (under supervision of the U.S. Customs agents). The containers are loaded onto the vessel when the risk evaluation and inspection process are complete (Austin, 2003).

Table 1-2. Example list of acceptable and not acceptable container cargo descriptions (24-Hour Advance Vessel Manifest Rule, 2003).

Not Acceptable	Acceptable
Apparel, Wearing Apparel Ladies' Apparel, Men's Apparel	Clothing, Shoes, Jewelry (may include watches)
Appliances	Kitchen Appliances, Industrial Appliances, Heat Pump
Autoparts, Parts	New Autoparts, Used Autoparts
Caps	Baseball Caps, Blasting Caps, Bottle Caps, Hub Caps
Chemicals, hazardous Chemicals, non-hazardous	Actual Chemical Name (not brand name) Or U.N. HAZMAT Code Identifier #
Electronic Goods Electronics	Computers, Consumer Electronics, Telephones, Electronic Toys (can include Gameboys, Game Cubes, Dancing Elmo Doll etc.), Personal/Household Electronics (PDA's, VCR's, TV's)
Equipment	Industrial Equipment, Oil Well Equipment Automotive Equipment, Poultry Equipment etc.
Flooring	Wood Flooring, Plastic Flooring, Carpet, Ceramic Tile, Marble Flooring
Foodstuffs	Oranges, Fish, Packaged Rice, Packaged Grain, Bulk Grain
Iron	Iron Pipes, Steel Pipes
Steel	Iron Building Material, Steel Building Material
Leather Articles	Saddles, Leather Handbags Leather Jackets, Shoes
Machinery	Metal Working Machinery Cigarette Making Machinery
Machines	Sewing Machines, Printing Machines Personal Effects, Household Goods
Rubber Articles	Rubber Hoses, Tires, Toys Rubber Conveyor Belts
Rods	Welding Rods, Rebar, Aluminum Rods Reactor Rods
Scrap	Plastic Scrap, Aluminum Scrap, Iron Scrap
STC (Said to Contain), General Cargo, FAK (Freight of All Kinds), "No Description"	
Tools	Hand Tools, Power Tools ,Industrial Tools
Tiles	Ceramic Tiles, Marble Tiles
Wires	Electric Wires, Auto Harness Coiled Wire (Industrial)
Pipes	Plastic Pipes, PVC Pipes, Steel Pipes Copper Pipes
Plastic Goods	Plastic Kitchenware, Plastic Houseware, Industrial Plastics, Toys, New/Used Auto Parts
Polyurethane	Polyurethane Threads, Polyurethane Medical Gloves

1.7.3 CSI Role Upon Container Arrival into the Port of Baltimore.

The next step in the process is for the vessel to travel to the U.S. If the vessel stops at a foreign port and additional containers are loaded onto the vessel, then the carrier is again responsible for listing the changes in cargo and destination. The additional containers must have their own manifests and must go through the risk evaluation process. The U.S. Customs Service and the local port authorities coordinate the activities of the vessel as it approaches and arrives at the off-load port. Some containers are simply off-loaded from the vessel onto another vessel and taken to another port. Yet, once the containers are off-loaded onto the pier, inspections are conducted on 5% of the containers at the Port of Baltimore (Costello, 2003). The off-loaded containers are typically placed on flatbed tractor-trailers. These vehicles are randomly inspected by the Mobile VACIS (Vehicle and Cargo Inspection Systems), or by Landed Quantity Verification (LQV). The details of the Mobile VACIS and its performance are provided in section 1.8 of this report. The LQV involves opening the containers and visually checking to see if the container contents match what is listed on the container manifests (Austin, 2003). The cargo is not off-loaded in this process.

The Mobile VACIS uses gamma radiation to penetrate the containers. On the opposite side of the gamma source, scintillation detectors measure the decrease in the gamma intensity. This information is processed into a display showing the container contents. The density of the material displayed is compared with what is actually in the containers according to the container manifests. Approximately 5% of the off loaded containers are actually inspected by the Mobile VACIS units. In both the LQV and Mobile VACIS inspection processes, if anything unusual is detected (such as a higher density material showing up in low density cargo - not in accordance with the manifest) the container contents are inspected by the opposite inspection that was initially performed. If nothing unusual is spotted, the containers are placed at a storage site within the port until the cargo owners arrive to pick up and move their property out of the port. Port authorities store containers at the Port of Baltimore for an average of 5 days (Costello, 2003). The ports have designated storage areas where containers are temporarily placed until the owners remove the containers. Typically the Port of Baltimore processes 2000 containers per week. Cost information concerning the handling of containers in the port of Baltimore is provided in Section 9.1. The time that each container is in port depends on when the cargo owner has scheduled time to pick up the container. Containers and their cargo contents leave by truck, rail, or other means.

While the containers are being stored they are subjected to random inspection using a radiation isotope detector. The radiation isotope detector is described in detail in section 1.10 of this report. The

detector is also used to inspect cargo not claimed by any owner, such as a small box of goods that may be separated from where it should be stored. Unknown items that are not immediately associated with know cargo shipments fall into this category and are inspected by the radiation isotope detector to determine if there is a radiological threat. Should anything unusual be found from the radiation isotope inspection then the cargo is passed through another inspection method (LQV or Mobile VACIS).

A portal monitoring system which is discussed in section 1.9, is currently being tested at Norfolk, Virginia. This system uses gamma sensitive scintillation detectors to determine the presences of a radiation isotope or any other element that may be giving off gamma radiation (Exploranium, 2002). The portal monitoring system will be used to inspect vehicles transporting the containers off the port property. This step in the inspection process is the last before the containers are no longer under the control of the U.S. Customs Service.

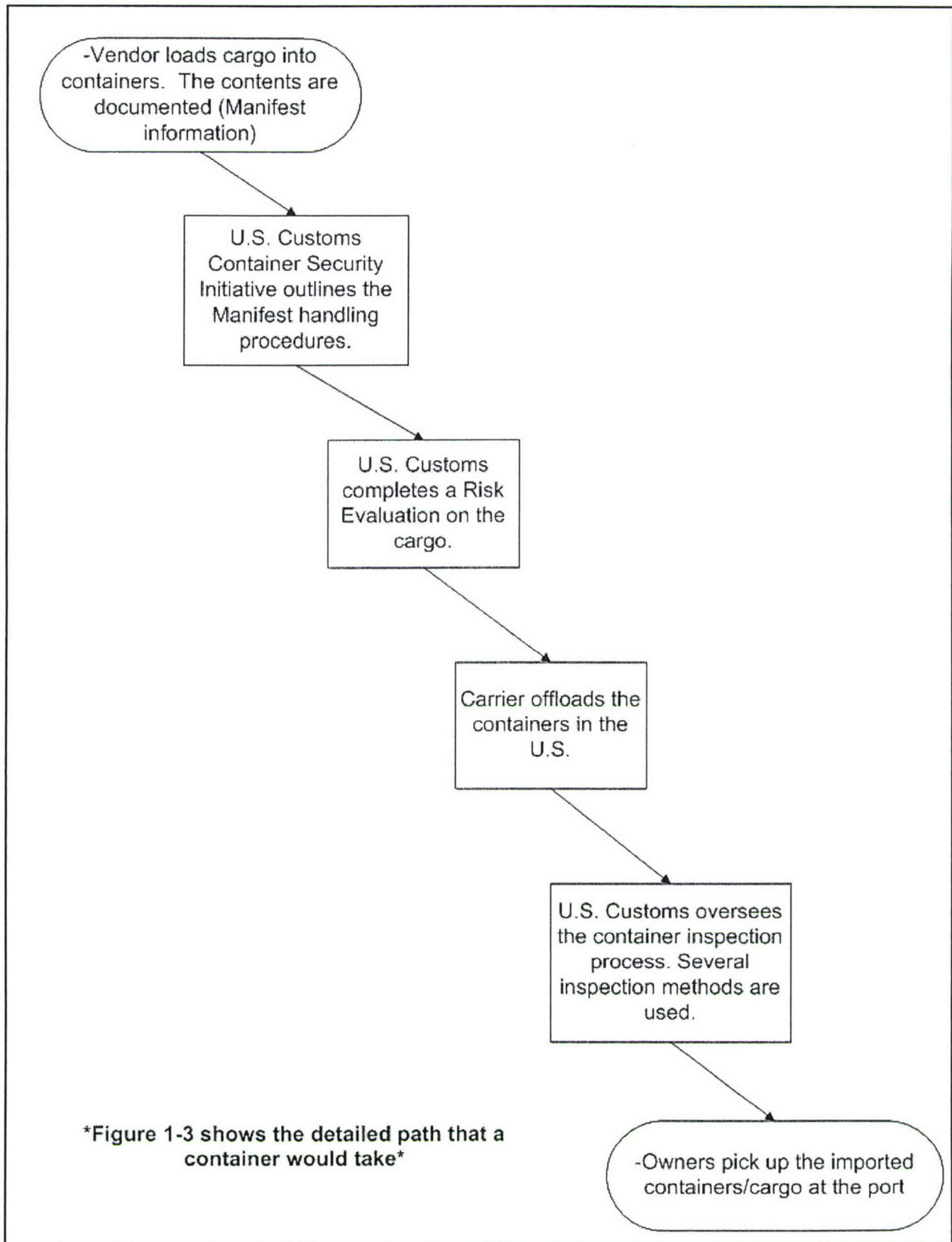
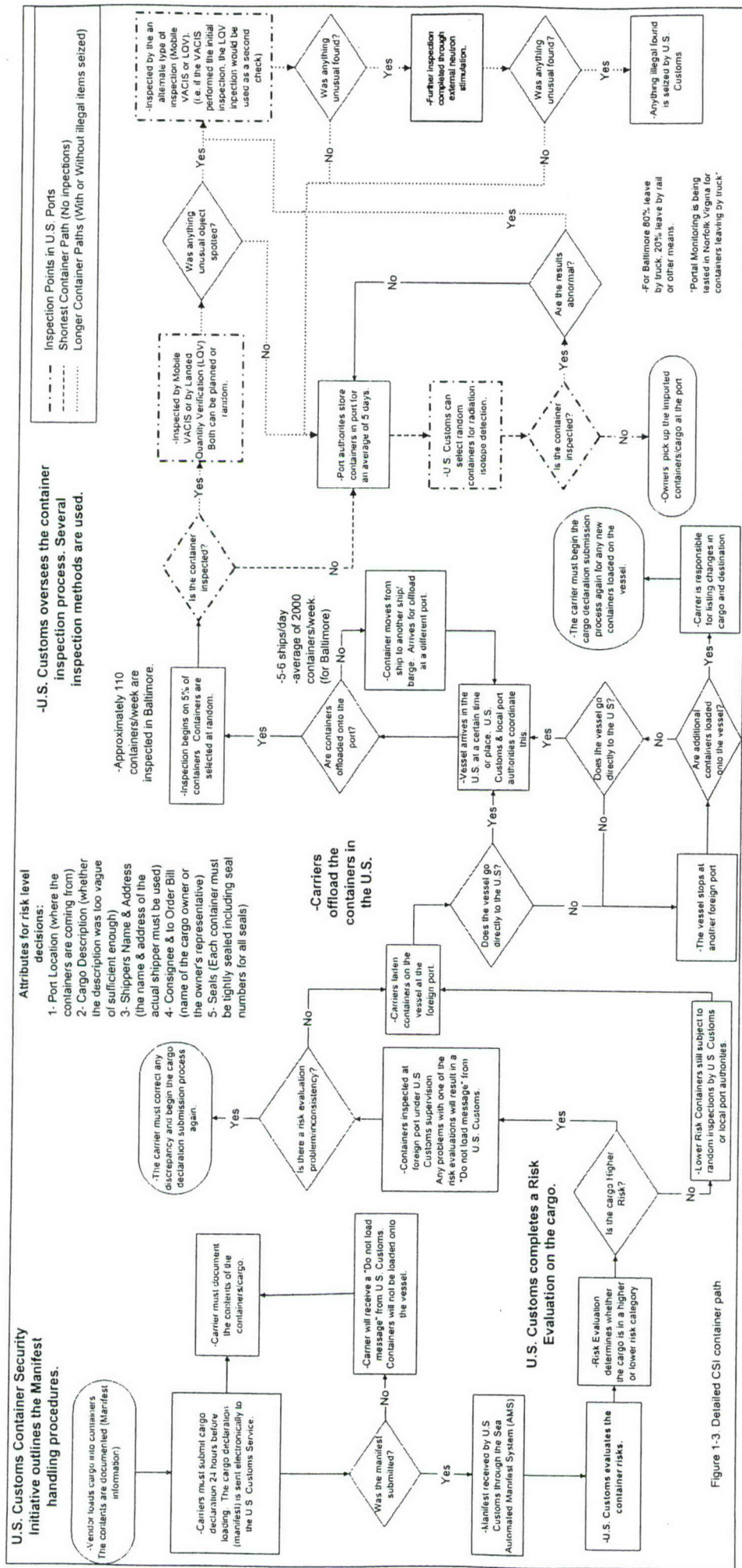


Figure 1-2. Container flowchart overview.



1.8 VACIS (VEHICLE AND CARGO INSPECTION SYSTEM).

In this section the Mobile VACIS is analyzed. The background and a history of the VACIS development are briefly discussed in section 1.8.1. The operation of the Mobile VACIS and how the cargo density is used to create the image is discussed in section 1.8.2. The radiation exposure that an operator or any other person would receive from system operation is prescribed in section 1.8.3. The vulnerabilities of the Mobile VACIS are discussed in section 1.8.4.

1.8.1 VACIS Background.

The VACIS was developed and first tested in 1998 as a non-intrusive detection system capable of providing an interior image of sealed cargo containers, trucks, and other vehicles. The purpose of such a device was to enable the U.S. Customs Service to identify illegal goods, primarily drugs, as they were smuggled into the country. The principle of the system is to measure the decrease in gamma intensity by placing a Cs-137 or Co-60 source on one side and a gamma detector on the other side of the container. Using this data an image of the container contents is produced, while the container or vehicle is never subjected to an extensive time consuming search.

The U.S. Customs Service, the Officer of National Drug Control Policy, and the Department of Defense initiated this project (Taylor, 2000). The Science Applications International Corporation (SAIC) developed the gamma ray detection technology (SAIC, 2003). The VACIS was designed by SAIC for many uses including fixed-site inspections, railcar inspections, and mobile inspections. The Mobile VACIS is used at shipping port of entries across the United States (Snell, 2001). A photo of the Mobile VACIS in operation is shown below in figure 1-4.



Figure 1-4. Mobile VACIS in use, inspecting containers at a port (Americana Impex Consulting Co, 2003).

1.8.2 VACIS Operation.

Gamma emitting sources, either Cs¹³⁷ or Co⁶⁰, are stored within a steel and tungsten housing. The Mobile VACIS uses the Co⁶⁰ source that emits 1.17 MeV and 1.33 MeV gammas. The source and housing container are placed on the opposite side of a container from the detection array. The array consists of 256 NaI photo-multiplier scintillation detection counters. The array is designed to minimize the image distortion and provide adequate resolution. Some of the specific system design characteristics are listed in table 1-3.

Table 1-3. VACIS characteristics (SAIC, 2003).

1. The spatial resolution for the Mobile VACIS is stated by the vendor to be 9 mm (0.345 inches).
2. The NaI detectors are each only 1.125 in ² in size. The use of many small detectors helps increase the spatial resolution, reduce the noise level, and improve the image quality.
3. The Co-60 source has an activity of 0.75 Ci, and an average gamma ray energy of 1.25 MeV. The Cs-137 source is used in rail VACIS systems, so it is not examined in this study.
4. The penetrating distance for the Mobile VACIS, using the Co ⁶⁰ source, is 6.5 inches (16.5 cm) of steel. Steel thicker than 6.5 inches attenuates the gammas to a level where they can no longer get an accurate image. To achieve the maximum penetration the scan time must be slowed to approximately 0.911 feet per second.
5. The intensity of the beam cannot be changed since the source decay and gamma energy are constant (in an x-ray detection system, the intensity of the x-ray can be varied).
6. The scan area is 13 feet high x 8 feet wide. There are no restrictions on the length of the cargo.
7. The scanning speed is monitored and the image (similar to a highly detailed x-ray image) is corrected for any change in scanning speed. This correction is intended to minimize any distortions in the image geometry.

For more specific information regarding the Mobile VACIS further information is found in the Mobile VACIS (Vehicle & Cargo Inspection Systems) section of appendix C.

The intensity of the uncollided gammas detected by the scintillation counter after passing through the material determines the density of the material being scanned. Gammas, which undergo scattering collisions crossing the container will lose energy and can be distinguished from those gammas which undergo no collisions by the NaI detector. Materials of different densities show up as different scales of gray in a black and white image. Materials of similar densities are not easy to distinguish. A program called "pseudo-color" is used to display small density differences in color instead of black and white (Richardson, Verbinski, and Orphan, 2001).

The uncollided gamma intensity decreases exponentially across the container as given by equation (1.2).

$$I=I_0e^{-(\mu/\rho)\rho x} \quad (1.2)$$

where

- I = Uncollided gamma intensity by NaI detector, disintegrations/sec
- I_0 = Initial source intensity, 750 mCi, initially in system, disintegrations/sec
- x = Distance the gamma travels from the source to detector, cm
- μ/ρ = Average container material mass attenuation coefficient, 0.0564 cm²/g
- ρ = Density of the container material, g/cm³

Equation (1.2) can be rearranged and the container material density (ρ) is found through equation (1.3) as follows:

$$\rho = \frac{\ln(I / I_0)}{\frac{\mu}{\rho} x} \quad (1.3)$$

Since μ/ρ is relatively independent of material when irradiated with a 1.25 MeV gamma and the distance x is known, the density can be determined by measuring the ratio of detected intensity to initial source intensity. Table 1-4 gives the mass attenuation coefficients for common materials with 1.25 MeV gammas. As can be seen in table 1-4 the smallest μ/ρ value is for copper with a value of 0.0521 cm²/g and the largest is water with a value of 0.063 cm²/g. The average μ/ρ value of these ten materials is 0.0564 cm²/g. Finally, the VACIS software converts the calculated densities into the images that are observed by an operator.

Table 1-4. Mass attenuation coefficients for 1.25 MeV gamma in ten different materials.

Material	Mass Attenuation Coefficient (cm ² /g)	Material	Mass Attenuation Coefficient (cm ² /g)
Carbon	0.0568	Lead	0.0569
Aluminum	0.0548	Uranium	0.0615
Iron	0.0531	Air	0.0567
Copper	0.0521	Water	0.0630
Platinum	0.0554	Concrete	0.0567

Generally two or three trained personnel are required to operate the Mobile VACIS. The Baltimore port U.S. Customs Service agent stated that an operator must undergo 40 hours of classroom training followed by 40 hours of operational training (Austin, 2003). Extensive background education is not usually necessary for operation - such as a college degree. The operators work for the U.S. Customs Service

and not the local port authorities. The VACIS system is used to inspect containers while still on the transporting tractor-trailers. As a trailer gets finished with an inspection another tractor-trailer pulls in to be inspected. However, the container transport trucks do not wait in line to be inspected, and go directly to the storage site if another tractor-trailer is being inspected.

1.8.3 VACIS Source Exposure to Operators.

SAIC, the vendor that developed the VACIS inspection technology, states that a person working around the Mobile VACIS will only receive 0.005 mrem of exposure dose per scan (Orphan, Richardson, and Bowlin, 2001). Though this is not a very significant radiation dose, it may pose a health risk if someone is exposed for long periods of time. A dose equivalent calculation was made to understand the conditions of the vendor's dose claim. The methodology for determining the dose equivalent is based on using the "Dose Equivalent from Gamma Source" approach, and is given by equation (1.4), which is valid for an unshielded source: (Lamarsh, 2001).

$$H(r) = \frac{S}{4\pi r^2} \cdot E_o \cdot (\mu_a/\rho)^{tis} \cdot QF \cdot (C1 \cdot C2 \cdot C3/C4) \cdot t \quad (1.4)$$

where

H(r)	=	Dose equivalent (as a function of the distance from the source) to an individual due to the Co ⁶⁰ source used in the VACIS, mrem
S	=	Source strength for VACIS Co ⁶⁰ , 1500 mCi
r	=	Distance operator is from source, cm
E _o	=	Gamma energy, 1.25 MeV for Co ⁶⁰ decay gamma
(μ _a /ρ) ^{tis}	=	Mass absorption coefficient of tissue for 1.25 MeV gamma, 0.0288 cm ² /g
QF	=	Gamma quality factor, 1 rem/rad
C1	=	Conversion factor, 3.7x10 ⁷ dis/sec mCi
C2	=	Conversion factor, 1.602x10 ⁻⁶ ergs/MeV
C3	=	Conversion factor, 1000 mrem/rem
C4	=	Conversion factor, 100 ergs/gram rad
t	=	Operator exposure time, 1 sec

While Co⁶⁰ has a half-life of 5.27 years, the dose in equation (1.4) has been calculated with the initial source intensity of 1500 mCi. This activity value comes from the VACIS source intensity of 750 mCi multiplied by a factor of 2. The factor of 2 is necessary because 2 gammas are emitted per disintegration.

For maximum penetration, which improves the image that is displayed to the operator, the scan speed is approximately 1 foot per second. With this scan speed an operator standing in one spot would only be scanned for 1 second per container exposure. The distance that an operator is from the source will vary depending on the individual's

location relative to the source. For this calculation the distance analyzed assumed that the operator was standing between 5 cm (2 inches) to 762 cm (25 feet) from the source. Twenty-five feet was chosen as the maximum distance because this is the Mobile VACIS scan area (25 ft x target length) (Americana Impex Consulting Company, 2003). A plot of the resulting dose equivalent versus the distance from the source is shown in figure 1-5 using equation (1.4)

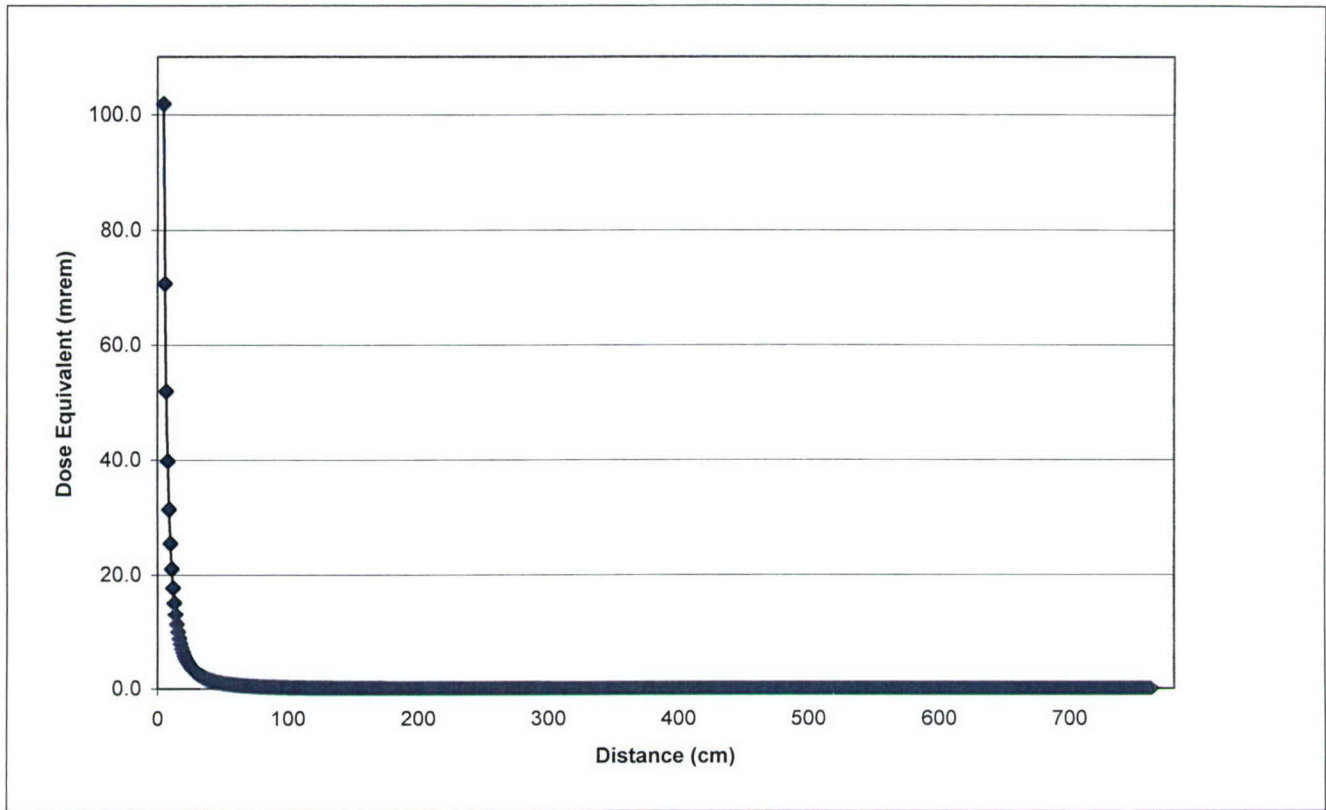


Figure 1-5. Dose equivalent plot for source distance of 5 to 762 cm (2 inches to 25 feet) for 1 second exposure per container from Mobile VACIS.

The plot in figure 1-5 shows that the exposure at 5 cm (first point in Figure 1-5) is approximately 100 mrem for one second of exposure. However, the exposure level quickly decreases and reaches the 0.005 mrem claim by the vendor at a distance of 504 cm (16.5 feet) from the source as shown in figure 1-5.

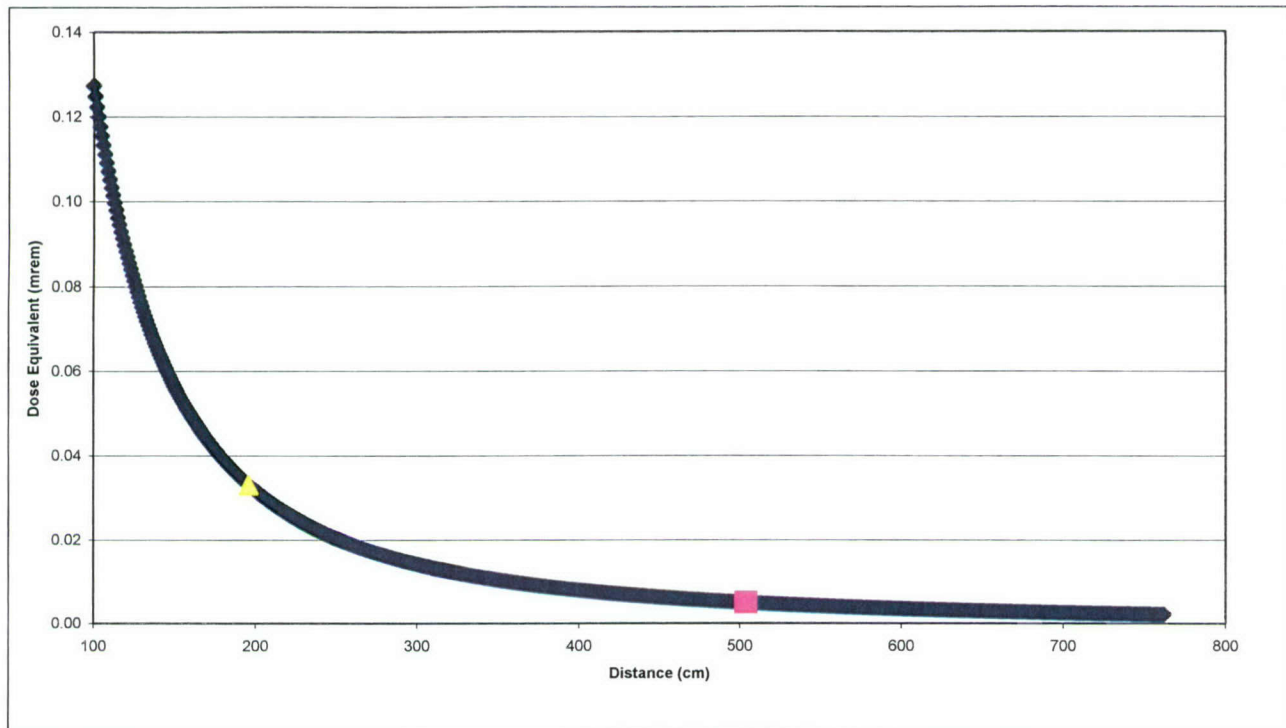


Figure 1-6. Dose equivalent plot for source distance of 100 cm to 762 cm for 1 second exposure per container from Mobile VACIS.

Figure 1-6 is a plot of equation (1.4), but evaluated between a distance of 100 cm to 762 cm with a 1 second exposure. The point where an individual receives 0.005 mrem has been highlighted and corresponds to an operator being at a distance of 500 cm. Beyond 762 cm, the dose equivalent continues to decrease inversely proportional to the square of the distance the operator stands from the source. Small exposures such as those measured to be in the thousandth of a mrem (μ mrem) range are likely not to pose a health risk (Orphan, Richardson, & Bowlin, 2001). The Mobile VACIS is also designed to emit only a collimated beam of radiation from the Co-60 source. Additionally, a "personnel restricted area" is designated behind the detectors where operators are not allowed during the normal operation. If the restricted area has a 196 cm (6.4 ft) radius from the source, the triangle in figure 1-6 shows that the dose will be brought down to 0.033 mrem per scan, assuming that this individual is standing on the edge. If 30 scans are conducted in an hour, then that individual would receive 1 mrem/hr. While such a dose rate is acceptable for radiation workers at naval commands (Naval Sea Systems Command, 1991), the VACIS worker(s) would be required to be treated as radiation worker(s) and wear radiation dosimetry badge(s). Additionally, the restricted area would need to be designated as a radiation area, which would restrict access to both non-radiation workers at the port as well as the general public.

1.8.4 VACIS Vulnerabilities.

The computer-generated images are created in the VACIS by the differences in the material densities. Calculations were performed to determine the thickness of different materials that could be placed between the HEU and the source in order to degrade the VACIS imagined capability.

Based on information in table 1-3, placing 16.5 cm (6.5 inches) of steel (assumed to be pure iron) between the gamma source and the detector will degrade the VACIS output such that it no longer provide accurate information ((Americana Impex Consulting Company, 2003).

By rearranging equation (1.2), the attenuation in beam intensity that this thickness of steel produces can be found as follows:

$$\frac{I}{I_0} = e^{-(\mu/\rho)\rho x} \quad (1.5)$$

where

I/I_0	=	Ratio of gamma uncollided intensity to initial source intensity
μ/ρ	=	Iron mass attenuation coefficient, 0.0531 cm ² /g (see Table 1-4)
ρ	=	Iron density, 7.87 g/cm ³
x	=	Iron thickness, 16.5 cm (6.5 inches)

Using the iron mass attenuation coefficient for a gamma ray energy of 1.25 MeV (from the Co⁶⁰ source), the solution for I/I_0 is found to be 1.01×10^{-3} (or 1/987). This fraction represents the attenuation of gammas emitted from a Co⁶⁰ source as it passes through 6.5 inches of steel. The solution indicates that the VACIS can provide accurate measurements until the beam intensity decreases by approximately 1000 times the original source intensity.

The VACIS only generates 2-D images; therefore it assumes that the thickness of each material is the same. Consequently, a thicker material of a lower density would appear as the same color as a thinner material of thicker density. In this case, the Mobile VACIS may not distinguish these materials from HEU, which is a potential vulnerability of the system.

To support the argument that materials of certain thickness can possibly "hide" 1 kg of HEU, the exponential decrease in beam intensity per emitted photon with HEU was found with the use of equation (1.6) below.

$$\begin{array}{l} \text{Exponential decrease in Beam Intensity} \\ \text{per photon emitted with 1kg HEU sphere} \end{array} = e^{-(\mu / \rho)_{\text{HEU}} \rho_{\text{HEU}} x} \quad (1.6)$$

where

$$\begin{aligned}(\mu/\rho)_{\text{HEU}} &= \text{Mass attenuation coefficient for HEU, } 0.0615 \text{ cm}^2/\text{g} \\ \rho_{\text{HEU}} &= \text{Density of HEU, } 19.1 \text{ g/cm}^3 \\ x &= \text{Mean cord length for a 1kg HEU sphere, cm}\end{aligned}$$

To evaluate, x in equation (1.6), the mean cord length of a particle crossing a sphere was used as shown in equation (1.7) (ICRU, 1983), since it was assumed the gamma could enter the HEU sphere from any direction.

$$x = \frac{4}{3} \cdot r = 3.09 \text{ cm} \quad (1.7)$$

where

$$r = \text{Radius of the 1 kg HEU sphere, } 2.32 \text{ cm}$$

By substituting equation (1.7) into equation (1.6) and solving, the decrease in beam intensity per emitted photon was found to be 0.0265. Using the densities of other materials, an average mass absorption coefficient of $0.0564 \text{ cm}^2/\text{g}$, the thickness needed to equal the same decrease in intensity as 1kg HEU was determined for various materials. The result of this calculation is given in table 1-5. This data shows that it is possible to place a material such as copper, with a thickness of 6.04 cm, and the VACIS image will appear as though it is a material with same density as HEU.

Table 1-5. Thickness of materials that would appear as the same material density as 1 kg of HEU in VACIS.

Material	Density (g/cm ³)	Thickness (cm)
1 kg of HEU	19.1	2.32 (radius of sphere)
C (graphite)	1.60	33.8
Cu	8.96	6.04
Fe	7.87	6.88
Pb	11.34	4.77
Pt	21.45	2.52
Al	2.70	20.0
Water	1.00	54.1

A concern with this situation is that an operator will look at the manifest and find what material is supposed to be in the container and the image will support the cargo manifest. The vulnerability associated with this condition is that if SNM is buried within the container contents, it may be overlooked. Also, this analysis demonstrates that in order to effectively smuggle small quantities of HEU into the United States, surrounding the HEU with shielding is not necessary. By placing the HEU deep within the containers of normal imports, such as iron, the HEU would be undetectable using the Mobile VACIS.

Another vulnerability of the VACIS system that cannot be overlooked is that the images are examined by U.S. Customs Agents. This means that human influence can play a large factor in whether the operator checks each image and container with the same consistency. A tired or lackadaisical worker may not look at the images as carefully as required and a small but significant inconsistency in cargo shape or density may go undetected.

While not analyzed in this study, X-ray imaging systems would likely have greater vulnerabilities to shielding than the VACIS, because they use lower energy photons. However, since these x-ray imaging systems examine backscattered radiation, the analysis presented in this section would not be directly applicable to them.

1.9 PORTAL MONITORING SYSTEM.

The concept of a Portal Monitoring Facility has been considered by the U.S. Customs Service for use in U.S. Ports to help detect illegal radioactive material inside shipping cargo. The sources that would be most susceptible to this type of detection are highly enriched uranium and plutonium. There are other installations in the United States that use similar monitors, namely uranium enrichment facilities and other nuclear research facilities. Portal monitors at these facilities are passive and are normally used for large objects such as trucks. In order to prevent false positive readings, the system uses an algorithm to measure radiation changes for a certain statistical confidence level above background levels.

1.9.1 Portal Monitoring System Operation.

Portal monitors are usually designed from scintillation detectors that can measure gamma rays from radioactive sources. The detectors are typically made of plastic scintillations that produce electron excitations by the entering radiation. Polyvinyl Tolulene (PVT) is a common material used as a scintillation detector (Knoll, 2002). Upon returning to the ground state, the excited electrons give off blue light (i.e. 450 nm wavelength) and the resulting photons are measured by a photomultiplier and converted into electric pulses that are counted by the detecting system. PVT is useful for these purposes, because it can be easily shaped into different shapes and sizes and its low internal absorption of visible light. The detectors that have been considered for large operations like a vehicle portal monitor usually have two photomultipliers for each scintillation detector in order to improve the signal to noise ratio. Lead shielding is placed around the detector to minimize any false detection from background radiation. The detector system is both passive and non-intrusive, and therefore can be ideal for shipping containers that are exiting a port on trucks or by rail.

The U.S. Customs Service began an experimental program for the Norfolk International Shipping Terminals and Newport News Terminals in late 2002. The proposed placement for portal monitors is the exit gate for trucks leaving the port, and the total scan time takes approximately one minute for an average-sized truck leaving the port. Typical characteristics for an existing portal monitor system are listed in Table 1-6.

Table 1-6. Typical portal monitor system characteristics (Exploranium, 2002).

Detector Physical Specifications	70"x 36"x 8.25"
Detector Weight	300 lbs
Detector Volume	6000 cubic inches
Photomultiplier size	2" diameter
Background sensitivity	100 nanorem/h (10^{-4} mrem/hr)
Minimum Gamma detection energy	2 KeV

1.9.2 Portal Monitor Sensitivity to 1 Kg HEU With and Without Iron Shielding.

This section includes a calculation for the sensitivity of an Exploranium Vehicle Portal Monitoring Station described in table 1-6 and the effect of iron shielding thickness with 1kg of HEU present. This system's polyvinyl toluene (PVT) scintillator detector is advertised to have a sensitivity of 10^{-4} mrem/hour (Exploranium, 2002). However, the detector can become too susceptible to false positive readings if its threshold level of sensitivity is only slightly above the background radiation. Assuming the background radiation at the facility is 10^{-3} mrem/hour (Dirk, 2002), then a 10:1 background sensitivity ratio would require that the sensitivity for the detectors be set to 10^{-2} mrem/hour. Likely the exact sensitivity of a portal monitoring system may not be made available by the US government for security reasons. The determination for the portal monitor's response to 1 kg HEU with iron shielding is given by equation (1.8) as a function of its distance from the source:

$$\dot{H}(r) = \left(\frac{S}{4\pi(r^2)} \right) \cdot E_0 \cdot \left(\frac{\mu_a}{\rho} \right)^{tis} \cdot QF \cdot \left(C_1 C_2 \frac{C_3}{C_4} \right) e^{\left(-\left(\frac{\mu}{\rho} \right)^{Fe}_{(ap)} \right)} \cdot B_p \quad (1.8)$$

where

$\dot{H}(r)$	=	Dose rate measured by portal monitor, mrem/hr
S	=	Source strength of 1 kg HEU, 1.62×10^9 mCi (Gillet 92)
E_0	=	Gamma energy of source, 0.18 MeV
ρ	=	Density of Iron, 7.87 g/cm^3

$(\mu_a/\rho)^{tis}$	=	Mass Absorption Coefficient of tissue (assumed to match PVT), $0.02875 \text{ cm}^2/\text{g}$
$(\mu/\rho)^{Fe}$	=	Attenuation Coefficient of iron, $0.161 \text{ cm}^2/\text{g}$
QF	=	Quality Factor, 1
C1	=	Conversion Factor, $3.7 \times 10^7 \text{ dis/sec mCi}$
C2	=	Conversion Factor, $1.602 \times 10^{-6} \text{ ergs/MeV}$
C3	=	Conversion Factor, 1000 mrem/rem
C4	=	Conversion Factor, 100 Ergs/g rad
B_p	=	Dimensionless Buildup Factor, 40.2 for 5 inches of iron (Lamarsh, 2001)
r	=	Distance of HEU source from detector, cm
a	=	Thickness of shield, cm

The source strength of 1 kg HEU for equation 1.8 is determined by multiplying its mass by its specific activity ($1,600,000 \text{ Bq/g}$) (Brown and Firestone, 1986). The calculation was done first assuming that there was no shielding (i.e. $B_p = 1$), and the distance of the source from the detector was permitted to vary from 100 to 2,000 cm. The gamma strength fell below 10^{-2} mrem/hr when the source was 1,948 cm or about 64 feet from the detector as shown in figure 1-7.

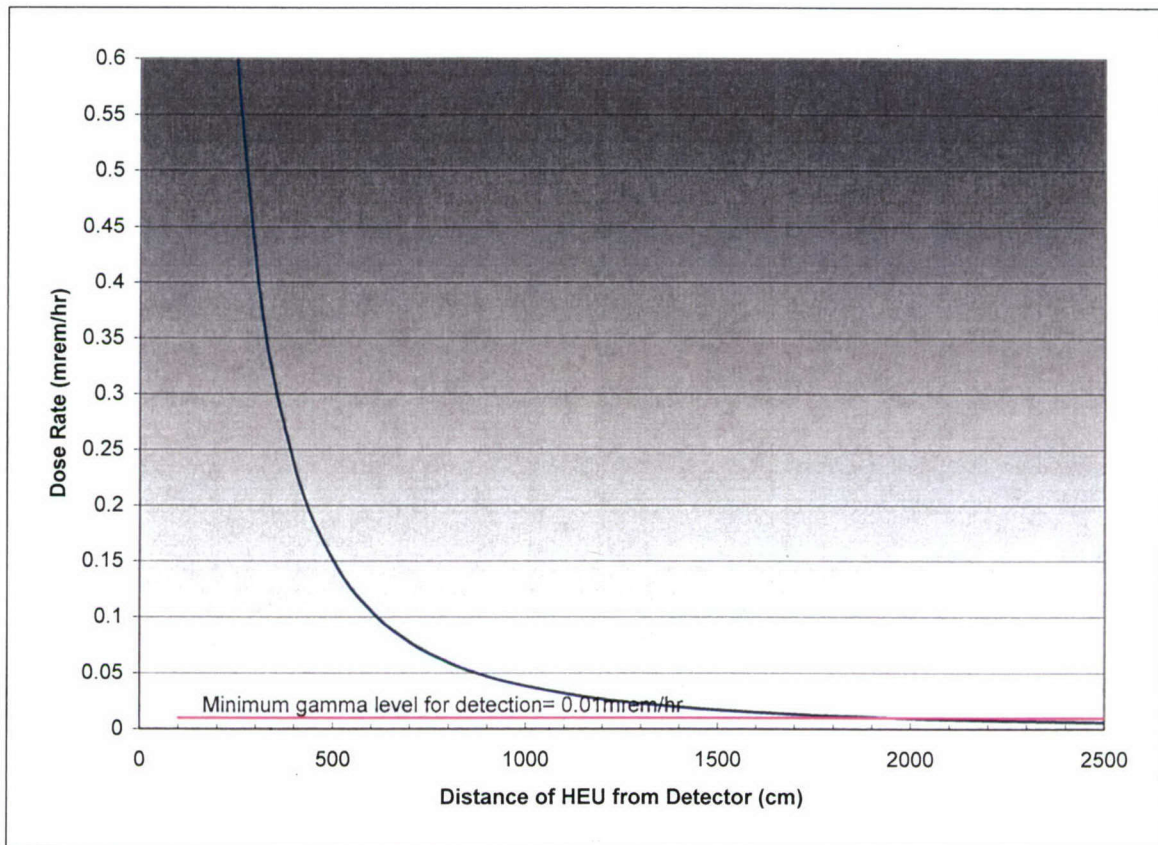


Figure 1-7. Plot of the effects of source distance on dose rate for a portal monitoring station with no shielding.

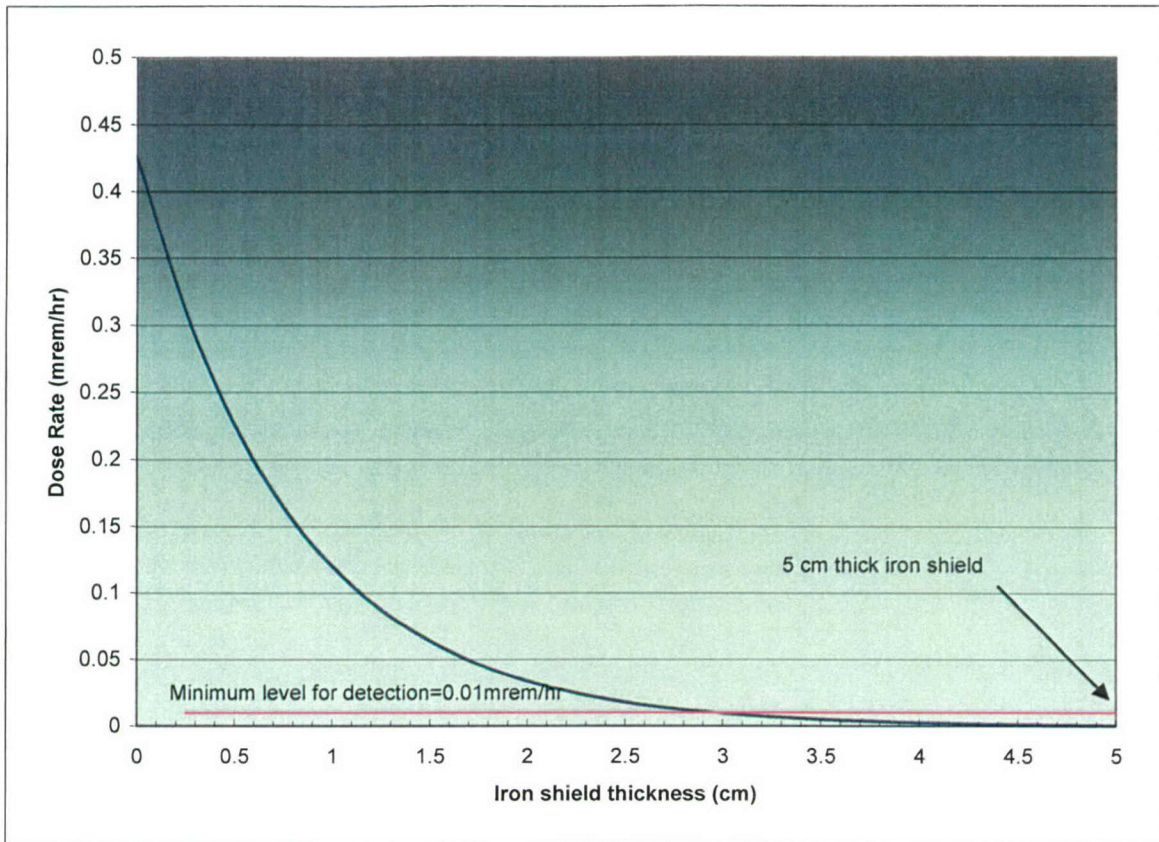


Figure 1-8. Plot of effect of iron shield thickness on the dose rate measured by the portal monitoring system with 1kg HEU at 304 cm.

With 5 cm of iron shielding, the radiation was found to be undetectable by the PVT detectors, even when the source was close to the detector. This shielding calculation was chosen on the assumption that an iron (steel) shield would be easier to create and pass through the VACIS, without attracting any unnecessary attention. As shown in figure 1-8, this shield would then be sufficient to pass through the portal monitoring station without detection, because the dose rate would be significantly below the minimum level for detection. For example, the engine block of a large tractor, when observed passing through the portal monitor would have several inches of steel between the source and the portal monitoring station.

A calculation using a distance of 10 feet or 304 cm for the distance between the HEU and a portal monitoring detector was also performed as a function of iron shield thickness and is shown in figure 1-8. Figure 1-9 shows such a vehicle portal monitoring station with such a distance of about 300 cm from the vehicle's centerline to the detector. The calculation showed that HEU would easily be detected at this distance without shielding. However an iron shield with a 2.93 cm thickness would reduce the dose to 9.8×10^{-3} mrem/hr or background radiation levels. The overall conclusion from this analysis is that a very small amount of shielding will be able to

fool a portal monitor that specializes in detecting gammas emitted from a source. Alternatively, the alarm level on the detector could be lowered to slightly above background. However, this approach would likely result in a large number of false positives.

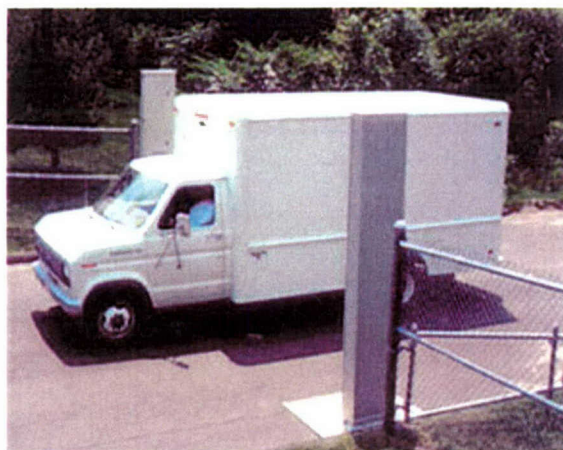


Figure 1-9. Example of a vehicle portal monitoring station.

1.9.3 Portal Monitoring Vulnerability Summary.

A portal monitoring system alone would not be sufficient for detecting HEU in cargo leaving a port because of the possibility of shielding placed around the specimen and the long half-life of HEU. However, the VACIS could be used in conjunction with a portal monitoring station to determine if there is an abnormal amount of shielding material inside of a container. With VACIS, abnormalities in cargo can be detected early in the offloading process for shipping containers. This would prevent the possibility of a shielded specimen of SNM breaching the portal monitoring station and leaving the port. Overall, the current implementation of portal monitoring systems in U.S. ports is still in its early stages, and the results of this trial period have not yet been determined.

1.10 RADIATION ISOTOPE DETECTOR.

A radiation isotope detector is under consideration for use in customs inspections in ports around the United States. Its main purpose is to determine if a container is carrying a radioactive isotope. The radiation isotope detectors can determine what element(s) are present, including SNM. This technique can be very powerful because it can help to distinguish between acceptable medical radioactive sources and SNM without opening the container and exposing workers to the radiation. The operation of the radiation isotope detector is discussed in section 1.10.1. Gamma spectroscopy, the basis of the detector's operation, is described in further detail in section 1.10.2. Section 1.10.3 evaluates the vulnerabilities of the radiation isotope detector while section 1.10.4 gives a summary of this section.

1.10.1 Radiation Isotope Detector Operation.

The Cryo3 is an example of a portable radiation isotope detector that is used in conjunction with US Customs. It was developed at Lawrence Berkeley National Laboratory (LBNL) and was made to be portable so that it could be more useful in the field. Figure 1-10 shows the Cryo3 and its relatively small size that makes it more accessible. The portable field product by Carbercat Exploranium was used to reference the Cryo3 because they share similar operations. The device uses a germanium crystal and uses the principles of gamma spectroscopy to determine the material present in the cargo container. An example of the photon emissions for U^{235} is shown in figure 1-1. This figure shows a number of distinctive photo peaks that can be used to recognize the presence or absence of U^{235} . The Cryo3 has an internal library that will compare the output of the detector to a large library of isotopes in order to find a match, which allows the system to identify the material present inside the cargo container.



Figure 1-10. Picture of the hand-held radiation isotope detector, the Cryo3.

1.10.2 Counts in Radioisotope with 1 kg HEU.

As previously mentioned, the Cryo3 uses gamma spectroscopy in order to match the photo peaks created from gamma interactions with the detector to those already in its library. Equation (1.9) gives the number of counts that the radiation isotope detector would produce from 1 kg of HEU in a given counting time (t_c):

$$N_c = \lambda_{HEU} N_{HEU} q t_c \epsilon_i \epsilon_g f_{sa} \quad (1.9)$$

where

- | | | |
|-----------------|---|--------------------------------------------------------------------------------|
| N_c | = | Number of counts detected by radiation isotope detector in count time t_c |
| λ_{HEU} | = | Decay constant of HEU, (sec^{-1}), given by eqn. (1.10) |
| N_{HEU} | = | Atoms of HEU in 1 kg, given by eqn. (1.11) |
| q | = | Fraction of gammas emitted per HEU decay, found from data in table 1-7, as 0.8 |
| t_c | = | Count time, seconds |

ϵ_i = Intrinsic efficiency, specified by LBNL as 0.25
 ϵ_G = Geometrical efficiency, given by equations (1.12) and (1.13)
 f_{sa} = Fraction of gammas that escape self-absorption, given by equation (1.15)

The decay constant of HEU is found from equation (1.10) as follows:

$$\lambda_{HEU} = \frac{\ln(2)}{(t_{1/2})_{HEU}} = 3.12 \times 10^{-17} \text{sec}^{-1} \quad (1.10)$$

where

$$(t_{1/2})_{HEU} = \text{Half-life of HEU, } 7.04 \times 10^8 \text{ years} \\ (2.22 \times 10^{16} \text{ sec})$$

The atoms of HEU in 1 kg of can be found from equation (1.11) as:

$$N_{HEU} = \frac{m N_{AV}}{A} = 2.56 \times 10^{24} \text{atoms} \quad (1.11)$$

where

A = HEU atomic weight, 235 grams/mole
 N_{AV} = Avogadro's number, 0.6×10^{24} atoms/cm³
 m = Material mass, 1 kg (1000 grams)

HEU predominately emits gammas with an energy between 143 KeV to 222 KeV. From the reference (ICRP, 1983), table 1-7 has been constructed which shows that 80.08 gammas will be emitted per 100 decays in HEU by energy.

Table 1-7. Number of gammas emitted for each energy in HEU between 143 KeV and 222 KeV per 100 decays.

Energy (KeV)	γ emitted per 100 decays (γ)
143.76	10.96
163.33	5.08
185.71	57.2
194.94	0.63
202.11	1.08
205.30	5.01
221.38	0.12
Total	80.08

Thus q in equation (1.9) was determined to be 0.8. The geometrical efficiency in equation (1.9) is calculated by equation (1.12) as follows:

$$\epsilon_g = \frac{SA}{4 \pi R^2} \quad (1.12)$$

where

$$\begin{aligned} \text{SA} &= \text{Surface Area of detector, cm}^2 \\ R &= \text{Distance of detector from HEU source, 152.4 cm} \end{aligned}$$

The largest distance of the detector to the HEU is the worst-case scenario because then the geometrical efficiency is the smallest. In the USNA MCNP model, this would correspond to the HEU being located in the center of the cargo container. If an extra foot is added to account for the most probable distance between the container and the location of the radioisotope detector, a total distance of 152.4 cm would exist between the detector and the HEU. The surface area of the detector was found by assuming its geometry to be circular, and is given by equation (1.13).

$$\text{SA} = \pi r_d^2 \quad (1.13)$$

where

$$r_d = \text{Cryo3 germanium detector radius, 2.5 cm}$$

Equation (1.13) yields the Cryo3 detector surface area to be 19.64 cm². Using this calculated surface area, and the worst-case scenario distance of the detector to the HEU of 152.4 cm, the geometrical efficiency was calculated to be 6.73×10^{-5} .

The self-absorption property of HEU due to its high density is another consideration because it reduces the gammas emitted by the HEU. Hence, fewer gammas can be detected by the radiation isotope detector. The mean free path length in HEU, λ_{HEU} , is given by equation (1.14) for a 185.5 KeV γ (most probable γ emitted by HEU).

$$\lambda_{\text{HEU}} = \frac{1}{\mu_{\text{HEU}}} = \frac{1}{\frac{\mu}{\rho} \cdot \rho} = \frac{1}{(1.54 \frac{\text{cm}^2}{\text{g}}) (19.1 \frac{\text{g}}{\text{cm}^3})} = 0.033 \text{ cm} \quad (1.14)$$

Assuming no gammas will travel farther than three mean free path lengths ($3\lambda_{\text{HEU}} = 0.099 \text{ cm} \approx 0.1 \text{ cm}$) in the HEU, then only those gammas near the surface will be emitted. Figure 1-11 illustrates this concept.

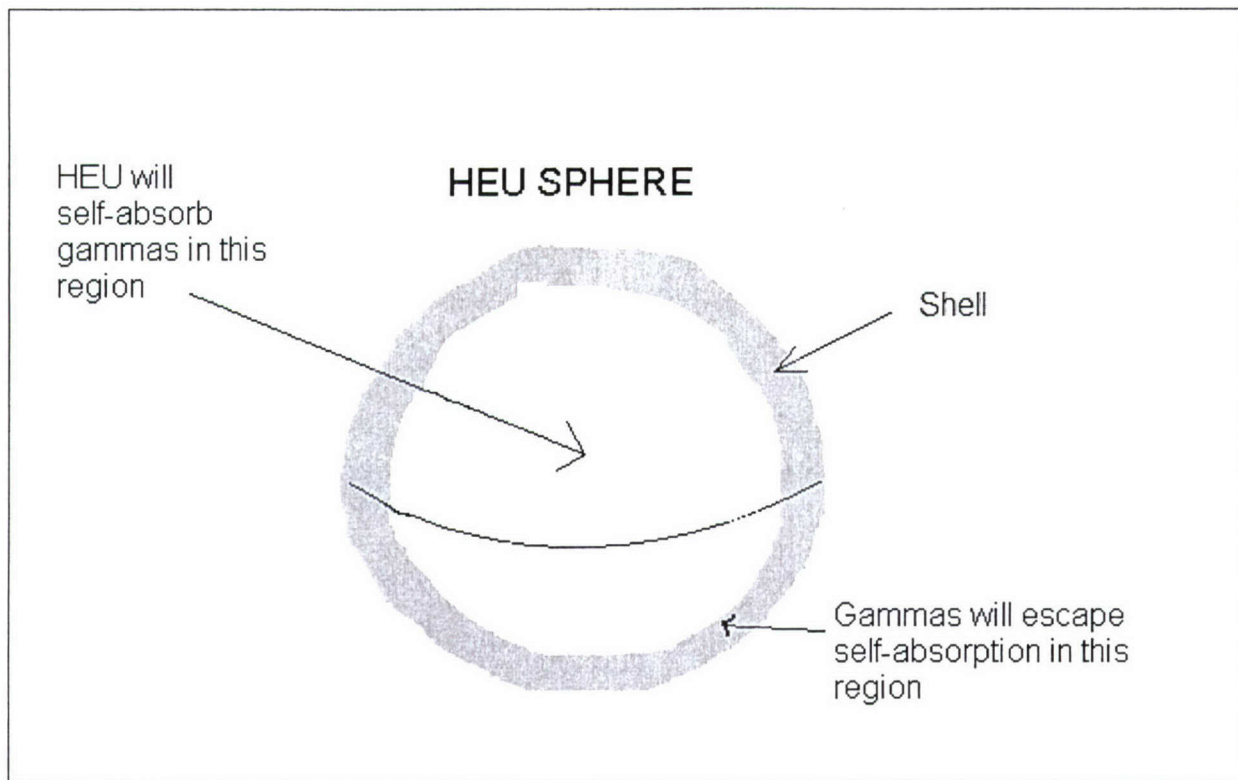


Figure 1-11. Pictorial view of the area in which the HEU will self-absorb gammas, and the area in which the gammas will escape.

From figure 1-11 it is apparent that only a certain fraction of the gammas will escape self-absorption from the HEU sphere. This fraction is defined as f_{sa} , and the equation used to find this fraction is given by equation (1.15) below.

$$f_{sa} = \frac{V_{shell}}{V_{sphere}} = \frac{4\pi r_1^2 \Delta r}{\frac{4}{3}\pi(r_1 + \Delta r)^3} \quad (1.15)$$

where

- f_{sa} = Fraction of gammas that escape self-absorption
- r_1 = Radius of HEU sphere which gammas will be self-absorbed, 2.22 cm
- Δr = Radial distance of HEU sphere which gammas will escape, 0.1 cm

Equation (1.15) yielded a fraction of gammas that will escape self-absorption as 0.12. Therefore, only 12% of the gammas will escape the HEU while 88% will be self-absorbed. Table 1-8 summarizes the parameters needed to evaluate equation (1.9).

Table 1-8. Summary of parameters to determine the number of counts from gamma spectroscopy for 1 kg of HEU.

Parameter	Value
Decay constant of HEU	$3.12 \times 10^{-17} \text{ sec}^{-1}$
Atoms of HEU	$2.56 \times 10^{24} \text{ atoms}$
Fraction of gammas that are Emitted per decay for HEU	0.80
Geometrical efficiency	6.73×10^{-5}
Intrinsic efficiency	0.25
Fraction of gammas that will escape self-absorption	0.12

An experiment was conducted in the USNA Subcritical Reactor Laboratory on a similar type of germanium detector to estimate background counts that would be produced in the count time when Cryo3 was in operation. The germanium detector used had many of the same features as the Cryo3; they both have similar surface areas and intrinsic efficiencies. In the USNA set-up, the germanium detector was surrounded by thick lead shield that substantially reduced the background counts from the subcritical reactor in the room. The experimental set-up is shown in figure 1-12.

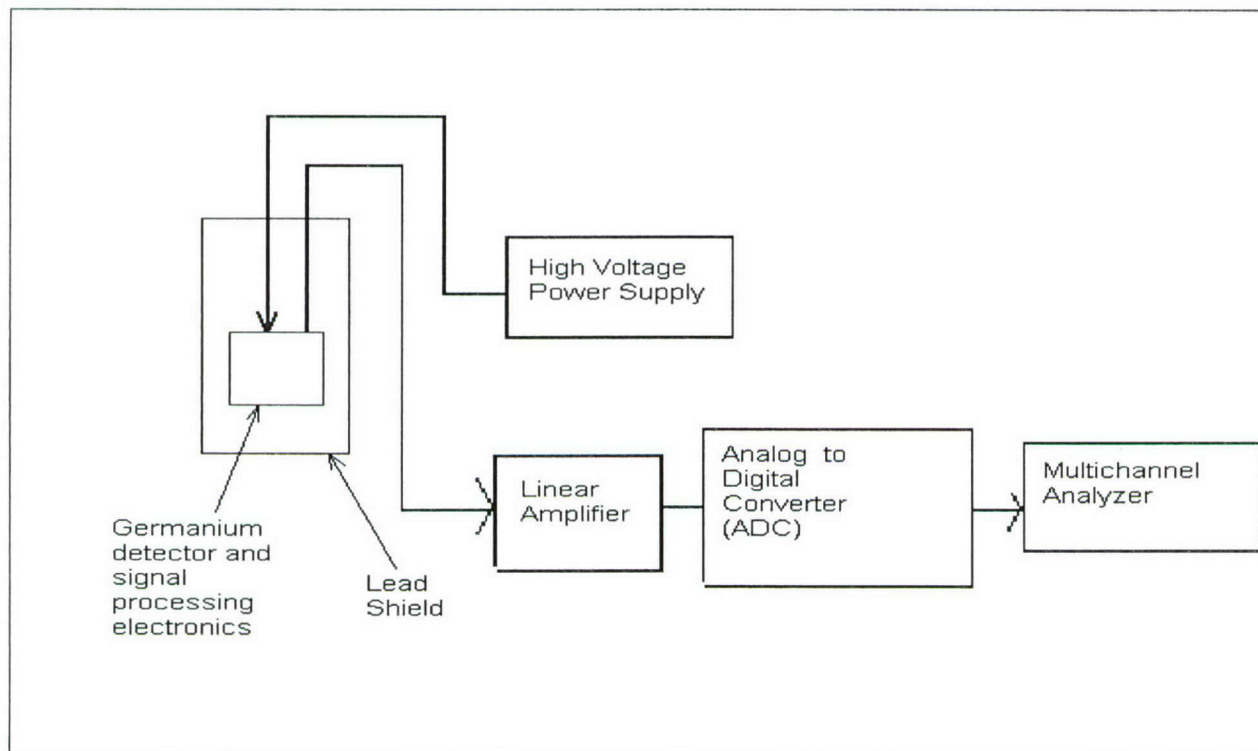


Figure 1-12. Experimental set-up of the gamma spectroscopy experiment at USNA using a germanium detector.

Before the experiment was conducted, the USNA germanium detector was energy calibrated with several sources (Co^{60} , Cs^{137} , Na^{22} , and Ba^{137}) in order to ensure that the integrating region of interest was set between 143 KeV and 222 KeV which is the main energy gammas that would be emitted from HEU.

The result of the experiment was a background count rate of 0.35 counts/second for the USNA germanium detector. Using this value, the Cryo3 background count was estimated to be 107 for a five minute count. Assuming that a HEU signal to background of 10 or greater is needed in order to get a clear HEU signal, N_c in equation (1.9) would have to be greater or equal to 1070 in 300 seconds.

The count time is not specified in equation (1.9) because it is a variable. Figure 1-13 shows the counts in the radiation isotope detector for 1 kg of HEU versus the counting time. The upper limit of 300 seconds was chosen because that is the integration time that the external neutron stimulation method utilizes.

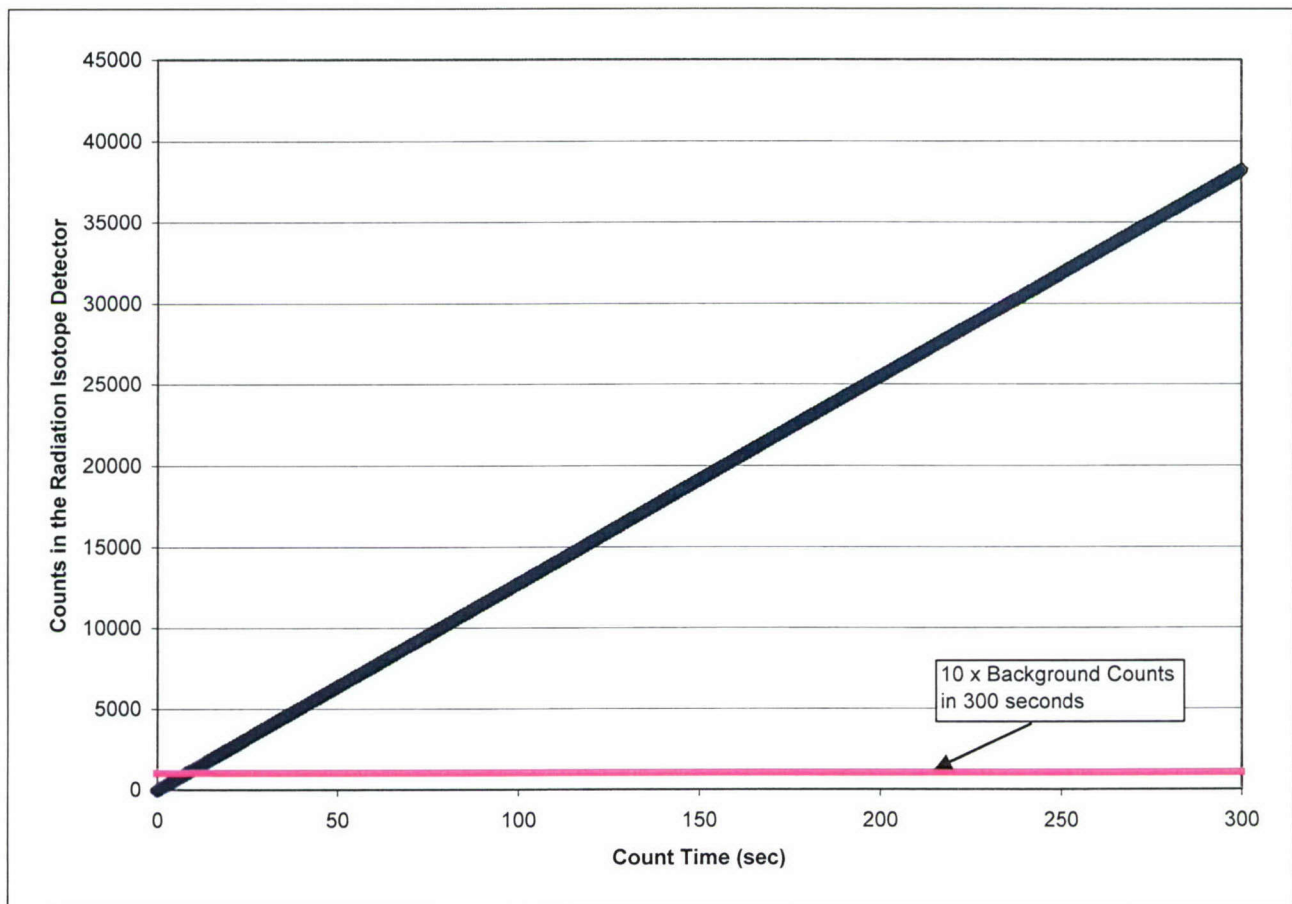


Figure 1-13. Counts in the radiation isotope detector versus counting time for 1 kg of HEU with Cryo3 and HEU located in worst-case scenario position.

As can be seen from figure 1-13, the Cryo3 can accurately determine the presence or absence of 1 kg of unshielded HEU since the number of counts in 300 seconds would be nearly 40,000 even with the HEU located in the worst-case scenario position, because this number is nearly 400 times greater than the corresponding background count of 107.

1.10.3 Radiation Isotope Detector Vulnerabilities.

One problem with using gamma spectroscopy as a primary means to detect HEU is that high atomic numbered materials (Z) are very effective at shielding gamma rays whose energies are less than 200 KeV (LaMarsh, 2001). Since U^{235} has most of its gamma emission lines below 200 KeV (see table 1-7), high Z materials can easily shield HEU gammas. Additionally, if 1kg HEU was shielded by lead such that the counts in five minutes was $1/400$ of the above 300 second count time value, this mass of HEU would probably not be detected because counts from the HEU (N_c) would be of the same magnitude as background counts (i.e. assuming the detector alarm threshold was not set at or below twice background). Consequently the thickness of lead needed to reduce the counts from the HEU by a factor of 400 was determined using the equation:

$$I = I_0 e^{-\mu x} \quad (1.16)$$

Solving for x in equation (1.16) gives the result:

$$x = \frac{\ln\left(\frac{I}{I_0}\right)}{-\mu_{Pb}} \quad (1.17)$$

where

$$\begin{aligned} \mu_{Pb} &= \text{Lead attenuation coefficient} \\ I/I_0 &= 1/400 = 0.0025 \end{aligned}$$

The attenuation coefficient in equation (1.17) can be found assuming the HEU gammas have an energy of 180 keV.

$$\mu_{Pb} = \left(\frac{\mu}{\rho}\right)_{Pb} \cdot \rho_{Pb} = 1.126 \frac{\text{cm}^2}{\text{g}} \times 11.3 \frac{\text{g}}{\text{cm}^3} = 14.21 \text{cm}^{-1} \quad (1.18)$$

where

$$\begin{aligned} (\mu/\rho)_{Pb} &= \text{Mass attenuation coefficient of gammas in lead,} \\ &\quad 1.179 \text{ cm}^2/\text{g} \\ \rho_{Pb} &= \text{Density of lead, } 11.3 \text{ g/cm}^3 \end{aligned}$$

The result of this calculation is that less than a 0.2 inch thick piece of lead will shield the HEU from gamma detection by the radiation isotope detector!

1.10.4 Summary.

Although the Cryo3 can easily detect 1 kg of HEU unshielded, it has an inherent vulnerability that it cannot detect 1 kg of HEU if it is shielded by as little as 0.2 inch piece of lead. Assuming that the HEU would be illicitly trafficked into the U.S., the person(s) responsible for its transport would most likely shield it so that it is not easily found through current modes of inspection. With such shielding, additional inspection technology beyond the radiation isotope detector would be needed to detect one kg of HEU.

1.11 FUNDAMENTAL PROJECT SCENARIO.

While considerable effort has gone into the detection of SNM, a difficult scenario would be the detection of a small mass of HEU in a very large container. Following discussions with the Defense Threat Reduction Agency (DTRA) personnel, it was specifically decided to study the feasibility of detecting for the presence or absence of 1 kg of HEU by the use of external neutron stimulation. Further, the HEU was to be located anywhere within a large shipping container that could be filled with a wide variety of different cargoes at a US port-of-entry that had been off loaded from a transoceanic cargo vessel. The cargo would act like a shield and hence make the detection of the HEU that much more difficult. This scenario reflects the concern that this material would be secretly smuggled into the US by a terrorist organization, attempting to assemble a crude nuclear device. Since 1 kg of HEU is below a critical mass, the assumption is that the terrorist group would then stockpile the HEU until such time that it had a critical mass. HEU was chosen as the SNM, because it is inherently much more difficult to detect than plutonium as discussed above in sections 1.1 and 1.2. Consequently, if the system was determined to be feasible for the detection of HEU, it would also be useful to detect plutonium.

The motivation to study HEU detection with external stimulation is fourfold. First, existing technologies as discussed in section 1.8-1.10 have vulnerabilities for short inspection times. Any system, which required lengthy examinations to achieve high statistical confidence would be impractical, because of its detrimental effect on commerce. Second, as discussed in sections 1.4 through 1.6, external neutron stimulation has been successfully implemented in well-logging, nuclear waste assaying in 55 gallon drums, and by commercial vendors for the interrogation of small packages. Third, this technique would be non-invasive if the source and detector were placed external to the container. Fourth, the detailed requirements for success of this approach had not been systematically studied and published elsewhere to the knowledge of the authors.

1.12 METHOD OF APPROACH.

The feasibility study was performed in ten steps. First, a benchmark facility was defined, which specified the container dimensions, wall materials, and the surrounding environment. Second, this facility was then modeled using both fundamental principles of neutron transport (deterministic approach) and using Monte Carlo techniques (stochastic approach). A description of the facility chosen and the Monte Carlo N-Particle (MCNP) technique used is given in sections 2.1 and 2.2. The deterministic approach was used in detail to study the 14 MeV pulsed neutron source in section 4.4, but was also used throughout the report in order to understand the results calculated by the MCNP based models. Third, using MCNP, important source variables such as its neutron emission energy, operational mode (continuous or pulsed), and strength were studied. Section 3 contains the results for a continuous source, while section 4 details the pulse source analysis without the presence of cargo. Also the effect of both the source and detector positions outside the container as well as the HEU location within the container are analyzed in these sections. Fourth, but in concurrence with the third step, the choice of detection mode (i.e. count neutrons, gammas, or both) had to be considered and is discussed in section 2.3. An important consideration at this point was that the presence of 1 kg HEU had to produce a signal that was significantly greater than that which would be produced by background radiation. Fifth, the effect of cargo within the container was studied and compared to the results without payload. These results are described in section 5. Sixth, a shielding analysis is provided in section 6. In this section, the dose rate emanating from the facility with a concrete shield is analyzed using two historical approaches and then these methods are compared to an MCNP analysis. In section 7, an analysis is presented on the effects of varying the source distance to the cargo container. A cargo activation analysis was performed and the results are in section 8. Next, in section 9, a feasibility study which consisted of examining federal rules and regulations on the facility operations. Also included in this study was a cost analysis, basic site layout, and four different stimulation facility designs. Comparison of gamma signatures in common cargo materials to that in HEU and reactor grade plutonium is given in section 10. Also included in this section is an MCNP analysis of gamma transport from a plutonium source within a shipping container and its interaction rate with a gamma sensitive detector located outside the container. Finally, project conclusions and recommendations are presented in section 11.

SECTION 2

BENCHMARK FACILITY DESCRIPTION AND MODEL DEVELOPMENT

In this section of the report, the benchmark facility and the modeling techniques used are described. Both the facility's physical and surrounding environmental features are given in section 2.1. Since the facility was analyzed using the MCNP (Monte Carlo N-Particle) transport code (Los Alamos National Laboratory 2000), section 2.2 has been included to briefly review important MCNP concepts. Appendix A contains a listing of the benchmark MCNP model used in this project. In order to eliminate geometry errors within the model and to improve system visualization, both the SABRINA software code (Van Riper 2002) and the MCNP geometry plotting routines were employed. Section 2.3 describes both the SABRINA code as well as the MCNP plotting routines used in the project. An important feature of the problem was the neutron detector used to measure the neutrons produced by the external stimulation. In this project the Optimized Neutron Detector for Arms Control (ONDAC) (Millett 1997) was used and its description is given in section 2.4.

2.1 BENCHMARK FACILITY DESCRIPTION.

In order to develop a benchmark facility, a web-based search was performed which yielded a wide array of different types and sizes of commonly used maritime containers. Table 2-1 lists the different maritime container types, their physical dimensions in which they are available from the vendor, and general use that was found from one website (Maxx 2002).

Table 2-1. Types, physical dimensions, and general uses of maritime containers.

Container Type	Physical dimensions	General use
Dry freight container	20' x 8' x 8' 6" 40' x 8' x 8' 6"	General purpose
High cube container	40' x 8' x 9' 6" 45' x 8' x 9' 6"	For over height and voluminous cargo
Open top container	20' x 8' x 8' 6"	Removable tarpaulin for toploading of oversized cargo
Flat rack	20' x 8' x 8' 6" 40' x 8' x 8' 6"	For transportation of over-width and heavy cargo
Refrigerated container	20' x 8' x 8' 6" 40' x 8' x 8' 6"	For cooling, freezing or heating of foods and chemicals
High cube refrigerated container	40' x 8' x 9' 6"	For over height and voluminous cargo requiring cooling or freezing
Tank container	20' x 8' x 8' 6"	For transportation of liquid chemicals and food stuffs

Based on this information, it was decided to make the benchmark facility a dry freight container whose dimensions would be 20' x 8' x 8'. A picture of such a container is shown in figure 2-1. The maximum gross weight of this container would be approximately 30,000 kg, while the maximum payload would be approximately 28,000 kg.

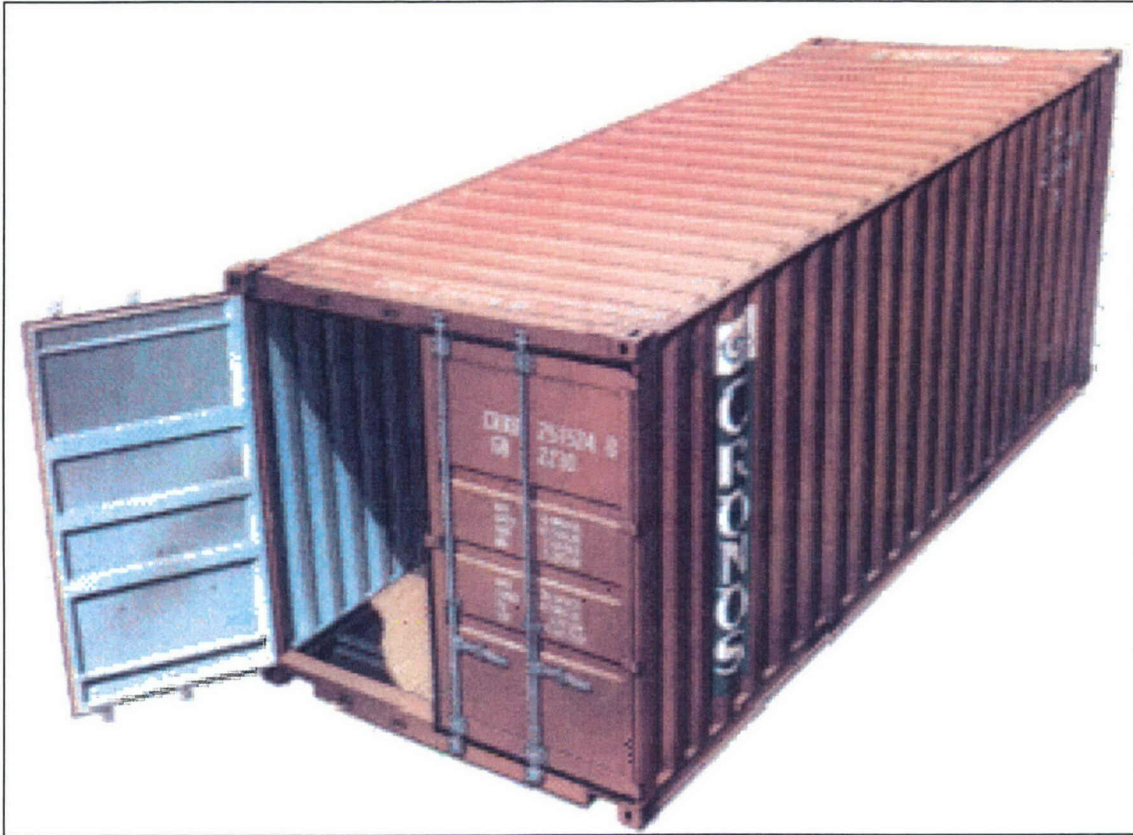


Figure 2-1. Benchmark facility: Dry freight container with dimensions 20' x 8' x 8' (photograph from Cronos website (Cronos 2002)).

With the physical dimensions established, other features were added to the model that simulated the container off-loaded from the vessel and placed on the ground. These features included a steel wall on each side, whose thickness was taken to be 1/4". Also 2" of soil was modeled to be beneath the container in order to account for ground scattering. Inside the container, 80 cylindrical dimensionally identical cargo drums were created along with air zones between these cylinders. Each drum was oriented vertically with a 4' height, in order to make drum height equal to half that of the container. All drums had a one foot radius. There was a top set and a bottom set of cargo drums. Each set consisted of 4 rows with 10 drums in each row. In this configuration, the drums touched each other. To monitor the escaping neutrons three high efficiency neutron detectors were located outside the container. The detector chosen for use in the model was the ONDAC detector. A description of the ONDAC and its

model locations is given in section 2.4. The model also contained a spherical cell, whose radius was taken to be 2.32 cm. In the project the sphere was moved to different locations in order to study the effect of ONDAC detector/HEU source separation distance. The material in this sphere was either HEU in order to simulate a 1 kg source or air in order to simulate the system response with no HEU present. Finally the model contained a point neutron source, which could be located externally or internally to the container. A three-dimensional SABRINA representation of this model is shown in figure 2-2.

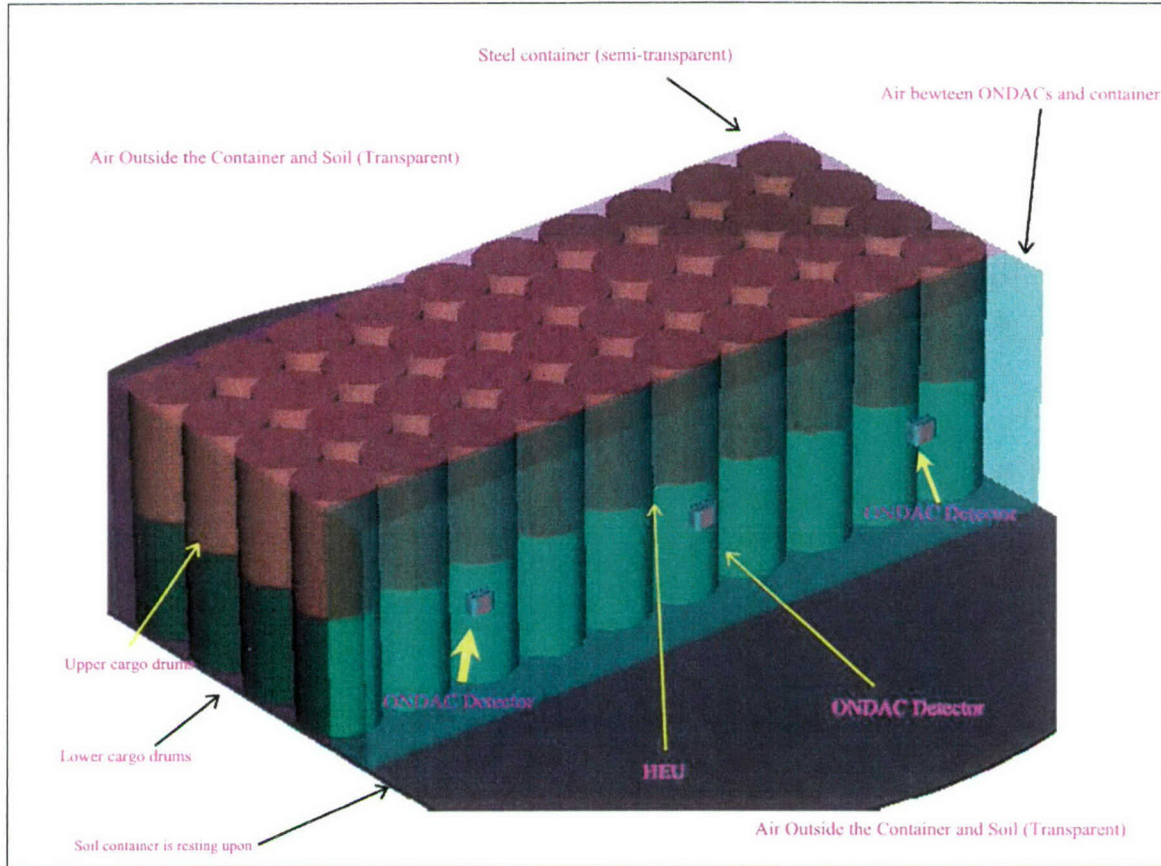


Figure 2-2. SABRINA representation of benchmark facility. Shown are the 80 cargo drums, three ONDAC detectors, 1 kg HEU sphere, and soil. The container wall has been made transparent. Not shown is the location of the neutron source.

2.2 MCNP MODEL.

Monte Carlo methods are numerical techniques, which use random sampling of probability distributions to create individual case histories. These histories are then averaged to estimate the solution to a physical problem. In particle transport problems, the simulation starts with a source particle and a modeled physical system. Distributions are sampled randomly to obtain the energy and

direction of flight of the source particles. Over a large number of source particle histories, the simulation eventually follows the physical source characteristics. After the particle leaves the source, it can interact and collide with atomic matter in many ways. The probability distributions of these interactions depend primarily on the colliding particle's energy, the type of particle, and the atomic properties of the matter. The "life" of one of these particles is governed by many random processes (Lux 1991). First the particle is started from the source. Then, the distance traveled in a medium between interactions, the energy of the scattered particle, its direction of flight, and the number of secondary particles that are created are all governed by probability distributions. Finally, when the particle's energy drops below a certain threshold or when the particle is absorbed, the simulation begins a new history. Random numbers are generated within distributions at each event to determine the particle's path and energy. This makes single interaction Monte Carlo solutions difficult. This life of randomly determined interactions is called the particle's random walk. The final solution to the problem involves averaging the particle's behavior over a large number of these particle histories or random walks. As the number of histories increases, the problem solution approaches the expected value.

The Monte Carlo simulation used in this project was the Monte Carlo N Particle transport code (MCNP). This program was developed at LANL and continues to be updated there. The version of MCNP used predominately throughout the project was MCNP4C2 (Los Alamos National Laboratory 2000). The program was obtained from the Radiation Safety Information Computation Center (RISCC) in Oak Ridge, Tennessee. The code is a computer based program that can currently be implemented on a large number of platforms. For this project, MCNP ran on Pentium-based personal computers. Prior to running any cases on any computer, test programs were run which ensured that MCNP was working properly. These test programs came with the code and are an essential part of the installation process. In all cases the test programs showed that there were no errors in the installation or in the execution of the program.

MCNP4C2 has various capabilities that were essential to this project. The program is able to model the transport of neutrons, photons, and electrons, although only the neutron and gamma transport feature was used in this project. The code has nuclear libraries of energy dependant cross sectional data for many isotopes and elements. The Evaluated Nuclear Data File-Version B (ENDF/B) library was used in this project, which contained neutron cross sections up to 20 MeV. Another feature of the MCNP4C2 program is its two dimensional graphical capabilities. However, as discussed in section 2.3, the SABRINA plotting package was used for this task due to its three dimensional plotting capabilities.

In each simulation, MCNP gives a relative error based on the statistics of the problem. As stated previously, MCNP approaches the expected solution to a given problem over a large number of particles. The relative error value given by MCNP varies inversely with the square root of the number of particles histories in the problem. For example, quadrupling the number of particle histories will halve the relative error value.

The MCNP standard deviation is calculated in the following manner:

$$\bar{R} = \frac{1}{N} \cdot \sum_{k=1}^N R_k \quad (2.1)$$

where

\bar{R} = output value of the MCNP tally (i.e. interactions per source particle in a cell)
 N = number of particle histories
 R_k = parameter calculated from the k^{th} particle history

$$S^2 = \frac{1}{N} \cdot \sum_{k=1}^N \frac{(R_k - \bar{R})^2}{N - 1} \quad (2.2)$$

where

S = standard deviation

Finally, MCNP finds the relative error, which is calculated by the following equation:

$$r = \frac{S}{\bar{R}} \quad (2.3)$$

where

r = relative error

For an MCNP simulation to be statically valid, it is recommended that the relative error be 0.05 or smaller. For most simulations conducted, r was typically less than 0.01, but this generally required 10^9 particle histories.

For all simulations, MCNP generates all random numbers from a random number seed. The random number seed determines the manner in which each distribution will be sampled throughout the problem. All subsequent random numbers are calculated using this seed. Two identical input files with the same random number seed will produce identical output parameters. Varying the random number seed between runs has little effect for problems with a large number of particles since the problem is approaching an expected value.

The random number seed can be changed by use of the DBCN command. The maximum number of particle histories was limited to 10^9 in this investigation because of the lengthy computation time in these cases. For simulations that required more than 10^9 particle histories in order to achieve a low relative error, multiple particle histories

were averaged together, but a different random seed number initiated each simulation.

Another artifact developed in Monte Carlo simulations is the occasional lost particle. When a particle is lost it is excluded from the MCNP tallying process. This problem can occur in models with complex or ill-defined geometries. Using the MCNP graphics plotting package as well as SABRINA, it was determined that the cause of this phenomenon was due to numerous surfaces and cells within the USNA model, and not due to an ill-defined geometry. This problem was noted to be statistically insignificant as in the worst cases only 1 in 10 million particles were lost.

The MCNP input files were created and continually modified with the principles contained in this subsection. The input file of a typical model created by this project is given Appendix A.

2.3 MODEL PLOTTING SOFTWARE.

Two tools for model plotting were used in the project: SABRINA and the MCNP plotting routines. SABRINA is an interactive program that produces two or three dimensional images (Van Riper 2002). Figure 2-2 is an example of a three dimensional picture produced by SABRINA. The program has the capability of graphically displaying an MCNP input in three dimensions using polygons and surface shading. MCNP input files are formatted with the required extension, and then read by SABRINA in order to construct an image. The 3-D model can be rotated for viewing at various angles, and can be resized as desired by the user. This rotation feature was found to be extremely useful when searching for possible voids or improperly defined cells during the model construction and validation process. In addition, the ability to assign colors by both material and surface allows for creation of an easily distinguishable representation of the MCNP model. SABRINA representations included in this report have been extracted from the SABRINA program and converted to the JPEG format for general use.

MCNP4C2 contains a two dimensional plotting routine, which was also used in the project. Because of its two dimensional limitation, any model constructed has to be viewed in separate planes, which can be a time-consuming process. Figure 2-3 is a typical example of a two dimensional plot produced by MCNP. In this figure an x-y view of a container model in the $z = -100$ plane is given, which gives a cross section view at 100 cm below the vertical mid-plane of the container or approximately 20 cm above the surface of the ground. One can see in figure 2-3 the four rows of containers, in which 10 cylindrical cargo containers are in each row. The numbers shown represent surfaces that have been defined within the model. For example, surface 64 represents the outer limit of the model. Particles crossing outside this surface enter the surrounding universe and are

no longer followed by MCNP. Zooming into a particular area is performed by changing the extent to the x and y axes.

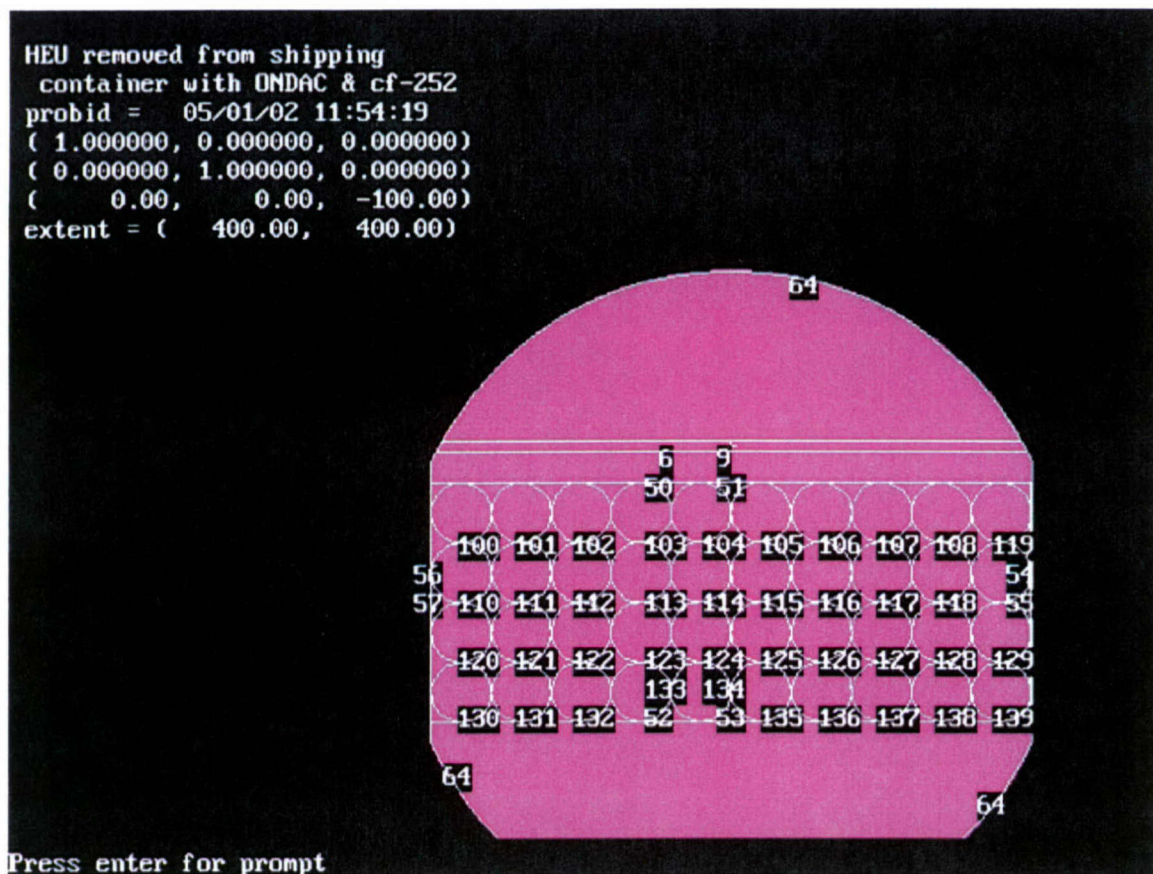


Figure 2-3. MCNP model of cargo container as viewed in the x-y plane. Origin of plot is at $x = 0$, $y = 0$, $z = -100$ cm, which corresponds to center of the container approximately 20 cm above the ground.

2.4 ONDAC DETECTOR.

In order to make the MCNP results more useful, a neutron detector was integrated into the model. Since it was known that the neutron signal from 1 kg of HEU would be small, an extremely high efficiency neutron detector was required. The detector selected for these purposes was the Optimized Neutron Detector for Arms Control (ONDAC). There were for two main reasons the ONDAC was selected. First, since the detector had been designed using MCNP at the USNA (Millett 1997 and Millett 1998), an MCNP detector model was available at the start of the project. Second, the ONDAC background response to cosmic ray neutrons had been measured in experiments conducted at LANL (Murphy 1999). While the cosmic ray neutron background will vary with location, these measurements gave the project a first order estimation of the instrument's background response. In turn this instrument data allowed the project to make HEU signal to background noise calculations.

The ONDAC detector is a lightweight high sensitivity instrument developed for potential use in arms control. A detailed description of the system is given by its operation and maintenance manual (Nelson 1997). The system uses nine one-inch diameter 10 atmosphere He^3 tubes surrounded by a polyethylene moderator. Fast or epithermal neutrons, which pass through the cadmium liner, are moderated by the polyethylene block. A cross section of the detector, showing the approximate tube layout and dimensions is shown in figure 2-4. The system dimensions were developed in order to have maximum neutron moderation combined with minimum neutron weight. Because the system has five tubes in the front row and four in the back row, it has a higher neutron efficiency when the front row is closer to the source. For use in the project, the ONDAC detector was evaluated with and without the use of its cadmium liner as discussed in section 3.3.

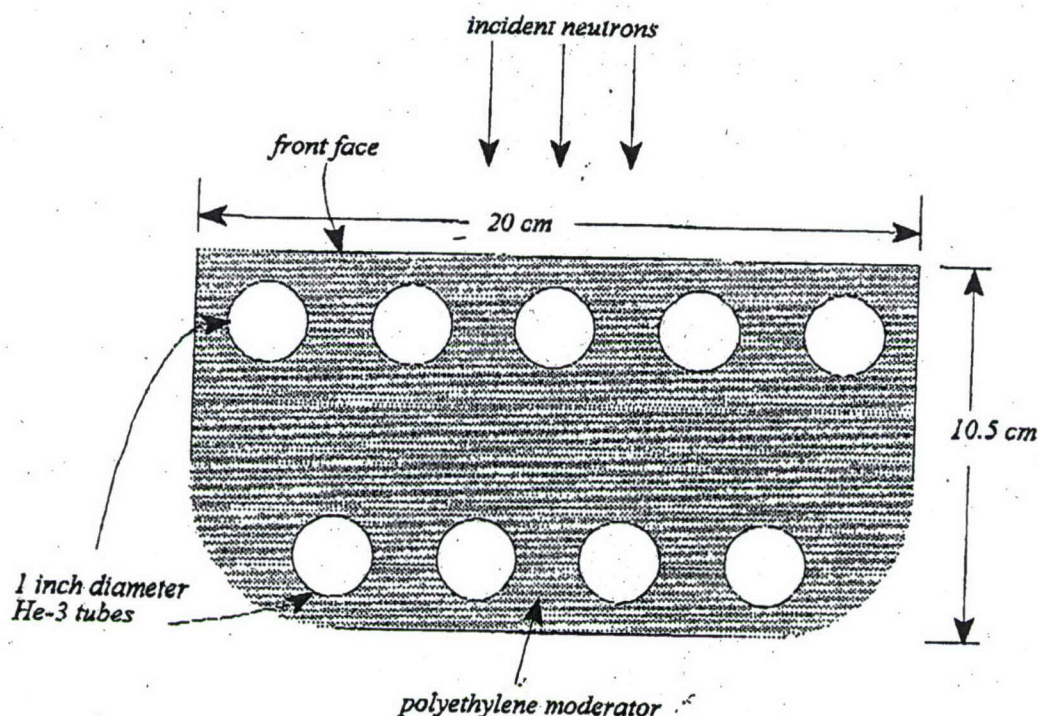


Figure 2-4. ONDAC detector cross sectional geometry.

Each He^3 tube has a height of 20 cm. The tubes are connected together in parallel with SHV connectors. The system is surrounded with a composite material case. This case, along with shock absorbing springs for the He^3 tubes, provides for ruggedness in field applications. The system readout and operating voltage of 2075 V is applied through the use of an EberlineTM E-600 survey meter. Figure

2-5 shows a photograph of the entire system, including the E-600 survey meter.

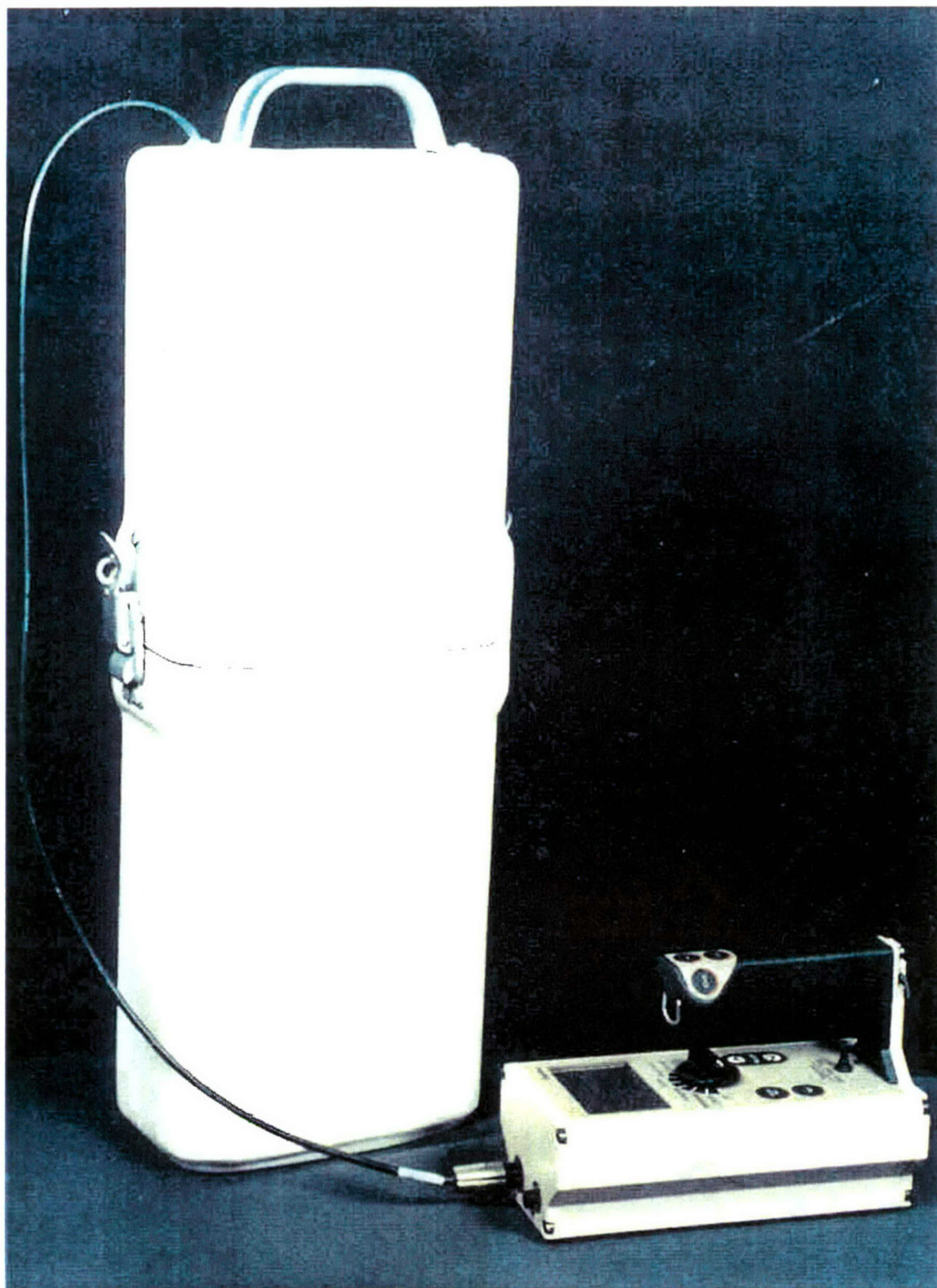


Figure 2-5. ONDAC system with composite case and Eberline E-600 survey meter.

In all MCNP models, three ONDAC detectors were inserted lengthwise along one side of the cargo container. In this way, distance effects between the HEU and the ONDAC detector on the number of interactions per source particle could be more easily evaluated. It was recognized that in an actual facility design, some modifications would likely be made to the detection system as modeled. For example, the detector(s) could be placed on a track and mechanically moved in order to perform lengthwise scans of the cargo container. However, such modifications were felt to be of secondary importance and did not need to be modeled in order to assess the feasibility of the stimulation concept.

SECTION 3

STIMULATION USING A CONTINUOUS NEUTRON SOURCE WITH PROMPT NEUTRON COUNTING AND NO CARGO

In this section the results of the neutron stimulation analysis are given in which the source emits neutrons continuously. Two examples of this type of source would be either Cf^{252} , which emits fission energy neutrons, or plutonium-beryllium, which emits neutrons with an average energy of 4 MeV. These sources produce prompt neutrons and in this section it was assumed that these neutrons are what would be counted. The general approach taken in this analysis was to use the MCNP4C2 code and compare the interactions per source particle in the stationary central and two side ONDAC detectors with and without HEU present in the container. The center ONDAC was positioned as the center of the Cartesian coordinate system (i.e. $x = 0$, $y = 0$, $z = 0$). The parameters analyzed included the effect of varying the distance of the HEU from the source, effect of using sources with different neutron emission energies, effect of using an epi-thermal versus a thermal detector, and the effect of using backscattered neutrons. In all cases, the inside of the container was modeled with air, which corresponds to the case of no cargo, and the neutron sources were assumed to be isotropic.

3.1 PARAMETER STUDY.

Figure 3-1 shows the effect of different source energies on ONDAC efficiency. In these simulations the source was on the direct opposite side of the container (i.e. $x = 0$, $y = -312.8$ cm, $z = 0$) from the ONDAC and the HEU was located in the exact center of the container (i.e. $x = 0$, $y = -159.6$ cm, $z = 0$). The sources were taken to be monoenergetic between 0.0253 eV (thermal neutron source) to 1 MeV along with a polyenergetic Cf^{252} , which is shown in figure 3-1 as a 2 MeV source. The MCNP cases used to obtain these results held both the source and HEU position constant while varying the source energy. Efficiencies were obtained by dividing the number of interactions in the ONDAC by the total number of possible interactions allowing for geometrical attenuation. Equations (3.1) and (3.2) below are the equations used to find the ONDAC efficiency and the maximum number of interactions in the ONDAC respectively.

$$\text{ONDAC efficiency} = \frac{\text{Interactions in ONDAC}}{\text{Maximum Interactions}} \quad (3.1)$$

$$\text{Maximum interactions} = \frac{\text{Total ONDAC detector frontal area}}{4\pi R^2} \quad (3.2)$$

The $4\pi R^2$ term in the denominator of equation (3.2) is the surface area of a sphere of radius, R . Shown in figure 3-1 are the efficiencies of both the side and central ONDAC detectors, both with and without HEU present. As can be seen in this figure the side ONDACs are slightly less efficient than the center ONDAC and that the presence of HEU decreases efficiency slightly. However, the major effect on efficiency is clearly source energy. The peak efficiency occurs at approximately 1 eV, which is very close to the large fission resonances that occur in U^{235} .

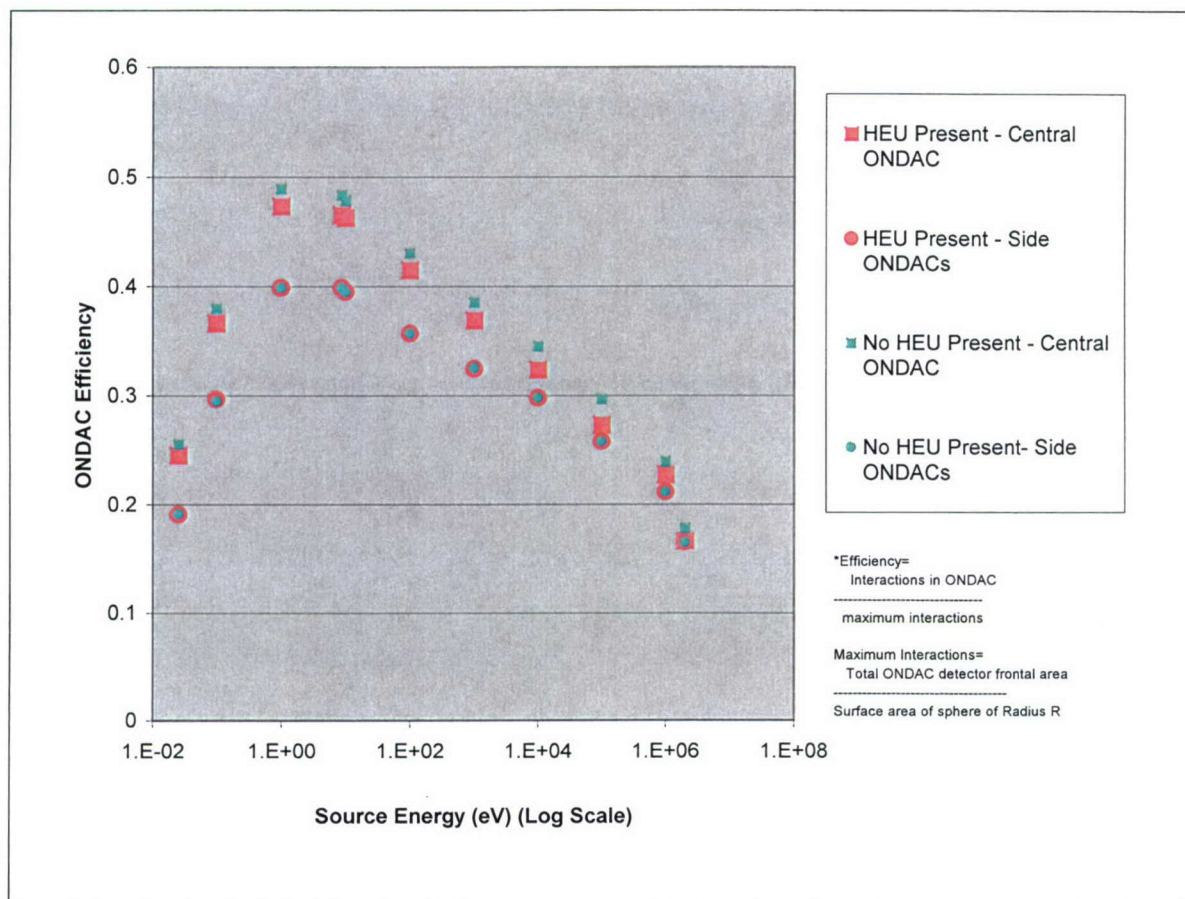


Figure 3-1. Effect of source energy on ONDAC efficiency.

Figure 3-2 is a plot the fission cross section of U^{235} , which shows the resonance structure. The largest fission resonance occurs at 8.77 eV and has a value of 713 barns (KAERI, 2002). Thus this energy was chosen to study the effect of varying the distance between the HEU and the source. The results of this study are given in figure 3-3. Displayed on the vertical axis is the interaction ratio of simulations run with and without HEU present in the container. In this study it was desired to find the conditions that produced the highest interaction ratios above unity. In the simulations with the HEU present, the HEU sphere was moved along the centerline of the container, but in all cases was in the direct line-of sight between the source and the ONDAC detector. In figure 3-3 the ONDAC distance

from source, which was held constant at 312.8 cm, has normalized all results. Surprisingly all the interaction ratios were less than unity! The explanation of this result was that HEU decreased the solid angle that neutrons emitted by the source could travel uncollided and still reach the ONDAC detector. In other words, the HEU produced a shadowing effect on the ONDAC detector. This shadowing effect dominated those neutrons that collided in the HEU and fissioned, because these fission neutrons were emitted isotropically and hence had a small probability of ever interacting with the ONDAC.

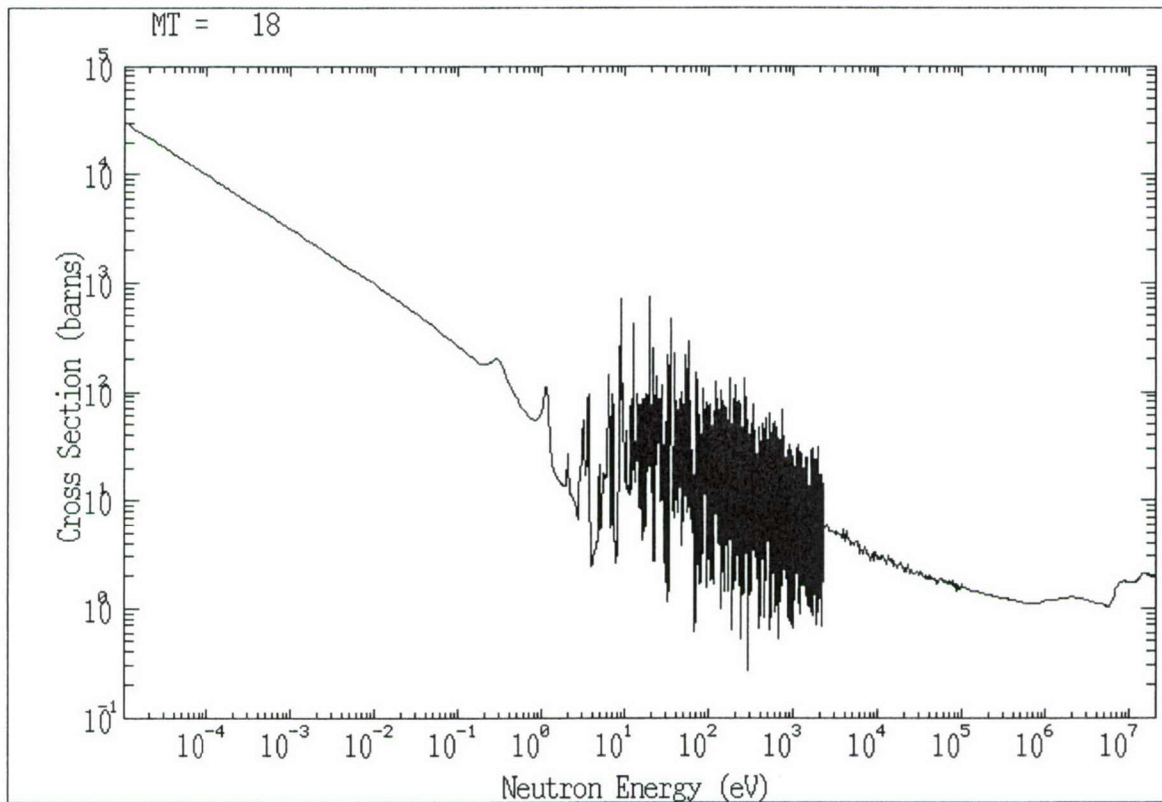


Figure 3-2. U^{235} fission cross section.

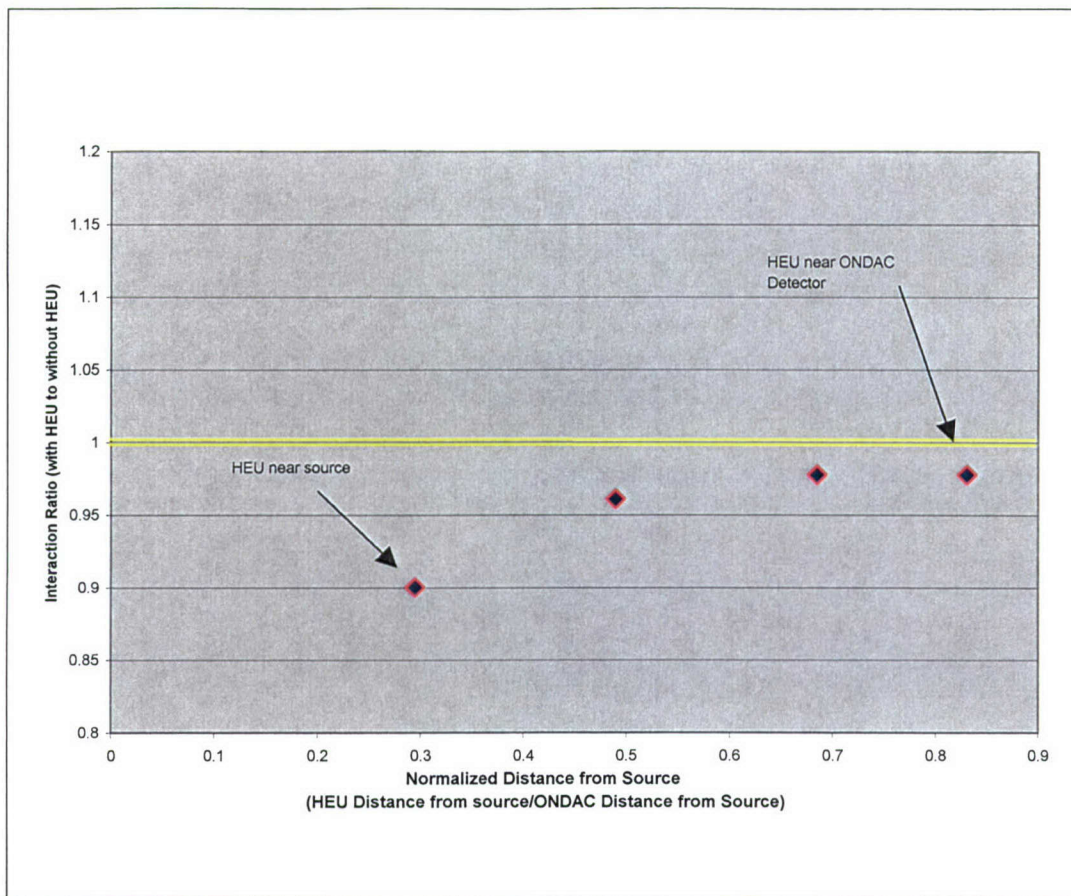


Figure 3-3. Resonance study - Normalized detector distance from source vs. response ratio in central ONDAC.

In order to find a combination of source and HEU positions that produced interaction ratios greater than unity, it was necessary to move the source and HEU very close to each other. Figure 3-4 displays the ONDAC interaction ratios with and without HEU present for various source energies with the HEU to source distance at 5 cm and the HEU 52.9 cm from the ONDAC. Physically, this would imply that the source was well inside the container and the HEU was relatively close to the ONDAC. Indicated by arrows in figure 3-4 are the energies of a Cf^{252} source and the 14 MeV source energy. It is clear from this figure that the higher source energy, the higher the interaction ratio with the 14 MeV source being superior to all others studied with a value of 1.2. There are two reasons for this result. First, more neutrons are released from fissioning by 14 MeV neutrons than by Cf^{252} neutrons with HEU. This effect increases the numerator of the interaction ratio. Second, the ONDAC has a higher efficiency to detect fission neutrons than 14 MeV neutrons based on extrapolating the results in figure 3-1. This latter effect increases the denominator in the interaction ratio for Cf^{252} neutrons compared to 14 MeV neutrons when no HEU is present. From this finding, the decision was made to only use 14 MeV sources for further analysis.

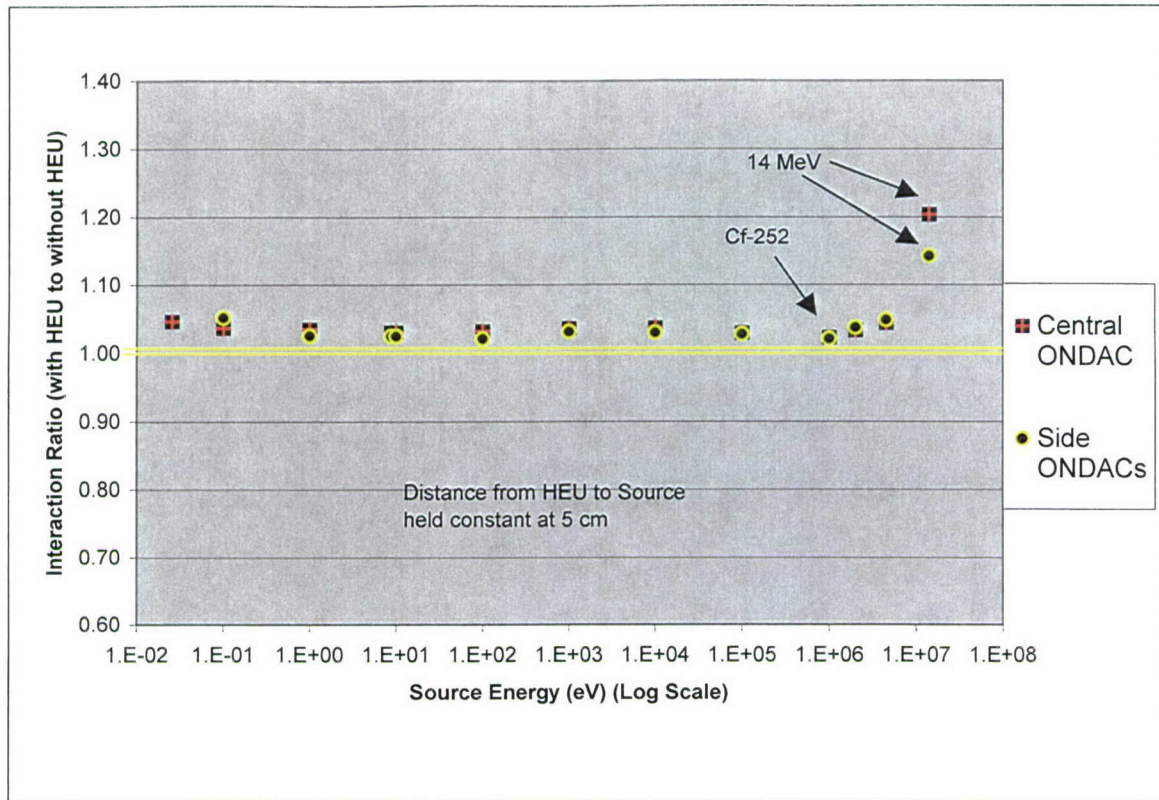


Figure 3-4. Interaction ratios in ONDAC detectors vs. source energy with HEU to source distance of 5 cm.

In the next study, 14 MeV sources were placed at different locations around the container as well as at further distances from the HEU. However, at a distance of only 13.0 cm between the source and the HEU and with the HEU only 52.9 cm from the source, the interaction ratio was found to be essentially unity as shown in figure 3.5. This near unity interaction ratio is a reflection of the fact that at HEU to source distances of 13 cm or larger, too few fission neutrons reach the ONDAC detector compared to those from the source itself. Obviously 13 cm is too short a distance to make this approach practical. Thus several techniques were studied to enhance the signal produced by the HEU compared to the source.

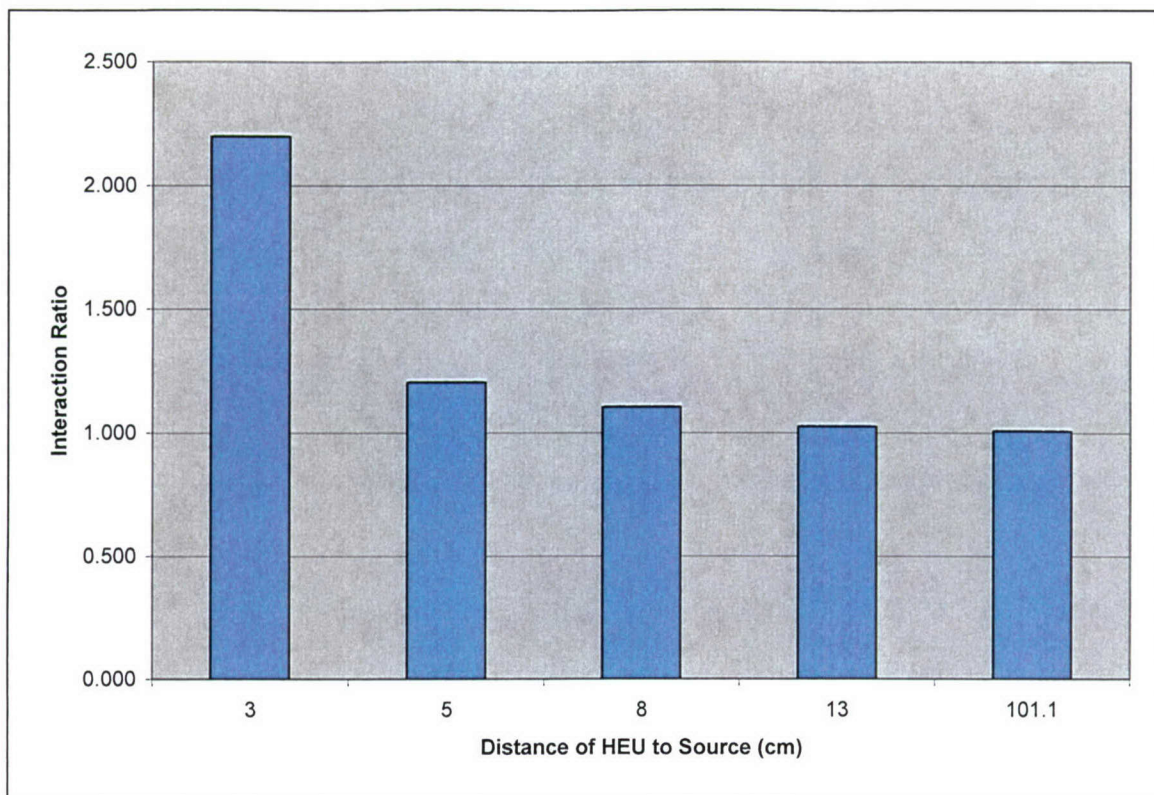


Figure 3-5. Effect of HEU distance to source with a 14 MeV source.

The first technique studied to improve the signal to noise ratio was to consider the use of backscattered neutrons. Since all 14 MeV sources are essentially isotropic, this approach had to be accomplished by the use of neutron shields. To accomplish this backscattering effect, both the ONDAC and the neutron source had to be placed on the same side of the container. The source itself was positioned closer to the container than the ONDAC (i.e. in front of the ONDAC) such that if neutron was emitted at 90° or less, it would not interact with the ONDAC. Then borated polyethylene, a large neutron absorber, was placed in a rectangular parallelepiped geometry box behind the source to prevent neutrons emitted at 90° or greater angles from reaching the ONDAC detector. The borated polyethylene shield couldn't be placed entirely around the source or else few neutrons would enter the container. Figure 3-6 illustrates the SABRINA model of this set-up.

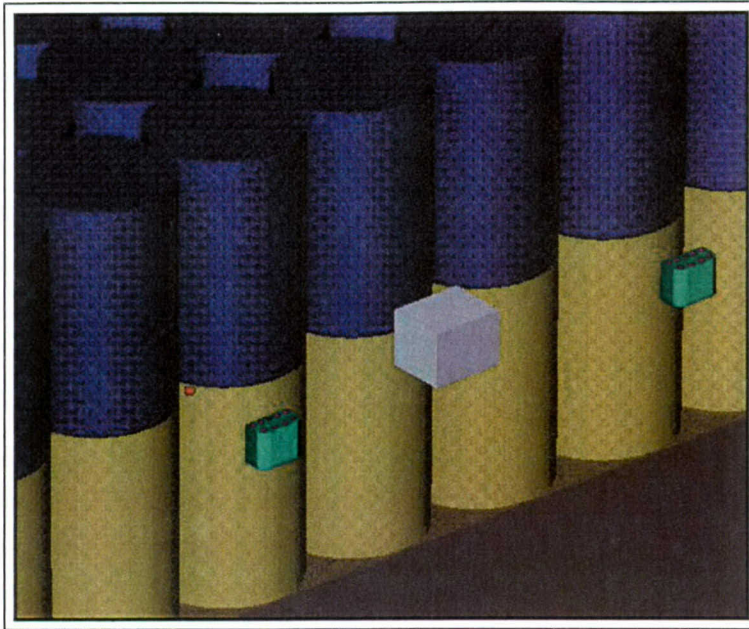


Figure 3-6. SABRINA model of borated polyethylene rectangular parallelepiped surrounding neutron source. Two ONDAC detectors were used in this model. Small dot in front of ONDAC represents the HEU sphere.

Figure 3-7 shows the effect of increasing the volume of the borated shield on the overall ONDAC interaction. In all borated polyethylene shield trials, the distance from the HEU to the 14 MeV source was held constant at 101.1 cm and the HEU was 52.9 cm from ONDAC, while the source was in the center of the shield. As expected, increasing the volume of the borated polyethylene shield reduced the number of neutrons interacting with the ONDAC detector, indicating that the shield was absorbing neutrons as expected. In the highest volume case (1.1025 m^3) the shield extends almost entirely between the source and the ONDAC detector.

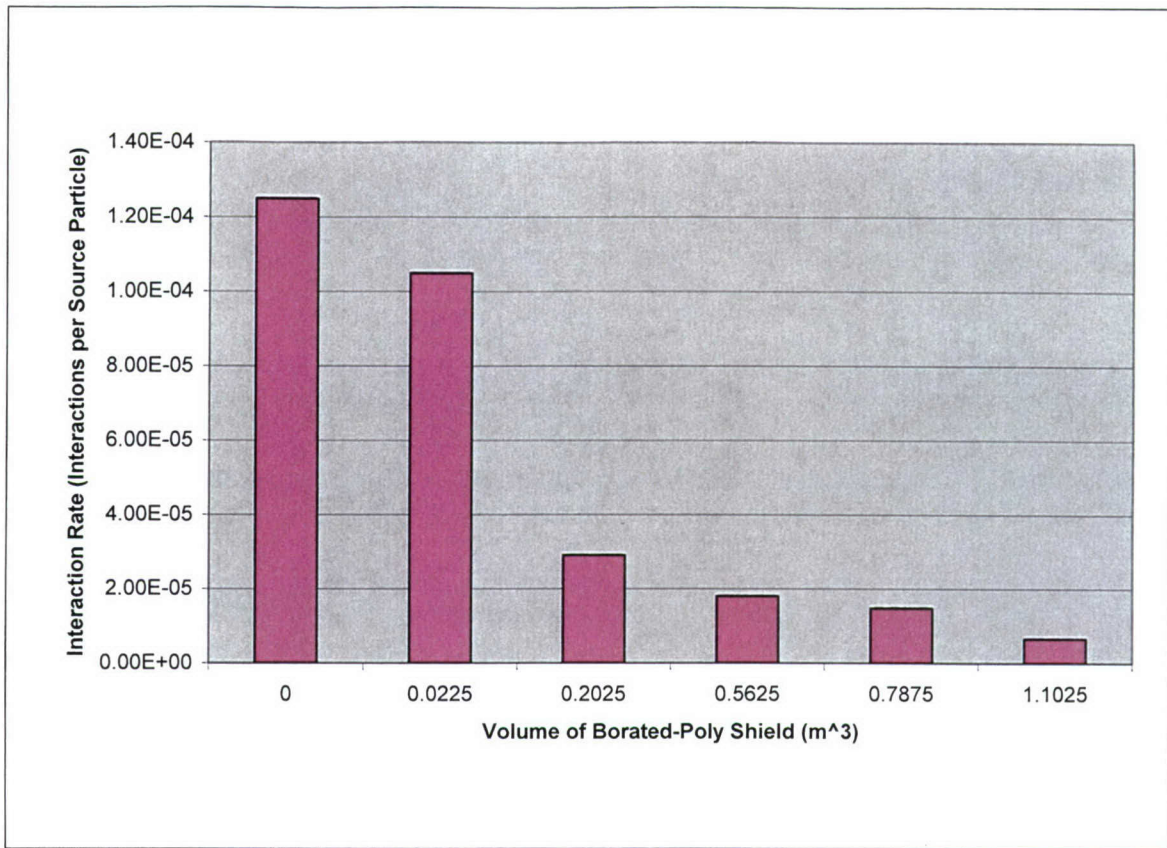


Figure 3-7. Effect of borated polyethylene shield volume on interaction rate in ONDAC using backscattered neutrons. Source in center of shield. Source is located 101.1 cm from HEU, while HEU is 50.9 cm from ONDAC.

The effect of a borated polyethylene shield on the ratio of interactions with and without HEU is shown in figure 3-8. In all cases of this study, the distance from the HEU to the source was held constant at 101.1 cm and the distance from the HEU to the central ONDAC was also constant at 50.9 cm. The unity interaction ratio is also displayed in this figure. As the volume of the borated shield increased, the ratio of interactions also increased, but never exceeded 1.1. Since figure 3-8 displays a case in which the source, HEU, and ONDAC were at relatively close distances, it was viewed that at larger distances the borated polyethylene would not be very effective.

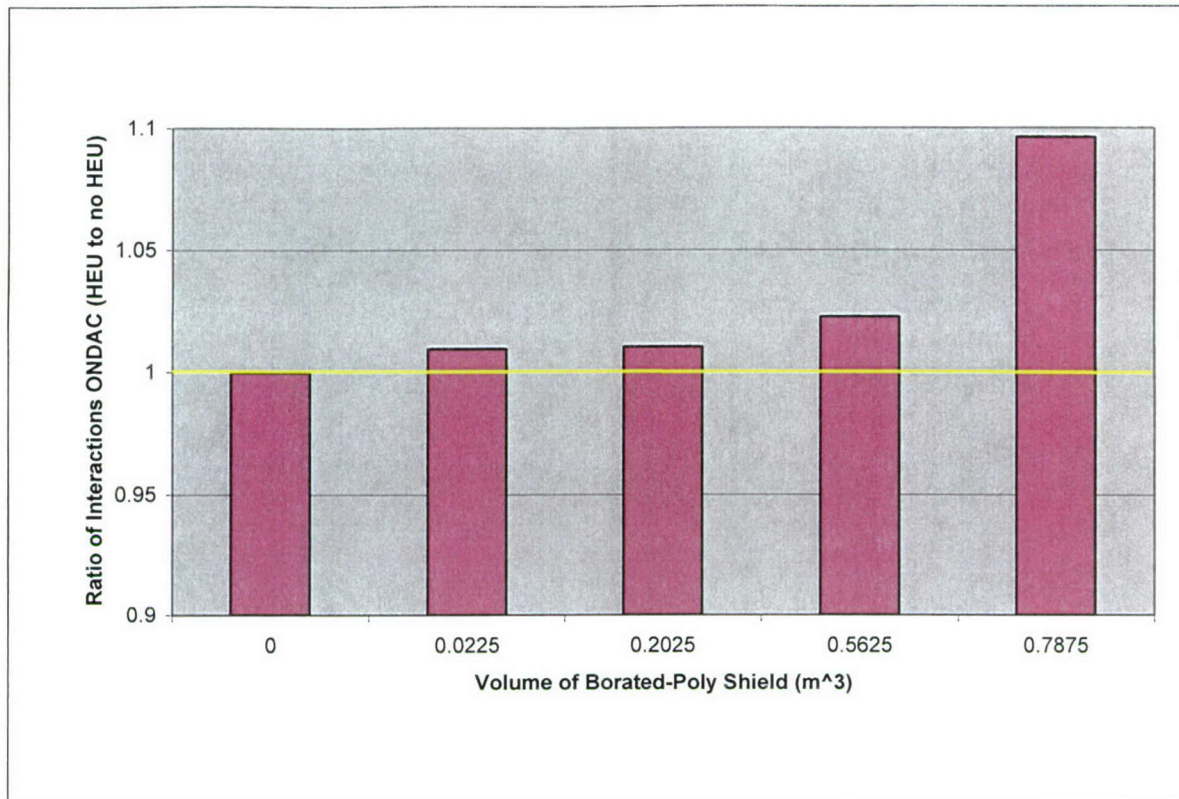


Figure 3-8. Effect of borated polyethylene shield volume on ratio of interactions (HEU present to no HEU present) in ONDAC with source in center of shield. HEU 101.1 cm from source and 50.9 cm from ONDAC.

The last effect studied was the use cadmium of shields around the ONDAC detectors in order convert the detector into an epi-thermal detector and hopefully improve the ratio of neutrons detected with HEU to that without HEU. The results of this study are displayed in figure 3-9. The conditions were the same as in the borated polyethylene study in that both the ONDAC and 14 MeV were on the same side of the container except that they was no borated polyethylene shields. The distance between the HEU and the source was 101.1 cm, while the HEU was 50.9 cm from the ONDAC. Then simulations were run with the HEU at distances between 3 cm and 101.1 cm from the source and without HEU. As can be seen in figure 3-9, the effect of the cadmium shield is to reduce the interaction ratio. Additionally, it was observed that the cadmium shield has a noticeable effect that occurs only when the HEU is several cm away from the source.

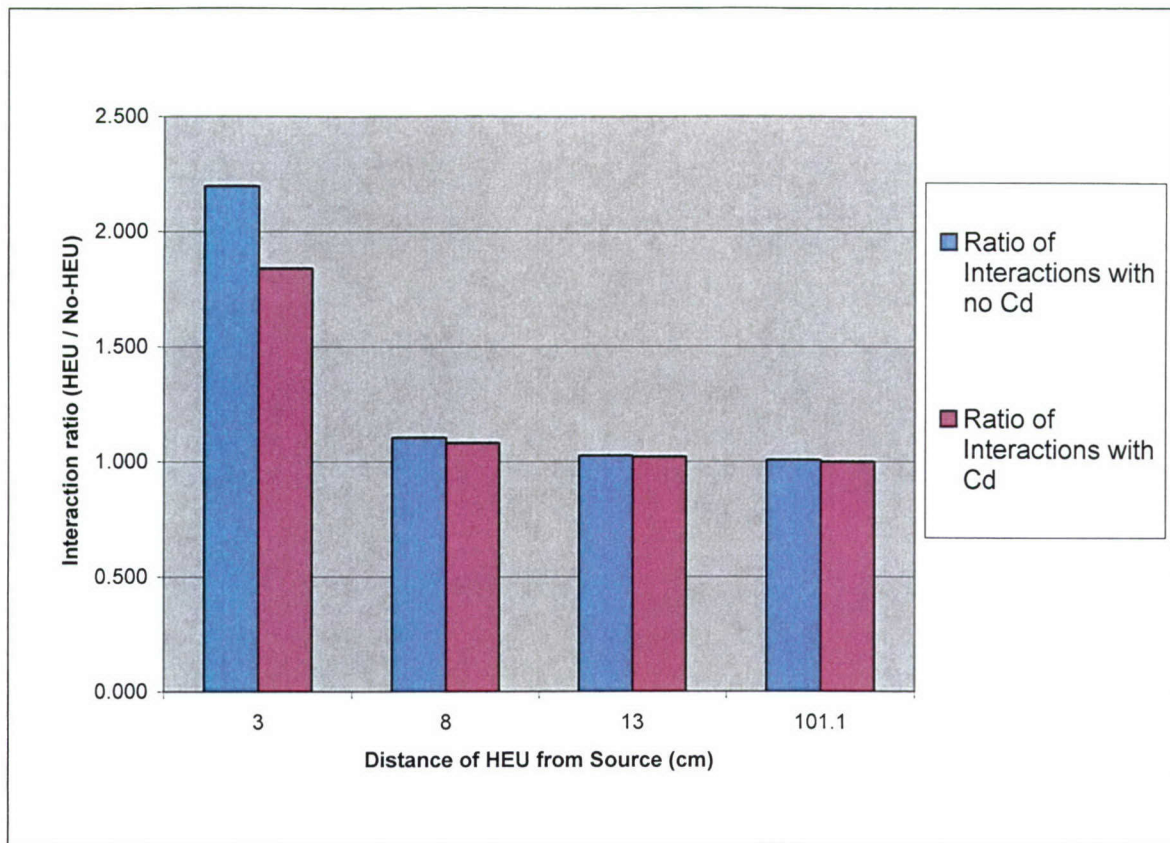


Figure 3-9. Effect of cadmium on ratio of interactions in center ONDAC detector with HEU present to interactions with no HEU present with a 14 MeV source. HEU 52.9 cm from source.

3.2 CONCLUSIONS.

The analyses presented in the preceding subsection leads to the strong conclusion that neutron stimulation with a continuous output source is not a feasible approach to detect 1 kg of HEU in a large cargo container. The reason for this conclusion is that the neutrons from the source dominate the fission neutrons created by the stimulation of HEU except in the case where the source is only several cm from the HEU. However, the stimulation source also creates delayed neutrons, which appear long after the prompt neutrons dissipate. A stimulation approach based on the use of these neutrons is described in the next section.

SECTION 4

STIMULATION USING A PULSED 14 MEV NEUTRON SOURCE AND COUNTING DELAYED NEUTRONS IN A CONTAINER WITH NO PAYLOAD

In this section of the report, an analysis of a pulsed 14 MeV source delayed neutron technique is presented. The underlying principles of the technique are described in section 4.1. In section 4.2 the advantages and disadvantages of a pulsed source compared to a continuous source are given. Section 4.3 reviews the commercial availability along with the capabilities of these sources. Also recent advances in pulsed 14 MeV neutron source technology at LLNL are described, which may be significant in making this approach feasible. A deterministic analysis on this technique is presented in section 4.4. This section describes the assumptions made, relationships developed, and results obtained. A MCNP analysis was also performed, which is described in section 4.5. Section 4.6 presents a comparison of the deterministic and MCNP methods under identical conditions. Recommendations of the operating parameters and minimum source pulse rate are given in section 4.7. Finally, section 4.8 summarizes the conclusions reached on this stimulation approach.

4.1 DESCRIPTION OF THE TECHNIQUE.

When neutrons interact with fissile material, both prompt and delayed neutrons are produced. The prompt neutrons are emitted simultaneously with the fission event. The delayed neutrons are produced from the decay of fission products. Of the nearly 200 fission products produced, approximately 40 emit delayed neutrons. The delayed neutrons have half-lives that vary from a fraction of a second to days. The average half-life of a delayed neutron emitter is approximately ten seconds (La Marsh 1982). In contrast prompt neutrons have life times that depend on the medium through which they diffuse, but in nearly all cases they will dissipate in less than four milliseconds or 4000 μ sec (Smith 1979). This large difference in life times means that if fissile material is bombarded with a pulsed neutron source, there will still be a neutron signature long after the source is turned off. In order to apply this technique, a 14 MeV neutron generator can be cycled by use of electronic timing gates, which as they open and shut, send signals that turn on and off the generator's voltage. When the voltage is applied, neutrons are produced. Neutron production ceases when no voltage is applied. These electronic gates also can produce signals that turn on and off a nearby neutron detector(s). In this technique, the detector only counts neutrons after the pulse has ended and the prompt neutrons have dissipated. An analysis of the optimum pulse and count times is presented for this technique in section 4.4. In figure 4-1, the normalized thermal neutron time response data is shown for fissile

material bombarded with a 100 microsecond 14 MeV pulse. As can be seen the neutron count rate builds up rapidly during the pulse and then exponentially decreases during pulse shutoff. As shown in figure 4-1, the time constant for decay is 1430 μ sec. Hence, initially the thermal neutron counts shown in figure 4-1 are coming from both prompt and delayed neutrons, but after a few msec (2000 μ sec) they will be predominantly due to delayed neutrons.

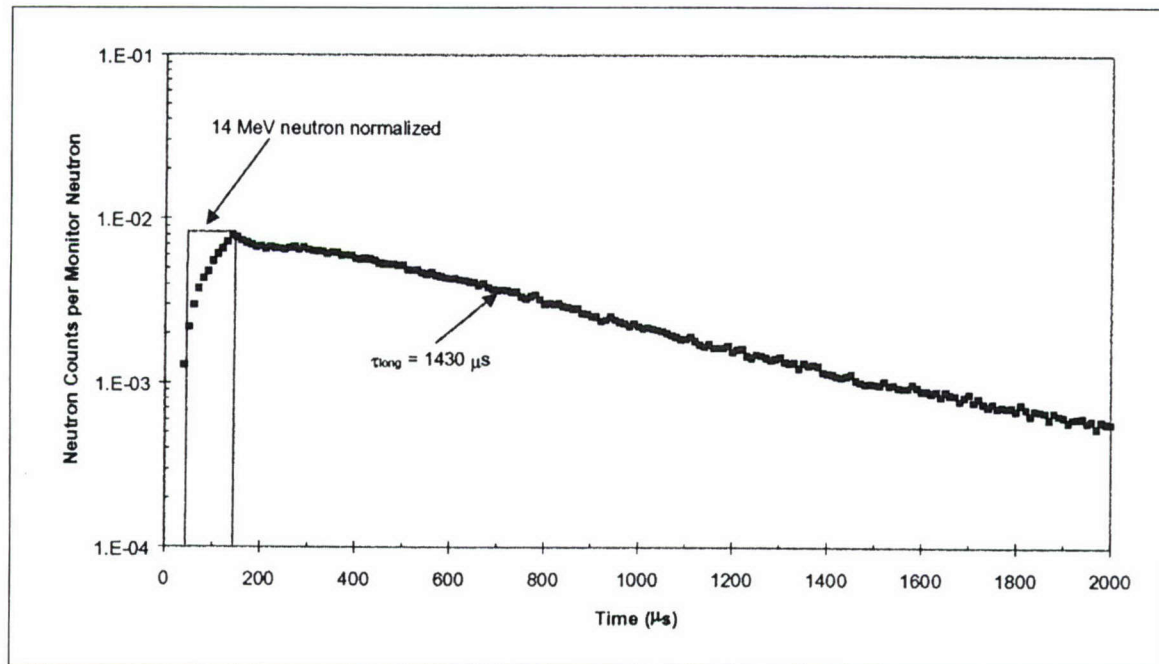


Figure 4-1. Neutron die-away characterization for a 100 μ sec 14 MeV pulse (Gozani 2002).

4.2 ADVANTAGES AND DISADVANTAGES OF PULSED 14 MEV NEUTRON SOURCES.

The pulsed source delayed neutron approach has a major advantage over a continuous source approach in that much higher HEU signal to noise ratios can be produced per source particle. The reason for this is that when using a continuous source, neutrons from the source tend to strongly interfere with the fission neutrons produced by the presence of HEU. There will still be some noise when counting delayed neutrons from two sources: background neutrons induced by cosmic rays and non-fissile radioisotope production that decays by neutron emission. However, the pulsed source delayed neutron approach will have a significantly lower limit of HEU detection compared to the continuous source method.

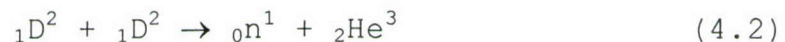
Neutrons can be produced either by the use of an ion accelerator or continuous source. An example of a continuous neutron source would be $^{98}\text{Cf}^{252}$. Ion accelerators have the advantage over continuous sources in that they require no shielding when not in use. Their

main disadvantage is that they require access to large amounts of power in order to produce the high outputs that would be needed for HEU detection applications.

Accelerators or neutron generators are commercially available, which produce both 2.4 MeV and 14.3 MeV neutrons. Generators make 14 MeV neutrons by accelerating deuterium nuclei (deuterons) into a target material, which contains tritium. For deuterium and tritium nuclei to interact, the deuterons are accelerated through a potential drop of over 200 kV, after which they have acquired sufficient kinetic energy to overcome the coulombic repulsive force due to the positive charge of both nuclei. The nuclear reaction, which occurs, is as follows:



This reaction is highly exothermic and produces on average a 14.3 MeV neutron, which is emitted nearly isotropically (Csikai 1987). Another possible way to produce neutrons in an accelerator is to use the following reaction between two deuterons:



This reaction is also exothermic and produces a 2.45 MeV neutron. However, the cross section for this reaction is nearly one hundredth of that of the D-T reaction. Thus, neutron generators that use the D-T reaction have a neutron yield approximately 100 times that as neutron generators, which employ the D-D reaction. For this reason D-T (14 MeV) neutron generators are superior to D-D (2.45 MeV) neutron generators.

Another advantage 14 MeV neutrons have over lower energy neutrons is that the number of prompt and delayed neutrons released per fission increases with increasing neutron energy that induces the fissioning. A 14 MeV neutron produces approximately 0.025 delayed neutron per fission, while ${}_{98}\text{Cf}^{252}$ self-fissioning neutron releases about 0.017 delayed neutrons per fission (Keepin 1965). Also the fission microscopic cross section is higher for 14 MeV neutrons (2.05 b) than for ${}_{98}\text{Cf}^{252}$ self-fissioning neutrons (1.27 b) in U^{235} . Both these effects improve the method's HEU detection capability.

In order to make neutron stimulation feasible, the half-lives of the radioisotopes produced from the container materials need to be short, so that the cargo's radioactivity will quickly return to near background levels and meet Department of Transportation (DOT) and Nuclear Regulatory Commission (NRC) regulations for release. An important characteristic of 14 MeV irradiations is that it produces isotopes with significantly shorter half-lives than that which would be induced by material irradiated with lower energy neutrons. For example, Cu^{63} (69.1% of naturally occurring copper) when irradiated

with thermal neutrons undergoes radiative capture and produces Cu^{64} which has a 12.87 hour half-life. However, Cu^{63} when irradiated with 14 MeV neutrons undergoes a (n,2n) reaction to produce Cu^{62} , which has a 9.8 minute half-life (Alfassi 1990). A more detailed discussion of this activation problem is provided in section 8.

4.3 AVAILABILITY OF PULSED 14 MEV NEUTRON SOURCES.

Neutron generators are available from a wide variety of commercial and government sources. While not meant as a definitive list, table 4-1 lists five potential sources that from which a pulsed 14 MeV neutron generator could be procured. The first two listed (Thermo MF Physics and Chapel Hill Logging Services) are US commercial vendors. The next two listed (Halliburton and Schlumberger) are large oil service companies that produce neutron generators for well-logging applications. The final name is a Russian organization, which markets neutron generators internationally. As a general rule, the maximum output of pulsed generators from these vendors is approximately 3×10^8 neutrons/sec with the exception of the Russian organization, which claims it can deliver a pulsed neutron generator with a yield of 10^{10} neutrons/sec. If these generators run in a continuous mode, then their maximum output is 10^{11} neutrons/sec.

Table 4-1. Potential pulsed 14 MeV neutron generator procurement sources.

Organization	Address/phone number	Comment
Thermo MF Physics	5074 List Drive Colorado Springs, Co 80919 719-598-9549	Commercial vendor
Chapel Hill Logging Services	PO Box 7 Chapel Hill, Texas 77426 979-251-2912	Commercial vendor
Haliburton Energy Services	PO Box 60078 Houston, Texas 77205 281-871-7276	Generators designed for well-logging applications
Schlumberger	PO Box 14484 Houston, Texas 77221 713-749-5835	Generators designed for well-logging applications
All Union Research Institute of Automatics	Moscow 101000 USSR Central Post Office PO Box 918 258-12-68	Government source

4.4 DETERMINISTIC ANALYSIS.

In a pulsed source approach each cycle consists of three components: neutron pulse, prompt neutron dissipation, and counting. The neutron detector is gated off while the source is pulsing and the prompt

neutrons dissipate and are gated on in order to count the delayed neutrons. The schematic in figure 4-2 shows this process for the first two cycles.

1 st Cycle			2 nd Cycle		
Neutron Pulse	Prompt Neutron Dissipation	Count Delayed Neutrons	Neutron Pulse	Prompt Neutron Dissipation	Count Delayed Neutrons
t_p	t_d	t_c	t_p	t_d	t_c
Detector gated off		Detector gated on	Detector gated off		Detector gated on

Figure 4-2. Schematic representation of time intervals in a pulsed neutron system approach.

In figure 4-2 the total cycle time is given by the equation:

$$t_{cyc} = t_p + t_d + t_c \quad (4.3)$$

where

t_{cyc}	=	total cycle time, sec
t_p	=	pulse time, sec
t_d	=	prompt neutron dissipation time, sec
t_c	=	count time, sec

Equation 4.3 neglects the transit time needed between each cycle. The following assumptions and conditions were made in the first part of the deterministic analysis:

- (1) constant pulse rate of \dot{Q} neutrons/sec;
- (2) isotropic 14 MeV source;
- (3) neglect the effects of neutron moderation on the source neutrons (i.e. 14 MeV neutrons interact with the HEU);
- (4) 1 kg of HEU located at a distance r_1 from the source;
- (5) 1 group delayed neutron theory applicable;
- (6) all prompt neutrons have dissipated while counting;
- (7) ONDAC neutron detector located at a distance r_2 from the HEU;
- (8) HEU isotopic composition is 100% U^{235} .

Figure 4-3 is a schematical representation of the deterministic model.

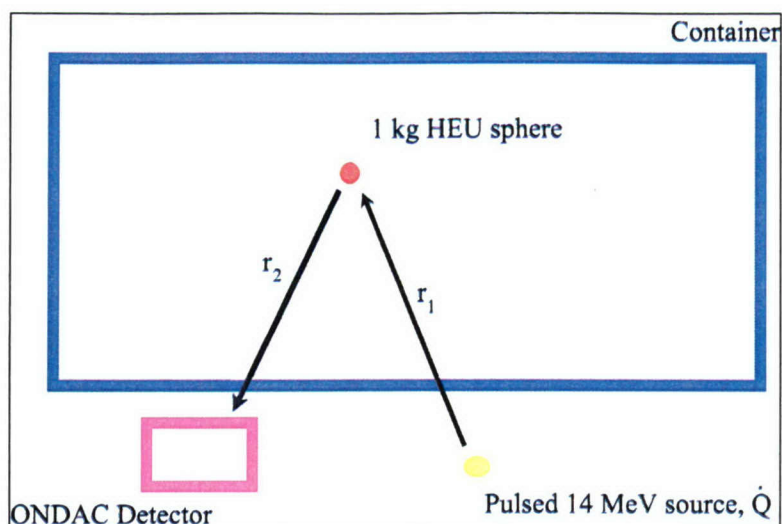


Figure 4-3. Schematic representation of the major aspects of components in the deterministic model.

The total number of 14 MeV neutrons/cm² or fluence (ϕ_0) that can reach the surface of the HEU sphere during a pulse of duration t_p is given by equation (4.4):

$$\phi_0 = \frac{\dot{Q} t_p}{4\pi r_1^2} \quad (4.4)$$

where

- \dot{Q} = 14 MeV neutron pulse rate, neutrons/sec
- t_p = pulse duration, sec
- r_1 = distance the 14 MeV source is from the HEU, cm

The total number of fissions in 1 kg of HEU can be found by the equation:

$$F = \Sigma_f \phi V \quad (4.5)$$

where

- F = total number of fissions in 1 kg of HEU in t_p
- Σ_f = HEU macroscopic fission cross section, cm⁻¹
- V = 1 kg HEU volume, cm³
- ϕ = 14 MeV fluence which interacts with the HEU, n/cm²

In order to evaluate equation (4.5), the volume of a 1 kg sphere of HEU was taken to be 53.9 cm³ based on using a HEU density of 18.55 gram/cm³. The 14 MeV HEU macroscopic cross section was determined from the equation:

$$\Sigma_f = N_{HEU} \sigma_f = 0.097 \text{ cm}^{-1} \quad (4.6)$$

where

- N_{HEU} = HEU 10²⁴ atom density, 0.047 per cm³
- σ_f = 14 MeV microscopic fission cross section of HEU, 2.046 b (Hansen, 1979)

The 14 MeV fluence that interacts with the HEU (ϕ) was found by correcting the surface fluence (ϕ_0) for self-absorption within the HEU, which results in a lower average fluence across the HEU than that seen by its surface. Since HEU has a high absorption cross section compared to its scattering cross section, diffusion theory doesn't apply, and the neutron fluence should decrease exponentially from the surface of the HEU sphere (LaMarsh 2001). This effect was estimated by exponentially adjusting the surface fluence with an exponent that was the ratio of the neutron mean chord length to neutron mean free path within the HEU sphere. Thus the average neutron fluence was found from the equation:

$$\phi = \phi_0 e^{-\frac{\ell}{\lambda}} \quad (4.7)$$

where

ϕ	=	average fluence within HEU sphere, n/cm ²
ϕ_0	=	fluence at HEU surface and found by equation 4.4, n/cm ²
ℓ	=	mean chord length traveled by neutrons crossing the HEU sphere, 3.09 cm
λ	=	14 MeV mean free path in HEU, 4.49 cm (Hansen 1979)

The mean chord length for particle crossing a sphere is known to be two thirds the diameter of a sphere (International Commission on Radiation Units and Measurements 1983). Since a 1 kg HEU sphere would have a diameter of 4.64 cm, the mean chord length was determined to be 3.09 cm. Then by combining equations 4.4 through 4.7, an expression for the total number of fissions (F) in the HEU sphere was found as follows:

$$F = 0.21 \frac{\dot{Q} t_p}{r_1^2} \quad (4.8)$$

To determine the number of delayed neutrons produced, the above F parameter was multiplied by the delayed neutrons produced per fission (β), which has a value of 0.025 for 14 MeV neutrons (Keepin 1965). Hence, the initial delayed neutron production (S_0) immediately following a pulse of duration t_p was calculated as follows:

$$S_0 = \frac{0.0052 \dot{Q} t_p}{r_1^2} \quad (4.9)$$

The delayed neutron source decays and become weaker with time following each pulse. To estimate this effect the one group kinetics model was employed (LaMarsh 2001). Hence, the number of delayed neutrons following a wait time t before counting after a pulse was given by the equation:

$$S(t) = S_0 e^{-\lambda \cdot t} \quad (4.10)$$

where

- $S(t)$ = delayed neutrons available to count after wait time t after pulse, neutrons
- S_0 = delayed neutrons available to count initially after pulse, neutrons
- λ = HEU one group delayed neutron decay constant, $0.076 \text{ seconds}^{-1}$
- t = wait time following pulse before counting, seconds

In order to calculate the interactions these delayed neutrons would make with the ONDAC, its intrinsic efficiency, the geometrical efficiency, and the following additional assumptions were combined:

- (1) no cargo in the container between the HEU and the ONDAC detector;
- (2) delayed neutrons emitted monoenergetically with an energy of 0.5 MeV;
- (3) delayed neutrons emitted isotropically.

The intrinsic efficiency (ϵ_i) of the ONDAC detector is defined as follows:

$$\epsilon_i = \frac{\text{total detector counts}}{\text{total neutrons incident on detector}} \quad (4.11)$$

For a 0.5 MeV neutron, the ONDAC intrinsic efficiency has been calculated to be 0.26 (Millett 1997). The geometrical efficiency (ϵ_g) of the ONDAC detector is given by the equation.

$$\epsilon_g = \frac{\text{surface area of the He-3 tubes in ONDAC}}{4\pi r_2^2} \quad (4.12)$$

where

- r_2 = distance between the HEU and the ONDAC detector

The total ONDAC detector counts per minute (CPM) was then found by combining equations (4.9) through (4.12) and adjusting this result for the fraction of time counting occurs during each cycle (f_d) and the number of cycles per minute (f). The resulting equation had the form:

$$CPM = \left(\frac{0.0052 \dot{Q} t_p}{r_1^2} \right) \epsilon_i \frac{A_{\text{ONDAC}}}{4\pi r_2^2} f_d f e^{-\lambda t} \quad (4.13)$$

where

- CPM = count rate in the ONDAC detector
- \dot{Q} = 14 MeV neutron pulse rate, neutrons/sec
- t_p = pulse duration, sec

r_1	=	distance the 14 MeV source is from the HEU
ϵ_i	=	ONDAC detector efficiency, .26
r_2	=	distance ONDAC detector from HEU, cm
A_{ONDAC}	=	surface area of all nine He ³ detectors in ONDAC, 900 cm ²
f_d	=	fraction of delayed neutrons that are counted in a cycle, t_c/t_{cyc}
f	=	cycles per minute, $60/t_{\text{cyc}}$
t	=	wait time following pulse before counting, seconds
λ	=	HEU one group delayed neutron decay constant, 0.076 seconds ⁻¹

Inserting the known numerical constants into equation (4.13) gave the equation used to estimate the ONDAC counts per minute (CPM):

$$CPM = \frac{5.784 \dot{Q} t_p f_d f e^{-\lambda t}}{r_1^2 r_2^2} \quad (4.14)$$

Equation (4.14) shows that the CPM will decrease as the fourth power of the distances between the HEU and the source and the HEU and the ONDAC.

Figures 4-4 through 4-7 demonstrate the effect on the maximum ONDAC detector counts per minute (CPM) by varying the count time in a 14 MeV pulsed source neutron detection system using equation (4.14) while holding both pulse width and dissipation time constant. In figures 4-4 through 4-7, the distance from both the source and the HEU to the ONDAC detectors has been fixed at 100 cm with the pulse source strength 10^{11} neutrons per second. Each figure also displays both the ONDAC background counts that would be encountered due to cosmic ray neutrons as well as the maximum ONDAC count rate. As discussed later in the subsection, this maximum CPM occurs after the source has been cycled a large number of times. The background count figures are based upon the ONDAC field test conducted at LANL, which determined that the background level was 180 counts per minute. (Murphy 1999).

The results in these figures are based on pulsing a source for a set period of time (t_p), then waiting 4 msec for the prompt neutrons to dissipate (t_d), and then finally counting the delayed neutrons for a set time period (t_c). The horizontal axis in figures 4-4 through 4-7 displays count time in milliseconds, while the vertical axis displays the maximum ONDAC detector counts per minute. In figure 4-4, the pulse width is 5 msec, while it increases to 10 msec, 15 msec, and 20 msec in figures 4-5, 4-6, and 4-7 respectively. The 4 msec dissipation time is held constant in all figures.

Figures 4-4 through 4-7 indicate that the ideal count time (t_c) is nearly equal to the pulse time (t_p) being used. For example in figure 4-7 the maximum ONDAC count rate is approximately 1200 CPM, which

occurs when count time and the pulse width are both 20 msec. This result is due to the fact that when a count time greater than the pulse time is used fewer particles are counted because less time is available to pulse the source, while using a count time shorter than the pulse time results in fewer particles being counted because the count time is too short.

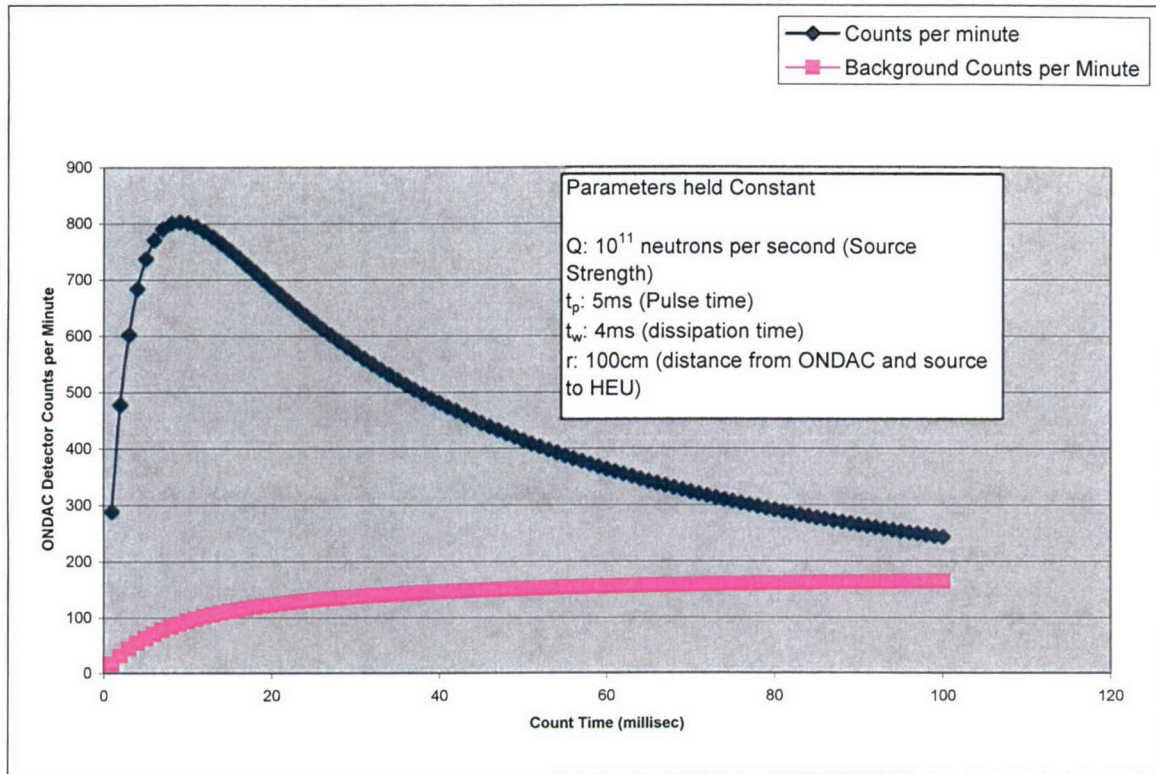


Figure 4-4. Effect of varying detector count time with a 5 ms pulse width on counting delayed neutrons from a 14 MeV pulsed source with an ONDAC detector. ONDAC background count rate also shown.

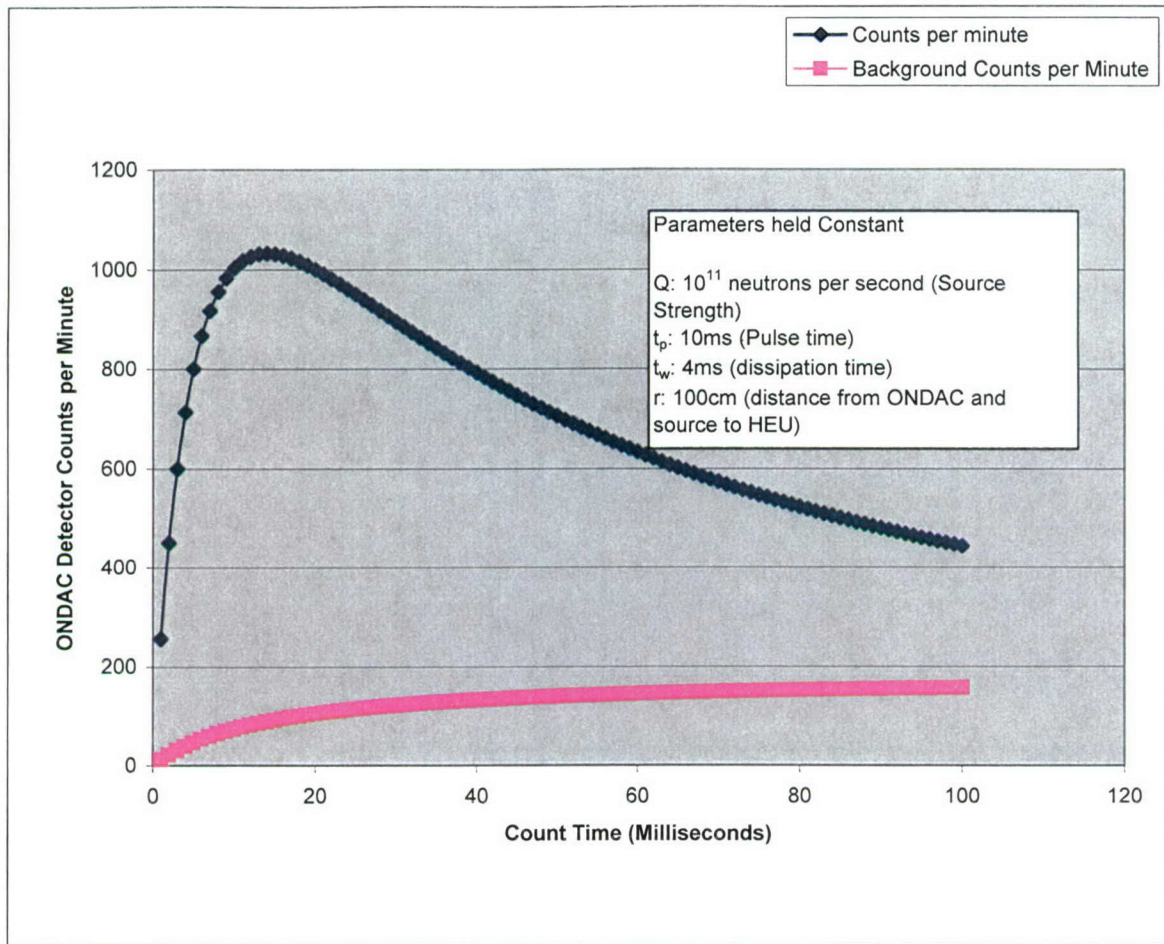


Figure 4-5. Effect of varying detector count time with a 10 ms pulse width on counting delayed neutrons from a 14 MeV pulsed source with an ONDAC detector. ONDAC background count rate also shown.

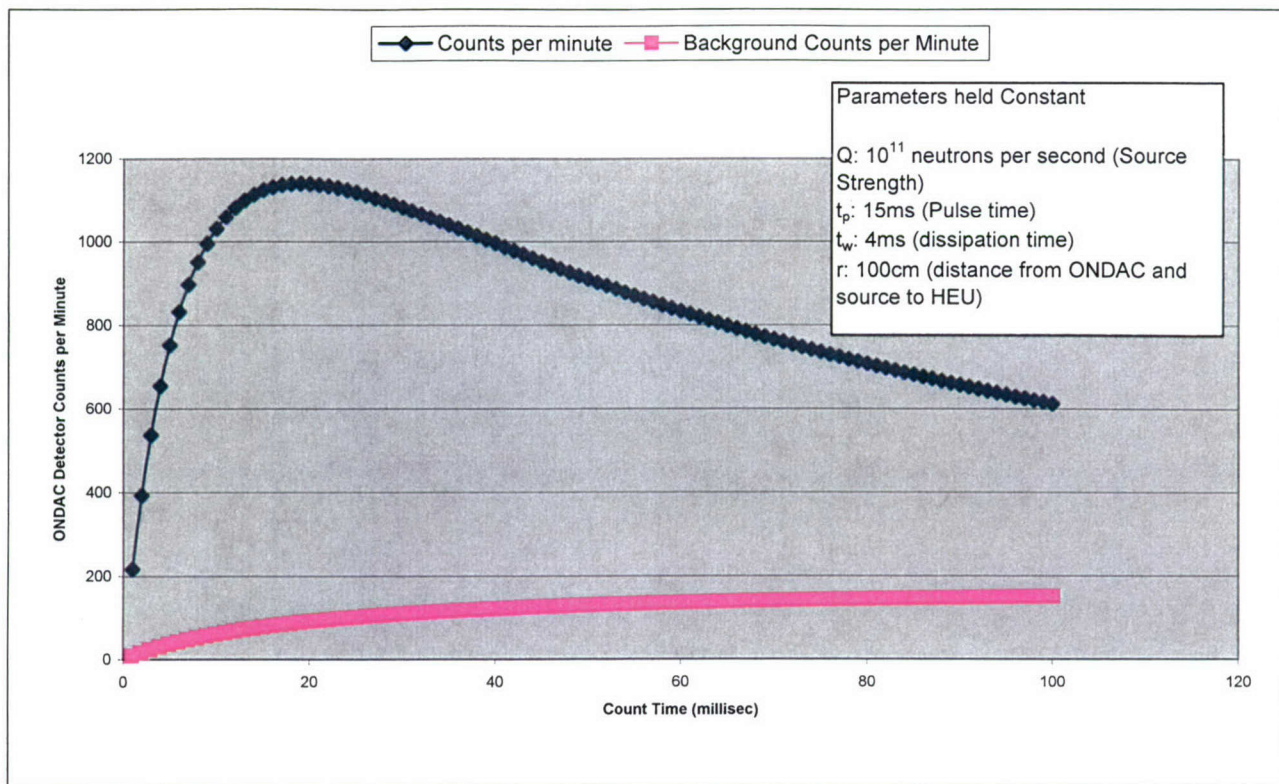


Figure 4-6. Effect of varying detector count time with a 15 ms pulse width on counting delayed neutrons from a 14 MeV pulsed source with an ONDAC detector. ONDAC background count rate also shown.

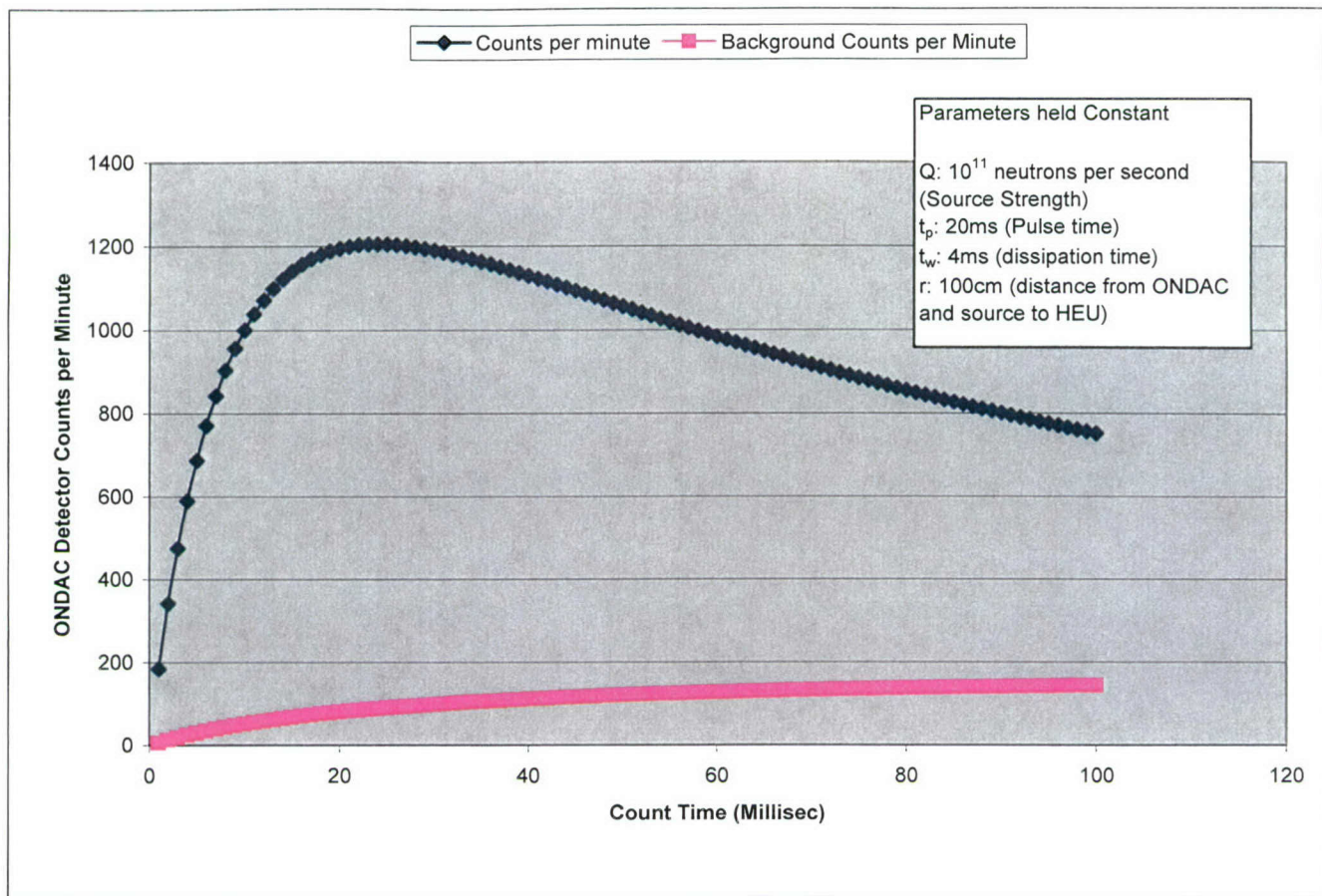


Figure 4-7. Effect of varying detector count time with a 20 ms pulse width on counting delayed neutrons from a 14 MeV pulsed source with an ONDAC detector. ONDAC background count rate also shown.

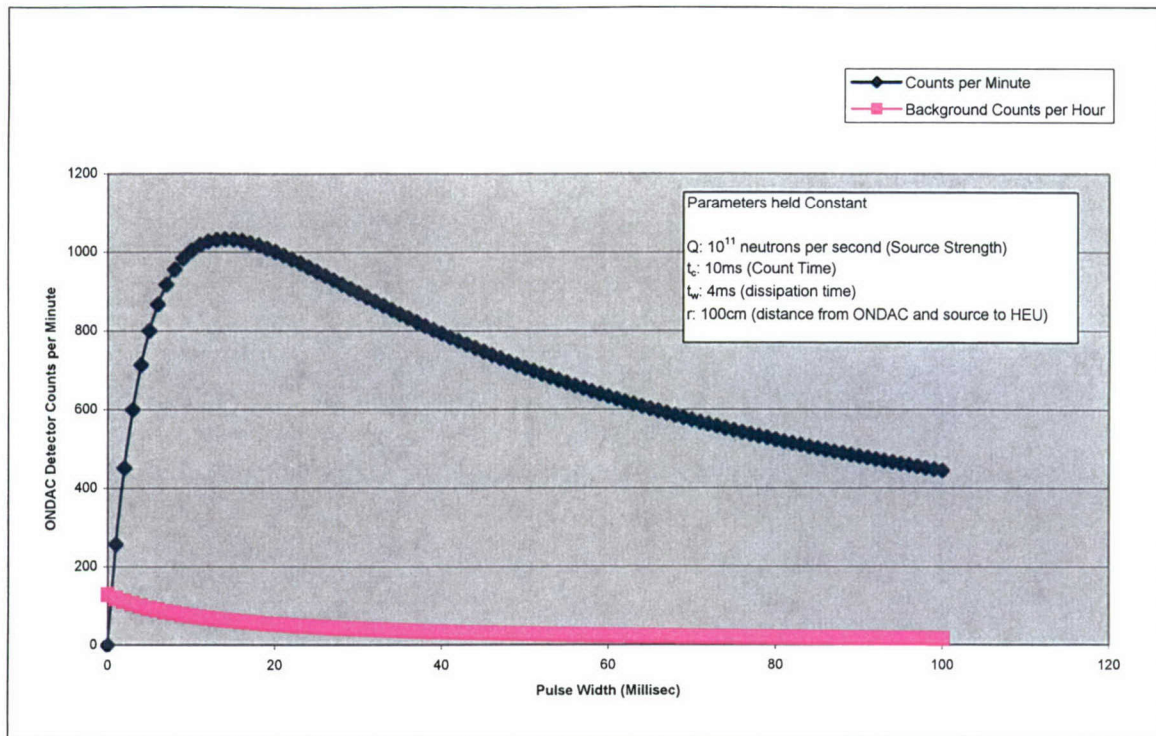


Figure 4-8. Effect of varying detector pulse width with a 14 MeV source on an ONDAC detector. ONDAC background count rate also shown.

Under conditions similar to figures 4-4 through 4-7, the effect of varying the pulse width from 0 to 100 msec while keeping the count time fixed at 10 msec was next studied. The result of this analysis is shown in figure 4-8. Figure 4-8 shows that the maximum ONDAC count rate was found to occur also when the pulse width equals the count time. Based on the results in figures 4-4 through 4-8, it was next decided to analyze the pulsed system under the condition that the count time is held equal to pulse time, while varying other parameters.

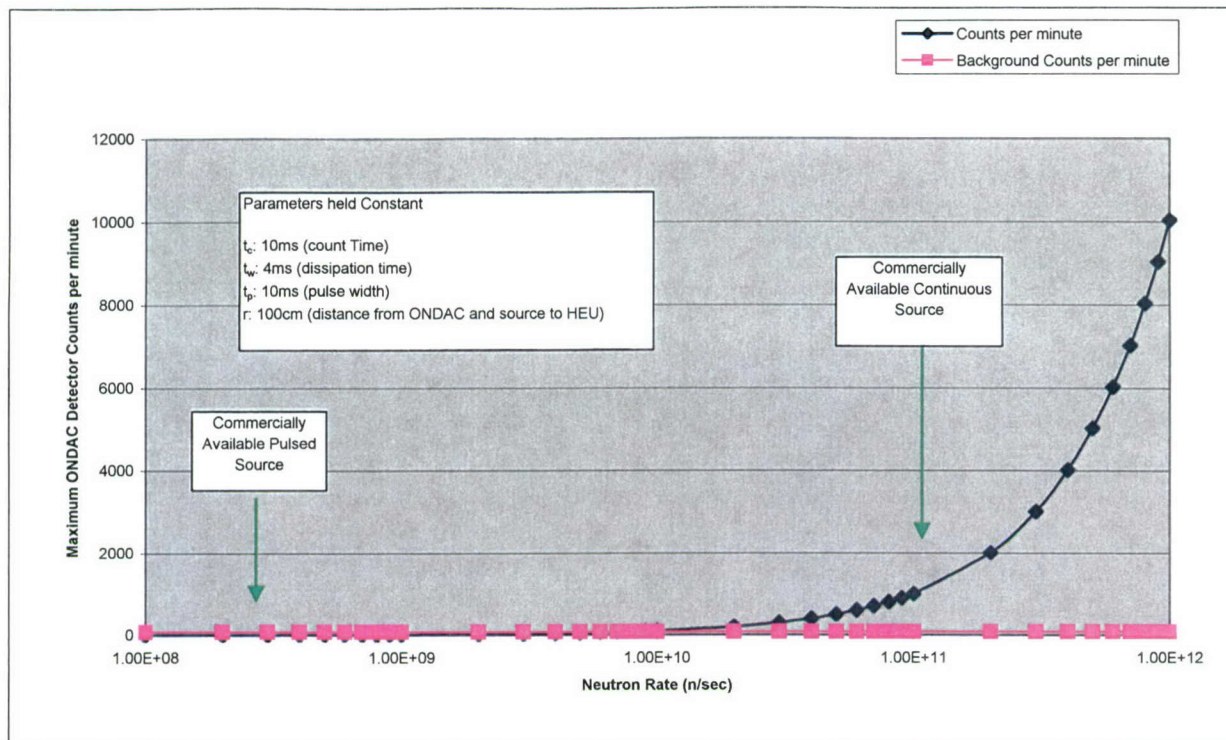


Figure 4-9. Effect of varying source neutron emission rate on counting delayed neutrons from a 14 MeV pulsed source with an ONDAC detector along with ONDAC background count rate.

Shown in figure 4-9 is the effect of various neutron source strengths on the maximum ONDAC count rate based upon equation 4.14 with parameters similar to those used in figures 4-3 through 4-8. Parameters held constant in this figure are the pulse width and count time (10 msec), the dissipation time (4 msec), and the distance from the central ONDAC and the 14 MeV source to the HEU (100 cm). The ONDAC background count rate is also shown in figure 4-9, which was calculated to be 75 counts per minute. As can be seen, the maximum ONDAC count rate doesn't significantly exceed this background count rate until the 14 MeV source neutron emission rate is 10^{11} neutrons/second. For comparison purposes the maximum 14 MeV source strengths currently commercially available of 3×10^8 neutrons/second for a pulsed source (Haliburton 2002) and 1×10^{11} neutrons/second for a continuous source (Thermo MF Physics 2002) are also shown in figure 4-9.

Figure 4-9 indicates that current commercially available 14 MeV neutron generators are not likely to be adequate for external neutron stimulation applications. However, recent research at Lawrence Berkley National Laboratory (LBNL) has shown strong promise in developing a coaxial and radiofrequency driven compact 14 MeV generator with neutron outputs of 10^{12} and higher (Ka-Ngo 2002). LBNL also indicated that these generators can be run in either the pulse or continuous mode. Additionally, such generators would have a long

tube lifetime and a fast fall-off time, which would be very desirable for pulsed operations. Thus it appears to be technically feasible to build a neutron generator with sufficient yield to make the neutron stimulation approach workable.

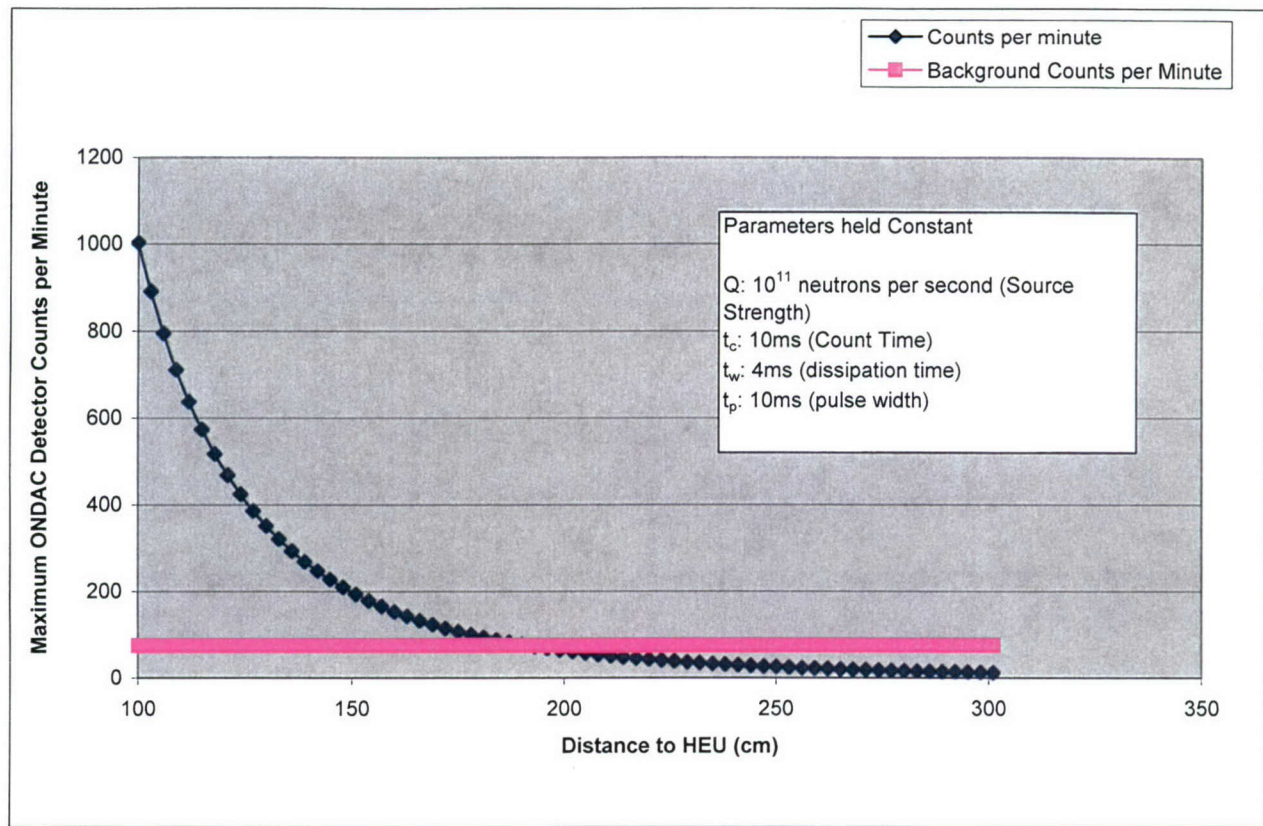


Figure 4-10. Effect of varying distance of source and detector to HEU on counting delayed neutrons from a 14 MeV pulsed source with an ONDAC detector. ONDAC background count rate also shown.

Figure 4-10 is a graph of the effect of ONDAC distance on a pulsed neutron detection system based on equation 4.14. Parameters held constant in this figure include the neutron source emission rate (10^{11} neutrons/second), pulse width and count time (10 msec), and dissipation time (4 msec). In figure 4-10, the distances to the 14 MeV neutron source and the ONDAC detector from the HEU are assumed equal. As can be seen by equation (4.14), the maximum ONDAC count rate will decrease as the one-fourth power of this distance. Figure 4-10 shows that in this case, the maximum ONDAC count rate approaches the background count rate at a distance of 175 cm. To make the stimulation approach practical to detect HEU at even larger distances, several system modifications would be needed. These modifications include increasing the source strength, placing multiple sources and detectors around the container, and/or employing a moveable detection system that could be designed to scan the container both vertically and horizontally.

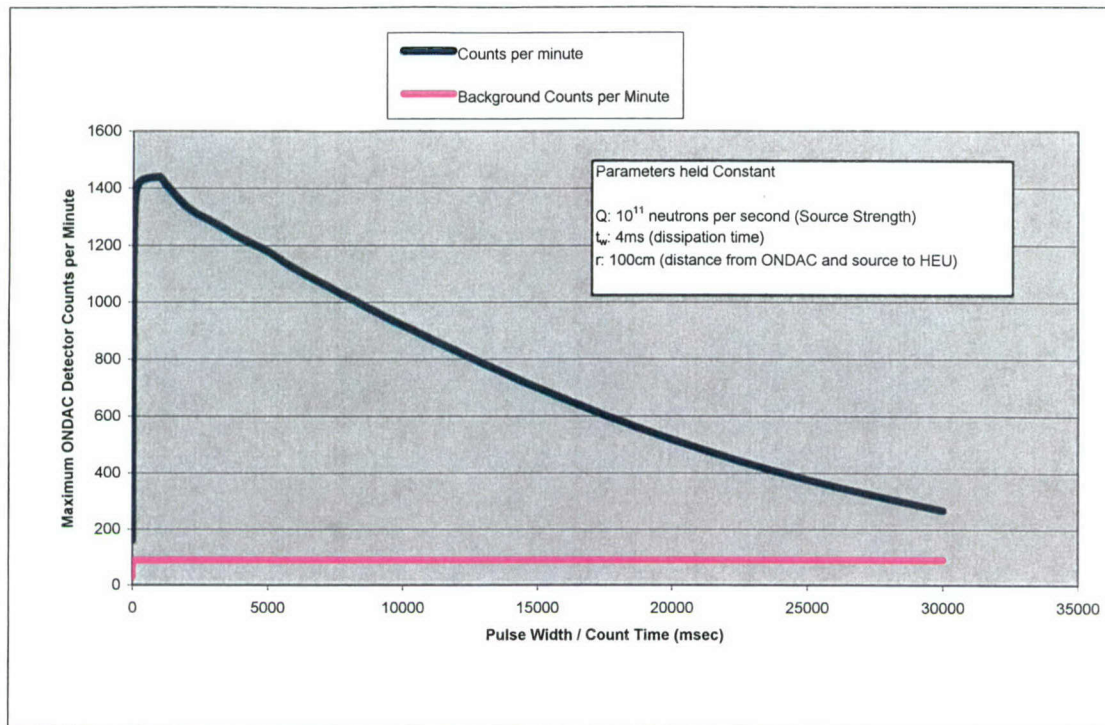


Figure 4-11. Effect on detector CPM of equal pulse widths and count times up to 35000 msec (35 seconds) on counting delayed neutrons from a 14 MeV source with an ONDAC detector. ONDAC background count rate also shown.

Figure 4-11 shows the effect on the maximum ONDAC count rate for equal pulse width and count times up to 35000 msec or 35 seconds. Parameters held constant in this figure include source strength (10^{11} neutrons/second), dissipation time (4 msec), and distance of the source and ONDAC from the HEU (100 cm). Figure 4-11 shows that the maximum ONDAC count rate occurs at approximately 2000 msec (2 seconds) pulse width and count time. This result is due to the fact that under these conditions neutron dissipation time is small compared to the pulse time, but count time is short enough that a significant fraction of the delayed neutrons have not decayed. This last statement can be explained by using one group theory. In this theory, the delayed neutron emission rate decreases exponentially as given by equation (4.10). It is recognized that this equation is not exact, but a first order approximation since it neglects decay of delayed neutrons during the pulse. As can be seen by equation (4.10), that when the pulse time and count time become large (i.e. greater than 10 seconds), then a significant fraction of the delayed neutrons will decay out by the end of the count time, which will in turn reduce the maximum ONDAC count rate achievable.

4.5 MCNP ANALYSIS.

The MCNP analysis was performed in two parts to determine the number of interactions in the ONDAC detector per source particle. In the first part, MCNP determined the gain in prompt fission neutrons per 14 MeV source particle by fissioning in the HEU. This result was then multiplied by the delayed neutron fraction (β), which was taken to be 0.0065 (LaMarsh 2001). In the second part, the interactions per delayed neutron source particle were found with the ONDAC detector. In this part, the source energy was taken to be that which is characteristic of delayed neutrons and the source location was that of the HEU in the container. The overall ONDAC interactions per 14 MeV source particle was then found by multiplying the results of the two parts together.

The MCNP cases for the second part were first evaluated using a monoenergetic source energy of 0.5 MeV, as this approximation was suggested by Keepin (Keepin 1965). However, since delayed neutrons are not all emitted at a single energy, two published polyenergetic spectra were studied (Burgly 1946, Batchelor 1956 and Bonner 1956). The probability of a neutron being emitted was divided into five bins for each spectrum and is shown in figure 4-12.

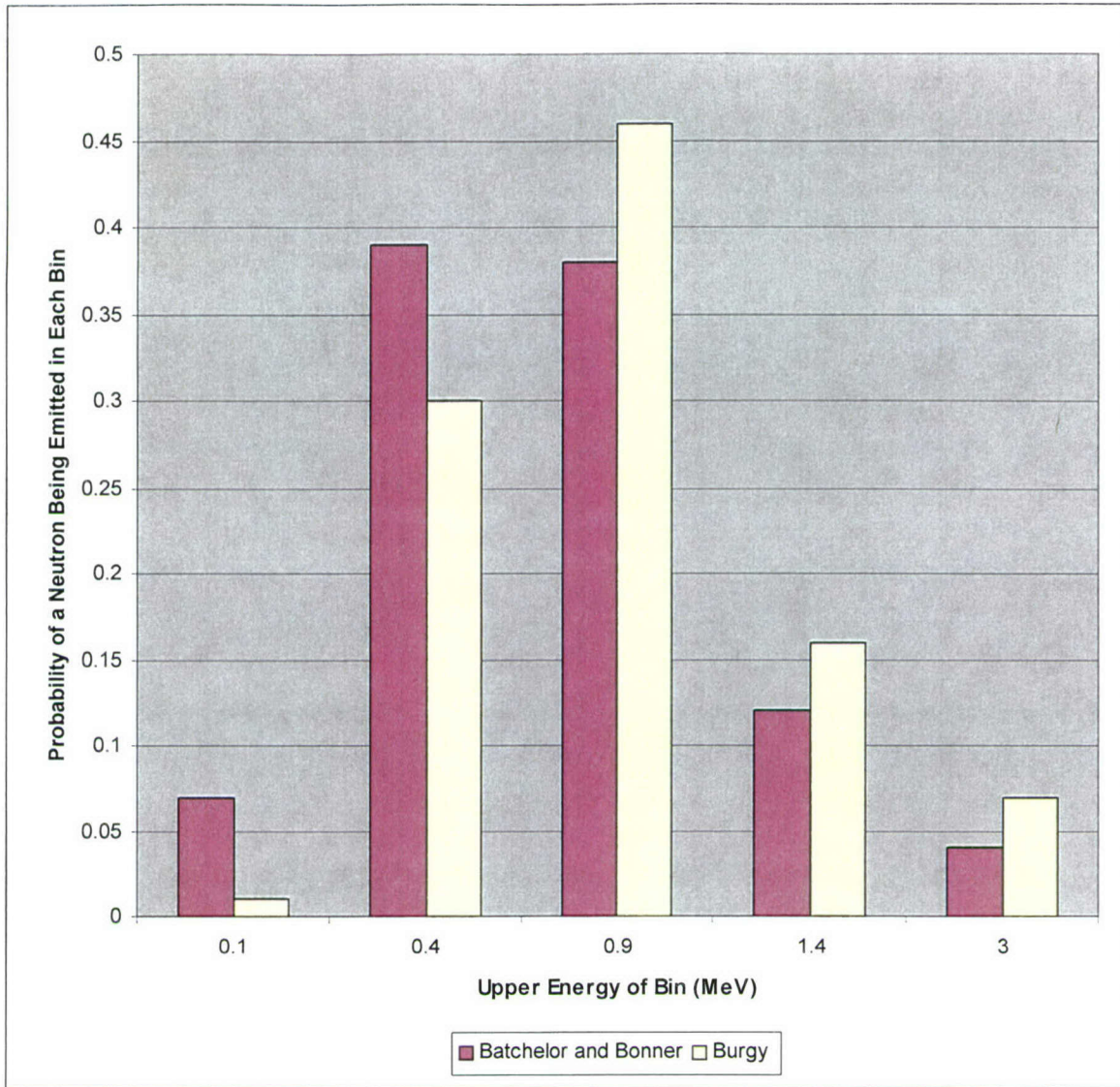


Figure 4-12. Delayed neutron probability distribution over five energy bins by Batchelor and Bonner and by Burgy.

The energy shown on the x-axis is the upper limit of the energy bin in MeV (i.e. 0.1, 0.4, 0.9, 1.4, 3). Hence the probability that a delayed neutron is emitted between 0.1 MeV to 0.4 MeV is 0.39 for Batchelor and Bonner, which is modeled in a darker color, and 0.30 for Burgy, which is modeled as the lighter color. The sum of the probabilities in all five bins equals one in both distributions. The average energy for each spectrum was found with equation (4.15) and the result is given in table 4-2.

$$\bar{E} = \frac{\sum_{i=1}^5 E_i P_i}{\sum_{i=1}^5 P_i} \quad (4.15)$$

where

- \bar{E} = spectrum average energy, MeV
 E_i = average energy in the i^{th} bin, MeV
 P_i = probability of the delayed fission neutron (DFN) being emitted in the i^{th} bin
 $\sum_{i=1}^5$ = summation over five energy bins in each spectrum

Table 4-2. Average energies for the Batchelor, Bonner, and Burgy energy spectra.

Spectrum	Spectrum Average Energy (MeV)
Batchelor and Bonner	0.575
Burgy	0.713

From table 4-2 Batchelor and Bonner's representation predicts delayed neutrons being emitted at lower energies, compared to the Burgy model. Thus, two MCNP cases were run with neutrons assumed to be monoenergetic with first the Batchelor and Bonner average energy and then the Burgy average energy shown in table 4-2. Additionally, two MCNP cases were run using the two polyenergetic spectra in order to test if this difference would have a significant impact on the model results. Including the initial tests run with monoenergetic neutrons at 0.5 MeV, a total of five cases were developed.

The results of these five cases are shown in figure 4-13. Figure 4-13 lists the different source energies analyzed using MCNP and the number of interactions per source particle in the center ONDAC detector. The numbers of interactions per source particle are plotted as a single point with 3- σ error bars based on the MCNP statistical relative error as given by equation (2.3). Figure 4-13 shows that the number of interactions in the center ONDAC detector per source particle varied insignificantly with the different spectra.

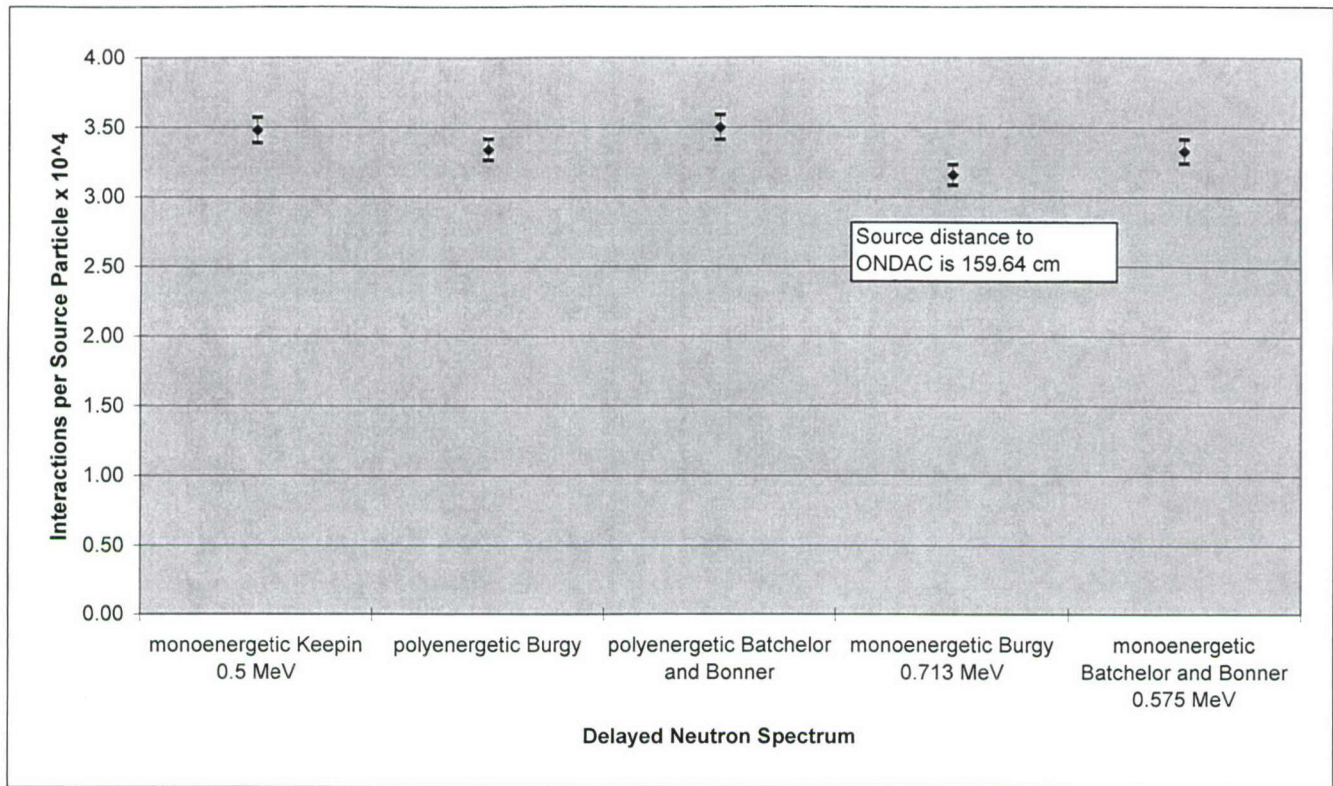


Figure 4-13. Interactions per source particle in center ONDAC detector versus source energy for five energy spectra analyzed with shipping container filled with air.

Table 4-3. Summary of five energy spectra MCNP computer run time and relative error.

Energy Spectrum	Monoenergetic Keepin	Polyenergetic Burgy	Polyenergetic Batchelor and Bonner	Monoenergetic Burgy	Monoenergetic Batchelor and Bonner
Energy Strength (MeV)	0.5	Spectrum	Spectrum	0.713	0.575
Particle Histories Run	5.09x10 ⁸	6.85 x10 ⁸	5.49 x10 ⁸	6.65 x10 ⁸	5.51 x10 ⁸
Computer Run Time (min)	1924	2639	2126	2388	2013
Relative Error (%)	0.87	0.77	0.85	0.79	0.86
Particle History Per Minute Run Time	2.65x10 ⁵	2.60x10 ⁵	2.58x10 ⁵	2.78x10 ⁵	2.73x10 ⁵

Table 4-3 is a summary of the five energy spectra with their MCNP computer run time, number of particle histories run, particle histories per run time, and relative error. For each spectrum approximately 5×10^8 particle histories were run before thirty particles were lost and the MCNP calculations ceased. As can be seen in table 4-3, the relative error is very low (less than 1%) and approximately the same for all spectra. However, since the particle history per run time was highest for the monoenergetic Burgy spectrum, this spectrum was chosen for container analysis with and without cargo. This analysis is presented in the next section.

4.6 COMPARISON OF THE DETERMINISTIC AND MCNP METHODS.

The deterministic method, which is given by equation (4.14), was evaluated under the same conditions as MCNP and the results compared. For convenience, equation (4.14) is repeated below:

$$CPM = \frac{5.784 \dot{Q} t_p f_d f e^{-\lambda t}}{r_1^2 r_2^2} \quad (4.14)$$

In this comparison the 14 MeV source was located 153.14 cm from the HEU (r_1), the HEU was 159.64 cm from the ONDAC detector (r_2), one neutron was emitted in the pulse time (i.e. $\dot{Q} t_p = 1$), the fraction of delayed neutrons counted was assumed to be unity ($f_d = 1$), CPM term on the left hand side of equation (4.14) was divided by the number of cycles per minute (f) to yield the total number of ONDAC counts, and the wait time following the pulse before counting was taken to be zero seconds ($t=0$). Under these conditions, equation (4.14) reduces to the following equation, which yields a value of 1.63×10^{-10} :

$$C = \frac{5.784}{(153.14)^2 (159.64)^2} = 1.63 \times 10^{-10} \quad (4.16)$$

where

C = number of ONDAC counts per 14 MeV source particle

By comparison, the MCNP simulation produced a value of 1.29×10^{-10} ONDAC counts per source particle, which represents an approximate 21% difference in the two methods. Given the numerous assumptions in the deterministic method, this percent difference was considered satisfactory and served to validate both methods.

4.7 RECOMMENDATIONS FOR OPERATING PARAMETERS AND MINIMUM PULSE RATE.

The problem of cyclic irradiation with an isotropic neutron source and counting delayed neutrons has been previously analyzed to determine the combination of pulse time, count time, and optimum number of cycles to produce the maximum detector counts for a given irradiation time (Alfassi 1990; Spyrou 1982; MacMurdo 1977). In the Alfassi analysis, it was determined that one would want the count time and pulse time equal, which was the same conclusion that this

project reached as described in section 4.4. Another variable that these studies found important in producing the maximum number of counts is the transit time, which is the time between the end of one cycle and the beginning of the next cycle. The transit time will be dependent upon two factors: (1) the electronic gating time between the detector and 14 MeV accelerator and (2) the time it takes to ramp up and shutdown the voltage in the accelerator. Assuming a 0.25 second transit time and a dissipation time equal to this transit time and a 300 second total examination time, Spyrou concluded that 2.43 second irradiation and count times and 56 cycles would produce the maximum number of net counts. Under similar conditions, MacMurdo and Bowman recommended 3.36 second irradiation and count times and 42 cycles to maximize the net counts.

The maximization of the signal to noise ratio is also very important in cyclical activation, where the noise is due to background counts. Since the background counts decreases linearly with the number of cycles, the maximization of the signal to noise ratio leads to a larger number of cycles than when considering only net counts (Alfassi 1990). For the case of equal irradiation and count time, the signal to noise ratio was found to be a maximum when these times are 1.81 times the half-life for the delayed neutrons (Binney 1978). For the case of 0.25 second transit time, Binney indicated that the main contribution will be from delayed neutrons with a 2.1 second half-life. In this case, the optimum count time would be 3.80 seconds. Since all three of these pulse and count times (i.e. 2.43, 3.36, and 3.80) are close to the maximum ONDAC CPM of 2.0 seconds shown in figure 4-11, it was decided to simply average all four approaches together. This resulted in a 2.9 second pulse and count times being chosen. With this value of count and pulse times, the 300 second total examination time would then consist of 48 cycles. Table 4-4 summarizes the final recommended operational conditions for examining a shipping container with a pulsed 14 MeV neutron source and counting the delayed neutrons.

Table 4-4. Recommendations for operational conditions to be applied when examining shipping container with pulsed 14 MeV neutron source and counting delayed neutrons.

Parameter	Value
Total examination time	302.4 seconds
Pulse time	2.9 seconds
Count time	2.9 seconds
Dissipation time	0.25 seconds
Transit time between cycles	0.25 seconds
Total number of cycles	48

Figure 4-14 displays the results of applying equation (4.12) for the worst-case scenario, using the parameters given in table 4-4 for a container with dimensions of the benchmark facility (i.e. approximately 600 cm in the lengthwise direction, 240 cm in the vertical and width directions) and three ONDAC detector positioned as described in section 2.1 (i.e. lengthwise at coordinates -200 cm, 0 cm, and +200 cm). In the worst case scenario, the HEU would be located within the container such that the ONDAC would have the minimum number of counts. This worst-case condition would place the HEU at either the bottom or top of the container, midpoint lengthwise between two of the ONDACs, at the midpoint widthwise, and have the HEU distance from the 14 MeV source equal the HEU distance from the ONDAC detector ($r_1 = r_2$). In this case it was calculated that the HEU would be at a distance of 197 cm from one of the three ONDAC detectors as well as that same distance from the pulsing source. Also shown in figure 4-14 is the background ONDAC count rate, which has been calculated to be 83 CPM. As can be seen, a pulsed source rate 10^{12} neutrons/sec would produce an ONDAC count rate of slightly over 800 CPM or ten times the background count rate. Consequently after 5 minutes, one would expect to average over 4000 ONDAC counts with 1 kg HEU present and 400 counts without HEU present. Recently a study has been completed on the cosmic ray background using He^3 detectors (Dirk 2002), which found it to vary by a factor two between many different locations in the Washington-Annapolis area. Thus, a high count rate in the ONDAC detector due to the presence of fissile material in the container can easily be distinguished from background variations.

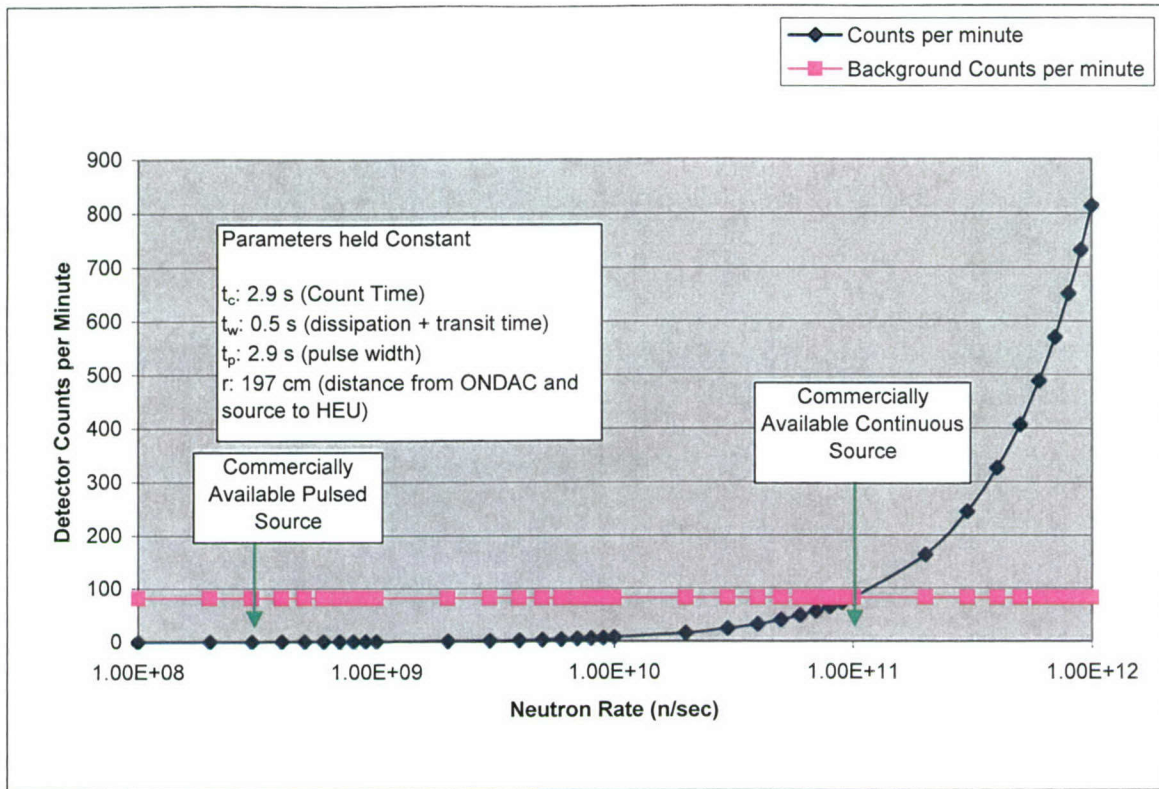


Figure 4-14. Effect of varying source neutron emission rate to detect HEU for worst case scenario in the benchmark facility when using three ONDAC detectors that are located at lengthwise coordinates -200 cm, 0 cm, and +200 cm and using operational parameters given in table 4-3.

4.8 CONCLUSIONS.

The analysis in this section shows that using a pulsed 14 MeV source and counting delayed neutrons is technically feasible to detect 1 kg in a large shipping container. However, to accomplish this, a 14 MeV neutron generator with a yield of 10^{12} neutrons/sec and an examination time of 5 minutes would be needed. These conclusions are based on the container having no cargo. In the next section, the effect of cargo material on the ONDAC signal is examined.

SECTION 5

EFFECT OF PAYLOAD WITHIN CONTAINER

This section will outline which types of cargo were studied, how they were modeled, and the results they yielded. Section 5.1 contains a description of how the benchmark MCNP model is modified by the presence of cargo. Numerical and graphical results are given in sections 5.2 and 5.3. Within these sections further analysis is conducted to ensure the results are consistent with the nuclear characteristics of each cargo material's constituents. Section 5.4 evaluates interference delayed neutron reactions. The effect of hydrogen within the cargo is examined in section 5.5. Overall conclusions on the effect of payload are given in section 5.6.

5.1 DESCRIPTION OF ADDING CARGO TO MCNP MODEL.

The detection of SNM, in particular HEU, must be possible with different types of cargo present in the container. This study examined six separate cargos, including lead, aluminum, iron, alcohol, cotton, and air (no cargo). An extra material card was added to the MCNP input file that specified the cargo's elemental composition and the atom fraction associated with each element. Then each of the eighty cargo drums was filled with the cargo material, and the material's density was specified in the cells that represented these drums. Two cases of each material were run; the first was from the 14 MeV neutron source to the HEU, and the second was from the HEU to the ONDAC detector. The second part of the study was conducted using a 0.713 MeV monoenergetic neutron source to model the polyenergetic delayed neutron source, for reasons that were discussed in section 4.5. To provide consistency throughout the study, there were several fixed conditions. First, in each cargo case run, the 14 MeV source location was fixed (at $x = z = 0$ and $y = -312.8$ cm) which placed it just outside the container, but on the opposite side from the ONDAC detector. Second, the HEU was modeled as the delayed neutron source at $x = z = 0$ and $y = -159.6$ cm which placed it in the center of the container in air that stood between the cargo drums. Additionally, the ONDAC detectors were located at a fixed position between each case run, with the center ONDAC located at the origin of the coordinate system (i.e. $x = y = z = 0$). Each case was run with a single homogeneous cargo material and the number of particles varied from $6.0E+07$ to $1.0E+09$.

The materials modeled as cargo have a variety of densities and atomic mass numbers. This was purposely constructed in order to gain an understanding of the effect of different atomic weights on the number of ONDAC interactions. For a mixture of cargo materials, it is expected that ONDAC predictions could be made by weighting the different homogeneous cargo results together.

5.2 NUMERICAL MCNP CARGO RESULTS.

A numerical summary of the results is included in table 5-1, while radiative capture, neutron producing reactions, and mean free paths that occur in the cargo material are given in table 5-2. Table 5-2 was constructed from the MCNP output in order to explain the table 5-1 results. In the first two columns of table 5-1, the neutron gain by fissioning in HEU per 14 MeV source particle and the delayed fission neutrons produced per 14 MeV source particle for each of the six payloads are compared. Columns three and four compare the interactions in the center ONDAC detector per delayed neutron source particle and per 14 MeV source particle. The last column was obtained by multiplying the results of columns two and three together. The first two columns in table 5-2 gives the sum of radiative capture in all eighty cargo cells for the 14 MeV source and the 0.713 MeV delayed neutron source particles for each cargo material. The third column lists the sum of the neutron gain from (n,xn) reactions per 14 MeV source particle in all the cargo cells. MCNP tallied these reactions by constituent for each cell listed in the model. The values of the sum of the gain of neutrons from the (n,xn) reactions were calculated by adding the gain from each material element in all 80 cargo cells. Columns four and five of table 5-2 compare the mean free path length (in centimeters) for both the 14 MeV source particle and the 0.713 MeV delayed neutron source particle for the various cargo materials. Since the mean free path will vary slightly with neutron location across the container, the values shown in table 5-2 were obtained by averaging the mean free path over all 80 cargo cells.

Table 5-1. Numerical summary of MCNP cargo analysis.

Cargo Material	Neutron Gain by Fissioning in HEU per 14 MeV Source Particle	Delayed Fission Neutron Produced per 14 MeV Source Particle	Interactions in Center ONDAC per per Delayed Neutron Source Particle	Interactions in Center ONDAC per 14 MeV Source Particle
Air	6.26E-05	4.07E-07	3.16E-04	1.29E-10
Aluminum	6.57E-05	4.27E-07	6.87E-04	2.93E-10
Iron	3.93E-05	2.56E-07	3.67E-04	9.40E-11
Alcohol	1.48E-05	9.60E-08	9.28E-07	8.89E-14
Cotton	8.90E-05	5.79E-07	6.79E-04	3.93E-10
Lead	2.31E-04	1.50E-06	6.17E-04	9.22E-10

Table 5-2. Summary of nuclear interactions and mean path lengths for different cargo materials.

Cargo Material	Sum of Radiative Capture per Source Particle in all Cargo Cells		Sum of Gain from (n,xn) Reaction per 14 MeV Source Particle in All Cargo Cells	Mean Free Path Length by Source Energy (cm)	
	14 MeV	Delayed neutrons (0.713 MeV)		14 MeV	Delayed Neutrons (0.713 MeV)
Air	0.001	0.000	0.000	12400.00	8720.00
Aluminum	0.090	0.143	0.006	12.55	13.26
Iron	0.109	0.553	0.094	7.70	7.94
Alcohol	0.267	0.971	0.000	2.09	0.51
Cotton	0.021	0.065	0.000	121.00	21.10
Lead	0.031	0.190	0.287	3.30	3.23

5.3 GRAPHICAL ANALYSIS OF MCNP RESULTS.

Figures 5-1 through 5-8 are a graphical analysis of the MCNP results given in tables 5-1 and 5-2. All of the data in Figures 5-1 through 5-8 have been constructed using error bars equivalent to three-sigma. The value of one- σ uncertainty is calculated through equation (5.1).

$$r = \sigma = \sqrt{r_1^2 + r_2^2} \quad (5.1)$$

where

- r = MCNP relative error (one- σ uncertainty)
- r_1 = relative error in MCNP output for 14 MeV neutron source to HEU
- r_2 = relative error in MCNP output for HEU to ONDAC

The three- σ uncertainty error bars in the figures were found by equations (5.2) and (5.3):

$$R_{upper\ limit} = \bar{R}(1 + 3r) \quad (5.2)$$

$$R_{lower\ limit} = \bar{R}(1 - 3r) \quad (5.3)$$

where

- $R_{upper\ limit}$ = upper limit of the three- σ uncertainty
- $R_{lower\ limit}$ = lower limit of the three- σ uncertainty
- \bar{R} = Output value from MCNP tally

The three- σ uncertainty ranged from 0.072 to 0.191 for all cargo materials studied except for alcohol. In fact, the low interaction rate in the case of alcohol with the ONDAC detectors produced a high uncertainty. In this case, $R_{lower\ limit}$ became negative, but was set equal to zero as there can't be negative interactions.

5.3.1 Neutrons Gained by Fissioning.

The neutrons gained by fissioning in the HEU per 14 MeV source particle for various cargo materials is graphed in figure 5-1. Surprisingly, it shows that the lead has the highest value (2.31×10^{-4}), making it the most easily detected cargo material. It was followed by cotton, aluminum, air, iron, and alcohol, in descending order. Lead had the highest value due to the large amount of neutrons gained from (n,xn) reactions per 14 MeV source particle (0.287) which can be seen in the middle column of table 5-2, or graphically in figure 5-2. The neutrons gained from (n,xn) reactions in air, alcohol, and cotton are shown as zero because MCNP tallies found that no neutrons gained from this reaction in 10^9 particle case histories. By comparison, lead gained more than three times the amount of neutrons from (n,xn) reactions compared to iron, and almost fifty times as many neutrons compared to aluminum. Subsequently, these neutrons, which are produced relatively uniformly throughout the container, had the possibility of interacting with the HEU and increasing the neutron gain by fissioning per 14 MeV source particle.

Iron was the other cargo material besides lead that produced neutrons from (n,xn) reactions (0.094). However, as seen in table 5-2, 14 MeV neutrons also have a high probability to undergo radiative capture in this cargo (0.109). As a result, fewer neutrons are produced by fissioning in iron compared to other cargo materials except alcohol.

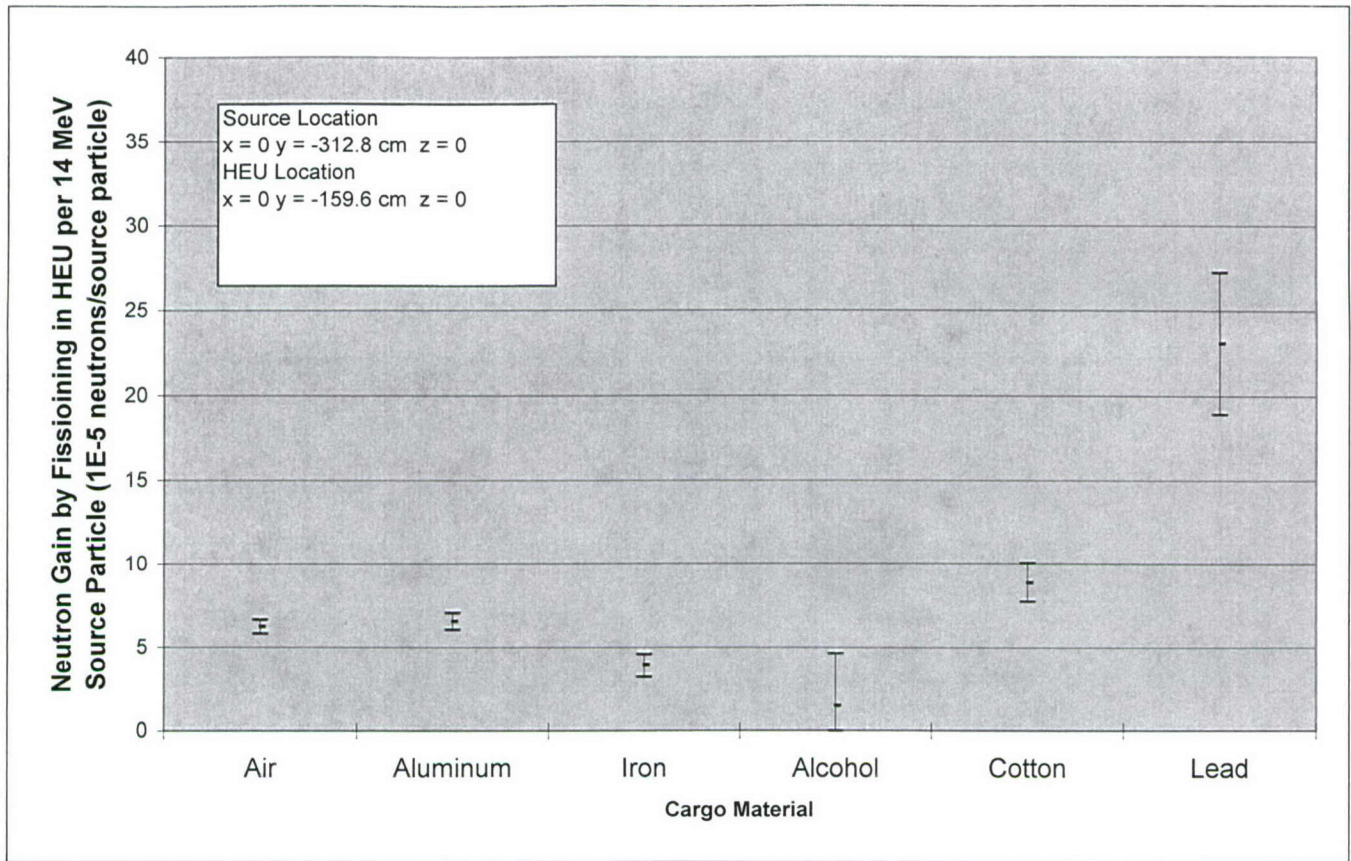


Figure 5-1. Neutron gain by fissioning in HEU per 14 MeV source particle for various cargo materials.

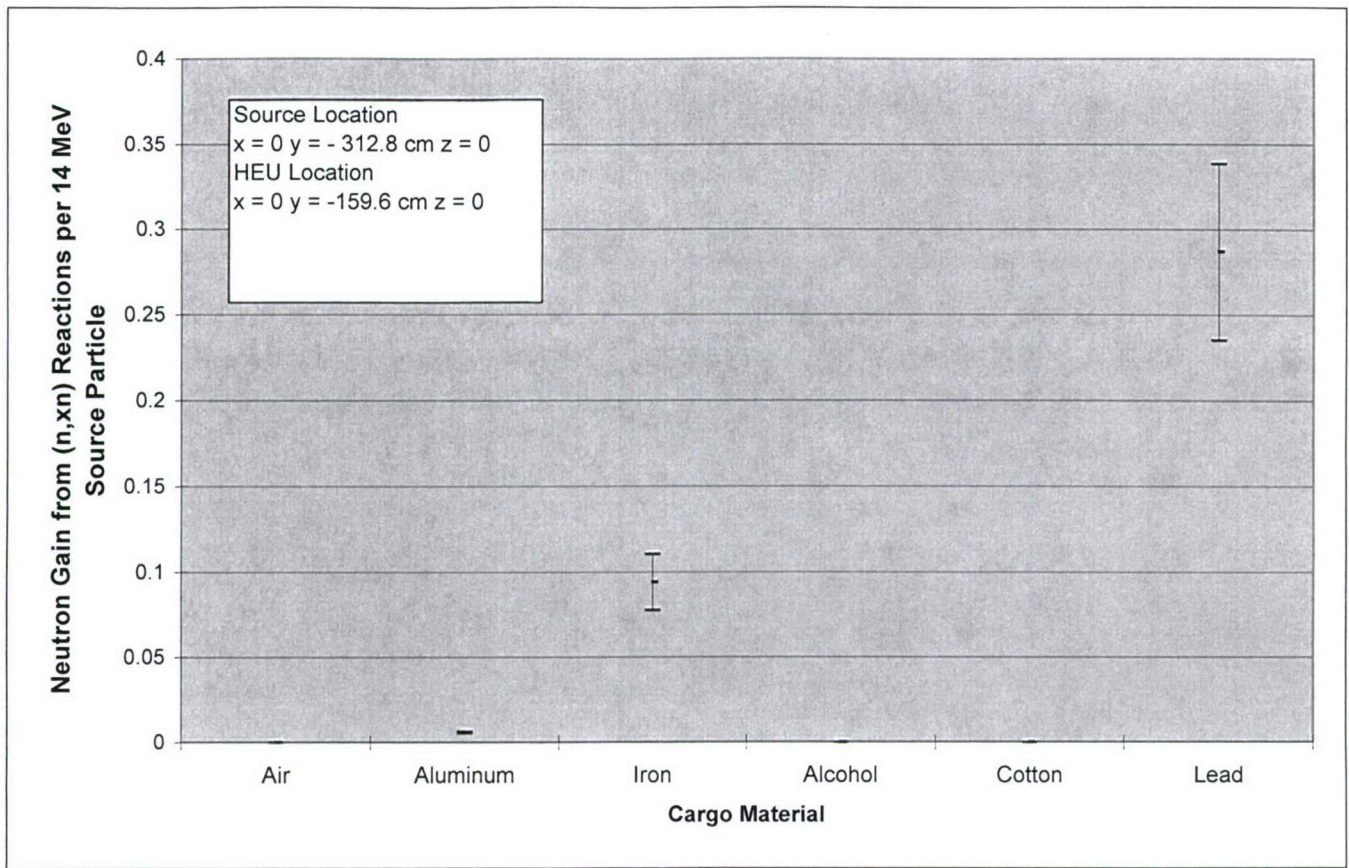


Figure 5-2. Neutron gain from (n,xn) reactions per 14 MeV source particle for various cargo materials.

5.3.2 Radiative Capture with 14 MeV Neutrons.

The fact that alcohol had the lowest value of the neutron gain by fissioning from the 14 MeV source particle (1.48×10^{-5}) is likely due to the fact that it had the most neutrons radiatively captured per source particle (0.267), leaving the least amount of neutrons available to interact with the HEU. A graph of the sum of neutrons radiatively captured per 14 MeV source particle for each cargo case run is included in figure 5-3. As can be seen, air, cotton, lead, and carbon had the least amount of neutrons radiatively captured per 14 MeV source particle.

Table 5-3 gives the radiative cross-section (KAERI 2002) of the cargo materials with 1 MeV neutrons and 14 MeV neutrons, which was developed in order to compare the MCNP results to material characteristics. The macroscopic radiative capture cross section in table 5-3 was found from the equation:

$$\Sigma_{\gamma} = N\sigma_{\gamma} \quad (5.4)$$

where

- Σ_{γ} = macroscopic radiative capture cross section, cm^{-1}
- N = material atom density, 10^{24} atoms/ cm^3
- σ_{γ} = microscopic radiative capture cross section, barns

The data shows that cotton has the lowest radiative capture macroscopic cross section at 14 MeV for these cargo materials, and was consistent with the MCNP calculation shown in figure 5-3 for the number of radiatively captured neutrons per 14 MeV source particle. Alcohol had the next lowest radiative capture macroscopic cross section for 14 MeV neutrons, followed by aluminum, lead, and iron. With the exception of alcohol, these material's macroscopic radiative cross sections correlated directly with the MCNP radiative capture results.

To explain the high radiative capture in alcohol, the slowing down power of each cargo material was calculated and is shown in table 5-4. The slowing down power is found from the equation:

$$\text{Slowing down power} = \xi N \sigma_s \quad (5.5)$$

where

ξ	=	logarithmic energy decrement
N	=	material atom density, 10^{24} atoms/cm ³
σ_s	=	microscopic scattering cross section, barns

Table 5-4 shows that the alcohol has a very high slowing down power while the cotton, iron, and lead have comparatively small slowing down powers. The slowing down power of the alcohol is over forty times greater compared to the cotton for 14 MeV neutrons. Therefore, the alcohol rapidly moderates the neutrons to lower energies. As the neutrons lose energy, their radiative capture cross section increases, which explains the high radiative capture per source particle shown in figure 5-3 for alcohol (0.267). The high statistical uncertainty shown is due to the smaller number of MCNP particle history cases completed for alcohol. This happened because the computer run time was much longer per particle history in alcohol than the other materials studied (i.e. neutrons had a shorter mean free path and underwent a larger number of interactions per particle history).

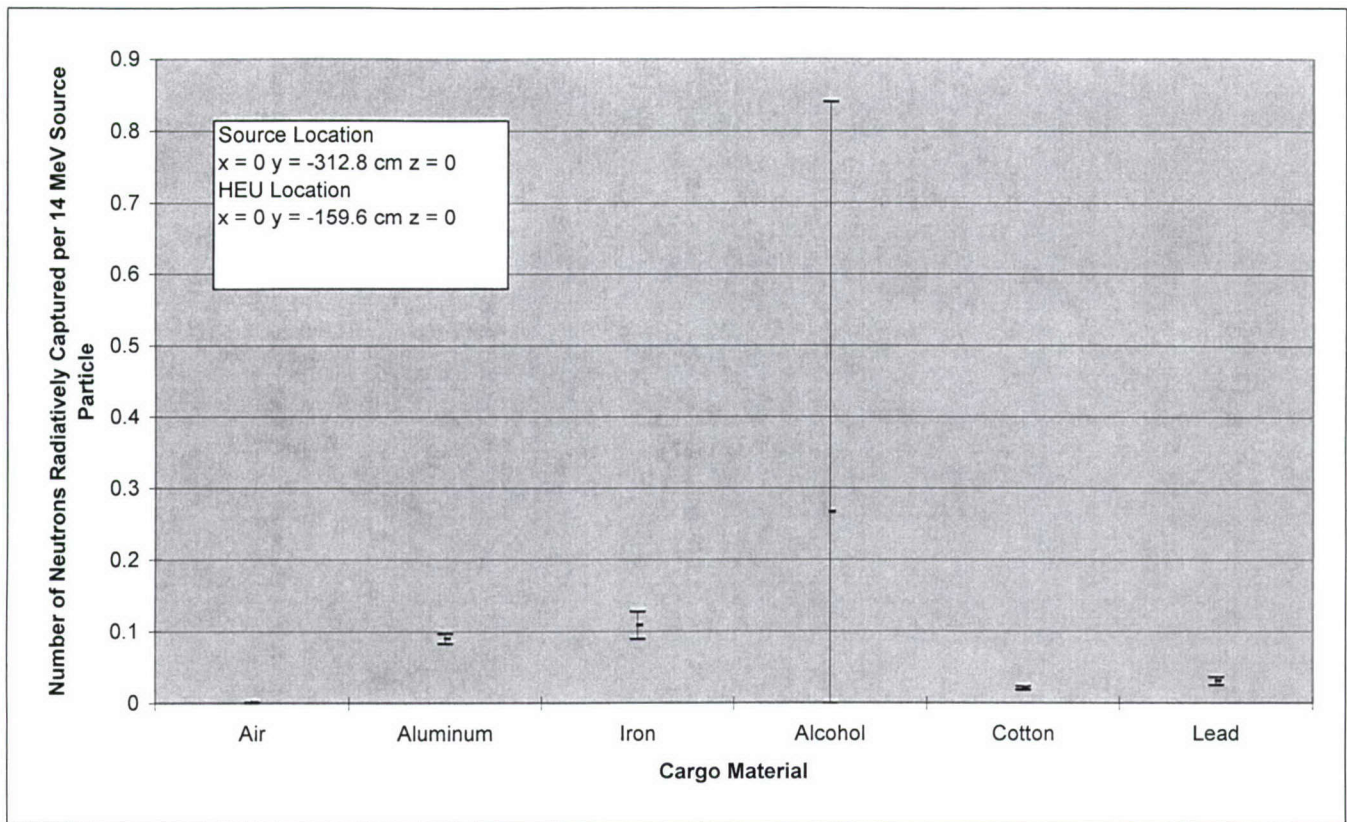


Figure 5-3. Radiative capture per 14 MeV neutron emitted to the center ONDAC detector for various cargo materials.

Table 5-3. Calculation of 1 MeV and 14 MeV macroscopic radiative cross-sections for various cargo materials.

Material	Relative Abundance	Atom Density (1E24 atoms/cm ³)	Microscopic Cross Sections (barns)		Macroscopic Cross Section (cm ⁻¹)	
			1 MeV	14 MeV	1 MeV	14 MeV
Aluminum						
Al-27	1.00	6.02E-02	1.30E-04	5.00E-04	7.83E-06	3.01E-05
				ALUMINUM	7.83E-06	3.01E-05
Lead						
Pb-206	0.241	3.30E-02	7.00E-03	1.20E-03	5.53E-05	9.48E-06
Pb-207	0.221	3.30E-02	6.00E-03	1.05E-03	4.54E-05	7.94E-06
Pb-208	0.524	3.30E-02	1.92E-04	1.20E-03	3.36E-06	2.10E-05
				LEAD	1.04E-04	3.84E-05
Iron						
Fe-54	0.058	8.49E-02	2.90E-03	7.95E-04	1.43E-05	3.93E-06
Fe-56	0.917	8.49E-02	2.60E-03	7.30E-04	2.02E-04	5.68E-05
Fe-57	0.022	8.49E-02	2.95E-03	7.95E-04	5.48E-06	1.48E-06
Fe-58	0.003	8.49E-02	2.70E-03	7.95E-04	7.56E-07	2.23E-07
				IRON	2.23E-04	6.24E-05
Cotton	(C6 H10 O5)					
C	0.286	1.43E-03	1.27E-06	1.16E-04	5.18E-10	4.73E-08
H	0.476	2.38E-03	3.50E-05	3.00E-05	3.97E-08	3.40E-08
O	0.238	1.19E-03	3.02E-08	8.08E-09	8.56E-12	2.29E-12
				COTTON	4.02E-08	8.13E-08
Alcohol	(C2 H5 OH)					
C	0.222	2.60E-02	1.27E-06	1.16E-04	7.33E-09	6.70E-07
H	0.667	7.80E-02	3.50E-05	3.00E-05	1.82E-06	1.56E-06
O	0.111	1.30E-02	3.02E-08	8.08E-09	4.36E-11	1.17E-11
				ALCOHOL	1.83E-06	2.23E-06

Table 5-4. Calculation of 1 MeV and 14 MeV slowing down powers for various cargo materials.

Material And Constituents	Atomic Mass	Logarithmic Energy Decrement (ξ)	Atom Density ($\times 10^{24}$) (atoms/cm ³)	Atomic Relative Abundance in Material	Microscopic Scattering Cross Section (barns)		Slowing Down Power	
					1 MeV	14 MeV	1 MeV	14 MeV
ALUMINUM								
Al	27	7.23E-02	6.02E-02	1.00E+00	2.36E+00	6.51E-01		
						ALUMINUM	1.03E-02	2.84E-03
COTTON								
C ₆ H ₁₀ O ₅								
O	16	1.20E-01	1.19E-03	2.38E-01	8.15E+00	9.54E-01	2.77E-04	3.24E-05
C	12	1.58E-01	1.43E-03	2.86E-01	2.58E+00	8.19E-01	1.66E-04	5.28E-05
H	1	1.00E+00	2.38E-03	4.76E-01	4.26E+00	6.89E-01	4.82E-03	7.81E-04
						COTTON	5.27E-03	8.66E-04
ALCOHOL								
C ₂ H ₅ OH								
O	16	1.20E-01	1.30E-02	1.11E-01	8.15E+00	9.54E-01	1.41E-03	1.65E-04
C	12	1.58E-01	2.60E-02	2.22E-01	2.58E+00	8.19E-01	2.35E-03	7.47E-04
H	1	1.00E+00	7.80E-02	6.67E-01	4.26E+00	6.89E-01	2.22E-01	3.58E-02
						ALCOHOL	2.25E-01	3.68E-02
LEAD								
Pb-206	206	9.68E-03	3.30E-02	2.40E-01	5.41E+00	2.84E+00	4.14E-04	2.17E-04
Pb-207	207	9.63E-03	3.30E-02	2.29E-01	4.88E+00	2.95E+00	3.56E-04	2.15E-04
Pb-208	208	9.58E-03	3.30E-02	5.31E-01	4.91E+00	3.00E+00	8.24E-04	5.03E-04
						LEAD	1.59E-03	9.35E-04
IRON								
Fe-56	56	3.53E-02	8.49E-02	9.17E-01	1.74E+00	1.21E+00	4.79E-03	3.32E-03
Fe-54	54	3.66E-02	8.49E-02	5.82E-02	3.13E+00	1.19E+00	5.66E-04	2.15E-04
Fe-57	57	3.47E-02	8.49E-02	2.19E-02	4.08E+00	1.21E+00	2.63E-04	7.81E-05
Fe-58	58	3.41E-02	8.49E-02	3.30E-03	4.84E+00	1.20E+00	4.62E-05	1.15E-05
						IRON	5.66E-03	3.62E-03

5.3.3 Delayed Neutron Production.

The second column of table 5-1 gives the number of delayed fission neutron particles produced per 14 MeV source particle in HEU. These values were calculated by multiplying the neutron gain by fissioning in the HEU per 14 MeV source particle, found in the first column of table 5-1 by the delayed neutron fraction, which was taken to be 0.0065 (LaMarsh 2001). The delayed fission neutron particles produced per 14 MeV source particle are also shown in figure 5-4 for the different cargo materials. This figure shows that lead produces the most delayed fission neutrons (15×10^{-7}) while alcohol produces the least amount (9.6×10^{-8}). This graph follows the same trend by cargo material as figure 5-1 since the delayed neutron production is directly proportional to the neutron gain by fissioning in HEU per 14 MeV source particle.

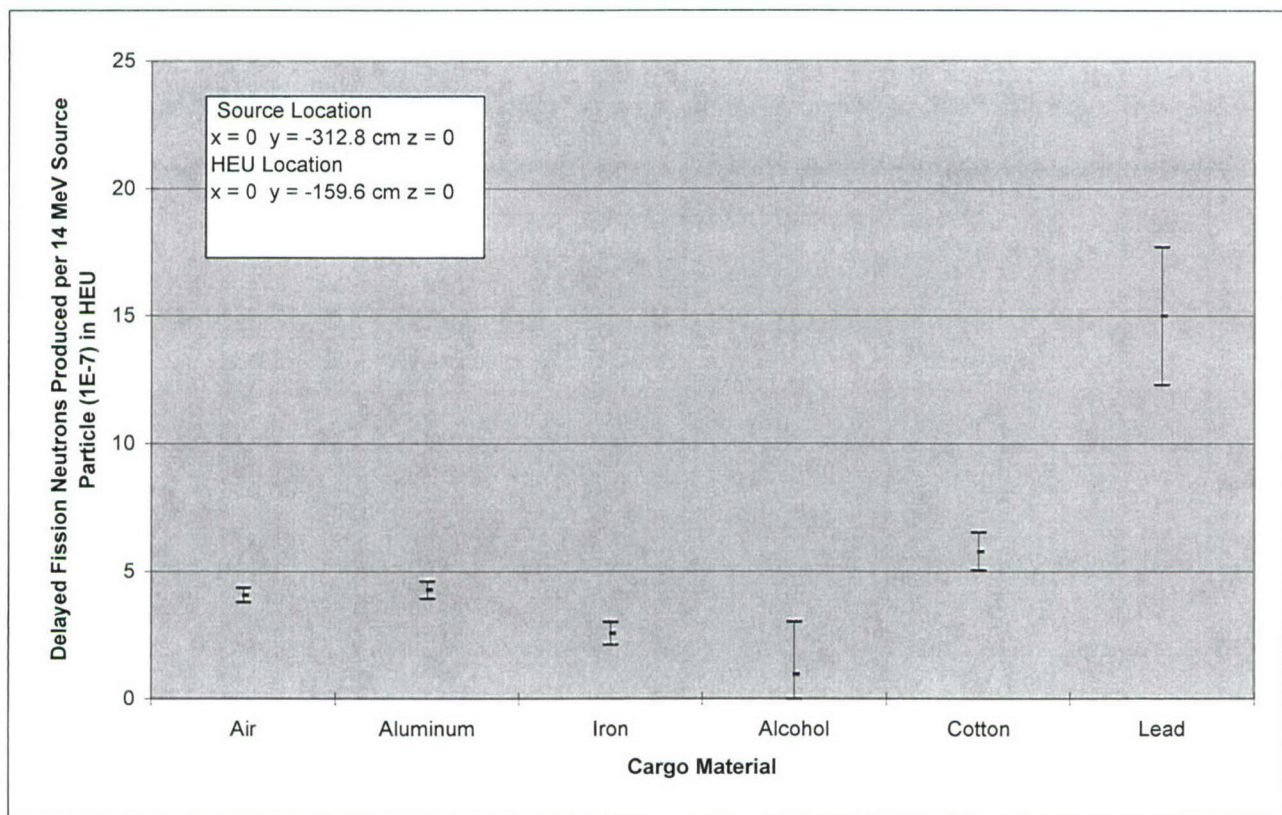


Figure 5-4. Delayed fission neutrons produced per 14 MeV source particle in HEU for various cargo materials.

5.3.4 Delayed Neutron ONDAC Interactions and Radiative Capture.

The third column of table 5-1 represents the number of interactions in the center ONDAC detector per delayed neutron source particle. These values are graphed in figure 5-5, and as was expected, alcohol has the lowest interaction rate (9.28×10^{-7}) because of the high probability of neutrons that are radiatively captured in alcohol per delayed neutron source particle. Figure 5-6 shows the radiative

capture per delayed neutron for various cargo materials. The radiative capture per 0.713 MeV delayed neutron source particle was at least two times greater than the radiative capture per 14 MeV neutron source particle for all cases examined except air. This result is generally consistent with the data shown in table 5-3 between the macroscopic cross section for radiative capture at 1 MeV and 14 MeV. A 1 MeV cross section was used to evaluate the 0.713 MeV neutron because information was readily available at this energy. The alcohol moderating effect strongly enhances radiative capture from the delayed neutrons as table 5-2 shows that 0.971 neutrons will undergo this reaction per delayed neutron source particle. Thus few delayed neutrons are able to reach the ONDAC when alcohol is present as the cargo material.

The ratio of radiative capture per source particle between 0.713 MeV and 14 MeV neutrons is not exactly proportional to the ratio of the macroscopic cross sections at these two energies. This is because some elements in these materials have a low energy resonance structure in which their values of σ_{γ} can vary greatly with small changes in incident neutron energy. Thus a point comparison does not take into consideration that the neutrons emitted from the HEU will moderate and take on a polyenergetic spectrum as they diffuse through the cargo container.

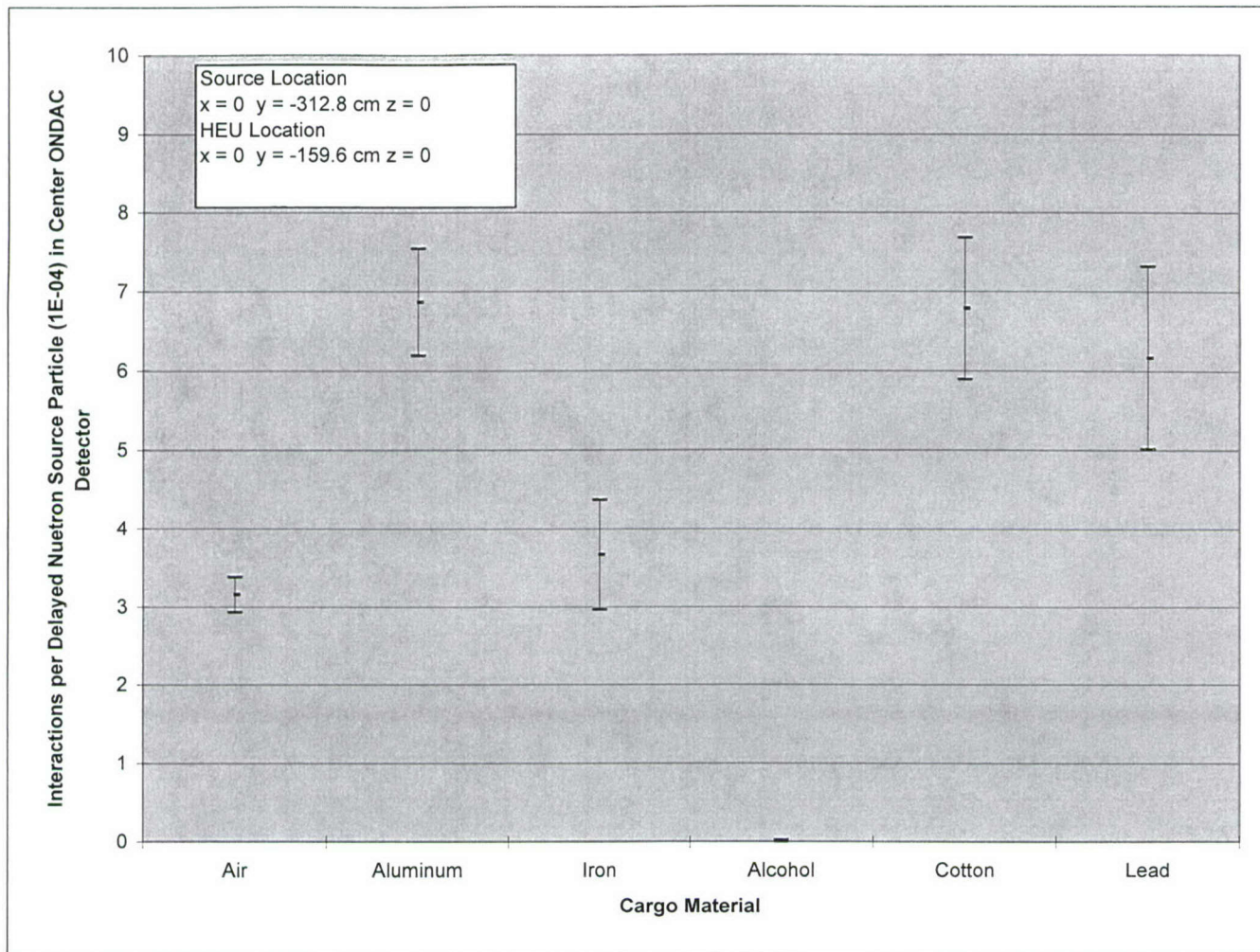


Figure 5-5. Interactions per delayed neutron source particle (1E-04) in center ONDAC detector for various cargo materials.

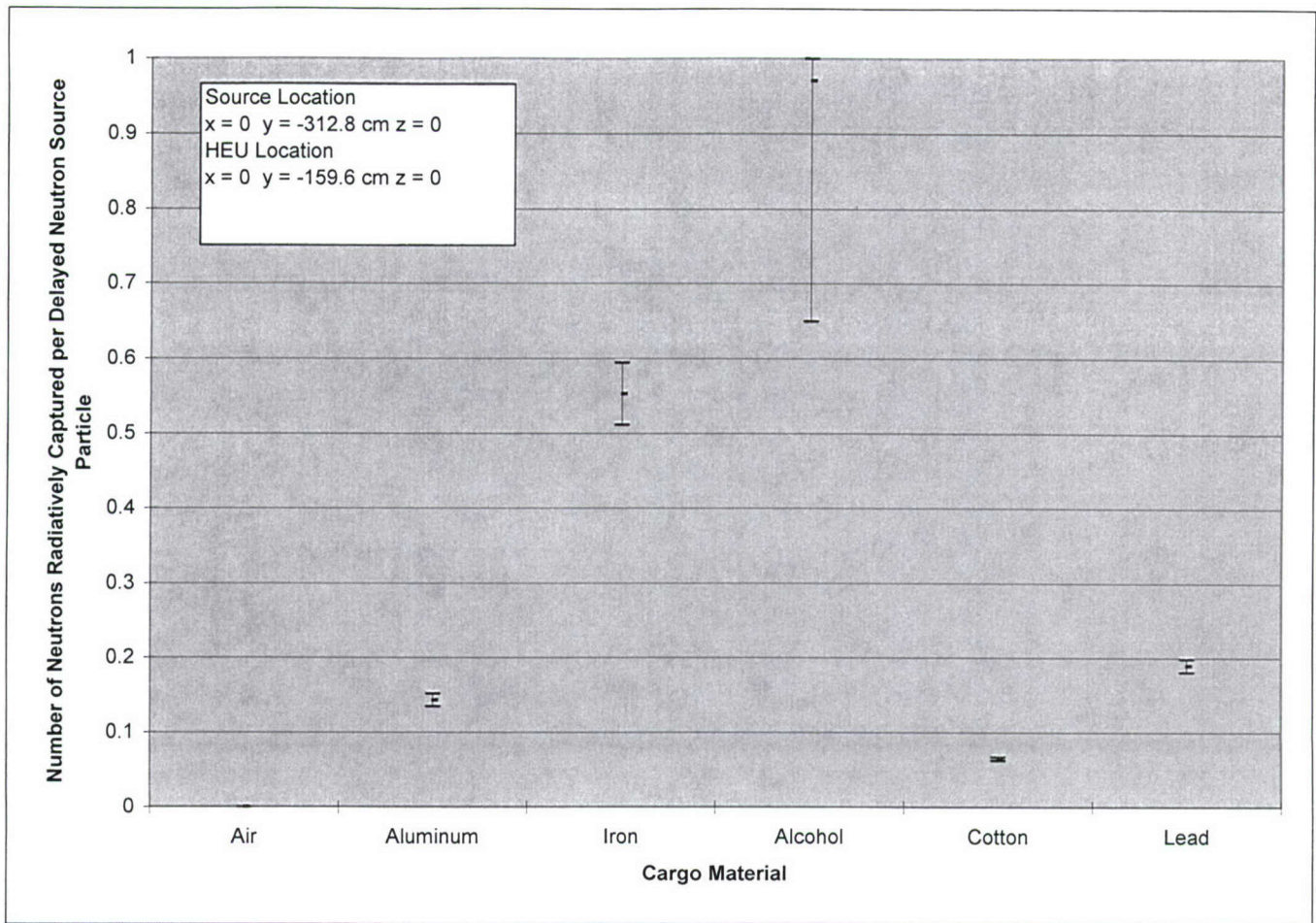


Figure 5-6. Radiative capture per delayed neutron emitted for various cargo materials.

5.3.5 ONDAC Interactions per 14 MeV Source Particle.

The final column of table 5-1 gives the center ONDAC neutron interactions per 14 MeV source particle and is shown graphically in figure 5-7. This figure is the most important in determining how the center ONDAC will detect one kilogram of HEU with the different cargo present. The values range from highest to lowest as lead, cotton, aluminum, air, iron, and alcohol.

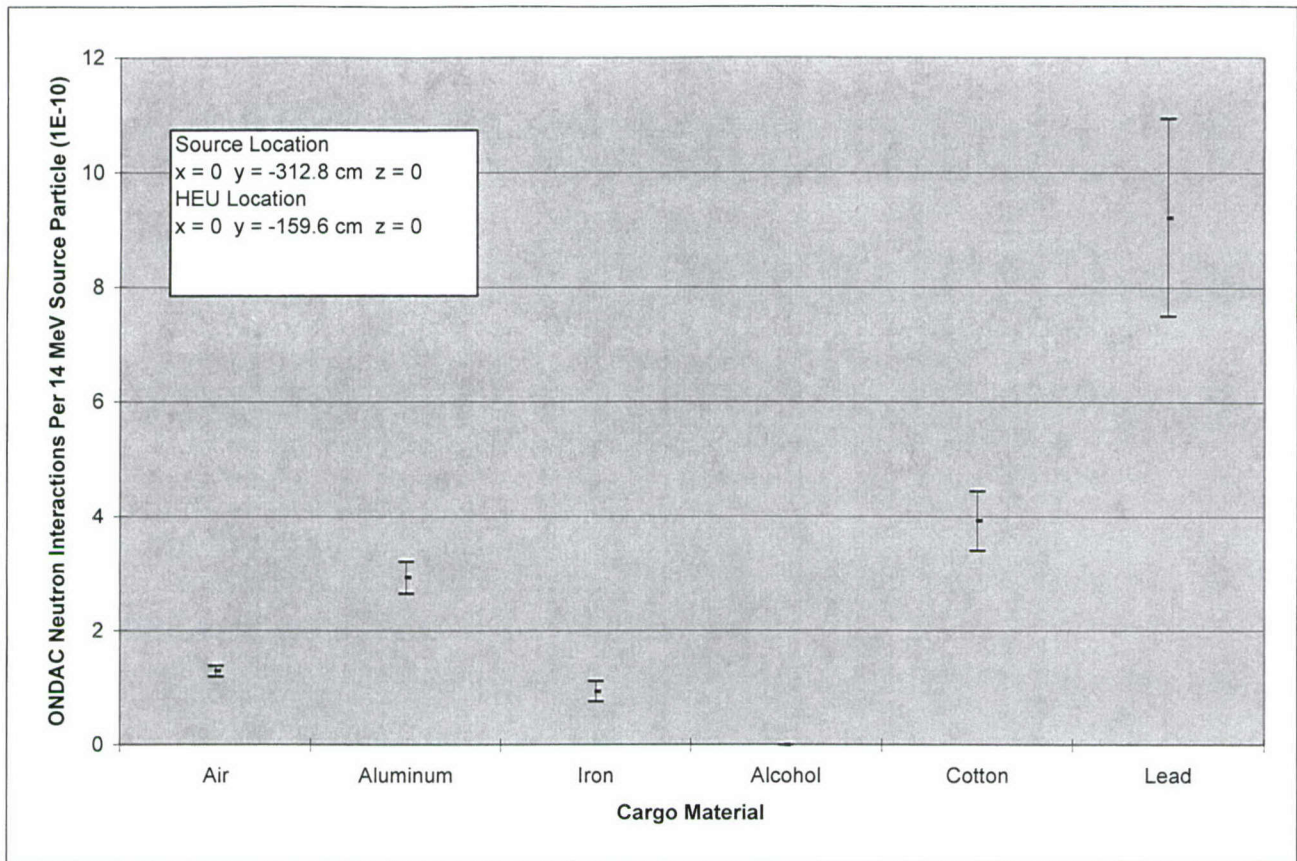


Figure 5-7. Neutron interactions per 14 MeV source particle in the center ONDAC detector for various cargo materials.

The cargo material carried in the cargo container can either enhance or reduce the output of the ONDAC detector. In order to see how each cargo material affects the ONDAC detector, the ratio of the interactions in the center ONDAC detector per 14 MeV source particle in air is compared to that of each cargo material, which is shown in figure 5-8.

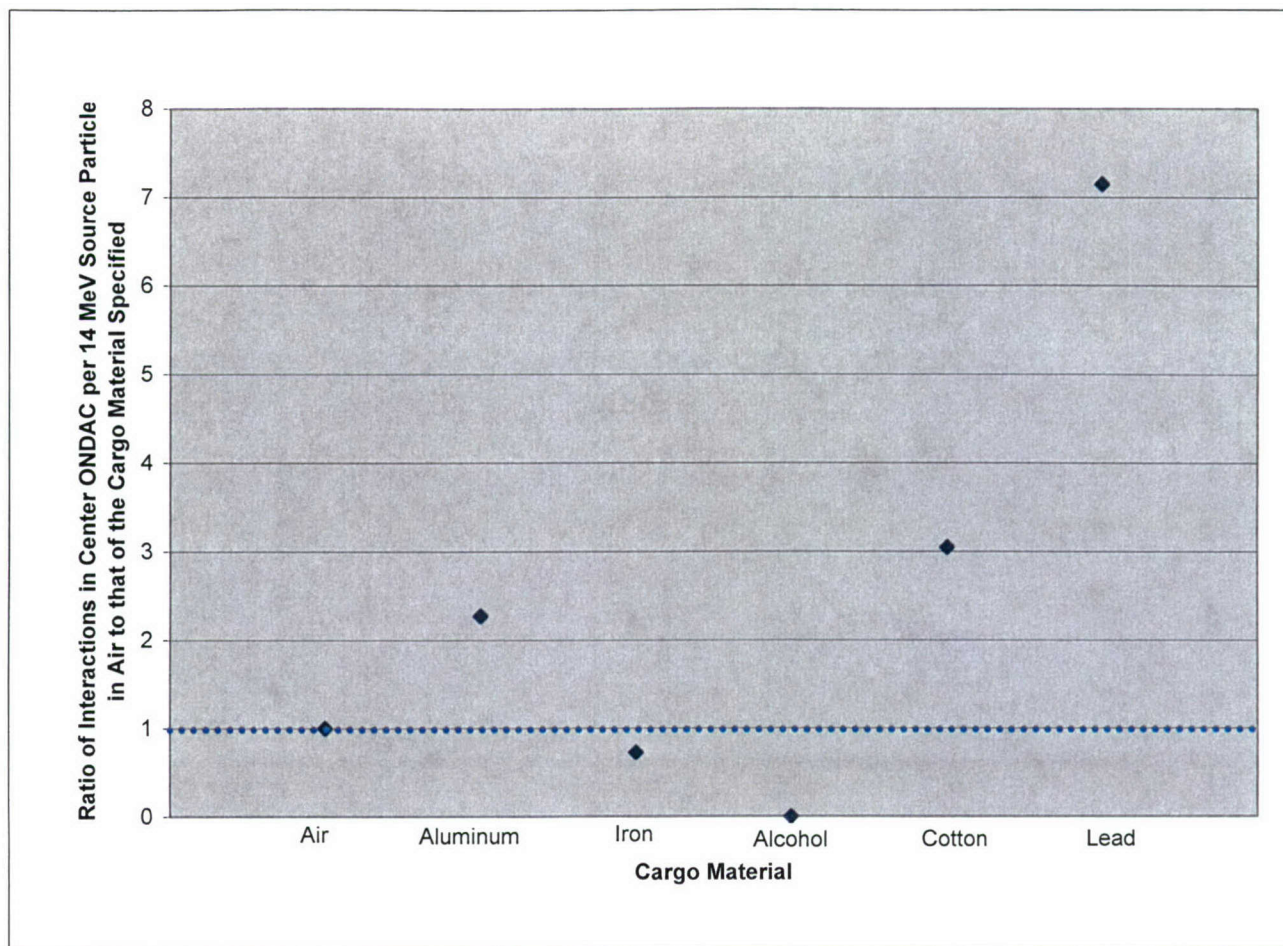


Figure 5-8. Cargo comparisons to air by the ratio of interactions in the center ONDAC detector per 14 MeV source particle in air to that of each cargo material.

The ratio of one is marked by a darkened dotted line in figure 5-8. Any material with a ratio higher than one is determined to enhance the ONDAC output while a material with a ratio less than one is determined to reduce ONDAC detector response. Lead had the highest ratio (7.15), while aluminum, cotton, and carbon materials are also considered to enhance the detector response. Iron should produce a slightly smaller ONDAC response than air (0.73), while alcohol's ratio (6.89×10^{-4}) was found to be significantly smaller than air.

Since lead, cotton, and aluminum have higher ONDAC interactions than air, their presence will not impede the sensitivity of this technique. With iron present, the ONDAC's sensitivity decreases by approximately 27%, which shouldn't be a problem as the signal to noise ratio of the ONDAC for air is 10:1, as discussed in section 4.7. However, clearly the technique would not work with alcohol for the source pulse rate (10^{12} n/sec) and the examination time (300 seconds) proposed in section 4.7. As the ONDAC interactions would be decreased by a factor of approximately 1450. To overcome this problem, the neutron generator pulse rate would have to be increased

from 10^{12} n/sec to 10^{15} n/sec, which is likely beyond current technical capabilities.

5.3.6 Study of Detector Distance Effect from HEU.

The MCNP code was also used to calculate the effect of distance on the interaction rate in the three ONDAC detectors: the center detector, and the two side detectors. The sensitivity of the ONDAC detector should vary inversely with the square of the distance (r) between the HEU and the ONDAC if neutron transport is occurring in a vacuum. The coordinates of the three detectors and the HEU are listed in table 5-5 along with their distances (r) to the HEU. The distance between each of the detectors and the HEU was found by applying Pythagorean's Theorem. The left and right detectors have equal distances to the HEU. The last column in table 5-5 gives the value of $1/r^2$ for each detector. To apply the $1/r^2$ rule, the value obtained for the center detector ($3.9\text{E-}05$) was divided by the value obtained for the side detectors ($1.5\text{E-}05$). This computation yielded numerically that the interaction rate in the center ONDAC should be about 2.57 times larger than the two side detectors.

Table 5-5. Cartesian coordinates of the three ONDAC detectors and the HEU and the distances to the HEU for each ONDAC detector in MCNP model.

Item	x (cm)	y (cm)	z (cm)	r, distance to HEU (cm)	$1/r^2$ (cm^{-2})
Right Detector	200	0	0	255.9	$1.5\text{E-}05$
Center Detector	0	0	0	159.6	$3.9\text{E-}05$
Left Detector	-200	0	0	255.9	$1.5\text{E-}05$
HEU	0	-159.6	0	N/A	N/A

The value of the ratio between the interaction rate in the center ONDAC to the interaction rate in the side ONDAC detectors are shown in table 5-6 and indicate that while the $1/r^2$ approximation is reasonable for air and cotton, it is off by over a factor of 2 for other cargo materials. This led to the observation that the longer the mean free path of the neutrons in a cargo material, the more closely the $1/r^2$ rule is followed. For example, from MCNP the 0.713 MeV delayed neutrons were determined to have a mean free path in air of 8720 cm, which is much greater than the benchmark container dimensions of approximately 250 cm. A pure vacuum would have an interaction ratio of 2.57, which is near the interaction ratio of 3.06 for air that is given in table 5-6.

Table 5-6. Ratio of the center ONDAC interaction rate to the side ONDAC interaction rate compared to the mean free path length by source energy for each cargo material.

Material	Ratio of Center ONDAC Interaction Rate To Side ONDAC Interaction Rate	Mean Free Path Length by Source Energy (cm)	
		14 MeV	Delayed Neutrons (0.713 MeV)
Air	3.06	12400.00	8720.00
Aluminum	5.97	12.55	13.26
Iron	12.70	7.70	7.94
Alcohol	217.80	2.09	0.51
Cotton	4.65	121.00	21.10
Lead	9.36	3.30	3.23

For cargo materials with a mean free path much less than the characteristic container dimensions, neutrons actually diffuse in this medium. In this case, equation (5.6) is the appropriate equation to estimate the neutron flux in these cargo materials (LaMarsh 2001).

$$\Phi(r) = \frac{S}{4\pi D r} \cdot e^{-Kr} \quad (5.6)$$

where

- $\Phi(r)$ = neutron flux at a distance r , neutrons/cm² sec
- r = distance away from point source, cm
- S = source strength of emitted isotropic neutrons, n/sec
- D = diffusion coefficient, cm
- K = reciprocal of the diffusion length, cm⁻¹

Equation (5.6) could be used to estimate the ONDAC response in this case, since the ONDAC interaction rate is proportional to the flux it sees.

5.3.7 Maximum Payload.

The maximum payload of the benchmark cargo container is approximately 28,000 kg due to its 20' x 8' x 8' dimensions. Table 5-7 shows the weight that each cargo would be if it filled all 80 cargo drums in the container. Any cargo weighing dramatically more than 28,000 kg would be an unrealistic case for the size and type of container specified in this project. Table 5-7 shows that any material having a density greater than 1 gram/cm³ will exceed the maximum payload for the benchmark facility if it occupies the entire volume of all 80 cargo cylinder drums.

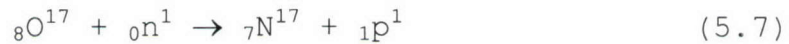
Table 5-7. Density and weight of cargo materials examined.

Material	Air	Aluminum	Iron	Lead	Alcohol	Cotton
Density (g/cm ³)	0.00118	2.70	7.87	11.34	1.0068	0.064
Weight (kg)	34	76,833	224,037	322,816	28,664	1824

Thus the cases of 80 cylinders filled with shipments of aluminum, iron, and lead are academic and these materials in practice would be shipped with partially filled containers. In this case, the result would be an ONDAC interaction rate between that given for air and the pure cargo material.

5.4 INTERFERENCE REACTION.

Interference can occur in the ONDAC detectors if neutrons undergo an (n,p) reaction in O¹⁷, (Browne, 1986) because the reaction product isotope N¹⁷ is a delayed neutron emitter with a 4.2 second half-life. This reaction is given below as equation (5.7).



O¹⁷ has a relative abundance of 0.037% in naturally occurring oxygen, so it can become a problem in cargo materials containing oxygen, namely cotton and alcohol that were evaluated in this study. However, the reaction has a neutron threshold energy of 8.5 MeV (KAERI 2002).

To evaluate the magnitude of this interference, the problem was evaluated in air with an interference ratio. In air few source neutrons would drop below the 8.5 MeV threshold as they cross the cargo container due to the fact that 14 MeV neutrons have a much greater mean free path (12400 cm) compared to the cargo container dimensions (250 cm). The interference ratio was calculated under the assumption that the flux seen by the air equals that seen by the HEU. The interference ratio, R, represents the number of delayed neutrons produced from O¹⁷ interactions divided by the number of delayed neutrons produced from HEU. The R parameter for air was then calculated by equation (5.8) as a function of decay time t as follows:

$$R(t) = \frac{0.957 \cdot N_{\text{O}^{17}} \cdot \sigma_a^{\text{O}^{17}} \cdot e^{-\lambda_{\text{O}^{17}} \cdot t}}{\beta \cdot F \cdot N_{\text{HEU}} \cdot \sigma_f^{\text{HEU}} \cdot e^{-\lambda_{\text{HEU}} \cdot t}} \quad (5.8)$$

where

- R(t) = Ratio of delayed neutrons produced by O-17 to that Produced by HEU at decay time t
- 0.957 = Probability that N¹⁷ nucleus will decay by neutron emission
- N_{O-17} = Number of O¹⁷ atoms in entire container if filled with air, 1.32x10²⁴ atoms

σ_a^{O-17}	=	Microscopic (n,p) cross section in O^{17} , 5.5 mbarns
λ_{O-17}	=	Decay constant of O^{17} , 0.165 sec^{-1}
t	=	Decay time, sec
β	=	Delayed neutrons produced per fission, 0.026
F	=	Flux depression in HEU, 0.502
N_{HEU}	=	Number of atoms in 1 kg of HEU, 2.4×10^{24} atoms
σ_f^{HEU}	=	Microscopic fission cross section for HEU with 14 MeV neutrons, 2.046 barns
λ_{HEU}	=	Decay constant of HEU produced delayed neutrons, 0.076 sec^{-1}

If the R parameter is much less than one for a given material, few delayed neutrons will be produced from O-17 compared that that from the HEU, and this interference effect will not be important. Figure 5-9 shows this interference ratio in the benchmark facility shipping container filled with air as a function of decay time. In this case, the maximum interaction ratio was found to be less than 0.005 at a decay time of zero seconds. For longer decay times, the interaction ratio decreases because O^{17} has a greater decay constant ($0.165 \text{ seconds}^{-1}$) than that of the delayed neutrons emitted from HEU fission products ($0.076 \text{ seconds}^{-1}$). Since the maximum value of this ratio is much less than one, interference reactions were considered to not be the significant in containers with or without cargos.

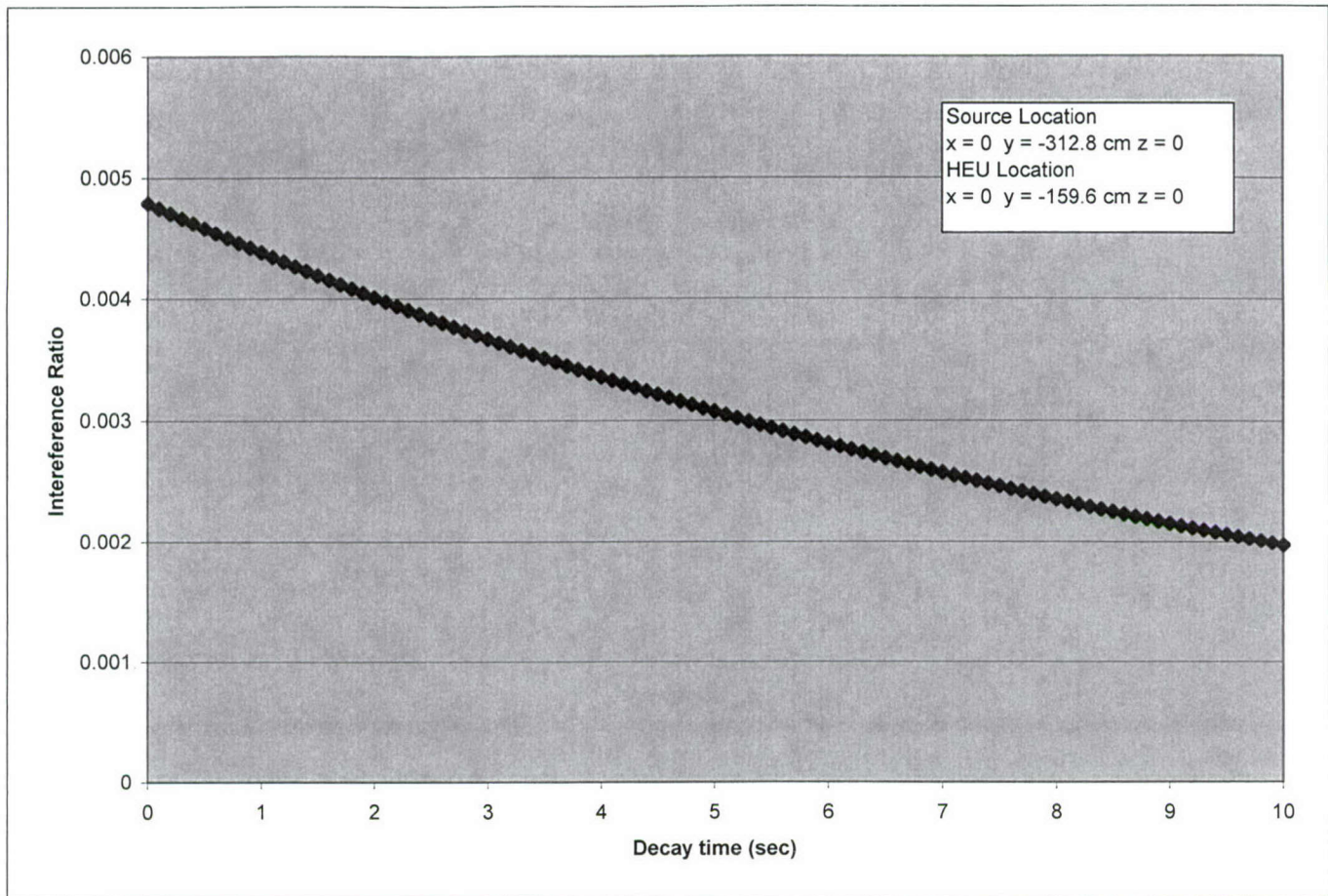


Figure 5-9. Interference ratio of oxygen in air versus decay time using benchmark facility dimensions.

5.5 EFFECT OF HYDROGEN ON ONDAC INTERACTIONS.

Section 5.3.5 showed that a small ratio of interactions exists in the center ONDAC detector per 14 MeV source particle of air to that in alcohol (6.89×10^{-4}). Therefore, a seventh cargo material was studied in order to gain a better understanding of why this occurs in alcohol. The chemical make up of alcohol is C_2H_5OH , so it is predominately composed of hydrogen. More precisely, alcohol's atom fraction is 66.7% hydrogen, 22.2% carbon, and 11.1% oxygen. Carbon was studied as the seventh cargo material in order to determine if the hydrogen was the main driving force in keeping the interactions in the center ONDAC so low. Table 5-8 compares the delayed fission neutron interactions per 14 MeV source particle in the center ONDAC detector for carbon and alcohol under identical conditions with the MCNP benchmark facility model. Table 5-8 also gives the center ONDAC interaction ratio between the carbon and alcohol cargo.

Table 5-8. Comparison of the delayed fission neutron interactions per 14 MeV source particle in the center ONDAC detector of carbon and alcohol under identical conditions with the MCNP facility model.

Material	Center ONDAC Delayed Neutron Interactions per 14 MeV Source Particle	Ratio of Carbon to Alcohol interactions per 14 MeV source particle
Carbon	1.20E-9	13,500
Alcohol	8.89E-14	not applicable

As can be seen in table 5-8, carbon produces a response 13,500 times stronger than alcohol in the center ONDAC detector. Hence, the low interaction rate of neutrons in the ONDAC in the presence of alcohol is not due to carbon. Further since carbon and oxygen have similar nuclear properties (KAERI 2002), it was concluded that the key element in reducing ONDAC interactions per source particle is hydrogen.

The ONDAC detectors response to the hydrogen atom percent of a cargo material was studied in order to find the maximum amount of hydrogen that will yield statistically valid results from the center ONDAC detector without having to increase the 14 MeV neutron source strength from 10^{12} n/sec as recommended in section 4.7. The cargo density of each case studied was held constant at 1 g/cm³, along with the location of the 14 MeV source (x = 0 y = -312.8 cm z = 0) and the HEU location (x = 0 y = -159.6 cm z = 0) while the atom percentage of the hydrogen was varied from 11.3%, 33.3%, 50.0%, and 66.7%. The amounts of carbon and oxygen also varied within these MCNP runs. However their relative amounts were held constant with the carbon having twice the atom percentage of the oxygen (i.e. the ratio of carbon to oxygen in alcohol) except for the 11.3% hydrogen case, which had 3.1% carbon and 85.6% oxygen. The results of the delayed fission interactions per 14 MeV source particle in the center ONDAC detector for the four cases of different amounts of hydrogen are shown plotted in figure 5-10.

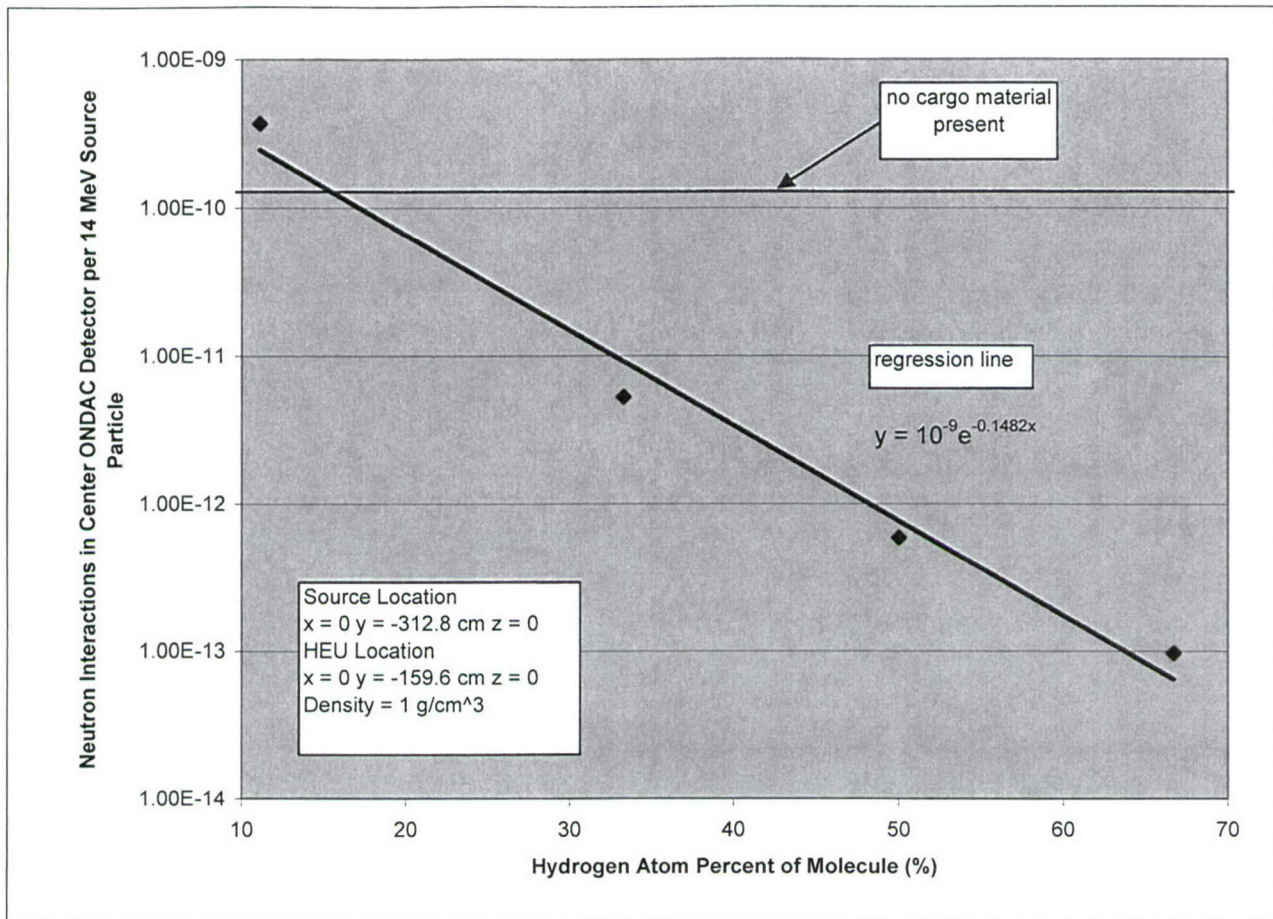


Figure 5-10. Neutron interactions per 14 MeV source particle in center ONDAC detector for various amounts of hydrogen in a cargo material composed of hydrogen, oxygen, and carbon based molecules.

Figure 5-10 shows that as the amount of hydrogen in a cargo material increases, the number of neutron interactions in the center ONDAC detector per 14 MeV source particle decreases significantly. Since the interactions decrease linearly on a semi-log scale, the decrease is exponential, and can be expressed empirically by equation (5.9) as follows:

$$y = 10^{-9} e^{-0.1482x} \quad (5.9)$$

where

- y = the number of neutron interactions in the center ONDAC detector per 14 MeV source particle.
- x = the hydrogen atom percent of cargo molecule, %

The coefficients in equation (5.9) were found by regression analysis and the line that resulted from this equation has been added to figure 5-10. The delayed fission neutron interactions in the center ONDAC detector per 14 MeV source particle is also shown for the case of no cargo material ($1.29\text{E}-10$). Wherever the number of interactions for hydrogen is greater than the number of interactions for air, the ONDAC should detect the HEU if a 14 MeV pulsed source of 10^{12} n/sec

and a total examination time of 300 seconds is used. Figure 5-10 shows that the number of interactions in the cargo containing hydrogen equals the number of interactions in the air when the hydrogen atom percent is 13.8%. Therefore materials containing less than 13.8% hydrogen should be detected using this technique. Also materials with slightly more than 13.8% hydrogen should also be detected, as the signal to noise ratio in the center ONDAC for air is 10:1, as discussed in section 4.7. Conservatively, the atom fraction of hydrogen in the cargo should still be limited to about 15%, assuming the neutron generator pulse rate is maintained at 10^{12} n/sec and the examination time is maintained at 300 seconds.

5.6 CONCLUSIONS.

This section has shown that the presence of cargo, which does not contain hydrogen, will not defeat the 14 MeV pulsed neutron technique with a 10^{12} n/sec source and a 300 second examination time. In fact, the presence of high atomic number materials, such as lead, actually will enhance the ONDAC response due to the (n,xn) reactions they induce. The technique also will work with hydrogen present if the cargo material has density well below that of water or alcohol (i.e. 1 g/cm³). If the cargo has a density of 1 g/cm³ or higher, 1 kg of HEU can still be detected if the atom fraction of the hydrogen in the cargo material is less than 15%. To detect HEU with cargo materials with a greater hydrogen atom fraction than 15% and a density of 1 g/cm³ or greater there are several options. First, one could increase the pulse rate of the 14 MeV neutron source, although this may not be technically feasible with current technology. Second, since hydrogen poorly attenuates the gamma emitted by the HEU, the system could be augmented with a high sensitivity gamma detector. Third, one could perform an internal inspection of the cargo container using portable neutron and high sensitivity gamma detectors. Fourth, multiple 14 MeV neutron generators, whose pulse outputs are synchronized, could be placed around the container in order to increase the neutron source strength.

SECTION 6

SHIELDING ANALYSIS

In this section, analysis of the shielding requirements for the benchmark facility is presented. Section 6.1 examines the dose rate that would be produced as a function of concrete shield thickness based on previously published empirical techniques. Section 6.2 repeats this analysis, but uses the MCNP code to perform the dose rate assessment. Finally, conclusions are presented with regard to these topics in section 6.3.

6.1 SHIELDING REQUIREMENTS-EMPIRICAL APPROACH.

Several empirical methods have been developed for calculating the shielding requirements for 14 MeV neutron generator facilities (Nargolwalla 1973). In this section two methods are evaluated for concrete shields. Concrete normally is the material of choice for shielding these facilities, because of its high hydrogen content, low cost, and structural durability.

The first method evaluated employs the removal cross section and has been described by both Cloutier (Cloutier 1963) and Nachtigall and Heinzelman (Nachtigall 1966). This method calculates the neutron dose rate in air behind the shield from the equation:

$$D(x) = D_0 B e^{-\Sigma_{rem} t} \quad (6.1)$$

where

$D(t)$	=	dose rate behind shield of thickness t cm, mrem/hr
D_0	=	dose rate without shielding, mrem/hr
B	=	14 MeV neutron flux build-up factor, dimensionless
Σ_{rem}	=	14 MeV removal cross section for concrete, $.08 \text{ cm}^{-1}$
t	=	shield thickness, cm

The dose rate without shielding (D_0) in equation (6.1) can be found from the equation for neutron diffusion from point source (LaMarsh 2001):

$$D_0 = \frac{S}{4\pi t^2 K} \quad (6.2)$$

where

S	=	neutron generator pulse rate, neutrons/sec
K	=	14 MeV dose to flux conversion factor, $6.8 \text{ n/cm}^2\text{-sec}$ per mrem/hr

The 14 MeV dose to flux conversion factor (k) of 6.8 in the denominator of equation (6.2) is based on recommendation of the International Commission on Radiological Protection (ICRP 1972). The National Institute of Standards and Testing (NIST) (formerly the National Bureau of Standards) recommended a build-up factor of 5 for

thick concrete shields (NBS 1967). The macroscopic removal cross section for 14 MeV neutrons in concrete (Σ_{rem}) was taken to have a value of 0.08 based on Berger (Berger 1967). The dose rate as a function of concrete thickness using equation (6.1) with the above described parameters is shown in figure 6-1. As can be seen in this figure for a 130 thick concrete shield, the dose rate would be 1×10^{-10} mrem/hr per 14 MeV neutron/sec emitted by the source.

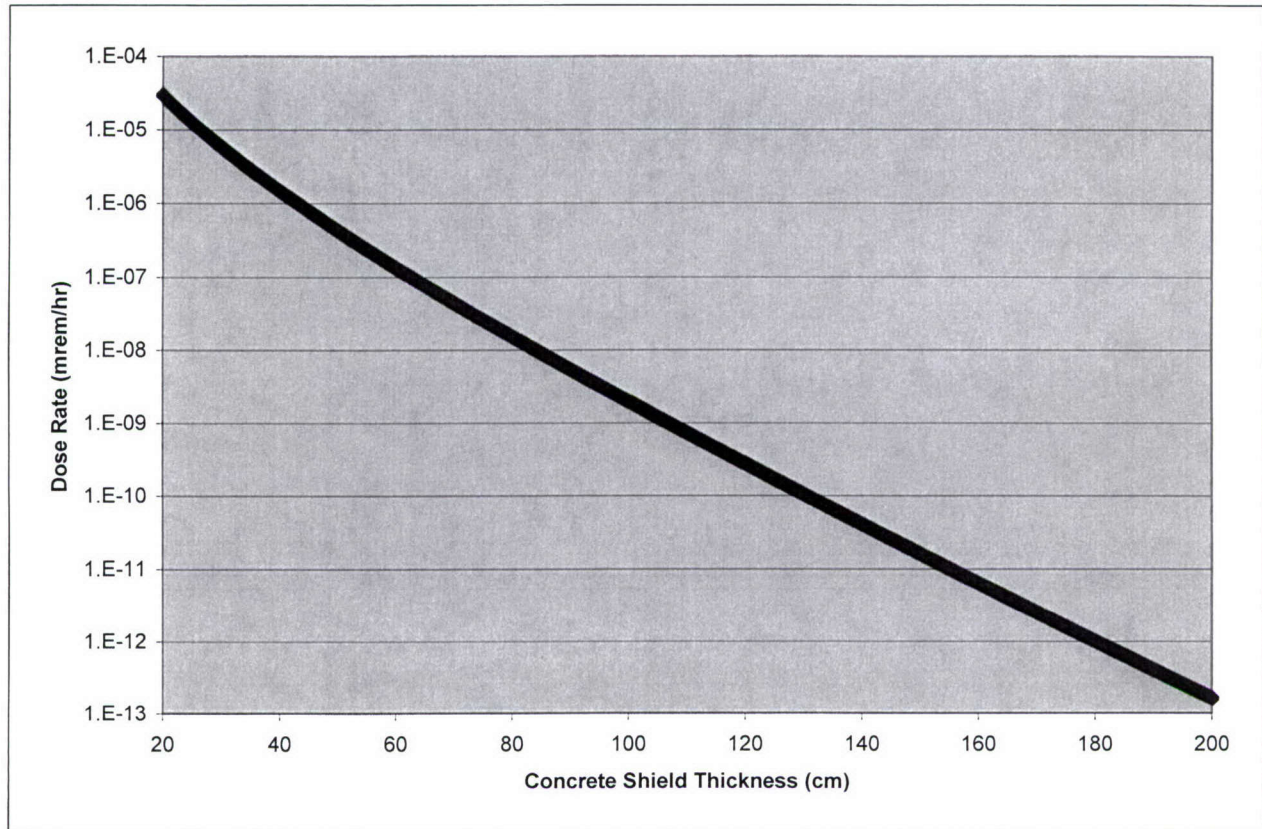


Figure 6-1. Effect of concrete shield thickness on the neutron mrem/hr dose rate in air as a function of concrete shield thickness per 14 MeV neutron emitted per second by the source using equation (6.1) (Cloutier 1963).

The second method evaluated was developed by Boerse and Van Werven (Boerse 1966) and is based on experimentally determined constants C and a neutron relaxation length (λ_n) that can be expressed in the relationship:

$$D(x) = D_0 C e^{(-x / \lambda_n)} \quad (6.3)$$

where

- $D(x)$ = dose rate behind shield of thickness x cm, mrem/hr
- D_0 = dose rate without shielding, mrem/hr

C = experimental 14 MeV neutron constant, 1.2
for concrete

λ_n = 14 MeV neutron relaxation length in concrete, 19.7 cm

The neutron dose rate versus concrete thickness using this approach is shown in figure 6-2. As can be seen in this figure the neutron dose rate for a 130 cm thick concrete shield would be approximately 1×10^{-9} mrem/hr per 14 MeV neutron/sec emitted by the source, which is approximately a factor of 10 higher than the Cloutier approach.

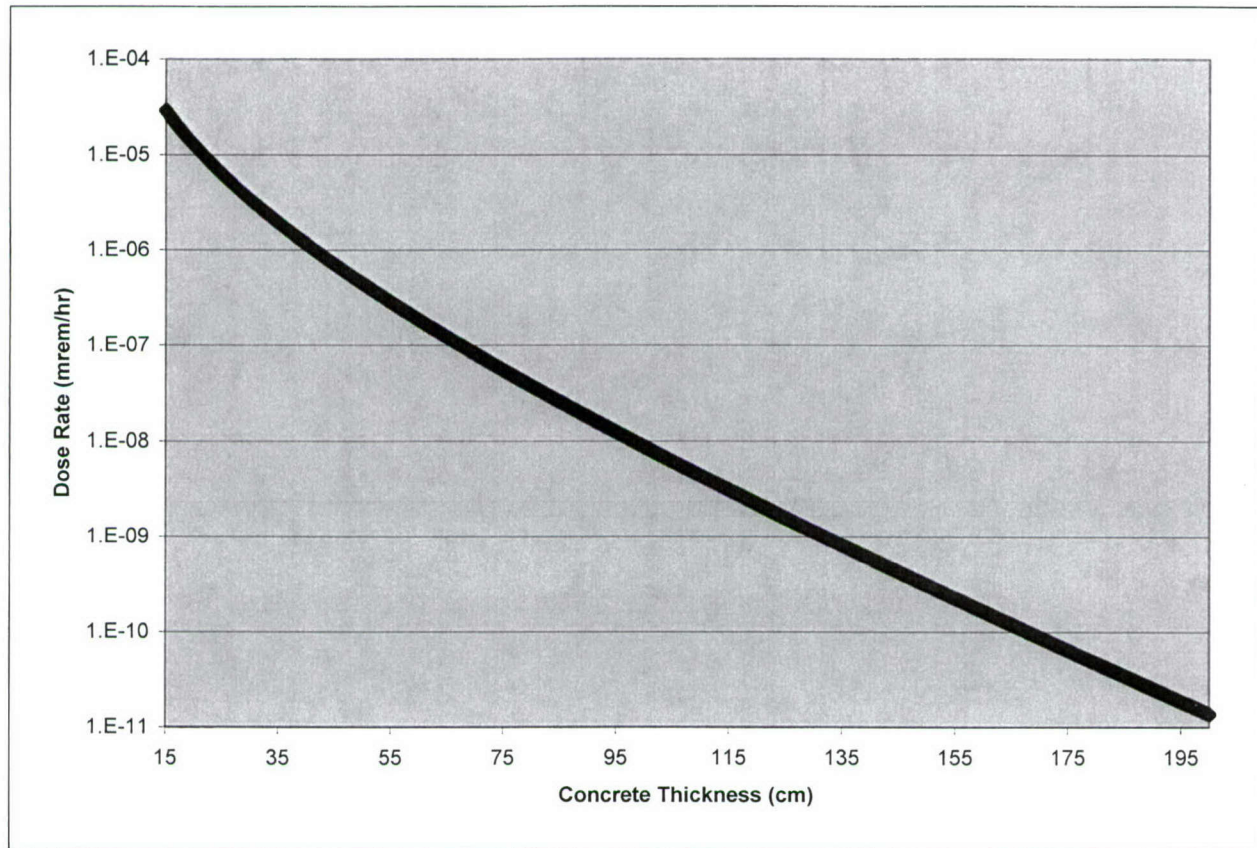


Figure 6-2. Effect of concrete shield thickness on the neutron mrem/hr dose rate in air as a function of concrete shield thickness per 14 MeV neutron emitted per second by the source (Broerse and Van Werven 1966).

6.2 SHIELDING REQUIREMENTS-MCNP APPROACH.

The concrete shielding requirement was also evaluated using MCNP. To perform this analysis a concrete slab was modeled in which a 14 MeV neutron source was placed on one side of the shield and the dose was calculated on the other side just outside the shield in air. The MCNP input file for this calculation is given in Appendix A. Figure 6-3 is the SABRINA graphical representation of this model, in which the sphere shown represents the point in space where the dose is calculated. Dose calculations were performed for concrete thicknesses that varied from 130 cm (4.25 ft) to 244 cm (8.0 ft). A

plot of the dose rate expressed in units of mrem/hr per neutron/sec emitted by the source is given in figure 6-4. With a 130 cm thick concrete shield, the neutron dose rate was calculated to be 5.38×10^{-10} mrem/hr per 14 MeV neutron/sec emitted by the source. This result was approximately 5 times that predicted by Cloutier using equation (6.1), but half of that predicted by Broerse using equation (6.3). Thus the MCNP model calculated a dose that was at the arithmetic mean of the two empirical approaches evaluated.

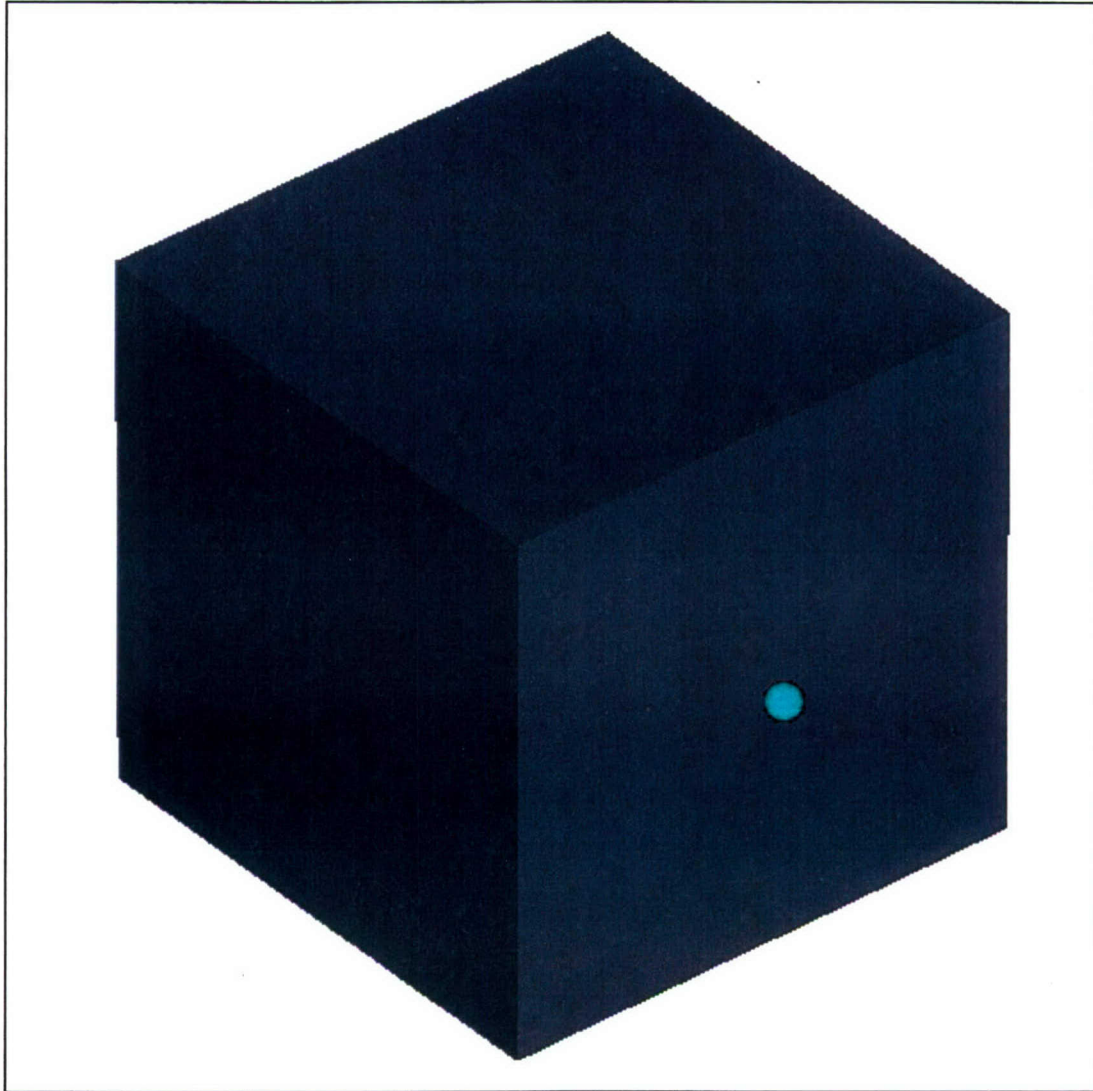


Figure 6-3. MCNP model to calculate dose behind concrete shield. Sphere represents point in space where dose is calculated.

At concrete thicknesses of 214 cm and 244 cm, MCNP found no neutrons that penetrated the shield in 4×10^8 cases and thus predicted a zero neutron dose. For these thicknesses, the photon contribution to the dose was then analyzed using MCNP and produced the dose results shown in figure 6-4. As can be seen for an 8 foot (244 cm) concrete shield, the photon and hence total dose rate was found to be $1.49 \times$

10^{-13} mrem/hr per 14 MeV neutron/sec emitted by the shield. Assuming a neutron source strength of 10^{12} n/sec and using the recommended source pulse time (2.9 sec), count time (2.9 sec), and dissipation time of (0.25 sec) as given in table 4.8, the dose rate outside the shield was determined to be .07 mrem/hr. Assuming a radiation worker at the facility worked 2000 hours a year and the facility was continuously operated, this worker would only receive 140 mrem in a year, which is far below the current standard for occupational exposure of 5000 mrem per year and 500 mrem/year for the general population (LaMarsh 2001). Thus a concrete shield of eight feet thickness would be more than adequate for shielding purposes. For concrete thicknesses of 214 cm and 244 cm, the total dose was found to be dominated by gammas, while at 130 cm, the dose was dominated by neutrons.

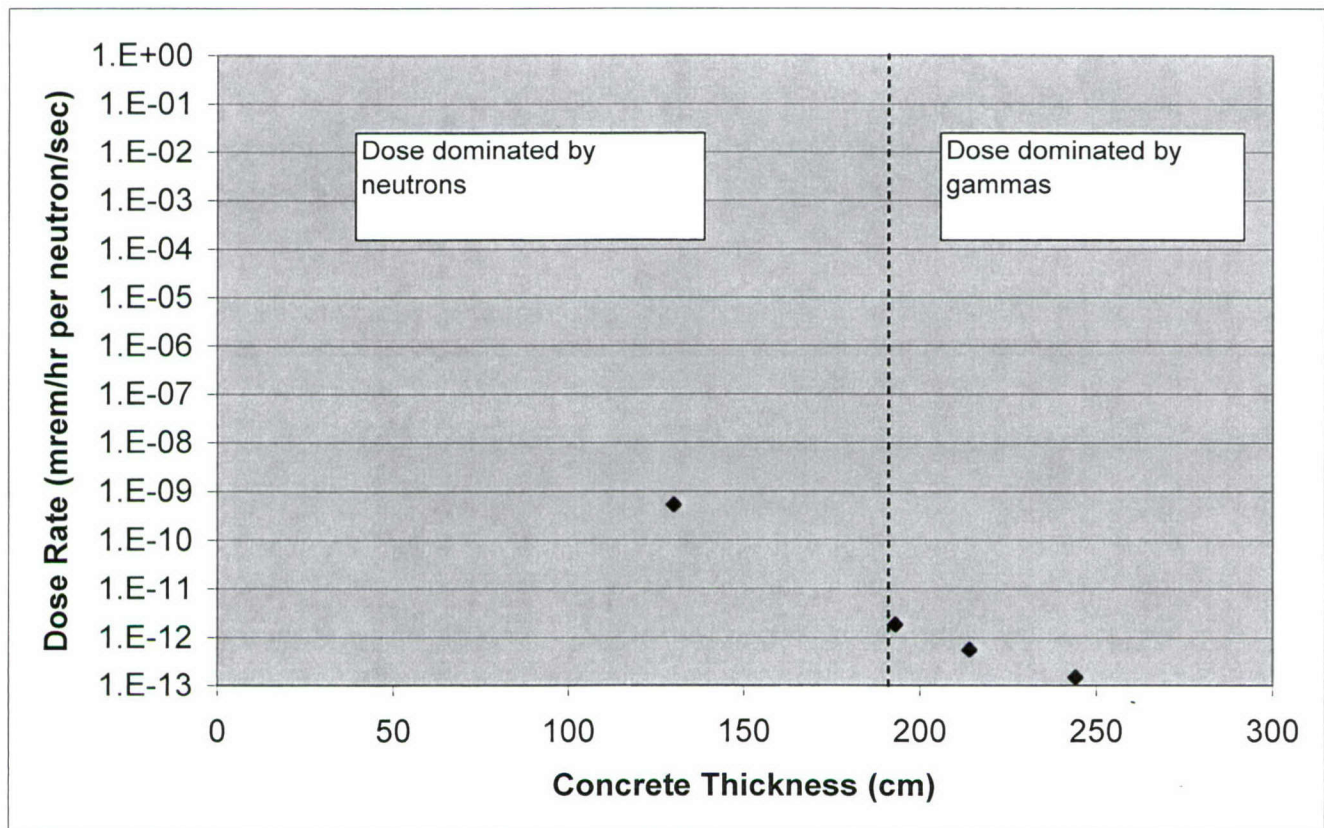


Figure 6-4. MCNP dose rate per 14 MeV source neutron/sec emitted through concrete.

A number of other combinations of shielding materials could be employed other than concrete. For example, 14 MeV neutron generator facilities have been designed with a combination of concrete and soil (Nargolwalla 1973). The US Naval Academy's 14 MeV neutron generator uses this approach in a portion of its shield design. A further study would be needed in order to reduce the shield size and cost, but such a study was beyond the scope of this project.

6.3 CONCLUSIONS.

This section has compared three approaches, two of which are based on historical empirical approaches, and third was based on numerical Monte Carlo techniques. All techniques agreed with each other to within one order of magnitude for the dose rate expected outside the shield. Using the Monte Carlo results, which predicted a dose rate between the two empirical approaches for a given concrete thickness, it was determined that a concrete shield of 244 cm or eight feet thickness would be necessary in order to reduce the dose rate for facility occupational workers and members of the public below current radiation protection standards.

SECTION 7

STUDY ON EFFECTS OF VARYING SOURCE DISTANCE TO THE CARGO CONTAINER

This section analyzes the effect of moving the 14 MeV stimulation source to different distances outside the container. The motivation for studying this effect, which can be referred to as source standoff, is described in section 7.1. Section 7.2 contains a description of how the benchmark facility MCNP model was modified to study this problem. Section 7.3 examines the effect of source standoff on neutron production from HEU for different cargo materials. The number of interactions in the center ONDAC detector is given in section 7.4 as a function of source standoff and for different cargo materials. Finally, conclusions on this effect are given in section 7.5.

7.1 MOTIVATION FOR DISTANCE STUDY.

The main motivation for this study is to determine how far the source can be moved from the container in order to disguise the inspection process. If a terrorist group is unaware that the cargo container in which they have placed their SNM is being examined, the material is much more likely to be discovered by the US Custom inspectors. Hence moving the source farther away from the container makes the inspection process less obvious. Another benefit of a large distance between the source and the container would be easier movement of the container out of the port and hence reducing the impact of the inspection process on the free flow of commerce.

7.2 MCNP MODEL TO STUDY SOURCE STANDOFF.

The detection of SNM, in particular HEU, must be possible with different types of cargo present in the container. This study examined three separate homogeneous cargos including lead, iron, and air (no cargo) in order to make generalizations about moving the neutron source away from the cargo container. Similar to the payload study in section 5, in order to specify a cargo material, an extra material card was added to the MCNP input file that identified the cargo's elemental composition and the atom fraction associated with each element. Then each of the 80 cargo drums was filled with the cargo material, and the material's density was specified in the cells that represented these drums.

There were two benchmark model adjustments that needed to be made to study the effect of the position of the neutron source. The first was that radius of the surrounding sphere in which MCNP tracks particles had to be increased, because MCNP requires that the neutron source to be located inside this sphere. The radius of the surrounding sphere was changed from 4.52 m, which was used in the

section 5 study, to 12 m. Second, the position of the source on the source card had to be altered to simulate the different distances between the neutron source and the outside of the cargo container. Table 7-1 gives the positions of source as they read on the MCNP source card, the distance from the source to the HEU in which was assumed to be the center of the cargo container, and the distance from the source to the side of the container.

Table 7-1. Source position data.

Source Position	Distance from the Source to the HEU in the Center of the Cargo Container (cm)	Distance from the Source to the Side of the Cargo Container (cm)
x = 0 y = -312.78 cm z = 0	153.18	30.5
x = 0 y = -412.78 cm z = 0	253.18	130.5
x = 0 y = -612.78 cm z = 0	453.18	330.5
x = 0 y = -812.78 cm z = 0	653.18	530.5
x = 0 y = -1012.78 cm z = 0	853.18	730.5

The center of the cargo container is defined to be located at x = 0 y = -159.6 cm z = 0. The distance from the source to the HEU in the center of the cargo container was found by taking the absolute difference in the y-position of the source position and the center position. The corresponding values for each different source position are shown in the second column of table 7-1. Since dimensions of the benchmark cargo model are 8 feet across, slightly more than 4 feet of space exists between the outside cargo container wall and the center of the cargo container where the HEU is assumed to be located. This space was subtracted from the distance of the source to the center of the cargo container (second column in table 7-1) to find the distance of the source to the side of the cargo container (third column in table 7-1). This distance was used to develop the results given in sections 7.3 and 7.4.

The first source position was that used in section 5 and places the neutron source approximately 1 foot (30.5 cm) outside of the cargo container. The subsequent positions moved the source an additional one meter (3.1 feet) to over seven meters (24 feet) away from its original position.

7.3 EFFECT OF SOURCE STANDOFF ON NEUTRON PRODUCTION FROM HEU FOR DIFFERENT CARGO MATERIALS.

The approach used to study this effect was to first determine neutrons gained by fissioning in HEU as the source is moved, because the technique for determining the presence or absence of the HEU is based on counting the delayed neutrons that are produced by the decay of fission products. As discussed in section 5, the delayed neutron production rate is directly proportional to the neutrons produced by the HEU fissioning. Second, this production rate was then multiplied

by the probability that such a fission neutron would then interact with the center ONDAC detector as was done in section 5. For all cases, this probability was based on the assumption that the HEU was located in the center of the container and the center ONDAC detector was in the same position as given in the benchmark facility description (section 2). The result of this process was the interaction in the center ONDAC per source particle as a function of source distance outside the container. Table 7-2 gives a numerical summary of the first step of this process for case of no cargo (air), as well as cargo materials iron and lead. Two additional assumptions made in producing these results were (1) that the neutron source was 14 MeV and (2) that no neutron moderation occurred external to the container.

Table 7-2. Numerical summary of neutron gain by fissioning in HEU per 14 MeV source particle with varied distances of the source to the side of the container.

Distance of Source to Side of Container (cm)	Neutron Gain by Fissioning in HEU per 14 MeV Source Particle		
	Air	Iron	Lead
30.5	6.26E-05	3.92E-05	2.31E-04
130.5	2.35E-05	1.14E-05	not found
330.5	7.50E-06	2.90E-06	2.04E-05
530.5	3.70E-06	1.40E-06	9.20E-06
730.5	2.20E-06	7.00E-07	5.10E-06

The neutrons gained by fissioning in the HEU per 14 MeV source particle for various distances of the source to the side of the cargo container is graphed in figure 7-1. Lead had the highest value of the 3 cases making it the cargo material that would most easily detect 1 kg of HEU compared to air and iron. The higher values for lead are due to its higher likelihood of neutron producing reactions. Iron had the lowest values due to its higher probability of neutrons undergoing radiative capture in this material. The relative value of the neutrons produced by fission decreased as the distance of the source increased with the same functional relationship for all materials. If the 4 feet distance the neutrons must travel inside the container to reach the HEU is added to the distance the source is located outside the container, then the neutron gain by fissioning will decrease approximately as the square of the sum of these two distances.

The delayed fission neutrons produced in HEU per 14 MeV source particle versus source distance from the side of the container is given in table 7-3. These results were obtained by multiplying the entries in table 7-2 by the HEU delayed neutron fraction (.0065), similar to the method used in section 5.

Table 7-3. Numerical summary of delayed fission neutrons produced in HEU per 14 MeV source particle with varied distances of the source to the side of the container.

Distance of source to side of container (cm)	Delayed fission neutron produced in HEU per 14 MeV source particle		
	Air	Iron	Lead
30.5	4.07E-07	2.56E-07	1.50E-06
130.5	1.53E-07	7.41E-08	not found
330.5	4.88E-08	1.88E-08	1.32E-07
530.5	2.40E-08	9.10E-09	5.98E-08
730.5	1.43E-08	4.55E-09	3.30E-08

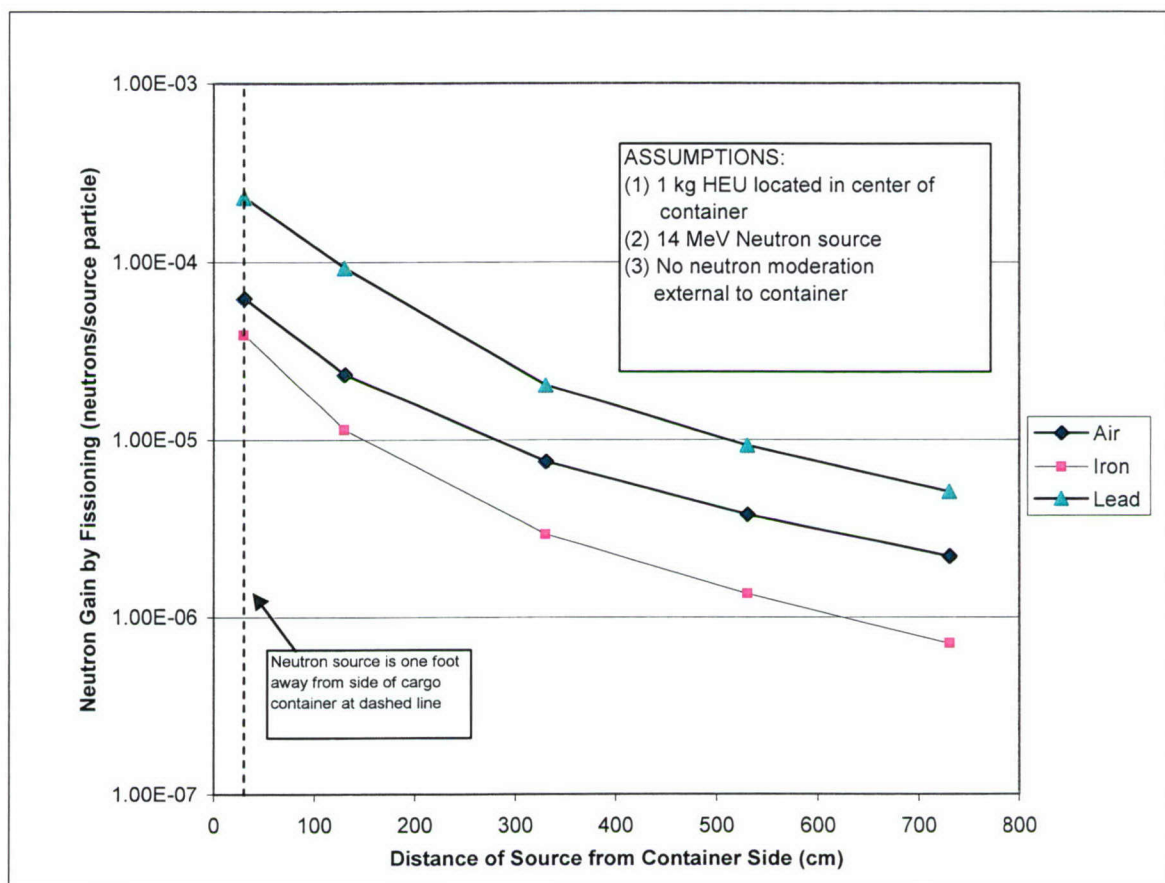


Figure 7-1. Neutron gain by fissioning in HEU with cargo container material in air, iron, and lead versus distance of source from container side.

7.4 INTERACTIONS IN CENTER ONDAC PER 14 MEV SOURCE PARTICLE.

The interactions in the center ONDAC per delayed neutron source particle was found using the results in section 5.2. This could be

done, because the distance from the HEU to the ONDAC detector and the energy of the emitted delayed neutrons were assumed to be unchanged in this problem from that analyzed in section 5. Table 7-4 gives a numerical summary of the values for the materials of air (no cargo), iron, and lead, which is a repeat of the information in the third column of table 5.1.

Table 7-4. Numerical summary of interactions in center ONDAC per delayed neutron source particle for air, iron, and lead.

Cargo Material	Interactions in Center ONDAC detector per Delayed Neutron Source Particle
Air	3.16E-04
Iron	3.67E-04
Lead	6.17E-04

The interactions in the center ONDAC per 14 MeV source particle were then found by multiplying the values of delayed fission neutrons produced in HEU per 14 MeV source particle as shown in table 7-3 to the values shown in table 7-4 for each material. The summary of the results is shown in table 7-5. The value for lead is not shown for the 107.6 cm case because the computer terminated the MCNP code prematurely and the data was not fully recovered.

Table 7-5. Interactions in center ONDAC per 14 MeV source particle for air, iron, and lead for various distances between the source and side of cargo container.

Distance of Source to Side of Container	Interactions in Center ONDAC Per 14 MeV Source Particle		
(cm)	Air	Iron	Lead
30.5	1.29E-10	9.40E-11	9.22E-10
130.5	4.83E-11	2.72E-11	not found
330.5	1.54E-11	6.90E-12	8.14E-11
530.5	7.58E-12	3.34E-12	3.69E-11
730.5	4.52E-12	1.67E-12	2.04E-11

Figure 7-2 graphically shows the data from table 7-5. The results follow the same trends as the neutron gain by fissioning in the HEU from figure 7-1.

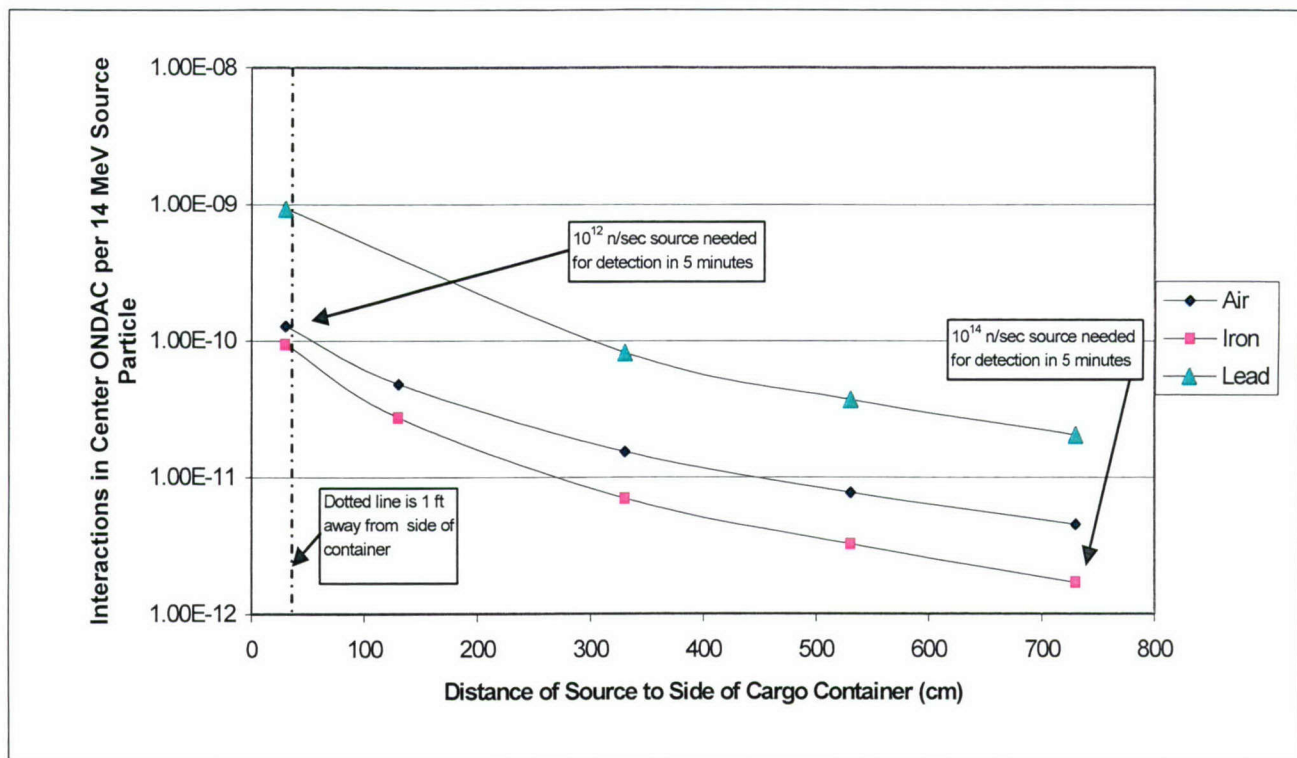


Figure 7-2. Interactions in center ONDAC per 14 MeV source particle in air, iron, and lead versus distance of source from container side.

To understand the effect of distance and cargo, figure 7-3 shows the normalized center ONDAC detector interactions as a function of distance the source is from the side of the container for cargo materials air, iron, and lead. As can be seen, if the source is 730.5 cm (slightly less than 24 feet) from the container, then with no cargo (air) the interaction ratio will have decreased by a factor of nearly 30, with iron cargo by a factor of 90, and with lead cargo by a factor of 12. However, the ONDAC response will be directly proportional to this ratio. In section 4, the operating conditions (i.e. 10^{12} n/sec pulsed source, 5 minute irradiation, 48 cycles), which would allow successful determination of 1 kg of HEU, were based on the source being 30.5 cm (one foot) outside the container. Assuming that the examination time can't be increased due to the resulting impact on the flow of commerce, then the only option would be to increase the neutron source strength in inverse proportion to the decrease in the normalized center ONDAC interactions. Thus to handle the case of iron cargo at 24 feet, the neutron source would have to be nearly 10^{14} neutron/sec.

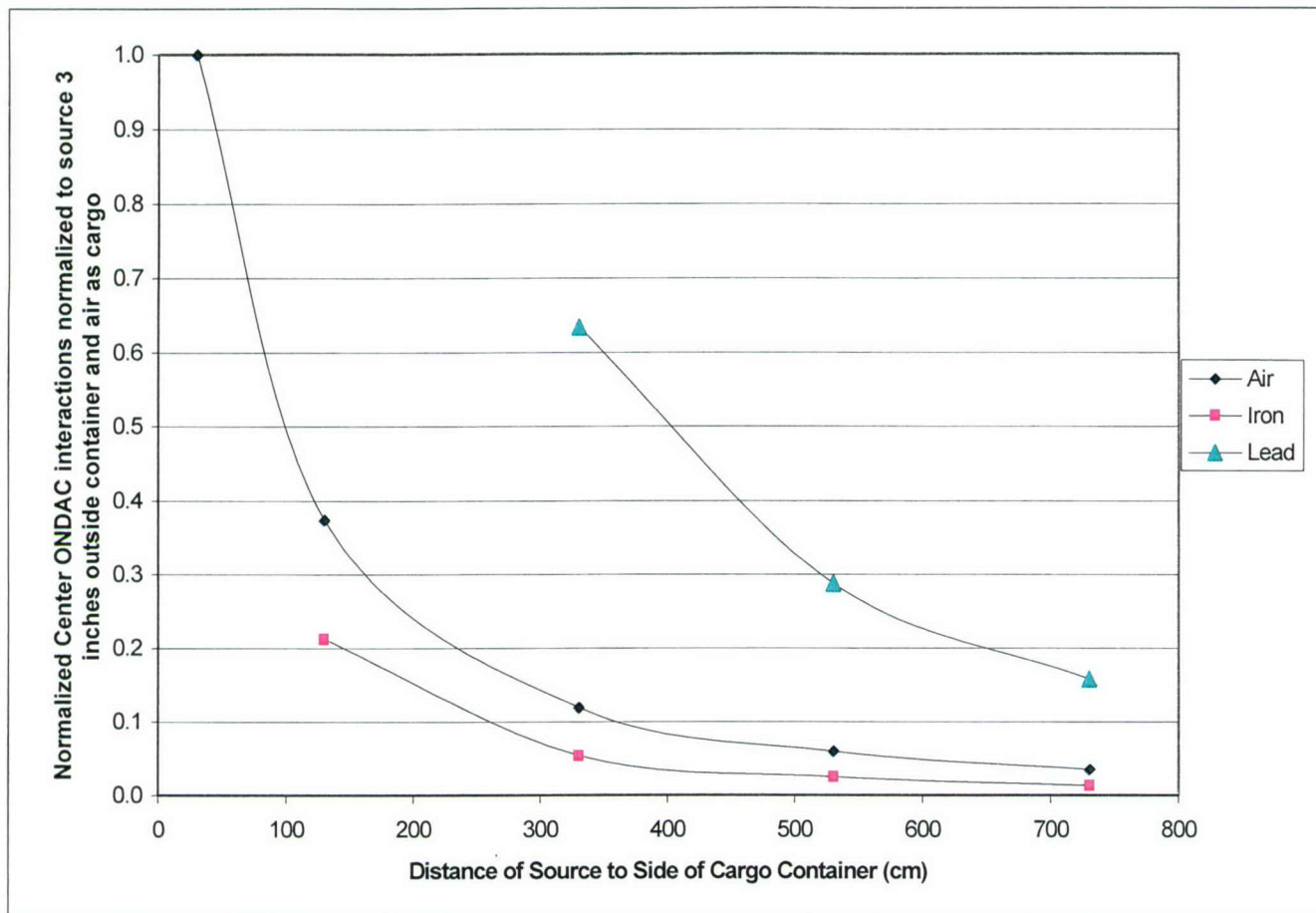


Figure 7-3. Normalized interactions in the center ONDAC detector with source 1 foot outside container for cargo materials air, iron, and lead as a function of source distance from side of container.

7.5 CONCLUSIONS.

As the distance of the source to the side of the cargo container is increased, the ability of the system to detect the presence or absence of HEU becomes more difficult. However, this effect can be compensated for by increasing the pulsed neutron source strength to 10^{14} n/sec. While scientists at LLNL believe it is technically possible to build such a 10^{14} n/sec source (Ka-Ngo 2002), this most likely would be the upper limit for the foreseeable future of this technology. Undoubtedly years of significant research time and funding would be required to accomplish this technical feat. Thus, it was concluded that the maximum distance away from the container this technique could reasonably be applied and still be successful to detect 1 kg of HEU is 24 feet, but this would require significant development costs. In practice, these results imply that the neutron stimulation source must be placed within several feet of the cargo container to be effective.

SECTION 8

CARGO ACTIVATION

In this section a methodology to assess cargo activation from the pulsed 14 MeV neutron source is presented. This analysis is necessary in order to determine the time that a cargo container must be retained before being released to the public due to induced activity from the neutron irradiation. Sub-section 8.1.1 discusses the major assumptions made in the analysis. Then sub-section 8.1.2 describes how the saturated activity was developed for a given cargo material. Sub-section 8.1.3 develops the activity during the pulsing and decay phase of each cycle, while section 8.1.4 analyses the effect of the average distance assumption used in the methodology. Then, section 8.2 provides the details of the activity calculation if iron, aluminum, or lead is the cargo material. Section 8.3 discusses the holding time for each material covered in section 8.2 based on that material decaying 10 half-lives, which is one governmental criterion for material release. Section 8.4 develops holding times to meet government regulations based on experimental data for these and other materials to reach background levels. Finally, conclusions drawn from this study are given in section 8.5.

8.1 METHODOLOGY.

8.1.1 Assumptions.

There are several assumptions that have been made to develop a methodology to find the amount of activity after a certain time period. The first is the assumption that the cargo container used has the same physical specifications as the USNA benchmark facility, (20' x 8' x 8' with 80 cargo drums). Second, all cargo drums are assumed to hold the same cargo material. Third, the examination process is completed in 302.4 sec, with a total of 48 cycles as recommended in section 4.7. The recommended operational times during the examination period are repeated here for convenience and given in table 8-1.

Table 8-1. Recommended times during the examination period.

Parameter	Value
Total examination period (48 cycles)	302.4 sec
Pulse time per cycle	2.9 sec
Count time per cycle	2.9 sec
Dissipation time per cycle	0.25 sec
Transit time between cycles	0.25 sec
Total number of cycles	48

The irradiation time in each cycle is 2.9 seconds as seen in table 8-1. The decay time however, is assumed to include any time that material is not irradiated. Therefore the decay time in a cycle includes the count time of 2.9 seconds, the dissipation time of 0.25 seconds, and the transit time between cycles, also 0.25 seconds. Thus, the total decay time in each cycle is 3.4 seconds. Fourth, the methodology also assumes that the neutron source is a 14 MeV neutron source with a source strength of 10^{12} neutrons/sec located one foot (30.5 cm) outside the container. The methodology also neglects neutron moderation in the cargo container from air and the container itself. If it were not neglected, the neutrons would lose energy through elastic and inelastic scattering collisions, which would greatly increase the complexity of the analysis.

8.1.2 Saturated Activity.

The saturated activity is the maximum activity that cargo can have. With the above assumptions, the saturated activity was found using the cargo material 14 MeV cross section and simply adjusting the neutron flux for distance from the source. To find the amount of activity that is present in a cargo container this activity must be found for each isotope in the cargo material in order that the total activity of the material can be determined. The saturated activity for the j^{th} reaction in the i^{th} isotope can be found from equation (8.1) (LaMarsh, 2001).

$$A_{\infty ij} = \frac{\Sigma_{aij} \phi V}{3.7 \times 10^{10}} \quad (8.1)$$

where

$A_{\infty ij}$	=	saturated activity of the j^{th} reaction of the i^{th} isotope, curies
Σ_{aij}	=	absorption macroscopic cross section for the j^{th} reaction of the i^{th} isotope, cm^{-1}
ϕ	=	neutron flux, neutrons/ cm^2 -sec
V	=	cargo volume in container, $2.84 \times 10^7 \text{ cm}^3$
3.7×10^{10}	=	conversion factor from disintegrations/sec to Curies

The macroscopic absorption cross section was found through equation (8.2).

$$\Sigma_{aij} = N_i \sigma_{aij} \quad (8.2)$$

where

N_i	=	i^{th} atom isotope density of material, 10^{24} atoms/ cm^3
σ_{aij}	=	microscopic absorption cross section for j^{th} reaction of isotope i , barns

The i^{th} atom isotope density of each material in equation (8.2) is needed because each isotope of the cargo material has different

microscopic absorption reaction cross-sections that will affect its saturated activity. It is found in equation (8.3) as follows.

$$N_i = \frac{f_i \rho N_{AV}}{A} \quad (8.3)$$

where

- f_i = Atom fraction of isotope i
- ρ = Material density, g/cm³
- N_{AV} = 10^{-24} times Avogadro's number, 0.6023 atoms/mole
- A = Atomic weight of material, g/mole

A data table is shown in table 8-2 for the cargo material iron which contains reaction information that occurs when its naturally occurring isotopes are bombarded with 14 MeV neutrons. Iron is composed of four isotopes, each having several reactions that occur when it is activated by 14 MeV neutrons. The table shows the four natural isotopes of iron, their atom fraction, the reactions that occur when it activated by neutrons, each reactions half-life and decay constant, and the microscopic cross section for absorption at 14 MeV for each reaction.

Table 8-2. Data table of natural isotopes of iron that shows their atom fractions, atomic numbers, neutron activated reactions, the reaction's half-life, decay constant, and the 14 MeV microscopic cross sections for absorption.

Natural Isotopes	Isotope Atom Fraction	Isotope Atomic Weight	Reactions	Half-life	Decay Constant (sec ⁻¹)	Microscopic Cross Section for Absorption at 14 MeV (barns)
Fe-54	0.0580	54	(n,p) Mn-54	312.5 days	2.57E-08	0.310
		54	(n,a) Cr-51	27.71 days	2.90E-07	0.098
		54	(n,2n) Fe-53	2.53 min	4.57E-03	0.001
		54	(n,2n) Fe-53	8.53 min	1.35E-03	0.016
Fe-56	0.9170	56	(n,p) Mn-56	2.582 hours	7.46E-05	0.103
		56	(n,2n) Fe-55	2.7 years	8.14E-09	0.440
Fe-57	0.0219	57	(n,p) Mn-57	1.59 min	7.27E-03	0.075
		57	(n,2n) Fe-56	Stable		
Fe-58	0.0031	58	(n,p) Mn-58	3 sec	2.31E-01	0.023
		58	(n,a) Cr-55	3.56 min	3.25E-03	0.022
		58	(n,2n) Fe-57	stable		

Table 8-3 shows similar information for aluminum. Aluminum however only has one natural isotope, Al-27. The data table does not show the atom fractions or the atomic numbers for Al-27 since they are all the same.

Table 8-3. Data table for aluminum which shows the neutron activated reactions, the reaction's half-life, the decay constant, and the 14 MeV microscopic cross sections for absorption.

Natural Isotopes	Reactions	Half-life	Decay Constant (sec ⁻¹)	Microscopic Cross Section for Absorption at 14 MeV (barns)
Al-27	(n,p) Mg-27	9.45 min	1.22E-03	0.075
	(n,a) Na-24	20.1 msec	3.45E+01	0.065
	(n,a) Na-24	15.02 hours	1.28E-05	0.116
	(n,2n) Al-26	6.35 sec	1.09E-01	1.70E-04

Table 8-4 shows the same information for lead as in tables 8-2 and 8-3 for iron and aluminum. Lead has four natural isotopes; however one neutron-activated reaction with Pb²⁰⁷ is stable. The table shows the four natural isotopes of lead, their atom fraction, the reactions that occur when it activated by neutrons, each reaction's half-life and decay constant, and the microscopic cross section for absorption at 14 MeV for each reaction.

Table 8-4. Data table of natural isotopes of lead that shows their atom fractions, atomic numbers, neutron activated reactions, the reaction's half-life, decay constant, and the 14 MeV microscopic cross sections for absorption.

Natural Isotopes	Isotope Atom Fraction	Isotope Atomic Weight	Reactions	Half-life	Decay Constant (sec ⁻¹)	Microscopic Cross Section for Absorption At 14 MeV (barns)
Pb-204	0.014	204	(n,2n) Pb-203	6.2 sec	1.12E-01	1.20
		204	(n,2n) Pb-203	52.1 hours	3.70E-06	1.74
Pb-206	0.241	206	(n,a) Hg-203	46.6 days	1.72E-07	2.70E-03
		206	(n,2n) Pb-205	5.1 msec	1.36E+02	1.10
		206	(n,2n) Pb-205	1.4E7 years	1.57E-15	1.92
Pb-207	0.221	207	(n,2n) Pb-206	Stable		
Pb-208	0.524	208	(n,p) Tl-208	3.054 min	3.78E-03	4.60E-04
		208	(n,a) Hg-205	5.2 min	2.22E-03	1.58E-03
		208	(n,2n) Pb-207	800 msec	8.66E-01	1.63
		208	(n,2n) Pb-207	stable		

The neutron flux was taken to be the same for each cargo material because of the assumption that there was no neutron moderation in the container. This flux can be found at any location within the container from equation (8.4).

$$\phi = \frac{S}{4\pi r_k^2} \quad (8.4)$$

where

S = source strength, 10^{12} neutrons/sec
 r_k = distance between the source and the k^{th} cargo drum

Since the cargo occupies a large area in the cargo container, the distance between the source and cargo could not be simplified to a single number without further approximations. With 80 cargo drums in different positions as shown in figure 8-1, an exact calculation would be very complicated. A cutaway of the benchmark facility is shown to refresh the reader on the layout of the USNA MCNP cargo container model. The location of the neutron source is also not shown, however it is located on the backside of the cargo container, directly in the center.

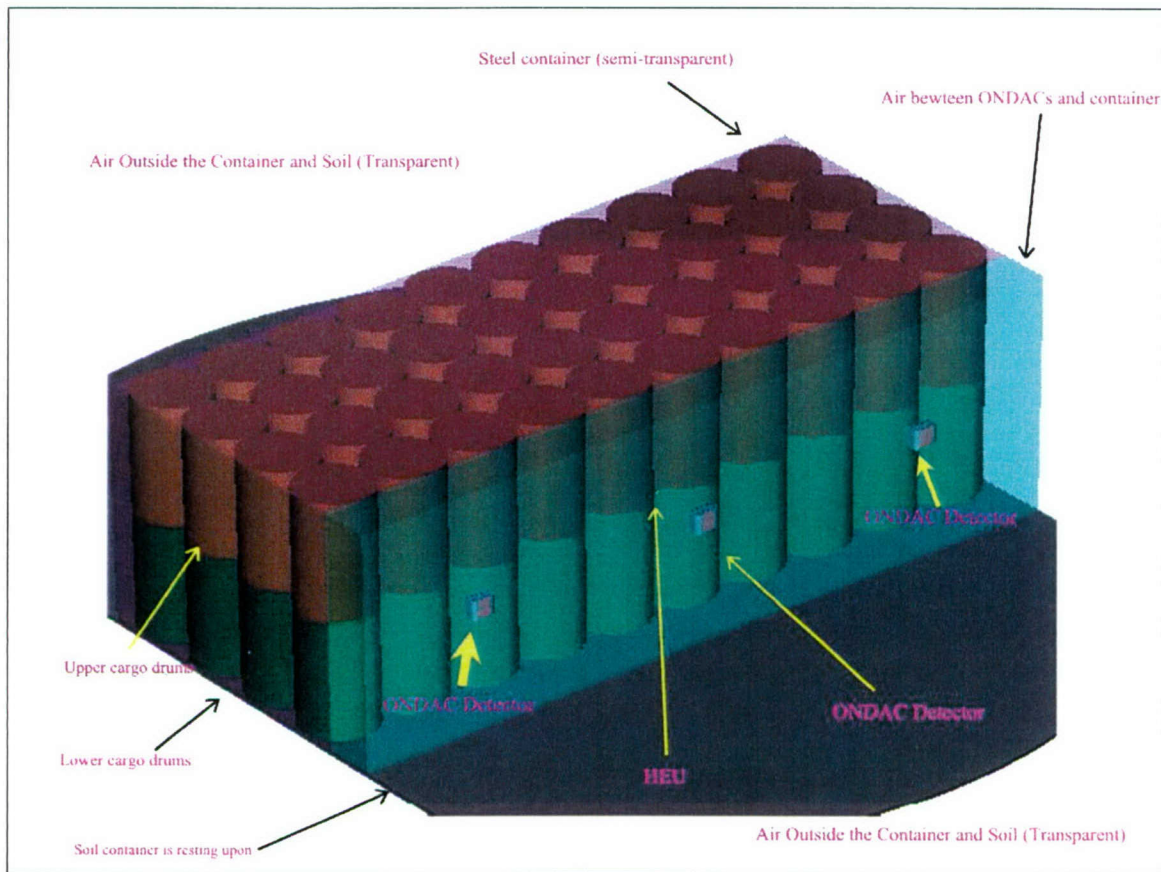


Figure 8-1. SABRINA representation of benchmark facility. Shown are the 80 cargo drums, three ONDAC detectors, 1kg HEU sphere, and soil. The container wall has been made transparent. Not shown is the location of the neutron source.

Using the geometrical layout as used in the MCNP code of the USNA model, which specifies the exact location of the source and cargo drums, the distance between the source and the cargo drums was calculated for each of the four rows shown in figure 8-1 and then

averaged. The result of the calculation yielded an average distance of 230 cm from the source to the cargo drums. The details of this calculation are included in Appendix B. With the average distance concept, the neutron flux was calculated as:

$$\phi = \frac{S}{4\pi\bar{r}^2} \quad (8.5)$$

where \bar{r} = average distance traveled by neutron from source to cargo, 230 cm

Using an average distance of 230 cm and a source strength of 10^{12} neutrons/sec, equation (8.5) yields a flux of 1.51×10^6 neutrons/cm²-sec.

The cargo volume in equation (8.1) was found by assuming each cargo drum was filled to its capacity. Since each drum is cylindrical with a 4 ft height and a 1 ft radius and there are 80 cargo drums in the cargo container, the total volume was determined to be 2.84×10^7 cm³.

Table 8-5 summarizes the major parameters used in finding the saturated activity. These values were assumed to remain constant regardless of the type of cargo being carried.

Table 8-5. Parameters and values used to find the saturated activity.

Parameter	Value
Average Distance	230 cm
Source Strength	10^{12} neutrons/sec
Flux	1.51×10^6 neutrons/cm ² - sec
Cargo Volume	2.84×10^7 cm ³

The saturated activity for each cargo material will be different depending on the material's nuclear cross sections. Table 8-6 shows the saturated activity for each of isotope reactions in iron expressed in both disintegrations/sec and Curies (1 Curie = 3.7×10^{10} disintegrations/sec).

Table 8-6. Saturated activity for each of iron's isotopes reactions. Also included is the 14 MeV macroscopic cross section for absorption.

Natural Isotopes	Atom Fraction	Reactions	Microscopic Cross Section For Absorption At 14 MeV Barns	Atom Isotope Density Atoms/cm ³	Macroscopic Cross Section For Absorption cm ⁻¹	Saturated Activity dis/sec	Saturated Activity Curies
Fe-54	0.0580	(n,p) Mn-54	0.310	5.09E-03	1.58E-03	6.75E+10	1.82E+00
		(n,a) Cr-51	0.098	5.09E-03	4.99E-04	2.13E+10	5.76E-01
		(n,2n) Fe-53	0.001	5.09E-03	4.28E-06	1.83E+08	4.94E-03
		(n,2n) Fe-53	0.016	5.09E-03	7.89E-05	3.37E+09	9.12E-02
Fe-56	0.9170	(n,p) Mn-56	0.103	7.76E-02	8.00E-03	3.42E+11	9.24E+00
		(n,2n) Fe-55	0.440	7.76E-02	3.42E-02	1.46E+12	3.95E+01
Fe-57	0.0219	(n,p) Mn-57	0.075	1.82E-03	1.37E-04	5.84E+09	1.58E-01
		(n,2n) Fe-56	Stable	1.82E-03		0	0
Fe-58	0.0031	(n,p) Mn-58	0.023	2.53E-04	5.83E-06	2.49E+08	6.73E-03
		(n,a) Cr-55	0.022	2.53E-04	5.45E-06	2.33E+08	6.29E-03
		(n,2n) Fe-57	Stable	2.53E-04		0	0

Table 8-7 shows the saturated activity for each of aluminum's neutron activation reactions.

Table 8-7. Saturated activity for the neutron activated reactions of Al²⁷. Also included is the data needed to determine the 14 MeV macroscopic cross section for absorption.

Natural Isotopes	Reactions	Microscopic Cross Section For Absorption At 14 MeV Barns	Atom Isotope Density Atoms/cm ³	Macroscopic Cross Section For Absorption cm ⁻¹	Saturated Activity dis/sec	Saturated Activity Curies
Al-27	(n,p) Mg-27	0.075	6.02E-02	4.52E-03	1.93E+11	5.23E+00
	(n,a) Na-24	0.065	6.02E-02	3.91E-03	1.68E+11	4.53E+00
	(n,a) Na-24	0.116	6.02E-02	6.98E-03	2.99E+11	8.09E+00
	(n,2n) Al-26	1.70E-04	6.02E-02	1.02E-05	4.39E+08	1.19E-02

Table 8-8 shows the saturated activity for lead's neutron activation reactions.

Table 8-8. Saturated activity for each of lead's isotopes reactions. Also included is the data needed to determine the 14 MeV macroscopic cross section for absorption.

Natural Isotopes	Atom Fraction	Reactions	Microscopic Cross Section For Absorption At 14 MeV Barns	Atom Isotope Density Atoms/cm ³	Macroscopic Cross Section For Absorption cm ⁻¹	Saturated Activity dis/sec	Saturated Activity Curies
Pb-204	0.014	(n,2n) Pb-203	1.2	4.69E-04	5.63E-04	2.41E+10	6.51E-01
		(n,2n) Pb-203	1.74	4.69E-04	8.16E-04	3.49E+10	9.44E-01
Pb-206	0.241	(n,a) Hg-203	2.70E-03	4.64E-04	1.25E-06	5.37E+07	1.45E-03
		(n,2n) Pb-205	1.1	4.64E-04	5.11E-04	2.19E+10	5.91E-01
		(n,2n) Pb-205	1.92	4.64E-04	8.91E-04	3.82E+10	1.03E+00
Pb-207	0.221	(n,2n) Pb-206	Stable			0	0
Pb-208	0.524	(n,p) Tl-208	4.60E-04	4.60E-04	2.12E-07	9.06E+06	2.45E-04
		(n,a) Hg-205	1.58E-03	4.60E-04	7.26E-07	3.11E+07	8.41E-04
		(n,2n) Pb-207	1.63	4.60E-04	7.49E-04	3.21E+10	8.68E-01
		(n,2n) Pb-207	Stable			0	0

8.1.3 Activity During Pulsing and Decay Phase of Each Cycle.

During the examination period, a pulse is applied for 2.9 sec and then the ONDAC output (see table 8-1) is counted for 3.4 sec. This occurs continuously for 48 cycles. While the pulse is being applied, the activity increases with the relationship given by equation (8.6) in the first cycle of irradiation.

(8.6)

where $\alpha_1 = A_{\infty ij}(1 - e^{-\lambda_{ij}t_e})$

α_1 = activity after irradiation in first cycle, Curies

$A_{\infty ij}$ = saturated activity of the ith isotope's jth reaction, Curies

λ_{ij} = decay constant of the ith isotope's jth reaction, sec⁻¹

t_e = exposure time during pulse, 2.9 sec

The cargo is allowed to decay for a time of 3.4 seconds. During this time, the activity decreases exponentially. The exact relationship that defines the decay in the first cycle is shown in equation (8.7).

$$\alpha_{1d} = \alpha_1(e^{-\lambda_{ij}t_d}) \quad (8.7)$$

where

α_{1d} = activity after first cycle irradiation and decay, Curies

α_1 = activity after first cycle irradiation, Curies

λ_{ij} = decay constant of the ith isotope's jth reaction, sec⁻¹

t_d = decay time between pulses, 3.4 sec

After the first cycle is completed, the activity after irradiation takes on a slightly different relationship. It still has an exponential build-up component that is shown in equation (8.6). However, the activity acquired from the previous cycles will continue to decay during the neutron pulse, which adds another term in the activity calculation. The equation describing this relationship for the second cycle is (8.8).

$$\alpha_2 = A_{\infty ij}(1 - e^{-\lambda_{ij}t_e}) + \alpha_{1d}(e^{-\lambda_{ij}t_e}) \quad (8.8)$$

where

α_2 = activity after irradiation of the second cycle, Curies
 $A_{\infty ij}$ = saturated activity of the i th isotope's j th reaction, Curies
 α_{1d} = activity after irradiation and decay of first cycle, Curies
 λ_{ij} = decay constant of the i th isotope's j th reaction, sec^{-1}
 t_e = exposure time during pulse, 2.9 sec

The second cycle establishes the pattern that prevails during the remainder of the 48 cycles of the examination period. It is noted that the first term of equation (8.8) is always α_1 while the second term is the activity after decay at the end of the previous cycle. For the n^{th} cycle, the activity can be found by equations (8.9), (8.10), and (8.11).

$$\alpha_n = A_{\infty ij}(1 - e^{-\lambda_{ij}t_e}) + \alpha_{(n-1)d}e^{-\lambda_{ij}t_e} \quad (8.9)$$

where

$$\alpha_{(n-1)d} = \alpha_{(n-1)}(e^{-\lambda_{ij}t_d}) \quad (8.10)$$

$$\alpha_{(n-1)} = A_{\infty ij}(1 - e^{-\lambda_{ij}t_e}) + \alpha_{(n-2)d}e^{-\lambda_{ij}t_e} \quad (8.11)$$

8.1.4 Effect of Average Distance Assumption on Flux.

The average distance was used to calculate the flux as given by equation (8.5). An analysis was conducted to determine the effect that this approximation introduced compared to a more detailed calculation. This subsection evaluates how a detailed approach would compare with an approach using a single average distance. With 20 numbers representing different positions, each position would have a weight of 0.05. The formula used to estimate the effect by the average distance procedure in percent is given by equation (8.12).

$$\begin{array}{l} \text{Estimated effect} \\ \text{in average} \\ \text{distance procedure} \end{array} = \frac{\sum_{i=1}^{20} \frac{wt}{r^2}}{\frac{1}{\bar{r}^2}} \times 100 \quad (8.12)$$

where

\bar{r} = Average distance from source to cargo drums, 230 cm
 wt = Weight of each position, (20 positions) 0.05
 r = Straight-line distance from the source to each cargo drum, cm

$\sum_{i=1}^{20}$ = Summation over 20 positions

Table 8-9 contains the data to evaluate equation 8.12.

Table 8-9. Data for estimating effect in average distance procedure between cargo drums and the source.

Row Position	Distance from Source to Cargo Drum (r) (cm)	Distance Representing Four Cargo Drums of the Same Distance (4r) (cm)	$\frac{1}{r^2}$ (cm ⁻²)	Weight	$\frac{wt}{r^2}$
1a	281.3	1125.3	7.90E-07	0.05	3.95E-08
1b	222.2	888.88	1.27E-06	0.05	6.33E-08
1c	164.5	657.95	2.31E-06	0.05	1.16E-07
1d	110.3	441.3	5.13E-06	0.05	2.57E-07
1e	68.8	275.09	1.32E-05	0.05	6.61E-07
2a	300.7	1202.6	6.91E-07	0.05	3.46E-08
2b	246.2	984.87	1.03E-06	0.05	5.15E-08
2c	195.7	782.78	1.63E-06	0.05	8.16E-08
2d	153.0	612.05	2.67E-06	0.05	1.33E-07
2e	126.4	505.5	3.91E-06	0.05	1.96E-07
3a	330.3	1321.1	5.73E-07	0.05	2.87E-08
3b	281.6	1126.5	7.88E-07	0.05	3.94E-08
3c	238.7	954.82	1.10E-06	0.05	5.48E-08
3d	205.2	820.69	1.48E-06	0.05	7.42E-08
3e	186.2	744.62	1.80E-06	0.05	9.02E-08
4a	367.7	1470.8	4.62E-07	0.05	2.31E-08
4b	324.7	1298.8	5.93E-07	0.05	2.96E-08
4c	288.3	1153.1	7.52E-07	0.05	3.76E-08
4d	261.2	1044.8	9.16E-07	0.05	4.58E-08
4e	246.5	986.14	1.03E-06	0.05	5.14E-08
	TOTAL	18398			2.11E-06

The value of $\frac{1}{r^2}$ that was needed to evaluate the denominator in equation (8.12) is:

$$\frac{1}{r^2} = \frac{1}{(230 \text{ cm})^2} = 1.89\text{E-}05 \quad (8.13)$$

The $\sum_{i=1}^{20} \frac{wt}{r^2}$ term was found as 2.11E-06 as shown in table 8-9 in the "TOTAL" row. Inserting this value and equation (8.13) into equation (8.12) gave the result:

$$\begin{array}{l} \text{Estimated effect} \\ \text{in average} \\ \text{distance procedure} \end{array} = \frac{\sum_{i=1}^{20} \frac{wt}{r^2}}{\frac{1}{r^2}} \times 100 = 11.2\% \quad (8.14)$$

The effect therefore associated with using the average distance from the source to the cargo drums in equation (8.5) was determined to be 11.2%.

8.2 ACTIVITY DURING EXAMINATION PERIOD FOR IRON, ALUMINUM, AND LEAD.

In order to find the cumulative activity of the entire cargo container, it is necessary to add each of the individual reaction's activities together for each material. Table 8-10 shows the first ten cycles of irradiation and decay for iron. This table 8-10 has two rows for each cycle, the first being irradiation time, while the second is the decay time for that cycle. The second through the fourth column gives the amount of time that the cargo material has been exposed, the amount of time the material has decayed, and the total amount of time that has elapsed in seconds. In addition, table 8-10 shows the activity in Curies at the given time for each particular reaction listed in table 8-2 for each iron isotope. The particular reactions are listed horizontally at the top. The final column is total activity from the cargo material after a given time. It is noted that iron has two reactions as shown in table 8-2 that produce stable isotopes and hence they are not shown in table 8-10. Using the saturated activity and equations 8.6 thru 8.11, the activity during the examination period was calculated for iron, aluminum, and lead.

Table 8-10. Activity in Curies for iron during the first ten cycles of the examination period. The activity for each reaction listed in the table is shown in addition to the total activity in the last column, which is the sum of the individual activities at a given time.

Time (sec)				ACTIVITY IN Curies									
Cycle	Exposed	Decay	Total Elapsed	Fe-54 (n,p) Mn-54	Fe-54 (n,a) Cr-51	Fe-54 (n,2n) Fe-53	Fe-54 (n,2n) Fe-53	Fe-56 (n,p) Mn-56	Fe-56 (n,2n) Fe-55	Fe-57 (n,p) Mn-57	Fe-58 (n,p) Mn-58	Fe-58 (n,a) Cr-55	TOTAL
1	2.9	0	2.9	1.36E-07	4.84E-07	6.50E-05	3.57E-04	2.00E-03	9.31E-07	3.29E-03	3.29E-03	5.89E-05	9.06E-03
1	2.9	3.4	6.3	1.36E-07	4.84E-07	6.40E-05	3.56E-04	2.00E-03	9.31E-07	3.21E-03	1.50E-03	5.83E-05	7.18E-03
2	5.8	3.4	9.2	2.71E-07	9.68E-07	1.28E-04	7.12E-04	3.99E-03	1.86E-06	6.43E-03	4.05E-03	1.17E-04	1.54E-02
2	5.8	6.8	12.6	2.71E-07	9.68E-07	1.26E-04	7.08E-04	3.99E-03	1.86E-06	6.28E-03	1.85E-03	1.15E-04	1.31E-02
3	8.7	6.8	15.5	4.07E-07	1.45E-06	1.89E-04	1.06E-03	5.99E-03	2.79E-06	9.44E-03	4.23E-03	1.73E-04	2.11E-02
3	8.7	10.2	18.9	4.07E-07	1.45E-06	1.87E-04	1.06E-03	5.99E-03	2.79E-06	9.20E-03	1.93E-03	1.71E-04	1.85E-02
4	11.6	10.2	21.8	5.43E-07	1.94E-06	2.49E-04	1.41E-03	7.98E-03	3.73E-06	1.23E-02	4.27E-03	2.29E-04	2.65E-02
4	11.6	13.6	25.2	5.43E-07	1.94E-06	2.45E-04	1.40E-03	7.98E-03	3.73E-06	1.20E-02	1.95E-03	2.26E-04	2.38E-02
5	14.5	13.6	28.1	6.79E-07	2.42E-06	3.07E-04	1.76E-03	9.98E-03	4.66E-06	1.50E-02	4.28E-03	2.83E-04	3.17E-02
5	14.5	17	31.5	6.79E-07	2.42E-06	3.02E-04	1.75E-03	9.97E-03	4.66E-06	1.47E-02	1.95E-03	2.80E-04	2.89E-02
6	17.4	17	34.4	8.14E-07	2.90E-06	3.63E-04	2.10E-03	1.20E-02	5.59E-06	1.77E-02	4.29E-03	3.36E-04	3.67E-02
6	17.4	20.4	37.8	8.14E-07	2.90E-06	3.58E-04	2.09E-03	1.20E-02	5.59E-06	1.72E-02	1.95E-03	3.33E-04	3.39E-02
7	20.3	20.4	40.7	9.50E-07	3.39E-06	4.18E-04	2.44E-03	1.40E-02	6.52E-06	2.02E-02	4.29E-03	3.88E-04	4.17E-02
7	20.3	23.8	44.1	9.50E-07	3.39E-06	4.12E-04	2.43E-03	1.40E-02	6.52E-06	1.97E-02	1.95E-03	3.84E-04	3.88E-02
8	23.2	23.8	47	1.09E-06	3.87E-06	4.71E-04	2.78E-03	1.60E-02	7.45E-06	2.25E-02	4.29E-03	4.39E-04	4.65E-02
8	23.2	27.2	50.4	1.09E-06	3.87E-06	4.64E-04	2.76E-03	1.59E-02	7.45E-06	2.20E-02	1.95E-03	4.35E-04	4.36E-02
9	26.1	27.2	53.3	1.22E-06	4.36E-06	5.23E-04	3.11E-03	1.79E-02	8.38E-06	2.48E-02	4.29E-03	4.89E-04	5.12E-02
9	26.1	30.6	56.7	1.22E-06	4.36E-06	5.15E-04	3.09E-03	1.79E-02	8.38E-06	2.42E-02	1.95E-03	4.84E-04	4.82E-02
10	29	30.6	59.6	1.36E-06	4.84E-06	5.73E-04	3.44E-03	1.99E-02	9.31E-06	2.70E-02	4.29E-03	5.39E-04	5.58E-02
10	29	34	63	1.36E-06	4.84E-06	5.64E-04	3.42E-03	1.99E-02	9.31E-06	2.63E-02	1.95E-03	5.33E-04	5.28E-02

A graphical representation of the activity build-up in Curies during the pulsing examination period is shown in figure 8-2 for iron. This graph also lists the major assumptions on which this figure is based.

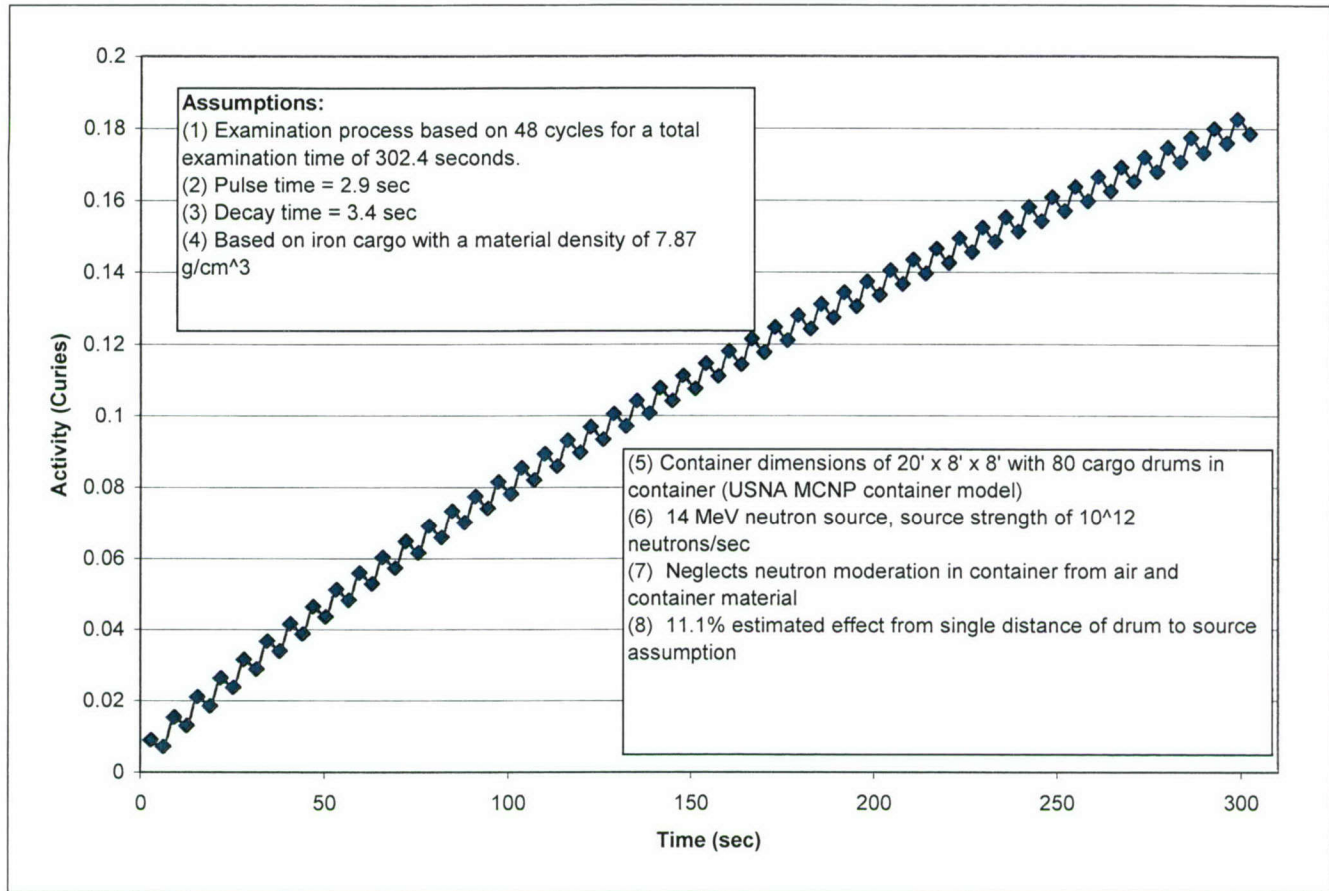


Figure 8-2. Activity versus time during the examination process with iron designated as the cargo material.

Figure 8-2 shows that the build-up of activity during the examination process in a cargo of iron essentially follows at a one minus the exponential function form which is a typical result of radioisotope production (LaMarsh, 2001). During the time of decay in each cycle, the activity decreases at an exponential rate. Moreover, the overall effect of the decay period is small for each cycle as can be seen in figure 8-2.

Aluminum and lead behaved differently than iron did during the examination period because of the presence of isotopes which have half-lives much smaller than the decay time. For example, as shown in table 8-3, aluminum undergoes a (n, α) reaction which produces Na-24 with a 20.1 msec half-life. As shown in table 8-4, irradiating lead produces short half-life isotopes (i.e. Pb²⁰⁵ with a half-life of 5.1 msec and Pb²⁰⁷ with a half-life of 800 msec). Using all of the same assumptions as were used in iron, the activity versus time during the examination period is shown in figure 8-3 for aluminum and

in figure 8-4 for lead. In figure 8-3 the material density of aluminum was taken to be 2.70 g/cm^3 and in figure 8-4 the material density of lead was taken to be 11.34 g/cm^3 .

Figure 8-3 shows that the activity of the aluminum during the examination period rises very slowly, but drops below 1 Curie during each cycle's decay time. Conversely, during the 2.9 seconds of irradiation time the activity increases rapidly to approximately 5 Curies. These two phenomena balance each other out to give a slow rise in activity over the examination period when the cargo material is aluminum.

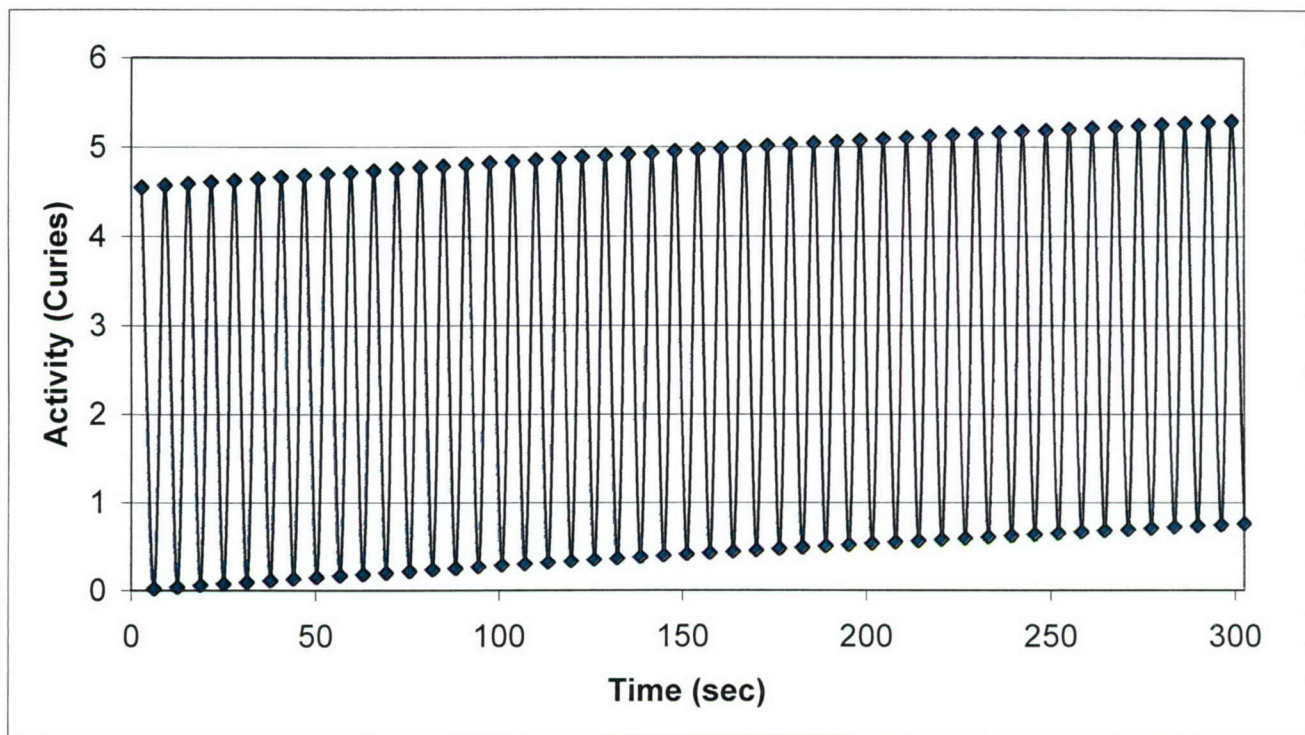


Figure 8-3. Activity versus time during the examination process with aluminum designated as the cargo material.

The activity as a function of time during the examination period for lead is similar in that it also oscillates between two extreme values of activity during the decay and irradiation times. Figure 8-4 shows that in the first few cycles, the activity will increase, but after approximately 50 seconds of examination, the activity oscillates between the two values of 1.75 Curies and 0.286 Curies.

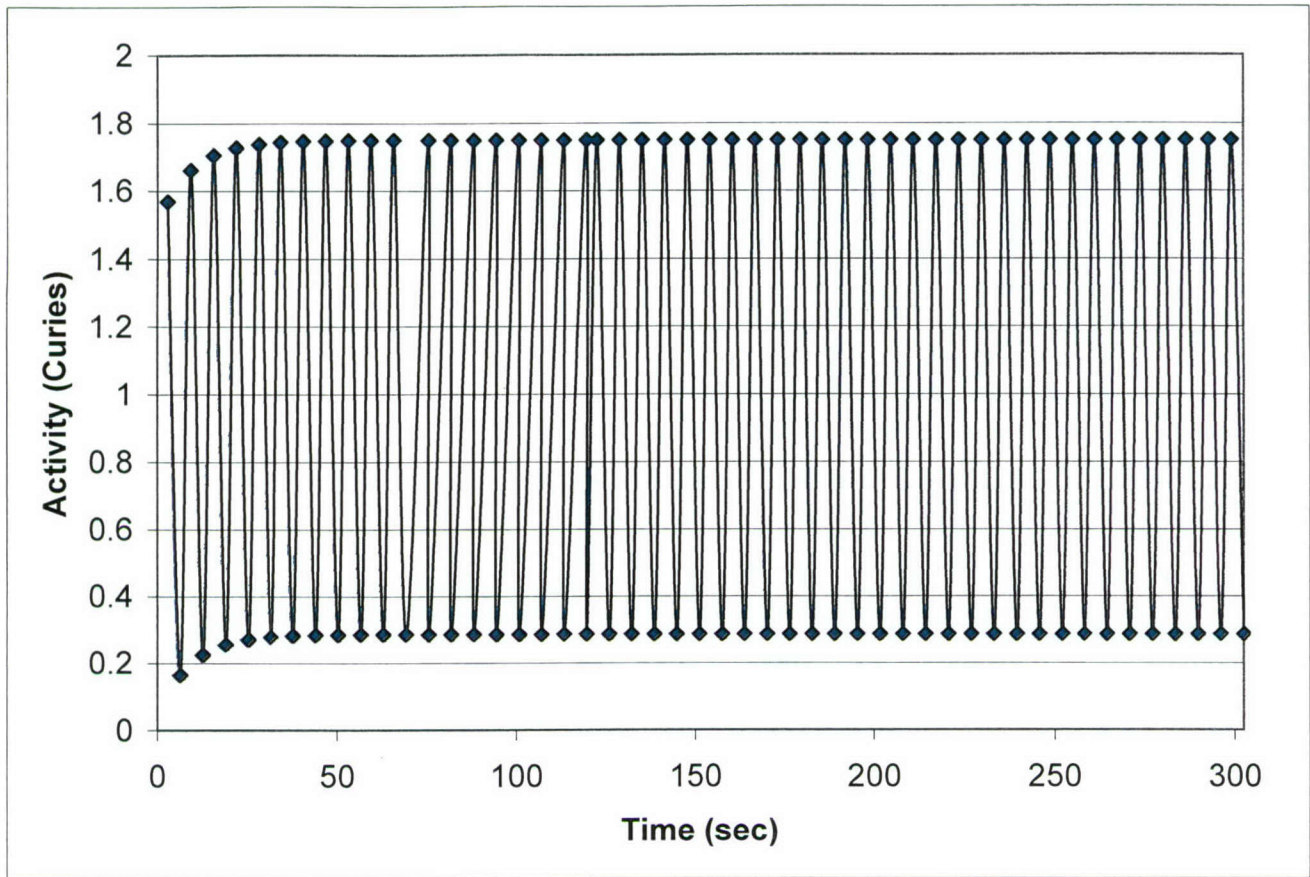


Figure 8-4. Activity versus time during the examination process with lead designated as the cargo material.

8.3 TIME FOR IRON, ALUMINUM, AND LEAD ACTIVITY TO DECREASE BY TEN HALF-LIVES TO MEET GOVERNMENT RELEASE REGULATIONS.

One requirement of accelerator produced activation isotopes is that the irradiated material must be held in storage, if it produces isotopes with physical half-lives of less than 120 days (Abkemeier, 2003). Since iron, aluminum, and lead all meet this condition, there will be a storage time for these materials. In addition, the irradiated material cannot be released to the public until the material can no longer be distinguished from background. As a rule of thumb, the cargo material should be indistinguishable from background after 10 half-lives (Abkemeier, 2003). Ten half-lives is approximately equal to reducing the activity by 1/1000 as seen below:

$$\left(\frac{1}{2}\right)^{10} = \frac{1}{1024} \approx \frac{1}{1000} \quad (8.15)$$

The remainder of this section calculates how long those three cargo materials would have to be held before their activity decreases by a factor of 1000. This investigation was carried out for iron, aluminum, and lead.

Iron cargo. After the examination period, the activity of iron is predicted to be 1.79×10^{-1} curies. Since $1/1000$ of that value must be obtained for it to decay 10 half lives, its activity must fall to 1.79×10^{-4} curies. A graph showing the activity of the iron cargo versus time during and after the examination period is shown in figure 8-5. It has been scaled to show the amount of time that it takes the activity to reach $1/1000$ of its initial activity after irradiation. As shown in figure 8-5, it will take approximately 1.67×10^6 seconds, which is approximately 19 days.

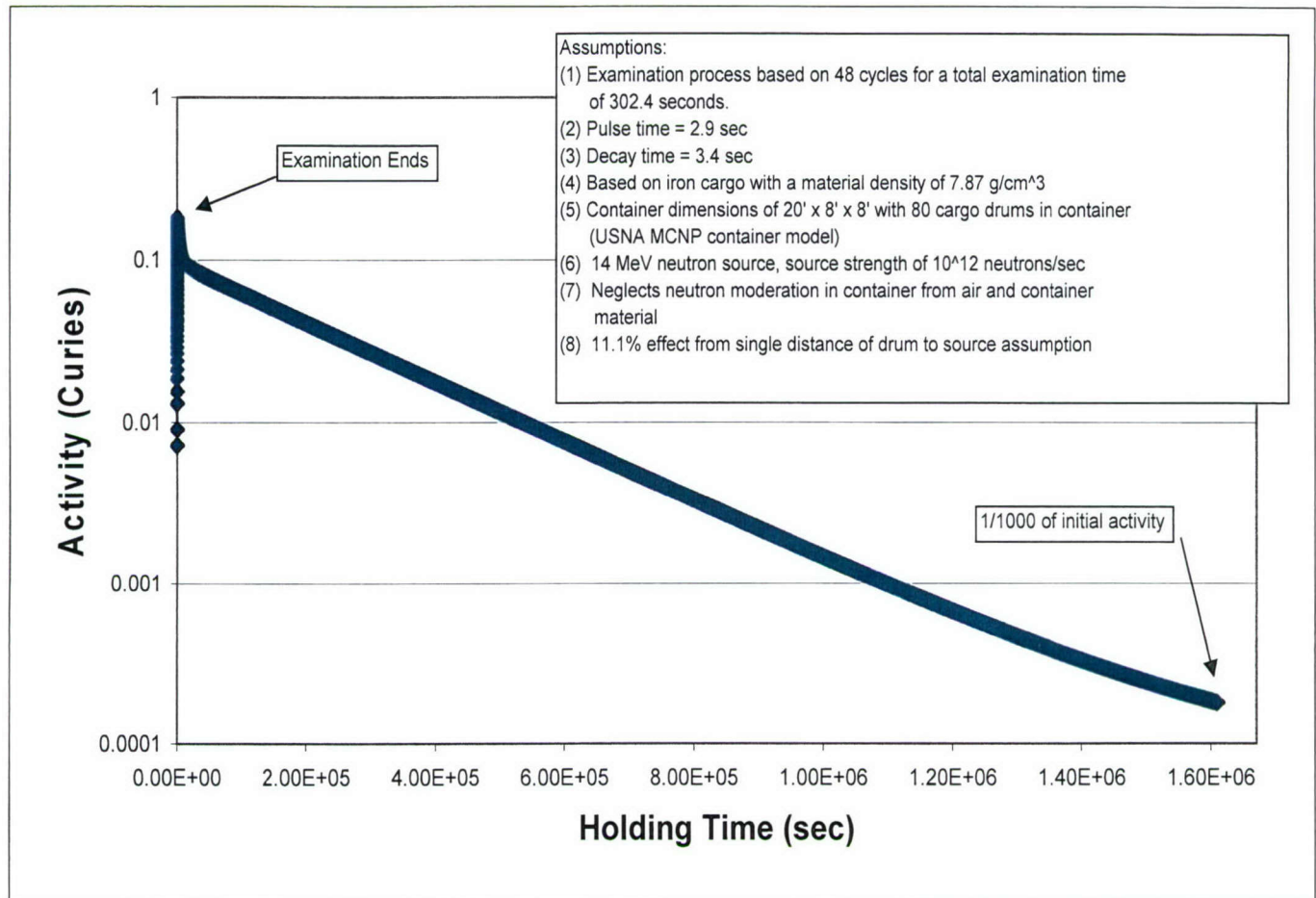


Figure 8-5. Activity versus holding time for iron cargo.

Aluminum cargo. Its activity after the 5 second irradiation is calculated to be 5.3 curies. Thus $1/1000^{\text{th}}$ of this value would yield an activity of 5.3×10^{-3} curies. Figure 8-6 shows a graph of the activity in aluminum cargo versus time. It shows that the cargo decay to a value of 5.3×10^{-3} curies after approximately 2.75×10^6 seconds. This is approximately 32 days. The same assumptions that were previously discussed, still apply for the aluminum cargo.

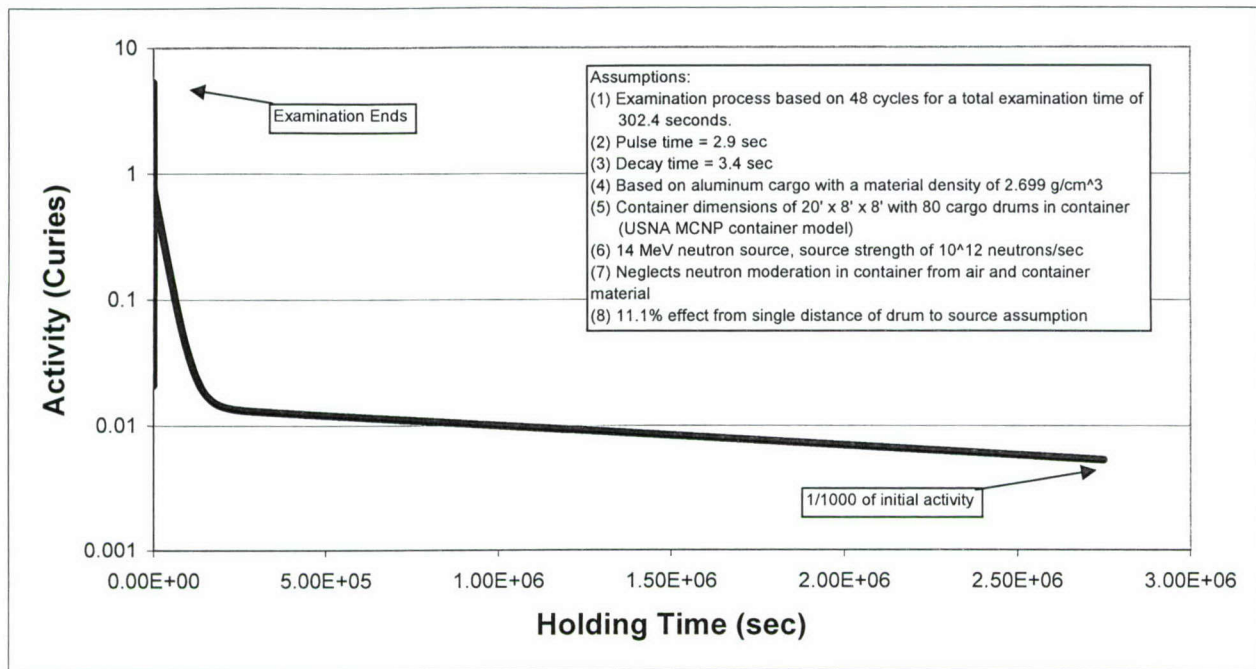


Figure 8-6. Activity versus holding time for aluminum cargo.

Lead cargo. Lead activity after the 5 second examination was calculated to be 1.75 curies. Ten half-lives of this activity is 1.75×10^{-3} curies. This occurs after only 54 seconds of decay time. This can be seen graphically in figure 8-7 by a very rapid drop-off rate of activity after the initial irradiation.

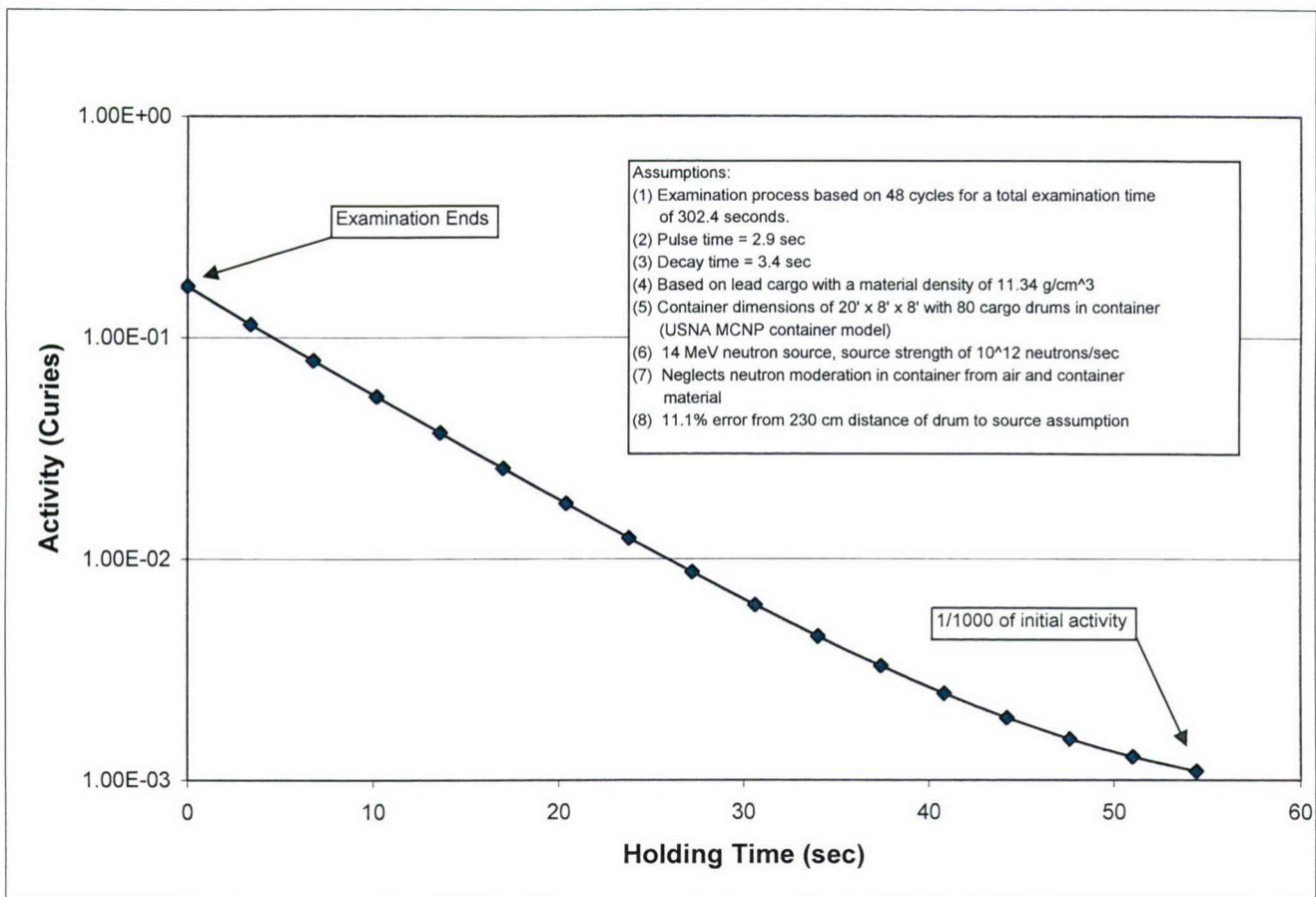


Figure 8-7. Activity in lead cargo versus holding time.

8.4 USNA IRRADIATION EXPERIMENT TO DETERMINE TIME IRON, ALUMINUM, LEAD, AND OTHER MATERIALS DECAY TO BACKGROUND.

In the field, cargo release would be based on inspectors with survey meters taking dose rate measurements. Government regulations indicate that cargo release would likely be granted when the container reached background radiation levels (Abkemeier, 2003). An experiment was then conducted using the USNA 14 MeV neutron generator to determine the time iron, lead, and aluminum would need to reach background readings. Latter experimental data was collected for a wide variety of other materials. In this experiment, samples of iron, aluminum, and lead were set at a fixed distance from the neutron generator target such that they would receive the same fluence as these materials would receive under the recommended examination conditions described in section 4.7. The set-up for this experiment is shown in figure 8-8.



Figure 8-8. Experimental set-up of the USNA irradiation experiment.

Figure 8-9 gives a closer examination of each of the samples of iron, aluminum, and lead.

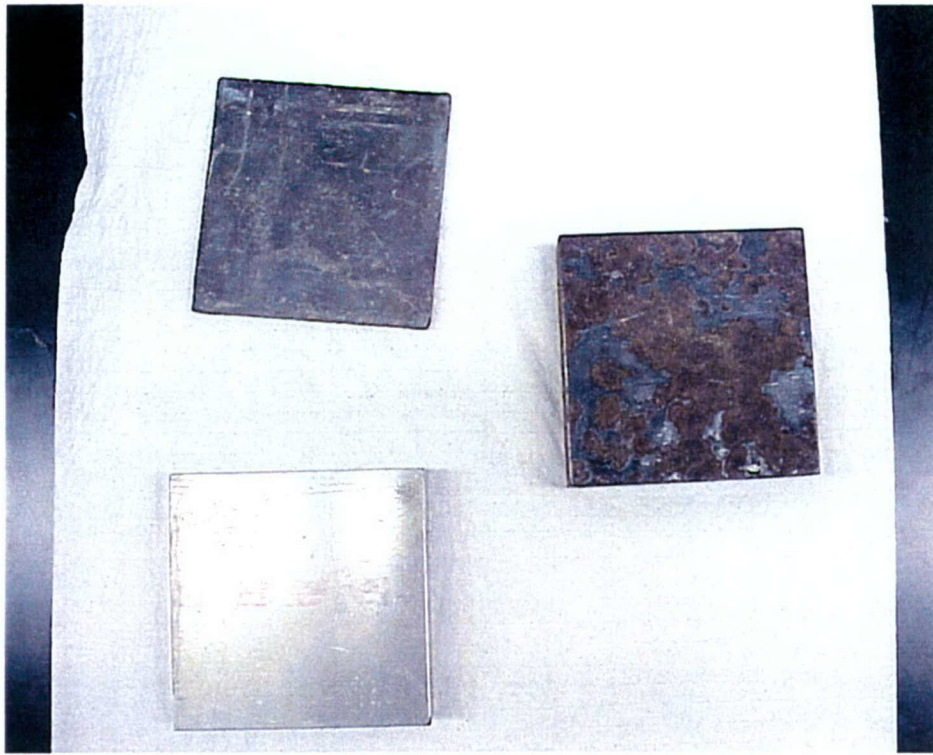


Figure 8-9. Sample of the iron, aluminum, and lead material irradiated in the USNA irradiation experiment.

The USNA neutron generator can only operate in continuous mode, so the effect of decay during each cycle couldn't be simulated. However, the effect of decay between cycles would reduce each material's radioactivity. Consequently, the test conditions would produce results that would overestimate the time a given material would need to reach background. The USNA neutron generator was operated at a constant source strength of 3×10^{10} neutrons/sec whereas the source strength of the neutron generator that is slated to be used in the benchmark facility is 1×10^{12} neutrons/sec. The equation for the flux (ϕ) from a point neutron source is given by equation (8.4) as:

$$\phi = \frac{S}{4\pi r_k^2} \quad (8.4)$$

where

S = source strength, 10^{12} neutrons/sec
 r_k = distance between the source and the k^{th} cargo drum

The experiment was conducted using a flux that would be received by the center of the cargo drum closest to the source. This drum center would be located 61.64 cm away from the source in the y-direction, and 30.5 cm away in the x-direction. Using Pythagorean's Theorem, the straight-line distance from the source to this drum was found by equation (8.16).

$$\text{distance between closest drum's center and source} = \sqrt{30.5^2 + 61.6^2} = 68.8 \text{ cm} \quad (8.16)$$

Next, the flux to this drum was calculated through equation (8.17) as:

$$\phi = \frac{10^{12} \text{ neutrons/sec}}{4\pi(68.8 \text{ cm})^2} = 1.68 \times 10^7 \frac{\text{neutrons}}{\text{cm}^2 \text{ sec}} \quad (8.17)$$

Hence all three materials were placed at the following distance from the generator's target:

$$r = \sqrt{\frac{S}{4\pi\phi}} = \sqrt{\frac{3 \times 10^{10}}{4\pi(1.68 \times 10^7)}} = 11.9 \text{ cm} \cong 12 \text{ cm} \quad (8.18)$$

Figure 8-10 illustrates the 12 cm distance between the neutron generator and the material sample. Each sample was then irradiated for 139.2 seconds, which corresponds to the recommended number of cycles and the pulse time per cycle (see table 8-1). Hence, the total neutron fluence delivered to these materials was $2.34 \times 10^9 \text{ n/cm}^2$.

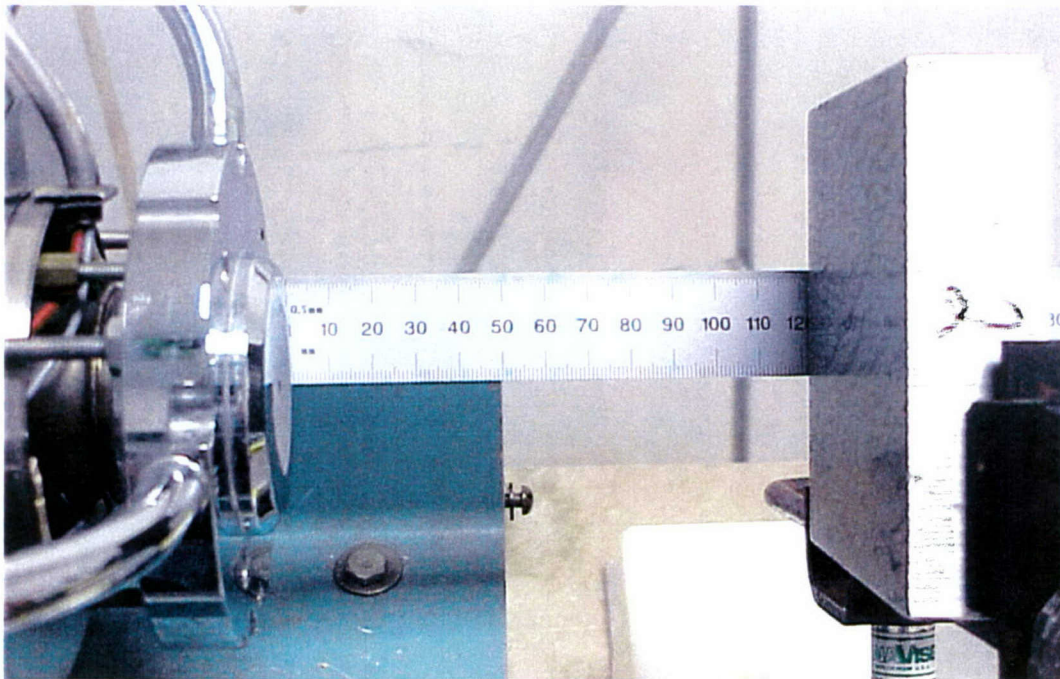


Figure 8-10. 12 cm distance between the neutron generator and the material sample.

In order to produce a neutron yield of 3×10^{10} neutrons/sec from the generator, it was operated with an accelerator voltage of 140 kV and

ion source current of 3 mA. The dose rate following exposure was measured with a calibrated AN-PDQ-1 survey meter with a DT-680 probe with its beta window open. When operated in this mode, the survey meter is sensitive to both beta and gamma radiation emitted by the sample. Figure 8-11 shows a picture of this equipment.

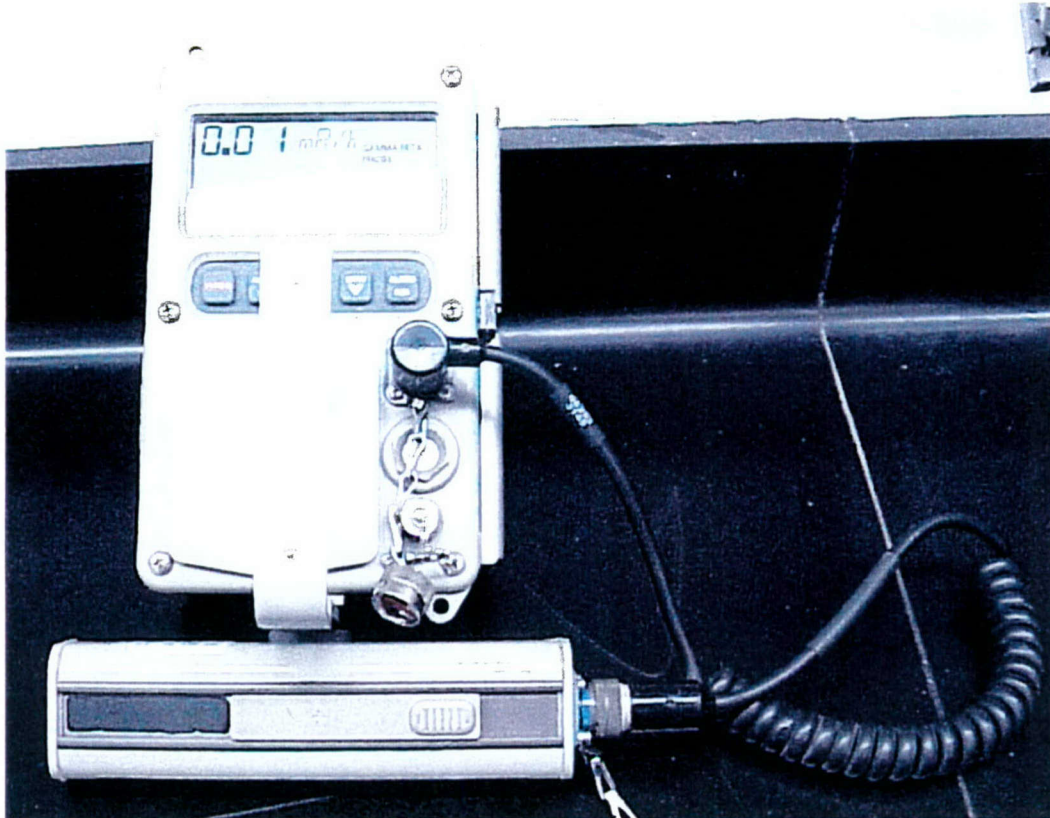


Figure 8-11. Picture of the AN-PDQ-1 with DT-680 probe used to monitor the activity of iron, aluminum, and lead samples during the USNA irradiation experiment.

Background measurements were taken prior to the irradiation of each material and determined to be 0.01 milliRoentgens/hr (mR/hr). Then the specimens were irradiated and the time recorded for each material to return to the background dose rate of 0.01 mR/hr. Each specimen was weighed and its mass is given in table 8-11 below.

Table 8-11. Mass of each specimen used in USNA irradiation experiment.

Material	Mass (kg)
Aluminum	0.745
Iron	2.085
Lead	0.775

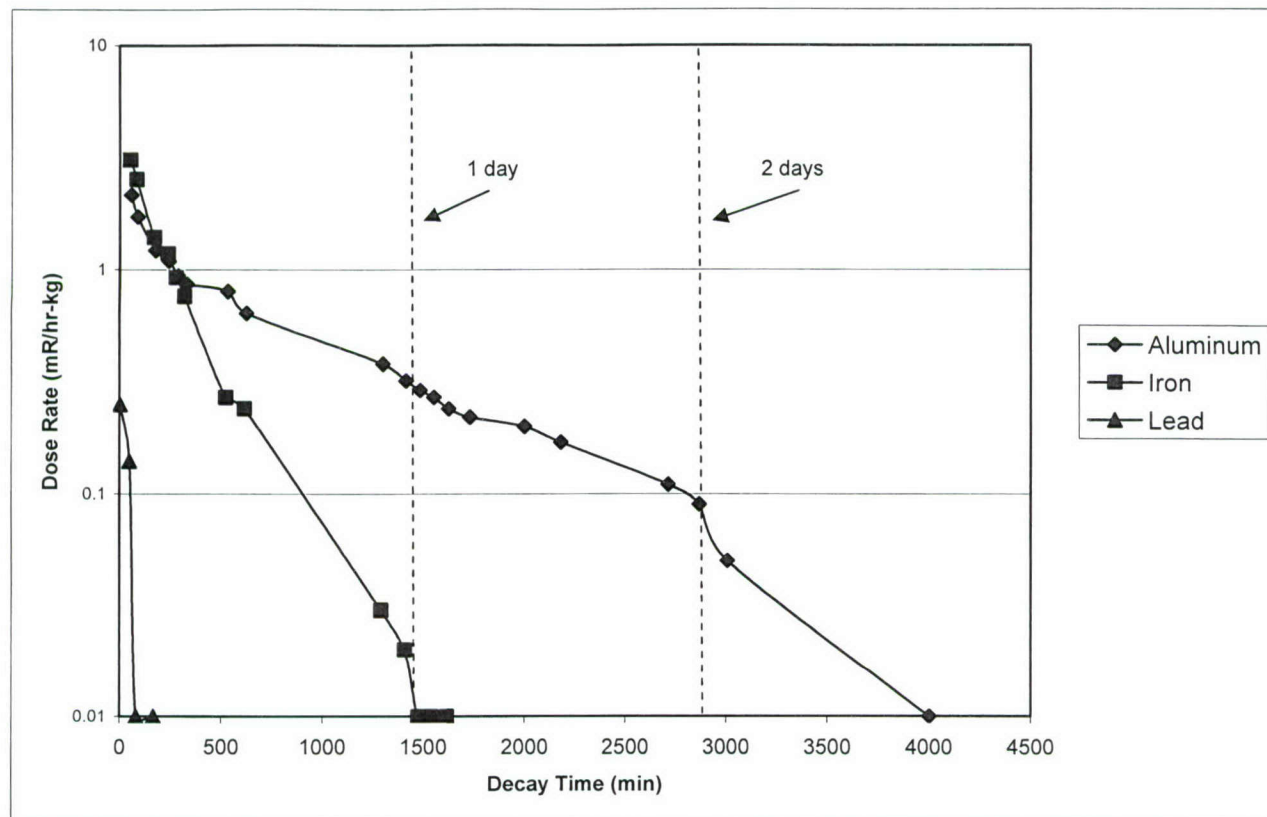


Figure 8-12. Dose rate per kilogram of aluminum, iron, and lead after irradiation.

Figure 8-12 shows the dose decay rate for each material expressed in units of mR/hr-kg. As can be seen in figure 8-12, lead was the first material to return to background and this occurred in 60 minutes. The next material to reach background was iron, which occurred in 1250 minutes (approximately 21 hours). The last material to reach background was aluminum and this occurred in 4000 minutes (50 hours).

Table 8-12 is a summary of the results from the theoretical activity to decay 10 half-lives performed in section 8.3 and the experimental results to reach background obtained with the USNA neutron generator and a survey material for each material.

Table 8-12. Summary of theoretical and experimental 14 MeV neutron activation study for aluminum, iron, and lead.

Material	Theoretical Time for activity to decrease by factor of 1000 (minutes)	Experimental time for irradiated material to reach background dose rate (minutes)
Aluminum	27,833	4000 (2.08 days)
Iron	45,833	1250 (0.87 days)
Lead	0.9	60 (0.04 days)

Table 8-12 shows that the survey meter approach allows release of aluminum and iron in much shorter times than the 1/1000 rule of thumb approach, while the release of lead would be slightly longer. However, in all cases, the survey meter approach indicates that these materials will return to background and be releasable in at most several days. Since the release of the materials would be based on the use of survey meters or radiacs, it is believed that the latter approach is the more valid approach to assess whether or not there is a cargo activation issue.

Consequently a series of similar experiments were conducted on a wide range of materials that would be typical cargo contents within a shipping container using the survey meter approach to determine their hold times. These materials evaluated included a wide variety of different chemicals, metals, household consumables, and personal items. For consumable items when irradiated in their container are so noted in table 8-13. Each material was irradiated with the USNA 14 MeV neutron generator under the same conditions as performed for aluminum, iron and lead. Then the time for each material to reach background was noted. The results of these experiments are given in table 8-13.

Table 8-13. Summary of weight and time for irradiated material to reach background after 14 MeV exposure to a neutron flux of 1.68×10^7 n/cm² sec for 139.2 sec. Total neutron fluence = 2.34×10^9 n/cm².

Item	Weight (grams)	Time to background (minutes)
Elmer's Glue	43.9	13
strontium chloride hexahydrate	599.4	198
calcium chloride dihydrate	282.9	120
magnesium sulfate	602.2	310
ferrous ammonium sulfate	548.0	186
sodium hydroxide	474.9	8
sodium carbonate	588.7	9
potassium chloride	609.0	203
nickels (3 rolls) (25% Ni, 75% Cu)	600.9	419
pennies (3 rolls) (2.5% Cu, 97.5% Zn)	404.6	294
rubber (3 pieces)	218.2	63
glass plates (wrapped with duct tape)	440.9	63
pine block	146.4	9
polyethylene block (CH ₂)	239.2	0
plywood (3/8" thickness)	75.7	8
pressure treated pine	164.1	9
shirt (75% polyester/ 25% wool)	164.1	9
zinc metal powder (in glass under argon)	122.3	208
chromium metal powder (2 bottles under argon)	229.8	59

Table 8-13. Summary of time for irradiated material to reach background after 14 MeV exposure to a neutron flux of 1.68×10^7 n/cm² sec for 139.2 sec. Total neutron fluence = 2.34×10^9 n/cm². (Continued)

Item	Weight (grams)	Time to background (minutes)
silicon metal powder (2 bottles under argon)	228.1	51
titanium rods (3 pcs. In plastic vials)	31.7	18
gold (in plastic baggie)	130.9	24
palladium rod	37.1	13
Lipton instant iced tea in glass jar	493.1	40
Ragu spaghetti sauce in glass jar	668.5	36
Sanka in glass jar	277.0	37
Amore Cocoa mix in 5 foil packs	189.7	20
crackers in cardboard	153.1	20
microwave popcorn (2 bags)	228.4	15
chocolate coated almonds	201.2	20
Squiggles gummi worms candy	107.2	8
Sunglory raisins 5 packs in Ziploc	112.4	7
3 "D" Energizer batteries (Zn/MnO ₂)	441.3	1000
Lipton instant iced tea in Ziploc	116.6	28

As can be seen in table 8-13, most materials reached background within 60 minutes of exposure. A few samples took 5-8 hours for materials that contained specific metals such as copper, zinc, or magnesium. By comparing the data in tables 8-12 and 8-13, the material that took the longest to reach background was aluminum, which took approximately 4000 minutes or slightly less than three days. Consequently, a large aluminum plate (2' by 2' by 1") was irradiated under similar conditions to determine, if the decay time would be a function of a specimen's size and mass. However, this large aluminum plate was observed to reach background in 4000 minutes, which was the same time as the much smaller sized aluminum blocks (4" by 4" by 1"), whose decay data is graphed in figure 8-12. Thus it was concluded that the decay time is relatively independent of sample shape and mass and the decay time observed for the many irradiated samples would be unchanged, if present in large bulk sizes such as in a large shipping container.

8.5 CONCLUSIONS.

As discussed in section 9, the average holding time for is a container in the port of Baltimore is 5 days. As can be seen from table 8-13, all materials tests returned to background radiation readings well within this time. Thus it was concluded that cargo activation would not impede the free flow of commerce for containers

leaving the port of Baltimore, assuming that they were immediately examined upon removal from the container ship.

SECTION 9

PORT OF BALTIMORE AND FEASIBILITY STUDY OF NEUTRON STIMULATION FACILITY

In this section the container operations at the port of Baltimore are reviewed and a feasibility study is presented in which important regulatory and engineering aspects of the facility were evaluated. Section 9.1 first reviews the basic operations at the Port of Baltimore based on a recent site visit. The major rules and regulations, which the facility would have to follow, are discussed in section 9.2. Also included in this section is a discussion regarding the storage requirements of activated cargo and the special requirements of the facility's high radiation areas. A cost analysis is presented in section 9.3, which considers procurement of the 14 MeV neutron, staffing, dosimetry, equipment, and maintenance cost. A basic site layout is given in section 9.4. Conclusions are given regarding the feasibility of building and operating such a facility are given in section 9.5.

9.1 PORT OF BALTIMORE.

Three midshipmen visited the port of Baltimore on February 5, 2003. The purpose of their visit was to interview both a port official (Costello, 2003) and a US Customs agent (Austin, 2003) in order to find out specific port operating information. The interview yielded information on the container-handling path, certain costs involved in the process, and current inspection methods and technologies. The port's inspection procedures and inspection technologies deployed or under consideration, have been presented in sections 1.7 thru 1.10. Appendix C provides a detailed list of questions asked and responses received by the midshipmen.

The port of Baltimore has a number of different container unloading sites. Figure 9-1 shows one such container shipping yard in the Baltimore port. Figure 9-2 depicts a container being moved at the Port of Baltimore, which is similar in design as the benchmark container used in this study. Figure 9-3 shows a container ship during loading operations in port. Finally, figure 9-4 gives a layout of the Port of Baltimore, including the locations of different general cargo facilities.



Figure 9-1. One of many container shipping yards in Baltimore Port.



Figure 9-2. Container being moved at the Port of Baltimore.



Figure 9-3. Container ship and container loading operations in port.

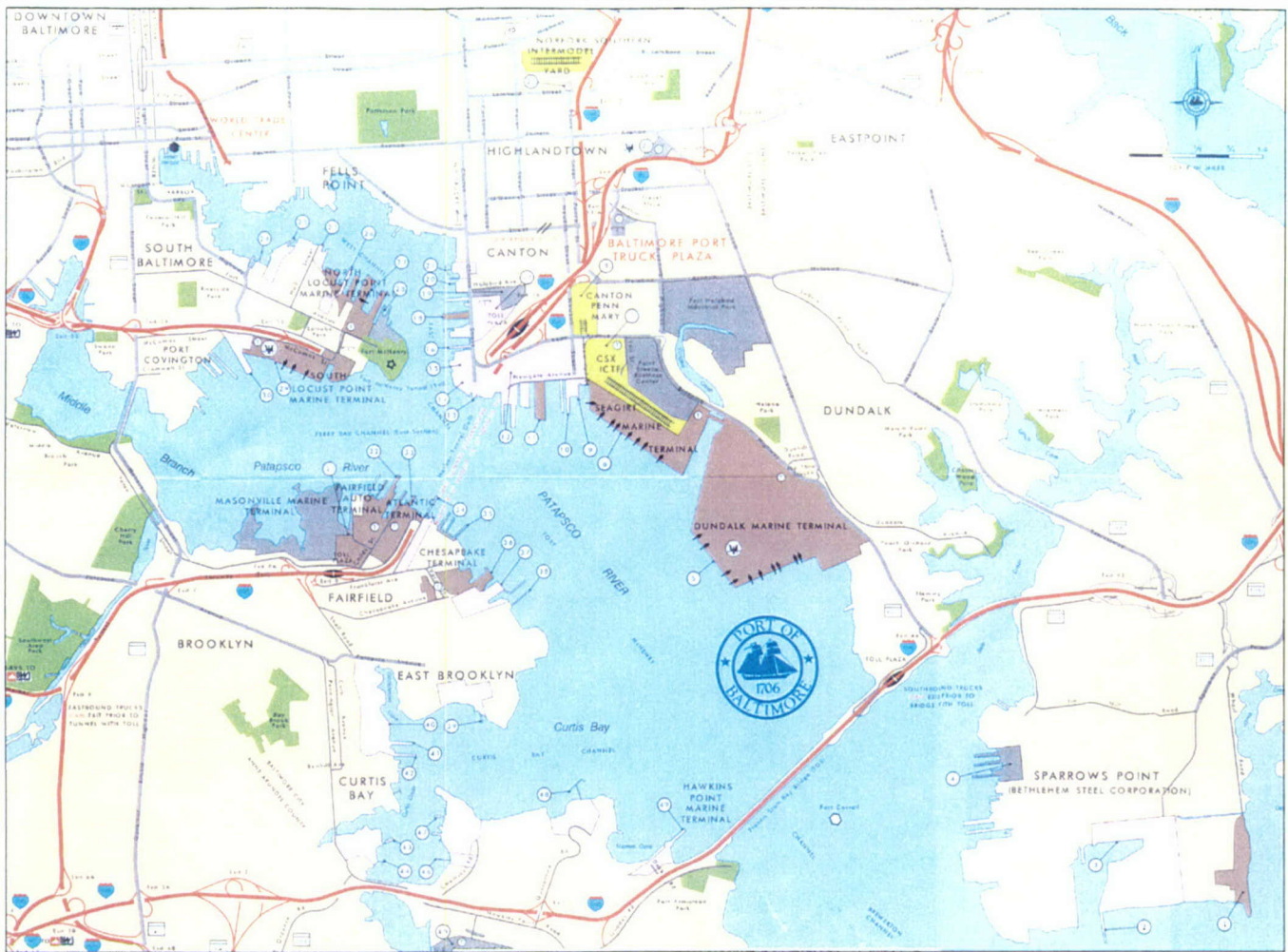


Figure 9-4. Layout of the Port of Baltimore. Areas 1, 5, 6, 11, 18, 27, 29, 31, 33, and 36 (dark areas) are general cargo facilities.

Table 9-1 presents the most important information gathered in the midshipmen's visit.

Table 9-1. Information on Shipping Containers for Port of Baltimore in 2003 (Costello, 2003).

Item	Answer
Average number of ships entering the port each day	5-6
Average number of containers off-loaded per week	2000
Average number of containers per ship	3000
Cost to gang crew to unload ship	\$2300/hour
Average time ship in port	8-10 hours (17 people)
Location of container storage	Throughout port (no specific location); if contents inside container need to be unpacked, container is sent to warehouse
Average container stay in port after unloaded	5 days

Using the data in table 9-1, the average cost to unload a container was calculated with the following assumptions:

- (1) 30 ships enter the port of Baltimore per week
- (2) 2000 containers are off-loaded in a week
- (3) 9 hours is the average off-load time with gang cost of \$2300/hour

$$\left(\begin{array}{l} \text{Average Cost} \\ \text{to off-load a} \\ \text{single container} \end{array} \right) = \frac{\left(\frac{\$2300}{\text{hr}} \right) \left(\frac{9 \text{ hr}}{\text{ship}} \right) \left(\frac{30 \text{ ships}}{\text{week}} \right)}{\left(\frac{2000 \text{ containers}}{\text{week}} \right)} = \$310.5/\text{container} \quad (9.1)$$

Additionally, the total unloading costs per year was estimated by multiplying the result in equation (9.1) by the number of containers off-loaded at the port per year, which yielded:

$$\left(\begin{array}{l} \text{Total cost to off-load} \\ \text{all containers in port} \\ \text{of Baltimore per year} \end{array} \right) = (310.5) (2000) (52) = \$3.23 \times 10^7 \quad (9.2)$$

The midshipmen were told that the port was typical of other US ports except for perhaps a little more waterline and cargo activity. It was also mentioned that 80% of the containers exit the port by truck and 20% leave by either barge or rail. Finally, of the 3000 containers on a ship, typically only a small fraction are unloaded at Baltimore.

The container inspection follows the Landed Quantity Verification (LQV) process. In this process each container number is recorded, and at the very least each container will be opened. The inspectors look for the presence of tampered seals, as well as 100% accuracy in the manifest information provided. The visual inspections do not preclude a latter x-ray or VACIS inspection, if the manifest raises an alarm or for random purposes. Typically about 110 containers are inspected per week or about 5% of the total containers arriving in the port. In these inspections, typically 20% of the cargo will be taken out of the container. Radiation survey meters are available to the inspectors for use in these situations. The port of Baltimore uses the VACIS system for inspections on selected containers. A detailed technical description of this technology is provided in section 1.8. The VACIS system creates a colorized 2-D video image, which shades cargo based on its density and shape. Its cost is approximately \$1,000,000. A competing technology used in some other US ports is Heiman x-ray machines, which cost approximately \$5,000,000. The port of Baltimore at the present time does not have either the Portal Monitoring System (see section 1.9) or the radioisotope detector system (see section 1.10). However, it was mentioned that the port of Norfolk is evaluating the Portal Monitoring System.

9.2 RULES AND REGULATIONS APPLICABLE TO A NEUTRON STIMULATION SPECIAL NUCLEAR MATERIAL MONITORING FACILITY.

In this section, the nuclear related rules and regulations that pertain to a special nuclear material monitoring facility are discussed. The rules and regulations are outlined in the Code of Federal Regulations (CFR) and the U.S. Nuclear Regulatory Commission (NRC) oversees the compliance to the standards. Section 9.2.1 gives the exposure dose standard that a worker or general member of the public can receive. The rules and regulations regarding storage of activated material are included in section 9.2.2. Section 9.2.3 gives the requirements needed to operate the facility in the locations that will be designated to be high radiation areas.

9.2.1 Exposure Dose Standards.

The primary effort of any safety program is to minimize the exposure to radiation to the public and workers. ALARA is a nuclear safety acronym for "as low as reasonably achievable" (10CFR20.1003, 2002). ALARA means that every worker must make every effort to minimize his or her own radiation exposure. There are dose limits and the goal is to stay well below those dose levels - according to what is practical. Decreasing the time near a radiation area, increasing the distance from the area, and providing shielding are three methods for minimizing exposure.

The occupational annual total effective dose limit for radiation workers is 5 rems (10CFR20.1201, 2002). Should a worker reach or exceed this limit, that worker can no longer work in a radiation area. To exceed the limit, typically an emergency, accident, or planned special exposure must occur. The doses received during any one of these three events must be subtracted from the limit that a person may receive during the year. The details regarding a planned special exposure are listed in detail in 10CFR20.1206. The annual total effective dose limit for a member of the public cannot exceed 0.1 rems per year or 2.0 mrem in a one-hour period, unless that individual is permitted to have special access to the controlled area (10CFR20.1301, 2002 and Abkemeirer, 2003). This latter condition would not be expected to occur during the operation of this facility.

The term "controlled area" is important because it is defined by the CFR as an area, which is outside of a restricted area but inside the site boundary, where a licensee can limit access. Such an area would be set aside to monitor containers and temporarily store containers with decaying activated cargo. Two other important terms are "licensee" and "restricted area." A licensee is the individual or organization that is issued a license to complete or undertake whatever task they were assigned. To get a license many different regulations must be met. In the case of a neutron stimulation facility, the U.S. Custom Service would be the licensee. A restricted area is an area that has limited access in order to protect individuals from unnecessary radiation exposure (10CFR20.1003, 2002). Like the controlled area, the U.S. Customs Service would have flexibility in assigning what port areas would be designated as a restricted area. The controlled and restricted area not only protects the public and non-radiation workers from unnecessary radiation exposure, but also helps create a physical barrier between these individuals and the containers. This setup certainly limits the interaction any member of the public would have with tampering with a container before it is removed from the port facility. For the controlled area, the site boundary would be designated to include the stimulation facility and an area for storing containers while the contents are radioactively decaying.

9.2.2 Storage of Activated Cargo Material.

When the container contents are irradiated, the materials can become radioactive. Details of the activation analysis are included in section 8 of this report. One concern is that once the material is irradiated it would pose a radiation hazard due to the gammas emitted by decaying isotopes. The regulations state that an irradiated material must be held in storage if it has a physical half-life of less than 120 days. However, once the radioactivity of the container contents can no longer be distinguished from the background radiation level, the container and the contents can be released (10CFR35.92,

2002). The time that common cargo materials take to reach background radiation levels are given in section 8.4 of this report.

9.2.3 High Radiation Area Requirements.

Because the neutron generator source strength in the facility would be 10^{12} n/sec, the space around it would be a restricted high radiation area. A high radiation area is defined as an area where the radiation levels will result in an individual receiving an exposure dose of 0.1 rem in 1 hour at 30 centimeters from the radiation source (10CFR20.1003, 2002). Several safety features are required to protect workers from the high exposure levels. A safety switch must be placed on the area's entrance and exit. When the doorways to this space are open, the neutron generator would be electrically isolated and could not operate. Once the doors are closed and the neutron generator is operating, then a locking mechanism would be installed to prevent the doors from being opened (10CFR20.1601, 2002). This space must also be posted as a high radiation area. For high radiation areas, a radiation symbol (as shown in figure 9-5) must be posted in a very noticeable manner along with the words "CAUTION, HIGH RADIATION AREA" or "DANGER, HIGH RADIATION AREA" (10CFR20.1902, 2002).

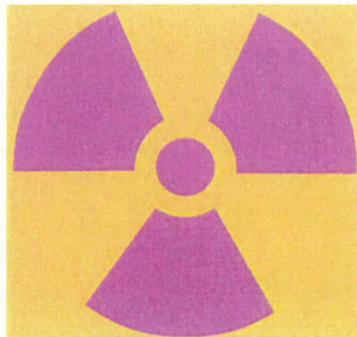


Figure 9-5. Standard radiation caution symbol.

9.3 COST ANALYSIS.

One of the objectives of this study is to examine the basic costs of using an external neutron source to stimulate the HEU to determine if it is present or not, should there be a need for the special nuclear material monitoring facility. This section examines the costs of the ONDAC detectors, the 14 MeV neutron source, the staffing, and the dosimetry requirements for the staff. Sections 9.3.1 and 9.3.2 address the costs of the ONDAC neutron detectors and the neutron generators respectively. Section 9.3.3 estimates the cost of building such a facility. The staffing requirements are outlined in section 9.3.4 while section 9.3.5 describes considerations for the cost of dosimetry. A summary of the annual cost is described in section 9.3.6 with the details provided in table 9-5 for the first

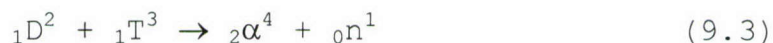
year of operation and table 9-6 for the subsequent years of operation.

9.3.1 Radiation Instrumentation Costs.

The delayed neutron signal would be measured by three ONDAC detectors. The cost of each ONDAC is estimated to be \$16,000 (Murphy, 1999), and three ONDACs would be needed in each facility. It is also recommended that there is a backup ONDAC on hand for maintenance or replacement purposes. This brings the detector cost to \$64,000 for four detectors. Additionally, there are initial and annual calibration costs associated with operating these detectors of \$15,000. Advanced nucleonic detection equipment will cost \$40,000.

9.3.2 Pulsed Neutron Generator Costs.

Pulsed neutron generators are commercially available (see vendors in table 4-1). Neutrons can be made through two different means, either through deuterium-tritium (D-T) reactions or through deuterium-deuterium (D-D) reactions. D-T reactions are more favorable because they emit 14 MeV neutrons. The D-T reaction is shown in equation (9.3).



Another specification for determining the costs of the neutron accelerators is its source strength. This project requires a pulsed neutron generator with a source strength of 10^{12} neutrons/sec. Currently, there is no commercially available neutron generator with this required source strength, but research at LLNL has lead scientists there to believe they could produce a pulsed neutron detector with an output as high as 10^{12} neutrons/sec. The cost for the D-T reaction at this source strength was quoted at the price of \$600,000 (Leung, LNBL).

The generator will also require a supply of insulating gas which costs around \$10,000 a year. General maintenance of the generator is estimated at \$6,000 a year based on USNA neutron generator expenses. In subsequent years, there will also be the additional cost of replacement parts such as the ion source, target head, and accelerator tube. These costs are estimated at \$100,000 per year. A significant amount of training will also need to be in place before the generator is operated, and additional training in subsequent years. The cost of worker training is estimated to be \$5,000 per year.

9.3.3 Facility Construction and Operation.

The estimated cost of constructing an appropriate facility for the neutron generator and detectors is \$400,000. Using design A from

section 9.4 it is estimated that over 1,000 yards of reinforced concrete will be needed to build an appropriate structure. The walls, ceiling, and floor of the facility will be made of concrete which shields any neutron radiation. The facility will have the required eight foot thick concrete wall behind the generator as described in section 6.2 and four foot thick concrete wall behind the ONDAC detectors. Included in this estimate is a control room placed behind the generator wall.

Also associated with the cost of the facility is a security system, area radiation detectors, and general maintenance. The security system and area detectors will cost \$20,000 and yearly maintenance costs are estimated at \$10,000 per year. Electrical power consumption at the facility including the operation of the neutron generator has been estimated to be \$5,400 per year. Facility related costs can be found in table 9-5 and table 9-6.

It is assumed that the port will have cranes available for use to get containers to and from the facility and hence no cost has been assigned this activity.

9.3.4 Staffing Costs.

It is expected that a stimulation facility would be adopted into the U.S. Customs Inspection Process, and used primarily in conjunction with the VACIS gamma-ray inspection system and the isotope identification system. The Port of Baltimore currently employs three officers on the VACIS at any time: a driver, a system operator, and a safety observer. All positions can be interchanged and are based around an 80-hour training system. This includes an initial 40 hours of "classroom" training and an additional 40 hours of on-the-job-training (OJT). The facility staffing requirements have been based upon estimates derived from the current staffing for the VACIS at the Port of Baltimore.

The United States Office of Personnel Management is the governing body for the pay tables of U.S. Customs employees. Customs officials are ranked on a system that is divided by time in service, and a rank denoting a certain amount of responsibility. The facility would be operated by a team of three individuals per shift, with differing levels of responsibility between team members. The team members will be required to operate a very sophisticated piece of equipment which has the potential to be a radiation hazard. Consequently, higher GS grade level individuals than used by the VACIS would be needed for operation of the facility.

It was assumed that the inspection team members for one shift on the facility will be composed of one GS-9 and two GS-11. These individuals will be qualified for other Customs duties like the VACIS, and those duties will rotate according to the port manager's

direction. A liberal estimate for a port's total staff will be 3 shifts, meaning a total of 9 operators. Additionally, one GS-12/13 level administrator will be needed to be present at the facility to make management-level decisions based upon detained cargo and radiological issues that may arise. Finally, one GS-5 level secretary will be necessary for paperwork and communication purposes. This last position would only require a regular 40 hour week. The overall pay tables for these four pay grades can be found on the Office of Personnel Management website. The pay table for the Baltimore/Washington area is listed in table 9-1. The pay tables are adjusted to allow for a 30% overhead that would be included in yearly operation. The nine operators and one supervisor at the four assumed highlighted grade steps will require a yearly total of \$721,763.00.

Table 9-2. Pay chart for U.S. Customs officials in Baltimore area (30% overhead), 2003.

Rank	Step 2	Step 4	Step 6	Step 10
GS5	\$35,501 x 1	\$37,791	\$40,080	\$44,659
GS9	\$53,793 x 1	\$57,264 x 1	\$60,733 x 1	\$67,675
GS11	\$65,087 x 2	\$69,287 x 2	\$73,487 x 2	\$81,888
GS13	\$92,765	\$98,750 x 1	\$104,735	\$116,706

9.3.5 Dosimetry Costs.

Each staff member will be required to wear proper dosimetry due to the use of neutron accelerators and because most cargo will activate. The cost estimates for the necessary dosimetry was found through Landauer®, the world's largest provider of radiation dosimetry services. The dosimetry will have to measure betas, gammas, and neutrons. The Luxel® dosimetry system was chosen to provide the worker with beta and gamma measurement. Table 9-2 shows the annual investment per person, effective October 1, 2002, for monthly, bimonthly, or quarterly service.

Table 9-3. Annual investment per person, effective October 1, 2002, for monthly, bimonthly, or quarterly service.

People	Investment (\$)
1	369.60
2	221.76
3	168.00
4	141.12
5	124.32
6	110.88
7	104.16
8	100.80
9	97.44
10	94.08
11	90.72
12-13	87.36
14-15	84.00
16-19	77.28
20-24	73.92
25-29	70.56
30-34	67.20
35-39	63.84
40-74	57.12
75-99	53.76

According to the staffing requirements, nine operators will be utilized, along with two additional supervisors. Crane gang members will be responsible for moving the irradiated cargo containers from the neutron irradiation facility to their holding site. During this time, these employees would wear dosimetry as well. It is estimated that five members of each gang will be responsible for moving these cargo containers to the inspection site and away after they have been inspected. Five was chosen such that the flow of containers coming in and out of the facility would minimize the effect on commerce. Assuming that there are three trained crane gangs at the port, this yields an additional fifteen required dosimetry badges. Hence, the total number of port personnel requiring dosimetry badges would be 26. Additionally, an extra 10 badges would be needed for any visitors to the site. From table 9-2, the annual investment per person will be \$63.84 since 36 badges would be required. The annual expense for beta and gamma dosimetry would total \$2,298.24.

The dosimetry will be required to account for fast and thermal neutrons as well, because the cargo containers will be irradiated with a 14 MeV neutron source. Landauer® offers the Neutrak® 144 to augment the Luxel® dosimeter. There are two types of services that can be added. Fast neutron services can be added for an additional \$70.56 per person, annually, in addition to the standard cost of the Luxel. Thermal neutron detection can also be added for an additional

\$73.92 per person, annually, in addition to the cost of the Luxel. Neutron detection will cost an extra \$144.48 per person annually, for a total of \$5,201.28 for all 26 badge-wearers and 10 guests.

There is also an additional set-up fee of \$2 per person that will be added in the first year for all 26 employees, for a total of \$52. This \$2 fee will also be applicable anytime another member is added to SNM monitoring facility team. Table 9-3 summarizes the costs required for dosimetry.

Table 9-4. Annual dosimetry costs for necessary personnel/visitors.

Service	Annual cost per person (\$)	Annual cost for the required 26 personnel (\$) +10 Guests
Luxel [®] gamma and beta detection	63.84	2,298.24
Neutrak [®] 144 fast neutron detection	70.56	2,540.16
Neutrak [®] 144 thermal neutron detection	73.92	2,661.12
Set-up fee	2.00	52.00
TOTAL	\$ 210.32	\$ 7,551.52

9.3.6 Summary of Annual Costs.

Table 9-5 describes the total cost for each component of the SNM monitoring facility during the first year of operation. It includes the detectors, the neutron source, the annual staffing requirements, and the annual dosimetry costs. The costs for subsequent years will be reduced because there will be no need for new equipment from the first year. The amount of training will also decrease in the second and subsequent years of operation. The target head on the 14 MeV neutron generator will need to be replaced annually for \$100,000.00 and the radiation training for the staff will need to be continued for an annual amount of \$2,500.00 (Nelson, 2003). Table 9-6 includes the final calculation of the cost to operate the neutron stimulation facility after the first year.

Table 9-5. Cost to build and operate a neutron stimulation facility for the first year.

Component	Unit cost (\$)	Number of units	Total cost (\$)
ONDAC detector	16,000	4	64,000.00
14 MeV Neutron Source Generator	600,000	1	600,000.00
Staff	Various	11	721,763.00
Dosimetry	210.32	36	7,551.52
Survey Instruments for Cargo Activation	15,000.00	1	15,000.00
Insulating Gas for Neutron Generator	10,000.00	1	10,000.00
Survey Instrument/ONDAC Calibration	15,000.00	N/A	15,000.00
Radiation Training for workers	5,000.00	N/A	5,000.00
Maintenance of Neutron Generator	6,000.00	N/A	6,000.00
Facility construction	400,000.00	1	400,000.00
Electrical power consumption	5,400.00	N/A	5,400.00
Security system and area radiation detectors	20,000.00	N/A	20,000.00
Advanced nucleonics detection equipment	40,000.00	N/A	40,000.00
		TOTAL	\$1,909,710.52

Table 9-6. Cost for subsequent years of neutron stimulation operation.

Component	Unit Cost (\$)	Number of Units	Total Cost (\$)
14 MeV Neutron and component ion replacement (i.e. source, target head, accelerator tube, etc.)	100,000.00	1	100,000.00
Staff	Various	11	721,763.00
Dosimetry	210.32	36	7,551.52
Insulating Gas for Neutron Generator	10,000.00	1	10,000.00
Survey Instrument/ONDAC Calibration and maintenance	15,000.00	N/A	15,000.00
Radiation Training for workers	2,500.00	N/A	2,500.00
Maintenance of Neutron Generator	6,000.00	N/A	6,000.00
Electrical power consumption	5,400.00	N/A	5,400.00
Facility maintenance	10,000.00	N/A	10,000.00
		TOTAL	\$878,215.52

The above expected cost per year for facility operations was estimated based on the assumption that the inspection process is a twenty-four hour per day operation, five days per week. Comparing these costs to the current cargo unloading costs of \$32.23 million per year (equation 9.2), it is estimated that the stimulation facility would increase the container unloading cost by 5.9% the first year and 2.7% in subsequent years. Table 9-7 compares these costs.

Table 9-7. Comparison of costs per year between unloading containers and facility operation.

Item	Cost (\$)
Unloading containers	$\$3.23 \times 10^7$
Facility operation – first year	$\$1.91 \times 10^6$
Facility operation – subsequent years	$\$8.78 \times 10^5$

Assuming five minutes are required for the inspection and five minutes to move the container into and out of the facility, a 24 hour per day, five days per week, three shift operation of the facility could inspect 720 containers per week. This is roughly 36% of the 2000 containers entering the port of Baltimore each week. By comparison, the VACIS inspection system currently inspects only 110 containers per week (approximately 16 per day) or 5% of containers entering the Baltimore port. Table 9-8 shows the percentage of containers that can be inspected if there is anywhere between one and three shifts or 40 to 120 hours of operation per week.

Table 9-8. Percentage of containers that will be inspected at the Port of Baltimore as a function of the hours facility is open per week.

Hours of Operation per week	Containers per week	Percentage of containers that enter the Baltimore port
40	240	12%
80	480	24%
120	720	36%

9.4 SITE DESIGN AND LAYOUT.

A preliminary site layout is given in this sub-section. The purpose of this section is to integrate the stimulation facility neutron source, the container examination area, the radiation shields, and the ONDAC neutron detectors into a single physical layout. The physical layout considered different options for containers entrance and exit from the facility, the space needed for the examination of a container the size of the benchmark container, the storage area following a container's irradiation, and the shielding arrangements to reduce the dose to as low as reasonable achievable (ALARA) for both facility radiation workers, other port non-radiation workers, and members of the public.

It is recognized that such a site design would vary from one port to another due to differences in waterlines and port activity. However, there were several overriding considerations in the site's design. First, it was desired to have a system layout, which could complete the examination in as short as time as possible so as to minimize the inspection's impact on the flow of commerce. Second, the size of the controlled and restricted areas was minimized in order to reduce system cost and improve security. Third, the ALARA principle was considered in sizing the controlled and restricted areas for the facility.

The neutron stimulation facility and associated storage areas would have to be built in close proximity to the receiving area within a port. Due to the radioactive decay of stimulated cargo containers, a controlled storage area must be included in the layout and protected while the containers are held.

The site will essentially encompass a controlled area, which consists of the stimulation facility and the storage area. Due to the presence of radiation, the workers in this controlled area would be classified as radiation workers and be monitored for their radiation exposure. Adequate security would be required in order to keep non-radiation workers out of the area so they have no chance of being exposed to radiation from the facility. This would involve at the

minimum, an adequate fence and perimeter security measures such as video cameras and motion detectors. Containers would move into the site at a controlled gate near the entrance of the facility. After the appropriate decay time following examination, the containers would exit at a separate controlled gate where they would be scanned to ensure they have reached background radiation levels. Throughout the site there would be radiation monitors to ensure the site is being maintained appropriately.

In the ensuing discussion, a controlled area means that access is controlled for security reasons. A restricted area means that access is controlled for radiological reasons.

Based on a five day waiting period the containers undergo before removal and assuming the container are examined on the first day, the site should have seven separate storage areas. Separate storage areas are important because stimulation causes a cargo container to become a radiation source, and in accordance with ALARA, it would not be appropriate to store a recently stimulated container adjacent to one that has decayed for a longer period of time. The seven storage areas are needed so that there would be one area for each day of their decay, one for newly stimulated containers, and one for containers ready to be removed. Seven storage areas actually allows for one extra day of storage if all the fifth day containers are not removed by the end of the fifth day of decay.

To develop the site layout show in figure 9-6, several assumptions were made. The neutron stimulation facility is assumed to cover an area of 120' by 120', where some proposed designs are slightly smaller or larger. Cargo containers dimensions are that of the benchmark container (20' x 8' x 8'), but in the storage area, an additional six inches are added to each side, making the effective container area 21' x 9'. If the containers are held in a 7 by 18 grid an individual storage area will be 147' by 162' and hold 126 containers not stacked and up to 252 containers if stacked two high. These areas are more than adequate for storing the expected 144 irradiated containers per day and this extra space allows for flexibility in stacking and moving the containers. Also, 40' spacing is assumed around the storage areas. Finally, it was assumed that the containers will be moved by an efficient crane system once inside the controlled area.

The proposed site layout in figure 9-6 is a simple rectangular design of 826' x 601'. This allows for a 40' space around each storage area and 40' from the fence that marks the controlled area so that containers can freely move around while entering or exiting the facility. In addition, there is 40' or more open space around the stimulation facility so as to keep that area clear. The design in figure 9-6 also includes an additional storage area of equal size to the other seven, in case additional space is required. This would

bring the container capacity to 3024. There is also extra space around the entrance and exits to be used as a staging area for containers to enter or exit, or as they wait to be placed in a storage area. This layout includes two exits so containers can quickly be removed on the fifth day which minimizes any interruptions to the flow of commerce. Upon departure, containers will be scanned by either inspectors with handheld radiation instruments or through a portal monitoring system to ensure they have reached background radiation levels.

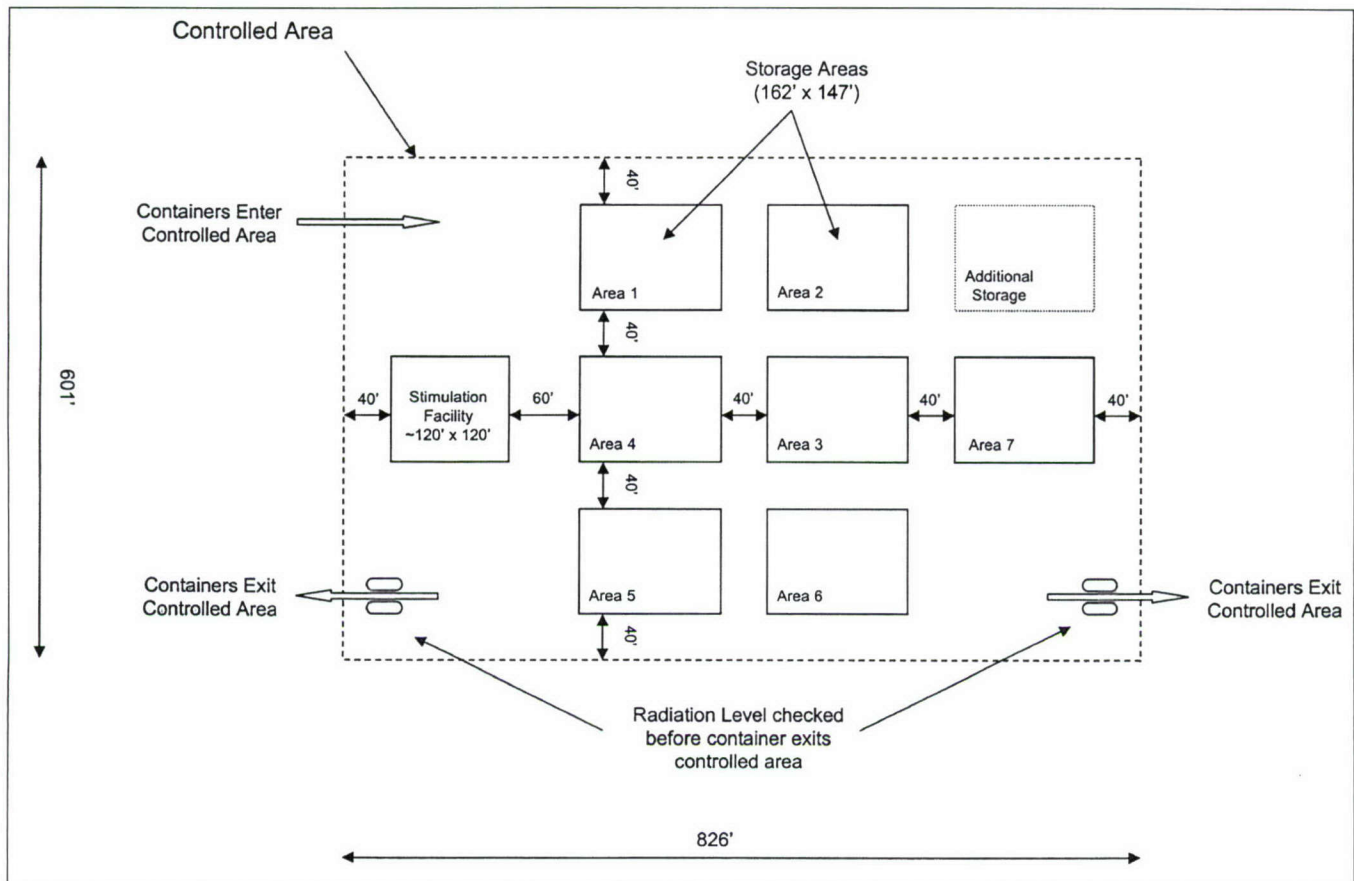


Figure 9-6. Site controlled area layout.

Stimulation Facility Designs

A neutron stimulation facility must be designed so that containers can meet the target time of 5 minutes/scan and minimize external radiation effects. As stated in section 6.2, 8 feet of concrete is needed behind the generator. However, because of the outer wall's greater distance from the source, only 4 feet of concrete was assumed to be needed behind them. In all designs, the ONDAC detectors would be located in front of this outer wall. Additionally, the designs below take the following three requirements into account and incorporate one or more additional goals. The first is to limit or totally block the line of sight of the neutron generator from the facility workers. Since the generator will be placed as closely as

possible to the container, this would leave angles which are nearly perpendicular to the detector completely unshielded. Second, to incorporate a waiting area within the facility in order to allow the container to remain shielded while the next cycle is performed. This waiting area would allow much of the initial decay to take place before the container is brought out of the facility and consequentially reduce the radiation exposure to the facility workers. This waiting area would be positioned such that it would not gain any additional radiation from the next stimulation taking place. Some designs incorporate underground facilities, as such designs can use soil as a shield, meaning less concrete would be needed, and a less expensive structure would need to be built. An additional benefit of building an underground structure is the minimum ground surface area used, allowing the contained area to be reduced in size. Another desirable goal is to eliminate the need for any workers to go inside the facility's restricted area between cycles to either move the container or attach/detach equipment. A final desired characteristic of a stimulation facility would be to minimize the time needed per scan. This would involve moving multiple containers within the facility at once instead of a single container entering, being scanned, and exiting before the next container even begins to move.

Design A (Tunnel Version 1). This design is the most basic of the four designs, and a top view is shown in figure 9-7. It is a facility that would be built above ground with an entrance and an exit. The container can enter the facility via multiple modes of transportation. The facility could be compatible for trucks to drive through, a simple rail car system, or a conveyor. Only one container would be in the facility while stimulation is taking place. As soon as the container begins to move towards the exit, the next container would enter. The shape of the facility is an arc so that the neutron generator's line of sight cannot penetrate the entrance or exit. The structure's outer wall would be concrete that varies in thickness depending on distance from the neutron source. As shown in figure 9-7, the wall behind the neutron generator would be 8' thick, but behind the ONDAC detectors, it would be 4' thick. As the walls approach the entrance and exit, they would be tapered down to 2'. A 4' concrete ceiling is proposed for this structure covering the entire facility from entrance to exit. A control building will be placed behind the 8' concrete wall. Figure 9-8 presents a 3-D view of this design.

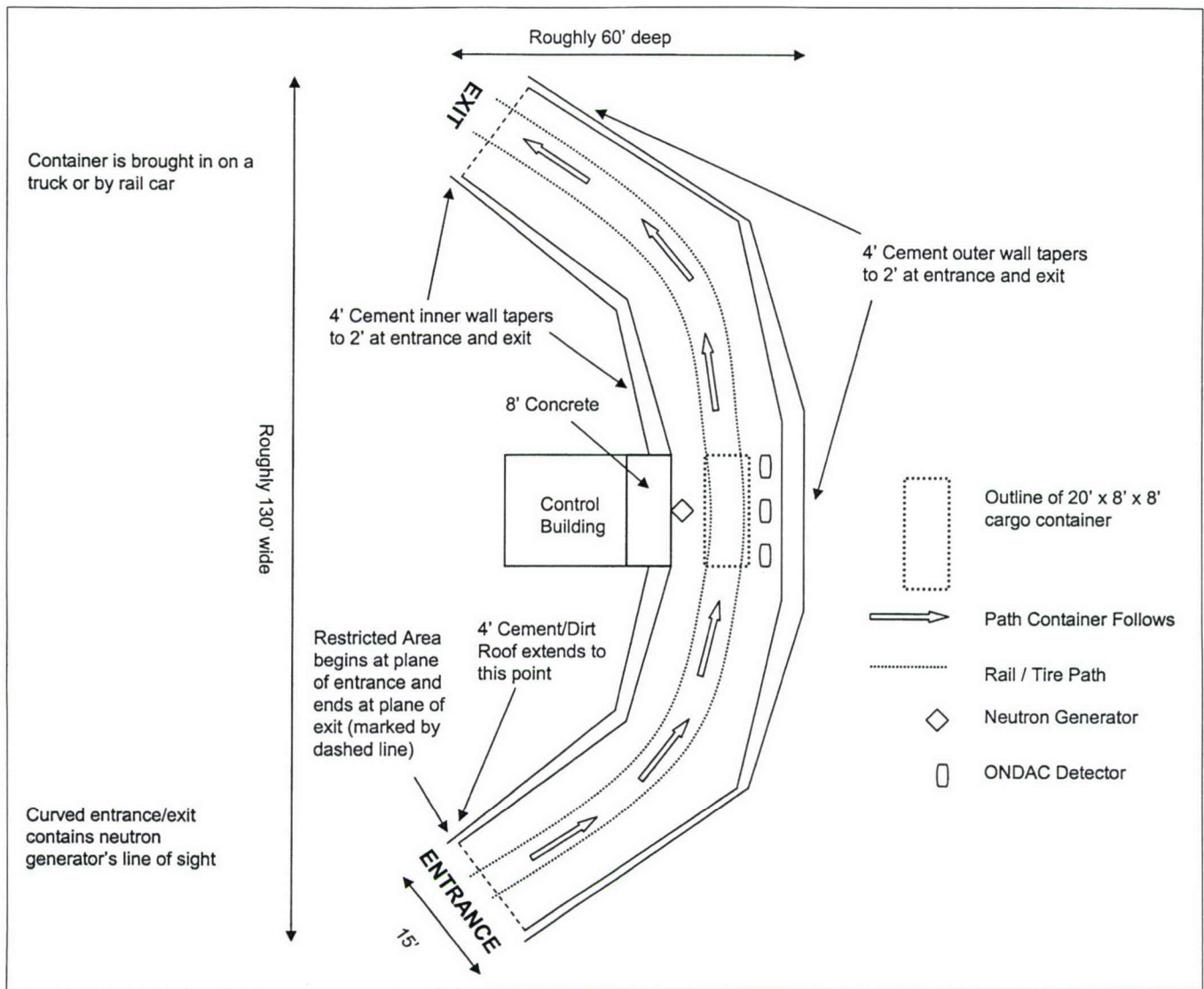


Figure 9-7. Top view of design A (tunnel version 1).

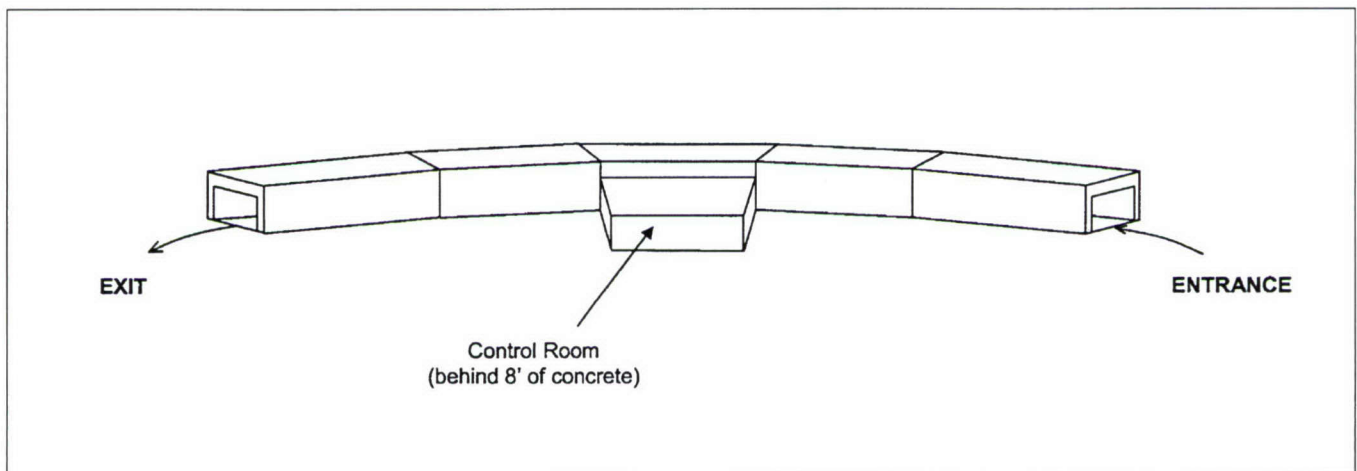


Figure 9-8. 3-D view of design A (tunnel version 1).

Design B (Tunnel Version 2).

The next design is the most compact facility design of the four, and a top view is shown in figure 9-9. This structure would be entirely above ground and contain the stimulation area and the control room within a 76' by 34' area. The containers would move through the facility on a system of conveyors and rollers. A container would be dropped off by a crane just outside the entrance and picked up by a crane once it exits the facility. The conveyor and roller system will allow the container to move without the aid of any workers within the facility. As the container moves within the facility it would only change its direction of motion and would not need to turn. The U-shape design of this facility adequately impedes the line of sight of the neutron generator. Again, there is 8' of concrete behind the neutron generator and 4' behind the ONDAC detectors. This facility would also have 4' walls and a 4' concrete roof covering the entire structure. A benefit of this design is that it would have an area where an irradiated container could wait and decay while the next container is stimulated (i.e. left leg of facility as shown in figure 9-9). This area is just before the exit and utilizes the concrete walls on three sides as a shield. This facility would allow at least two containers to be within the structure at once, and possibly three. The third container would be opposite the decay area, near the entrance, where it could be pre-positioned so that the examination time per container could be minimized.

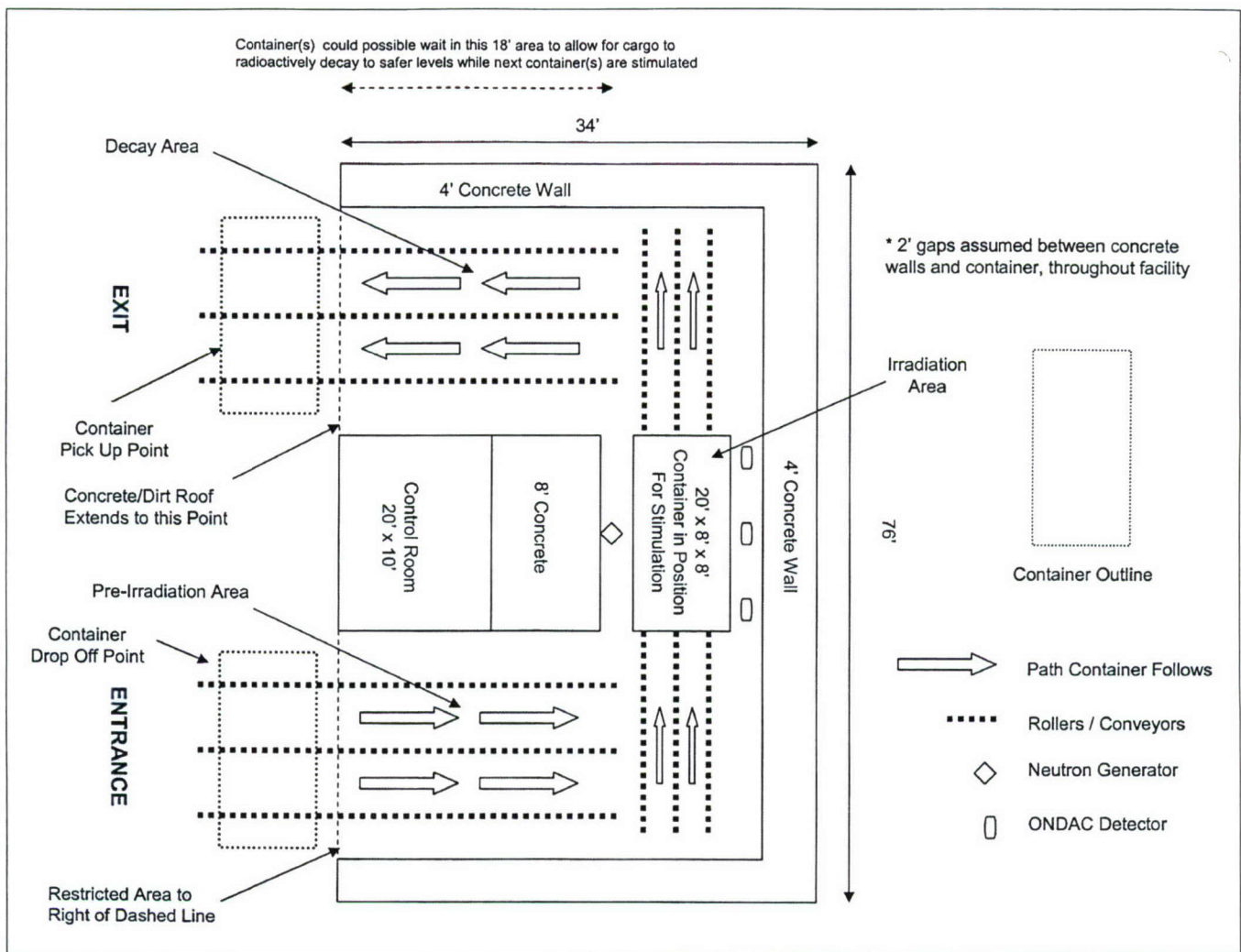


Figure 9-9. Top view of design B (tunnel version 2).

Figure 9-10 shows an end view of design B. As can be seen the overall tunnel length is 76' with the inside tunnel width of 12' and an outside width of 16'.

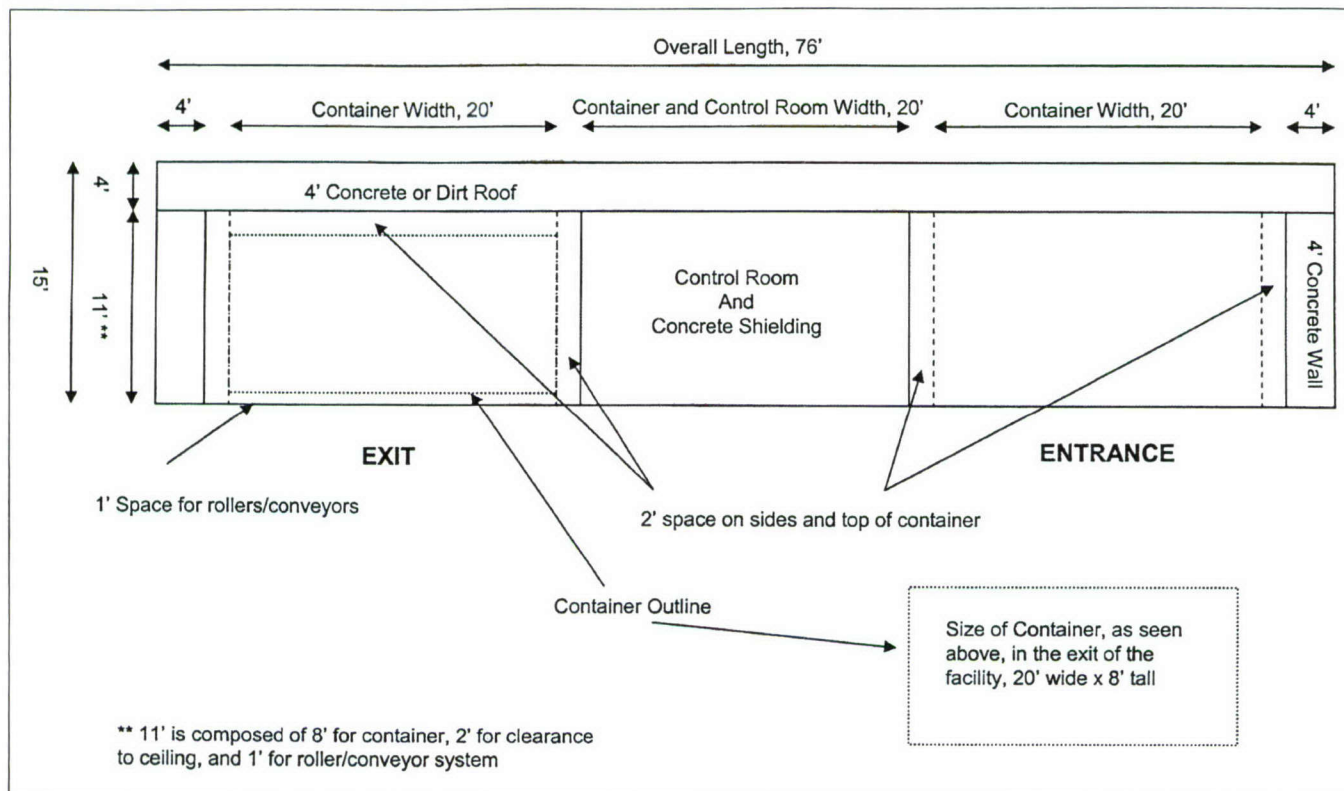


Figure 9-10. End view of design B (tunnel version 2).

The next two designs are subterranean facilities that take advantage of using the port's soil as neutron shielding material. This translates into less concrete being needed in the construction of the facility.

Design C (Subterranean Version 1). This design involves lowering a container by crane into an opening in the surface that leads to the facility. This design is shown in figure 9-11. At the bottom of this opening, which would be 10' beneath the surface, the container will come to rest on a set of rollers. The cables from the crane will be removed at this point and the container would then be rolled into position in front of the neutron generator and stimulated. Next, the container is moved forward down the track and would stop at the end where the crane cables are reattached to the container and it is lifted out of the facility. The length of tunnel the container passes through is 100'. By utilizing the underground design, the walls of this facility could be much thinner, and for this design it would be a uniform 2' thick concrete wall throughout the structure. Therefore this eliminates the need for 8' of concrete behind the neutron generator, which will save on construction costs. Figure 9-12 gives a side perspective of this design showing its outer shape. Figure 9-13 is also a side perspective, but showing the relationship of the facility to the surface. Finally, figure 9-14 gives a side perspective and shows the size of the tunnel and the location of the neutron generator and the ONDAC detectors.

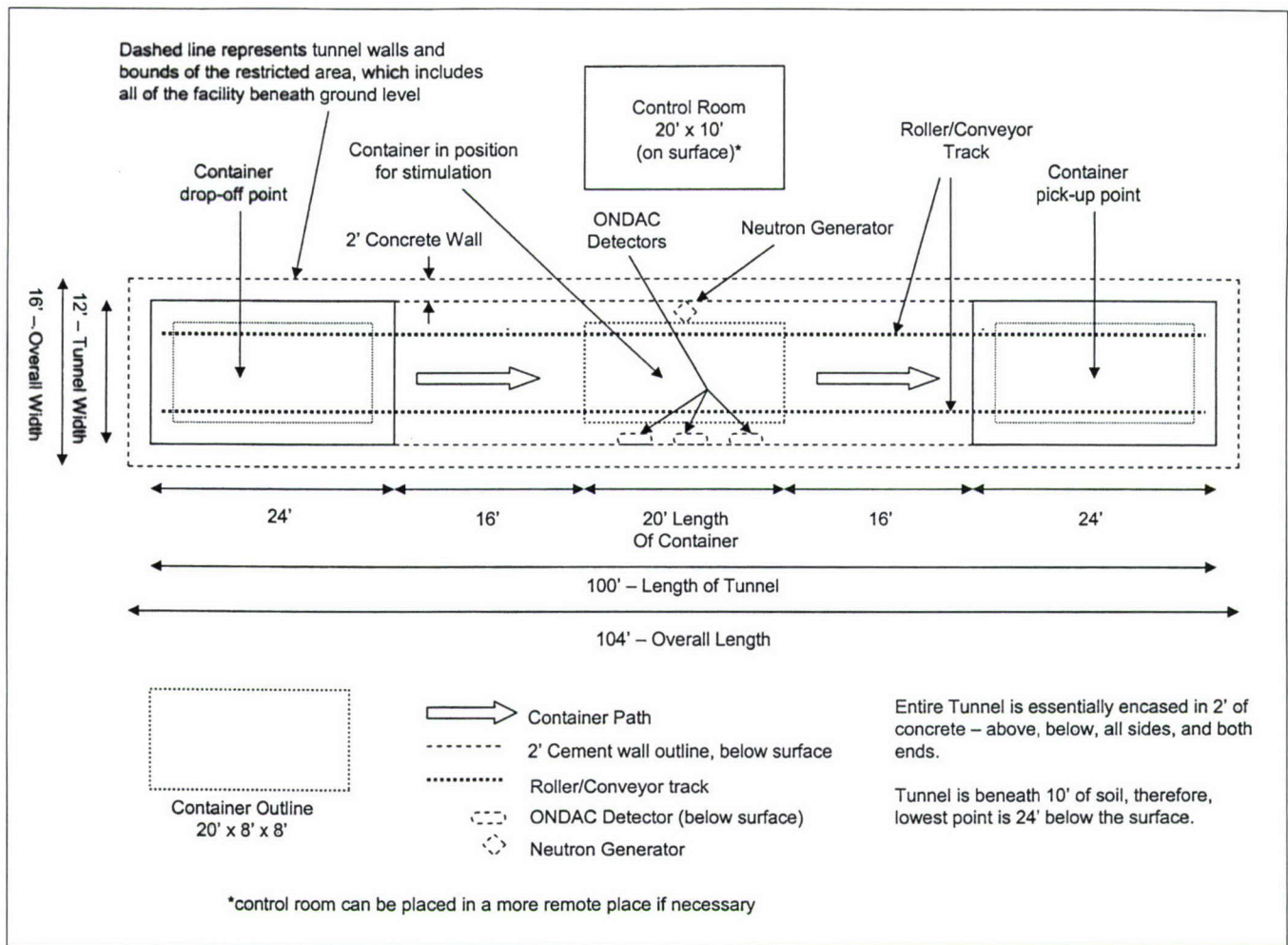


Figure 9-11. Top view of design C (subterranean version 1).

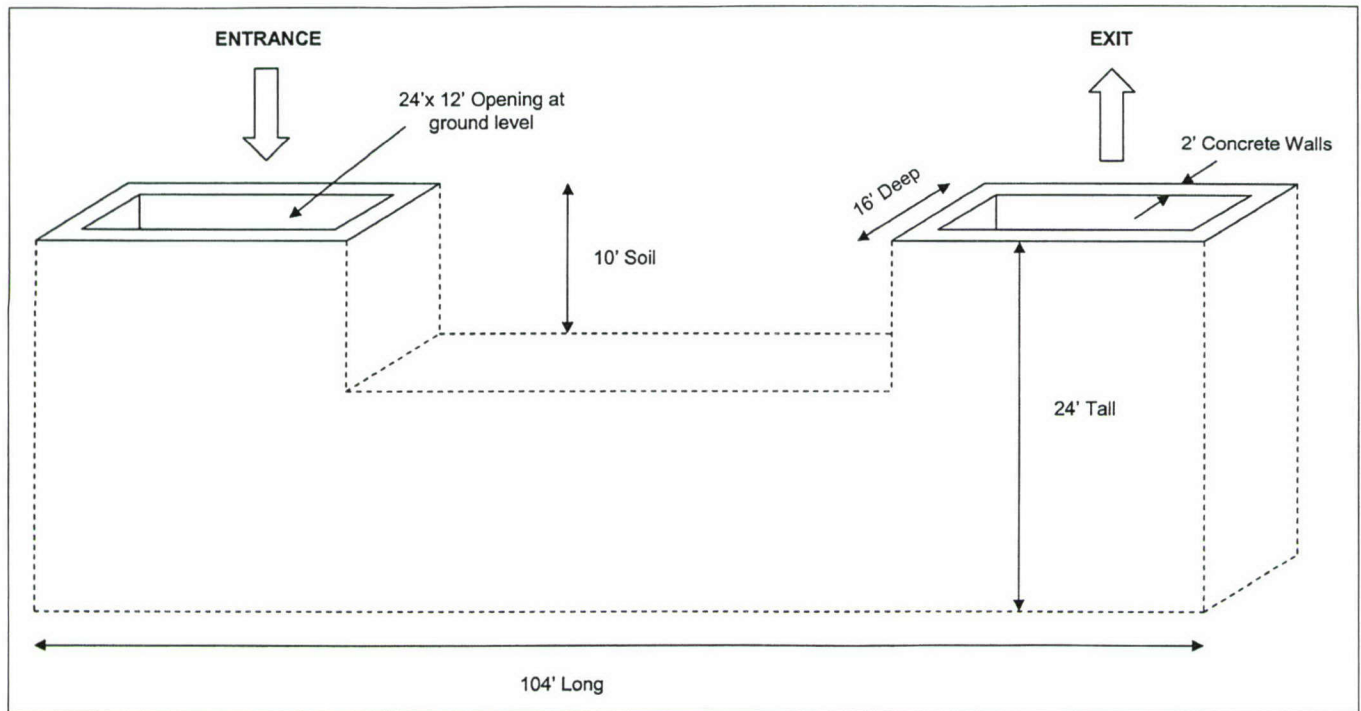


Figure 9-12. Side perspective of Design C showing outer shape of the underground facility.

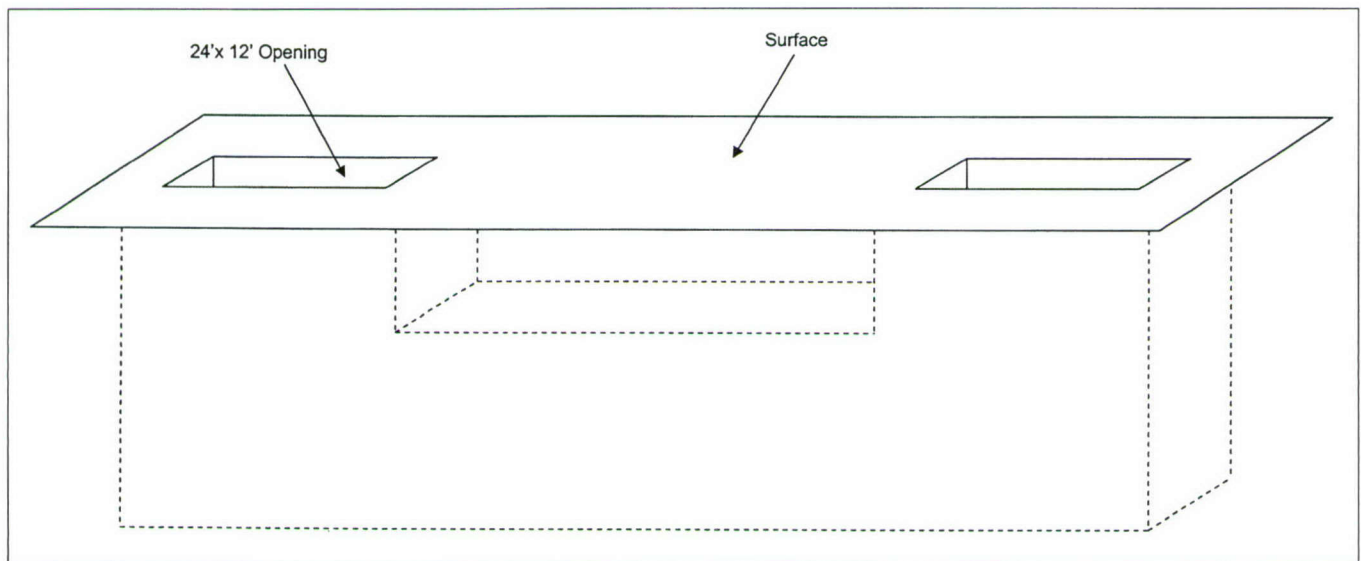


Figure 9-13. Side perspective of design C showing relation to surface.

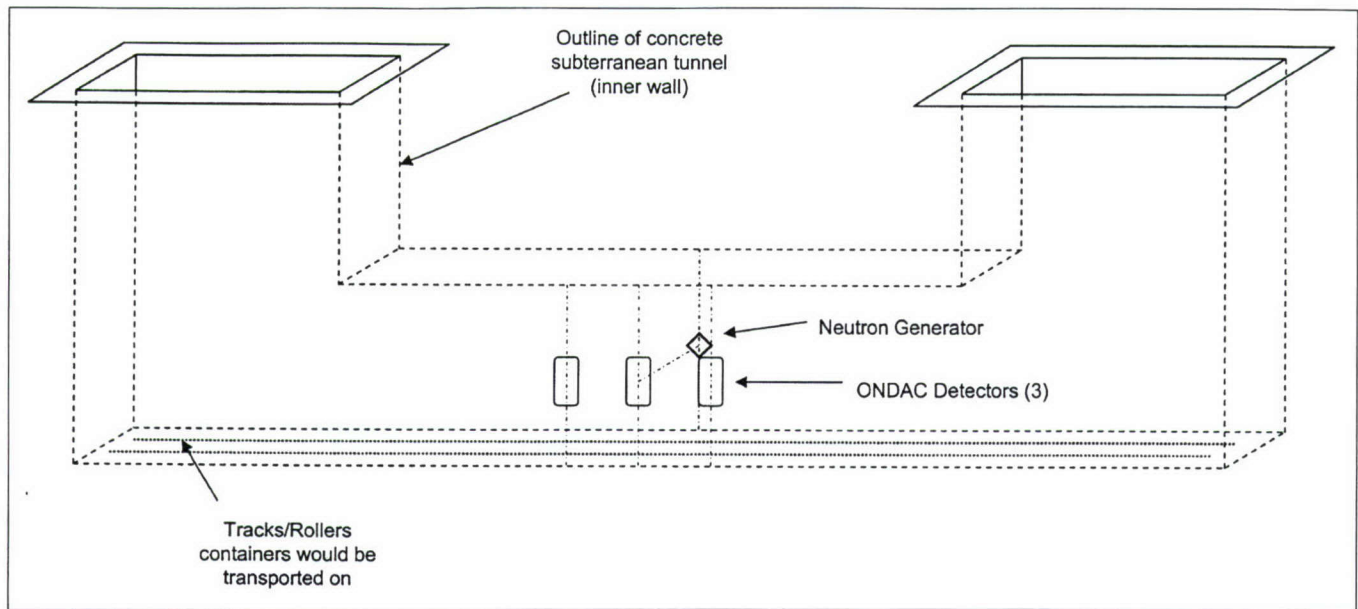


Figure 9-14. Side perspective of design C showing size of tunnel and location of neutron generator and ONDAC detectors.

Design D (Subterranean Version 2). The final design incorporates all the benefits of the three previous designs and is shown in figure 9-15. Like Design C, it is a subterranean facility where the containers must be lowered in by crane. However, instead of following a straight line path, Design D is a circular tunnel. It incorporates 12 railcars on a track that would use electric motors as propulsion. Every other car will have a container lowered onto it. The railcars in between the container carrying cars will be shielding cars and have a 3' thick concrete shield built onto them. At any given time, 5 containers can be inside this facility. The first would be a container being lowered onto a railcar, the second would be waiting to be stimulated, and the third would be the container being stimulated. After the stimulation stage, the fourth container would be in a waiting position as it safely decays with plenty of shielding surrounding it. Finally, the fifth position would be to lift the container back out of the facility. This would leave one rail car empty between the entrance and exit. This facility would have a diameter of 112' (maximum diameter of tunnel), or 116' including 2' concrete walls. Like Design C, this design also has minimal area on the surface, with only the two openings being the area taken up by the facility and a control room that can be placed at the most convenient location. This design has the added benefit of minimizing the time per container needed. Since five containers can be within the system at any given time, there is no wait time for one container to leave while the next one enters. A new container can be lowered, and one can be removed from the system, while the neutron generator is in operation. Therefore the only time between stimulations will be the time it takes to rotate the rail cars in order to line up the next container for examination. Figure 9-16 is

a perspective view of this design, showing the relationship of the surface to the circular path of the containers.

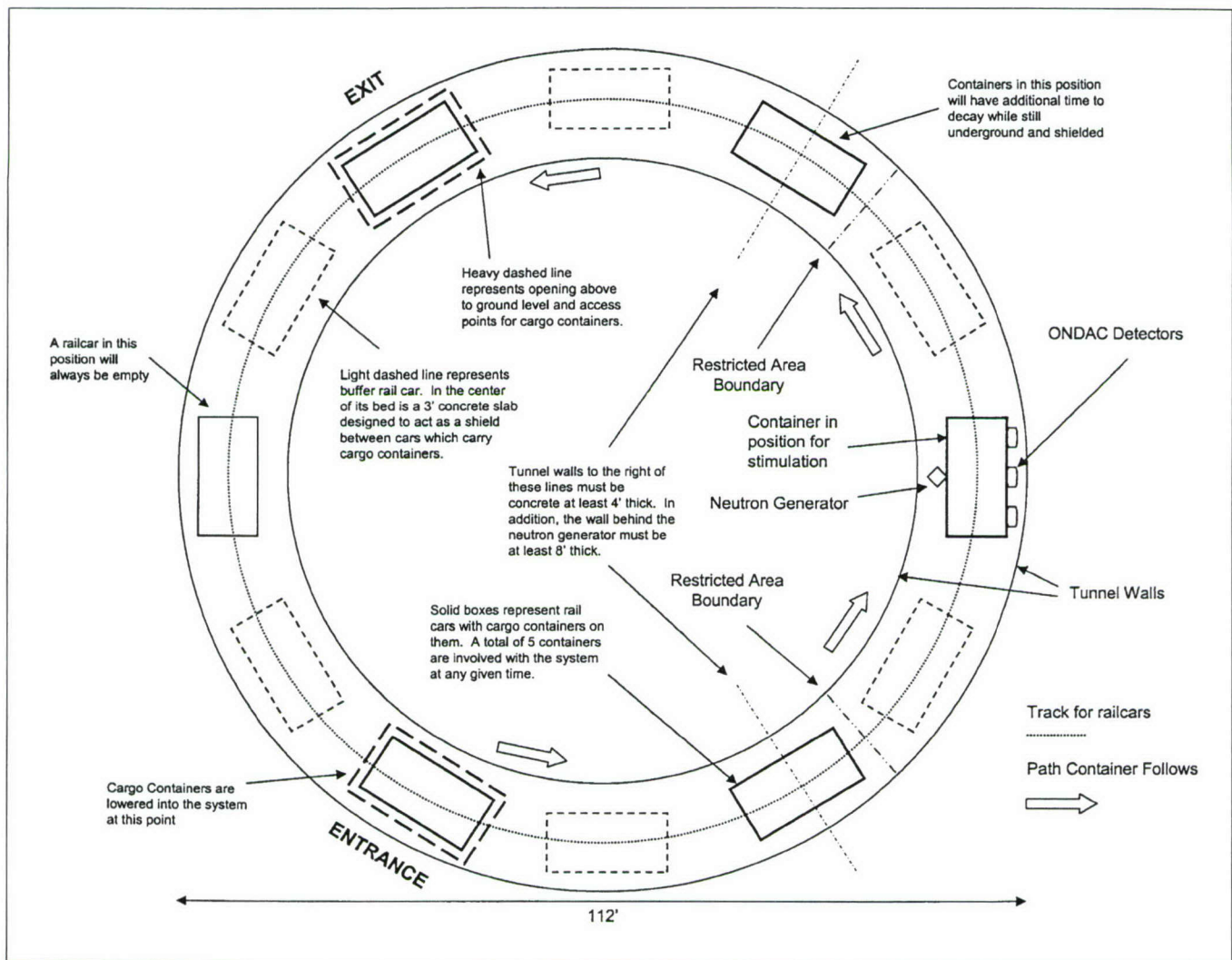


Figure 9-15. Top view of design D (subterranean version 2)
(outer concrete walls not shown).

This design also allows for the efficient integration of other existing technologies into the inspection process. For example, the container awaiting irradiation could be examined by both an x-ray imaging system and the VACIS. After the 14 MeV exposure, activation analysis using the radioisotope detection system could be performed, while the container is awaiting its removal from the facility. In this approach, vulnerabilities in one technology could be compensated for by the strengths in another technology.

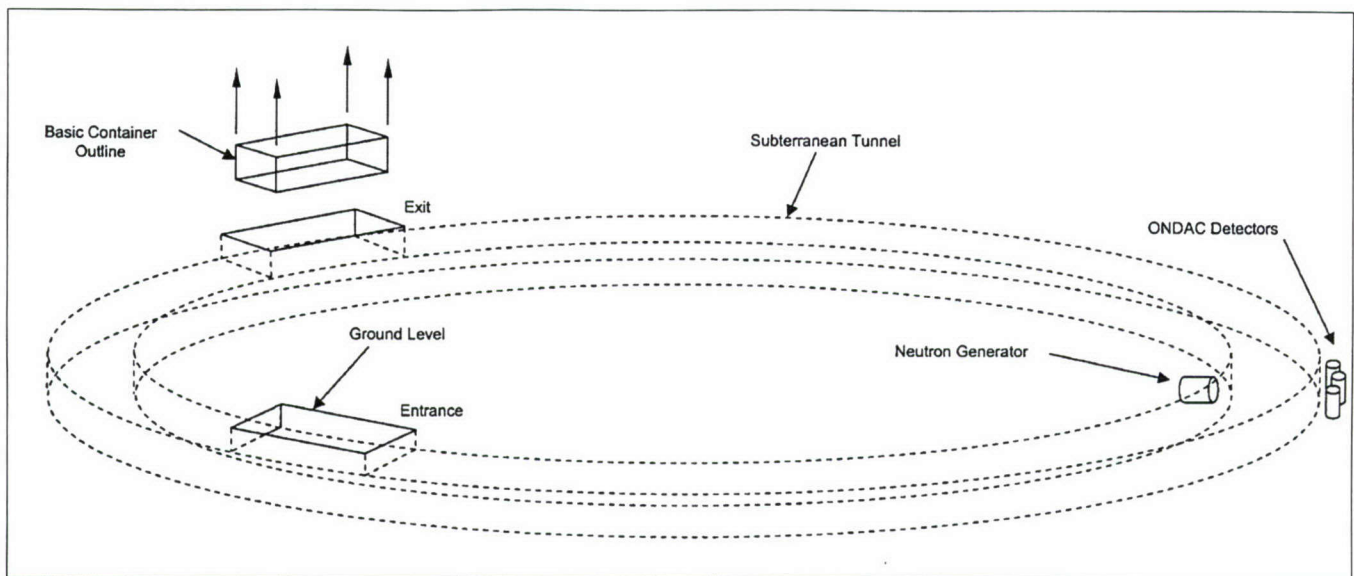


Figure 9-16. Perspective view of Design D showing relationship to surface and circular path of containers (subterranean version 2).

Every design except Design B requires workers to be within the facility to either move the container or attach the crane cable to the container. This may pose a radiation exposure risk for Design A and C since workers would have to get very close to the stimulation area immediately following operation of the neutron generator. This may not be a problem in Design C if the cable workers could find an easy way to enter and exit the facility between cycles. The entrance and exit areas in Design D would be unrestricted areas, since they would be located on the opposite side of the circular tunnel from the generator. There would also be two shielding cars between the generator and any workers in the entrance and exit wells.

9.5 CONCLUSIONS.

A number of important conclusions can be drawn from this section. First, the containers following irradiation will be radioactive. Based on current federal regulations it is most likely that all containers will need to be held in a controlled area until they reach background radiation levels, which should be no more than several days for nearly all cargo materials. Since cargo containers typically are held for five days at the Port of Baltimore, this storage requirement should not have a significant impact on the flow of commerce assuming the containers are immediately examined following their unloading from the ship. Second, the cost to build and operate a neutron stimulation facility for the first year would be slightly less than \$2 million. Less than half this amount would be required for subsequent years of operation. Third, the facility would have a capacity to examine 720 containers per week, which is 36% of the containers entering the Port of Baltimore each week. This

capacity should comfortably meet the inspection needs of the port. Fourth, a controlled area of dimensions 601' x 826' would need to be established at the port site to contain the irradiation facility and store the irradiated containers. The workers in this area would need to be given radiation dosimetry badges. Fifth, the facility design could be either that which employed a tunnel for the container's entrance and exit to the stimulation facility and located on the port's surface, or be underground with two surface openings for moving the containers into and out of the facility.

SECTION 10

COMPARISON OF GAMMA SIGNATURES IN COMMON CARGO MATERIALS TO THAT OF HEU AND REACTOR GRADE PLUTONIUM

In this section a comparison is made of the principle gammas energies emitted by common cargo materials to that generated by both HEU and reactor grade plutonium in order to assess the potential interference problems. Then these results are used to assess the feasibility of applying gamma spectroscopy techniques to detect the presence of these materials, which is the basis for the radiation isotope detector described in section 1.10. The key gamma lines of both HEU and reactor grade plutonium are reviewed in section 10.1. Section 10.2 gives the gamma emitting radioisotopes that could be contained within cargo materials along with their gamma energies and then assesses the feasibility of gamma spectroscopy analysis due to interference problems between these materials. Finally section 10.3 discusses an MCNP analysis of gamma transport from a plutonium source in a shipping container with a gamma sensitive polyvinyltoluene (PVT) detector, such as the type that would be used with the portal monitoring system described in section 1.9.

10.1 GAMMAS FROM HEU AND REACTOR GRADE PLUTONIUM.

For the purposes of this study, HEU has been taken to consist of 93% U^{235} and 7% U^{238} . Table 1-7 lists the major gammas emitted by U^{235} and their relative intensity. It is repeated below as table 10-1 for convenience.

Table 10-1. Gamma energy and intensity for decay of U^{235} (ICRP, 1983). Half-life = 7.04×10^8 years.

Gamma energy (KeV)	Intensity per 100 U^{235} decays
143.76	10.96
163.22	5.08
185.72	57.20
194.94	0.63
202.11	1.08
205.31	5.01
221.38	0.12

The U^{235} will dominate the gamma emissions in HEU due its much shorter half-life and higher intensity of gamma emissions per decay than U^{238} . The most important gamma emitted in the decay of U^{235} is that which is emitted with an energy of 185.72 KeV. As shown in table 10-1, this gamma will have over 5 times the intensity compared to the 143.76 KeV gamma, which is the isotope's second most frequent gamma emission energy. The gamma spectrum that would be produced by HEU with a high purity germanium detector (HPGe) and a 2000 channel multichannel

analyzer (MCA) is shown in figure 1-1 and repeated below as figure 10-1 for convenience.

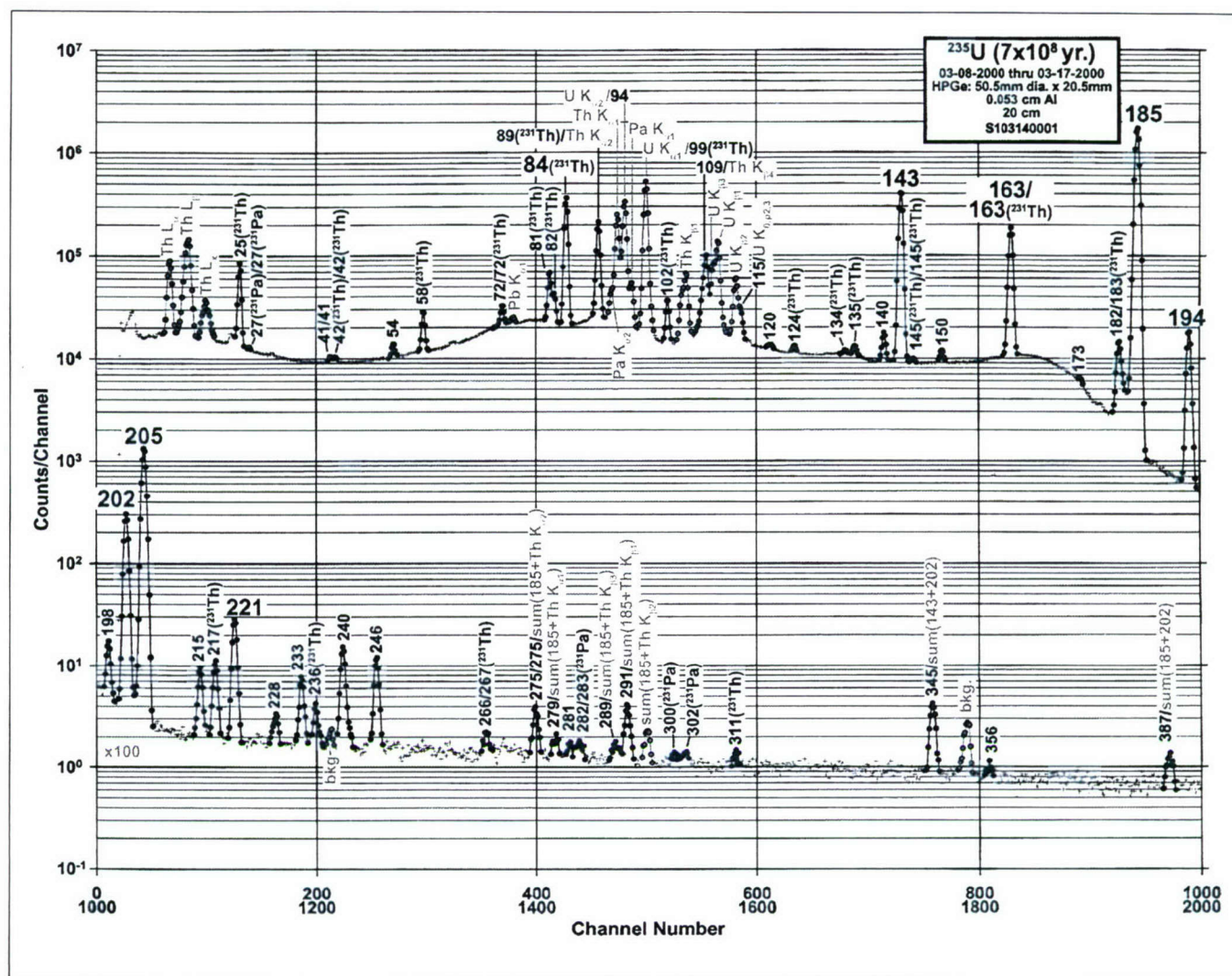


Figure 10-1. U^{235} gamma spectrum with HPGe detector and 2000 channel MCA (St. John, 2002).

Reactor grade plutonium is composed of approximately 93% Pu^{239} and 7% Pu^{240} . An underlying assumption in the above statement is that the plutonium has not been recycled in a nuclear reactor. Recycling would change the plutonium's isotopic composition and increase the importance of higher atomic weight isotopes within the material (i.e. Pu^{241} , Pu^{242} etc.). Unlike HEU, which has most of its gammas emitted at several different photopeaks, Pu^{239} emits over 200 different energy gamma rays. Its most intense gamma is emitted at 51 KeV and has an emission intensity of only .027 gammas per 100 decays. By comparison, HEU as shown in table 10-1, has an emission intensity of 57.2 gammas per 100 decays at 185.72 KeV energy. A gamma spectrum with an HPGe detector and a 4500 channel MCA for Pu^{239} is shown in

figure 10-2 and 10-3 between energies of 0 to 825 KeV. While there are numerous photopeaks in this spectrum, these figures show that the 51 KeV photopeak followed by the 129 KeV photopeak are the two most frequently counted gammas and would be the most reliable indicators for the presence of Pu^{239} . It should be noted that because the half-life of Pu^{239} is only 2.4×10^4 years compared to the 7.04×10^8 year half life of U^{235} , the time to collect a Pu^{239} spectrum is actually much less than that of a U^{235} spectrum.

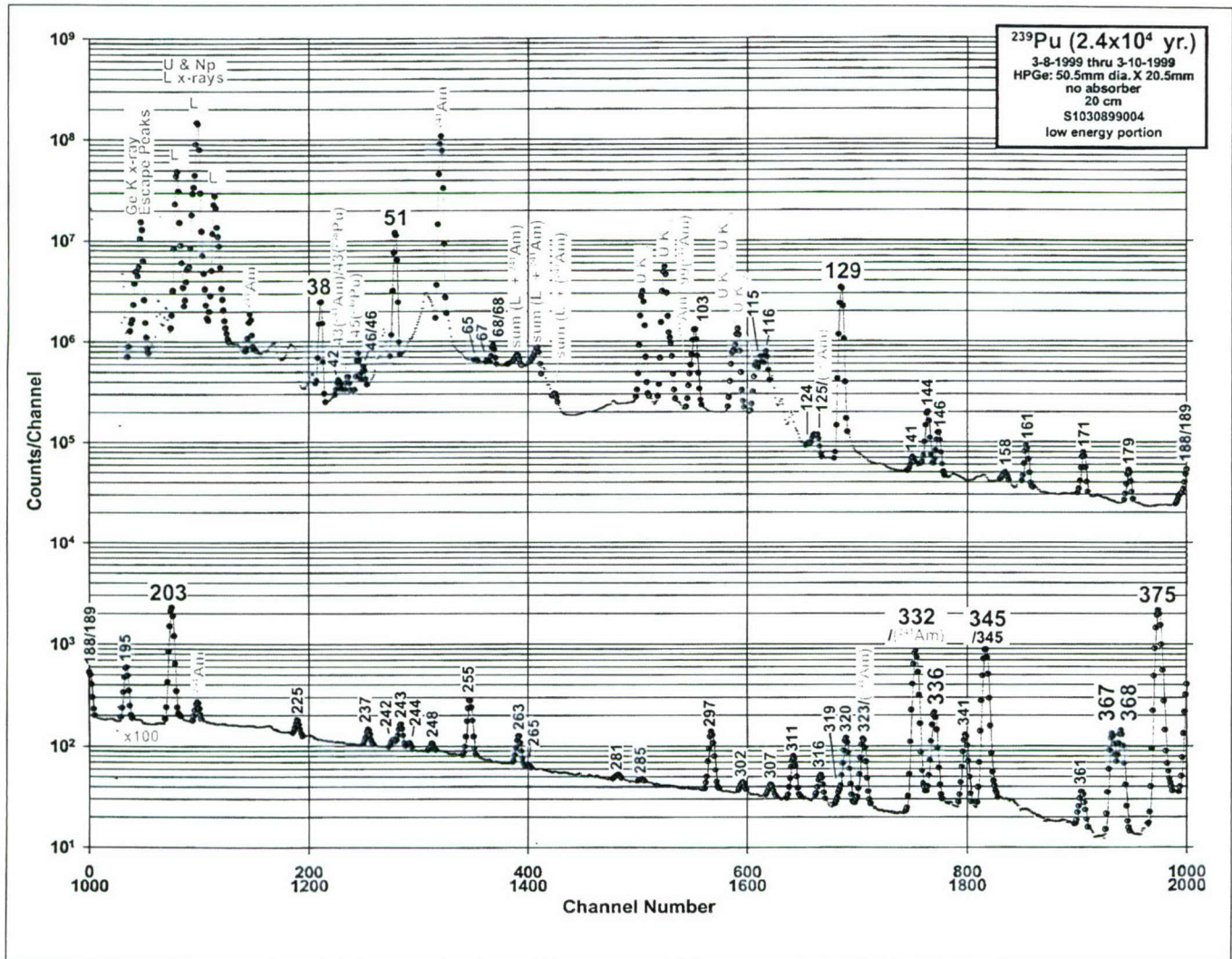


Figure 10-2. Pu^{239} gamma spectrum with HPGe detector and 4500 channel MCA (channels 1-2000) (St. John, 2002).

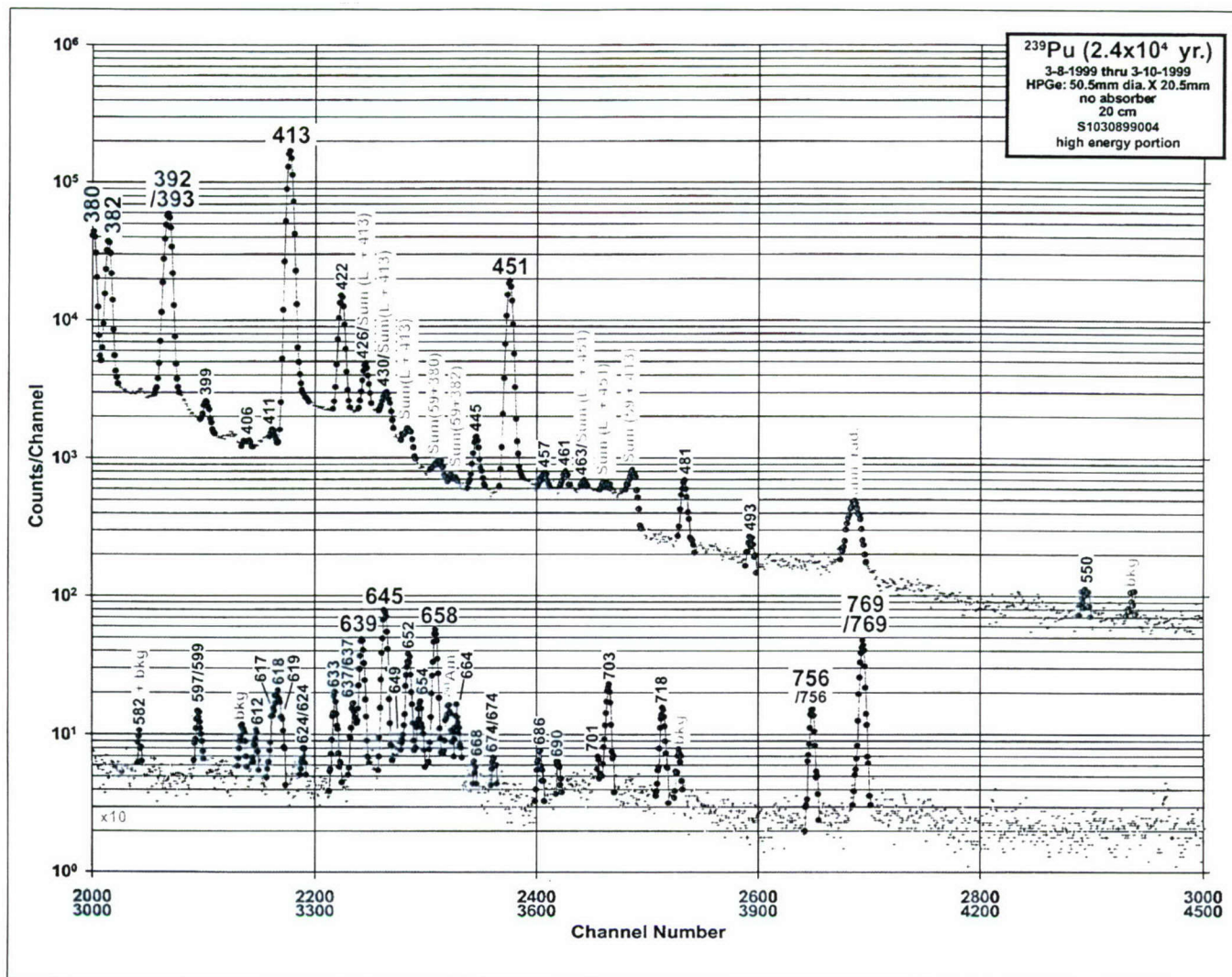


Figure 10-3. Pu^{239} gamma spectrum with HPGe detector and 4500 channel MCA (channels 2000-4500) (St. John, 2002).

The Pu^{240} gamma spectrum with an HPGe detector and a 4000 channel MCA is shown in figure 10-4. As can be seen in this figure, the two most identifying gamma energies are the 104 and 160 KeV photopeaks. Since Pu^{240} has a half-life of 6564 years or approximately one fourth the half life of Pu^{239} , it has the potential to identify the presence of reactor grade plutonium.

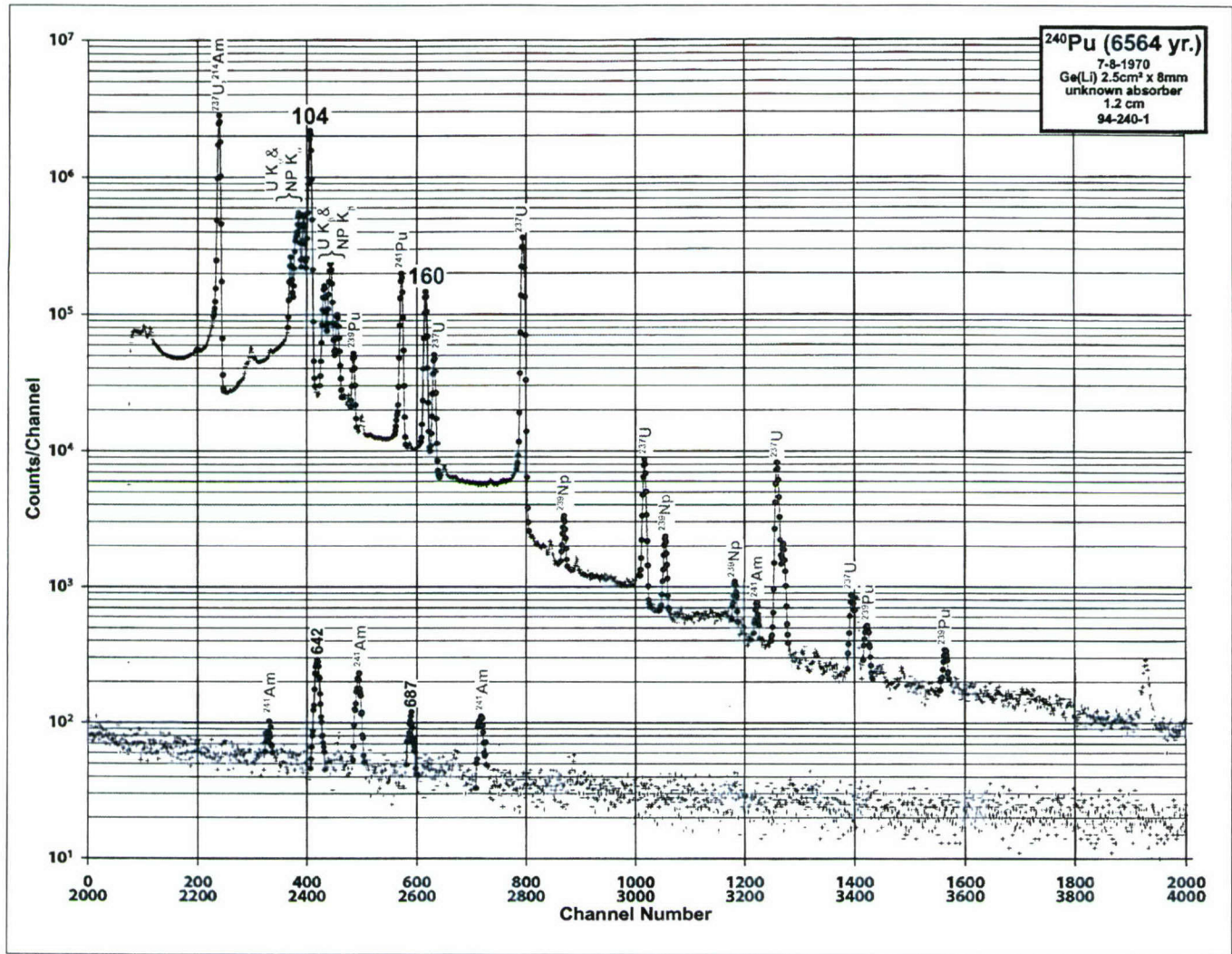


Figure 10-4. Pu^{240} gamma spectrum with HPGe detector and 4000 channel MCA (St. John, 2002).

A summary of the key gamma energy lines that would be used to identify presence of HEU and reactor grade plutonium are given in table 10-2.

Table 10-2. Summary of key gamma energies emitted by HEU and reactor grade plutonium.

Material	Identifying Gamma Energy (KeV)
HEU	186
Reactor grade plutonium	51

10.2 GAMMA EMITTING ISOTOPES IN CARGO MATERIAL.

Radioisotopes that appear in cargo materials can be divided into two classes. In the first class are those radioisotopes that occur singly, while in the second class are those isotopes that appear as

components of a radioactive chain. Table 10-3 is a list of those radioisotopes that are found in nature, along with typical cargo material in which they would be contained, the energy of the gamma(s) that they would emit, and their specific activity.

Table 10-3. Single naturally occurring radioisotopes present in cargo materials which are gamma emitters (Eisenbud, 1987).

Radioisotope	Cargo material	Gamma Energy (KeV)	Specific activity (pCi/gram)
K ⁴⁰	Many food items	1460	855.0
V ⁵⁰	Steel	780	0.003
La ¹³⁸	Specialized optical glasses	1430	20.7
Le ¹⁷⁶	Chemical catalyst	89, 203, 306	2400.0

By comparing the gamma energies in table 10-1 and table 10-2, no interference gammas are present from these radioisotopes in either HEU or reactor grade plutonium.

There are three radioactive chains that exist in nature: (1) uranium series, which originates with U²³⁸; (2) the thorium series which originates with Th²³²; and (3) actinium series, which originates with U²³⁵. The first and the last series are the constituents of HEU and cargo materials that contain high levels of isotopes in either of these series would give a gamma signature that would be a false positive. The most likely cargo materials that could serve as potential problems would be fertilizers. In particular those fertilizers, which contain a high concentration of phosphate rock from locations such as Florida or North Africa, would have elevated uranium concentrations (Eisenbud 1987). Thorium, which is the second above mentioned naturally occurring radioactive chain, is found primarily in igneous rocks and minerals. The radioisotopes in the thorium series, which are gamma emitters are given in table 10-4 along with their gamma energies.

Table 10-4. Gamma energies of radioisotopes in thorium series (Cember, 1983).

Radioisotope	Gamma Energy (KeV)
Ac ²²⁸	908, 966, 1590
Th ²²⁸	84
Ra ²²⁴	241
Th ²²⁶	542
Pb ²¹²	239
Bi ²¹²	40
Tl ²⁰⁸	2610

By comparing the gamma energies in table 10-2 and table 10-4, no interference gammas are present from these radioisotopes. The conclusion from this analysis is that only cargo materials with elevated uranium concentrations, such as fertilizers from specific locations, would cause interference problems leading to false positives with gamma spectroscopy.

10.3 MCNP ANALYSIS OF GAMMA TRANSPORT FROM A PLUTONIUM SOURCE IN A SHIPPING CONTAINER TO AN EXTERNAL PORTAL MONITORING SYSTEM (ST. JOHN, 2003).

To assess the feasibility of gamma spectroscopy in the detection of HEU or plutonium, not only the production of interference gammas needs to be evaluated, but the frequency needs to be estimated that the gammas emitted by nuclear material will interact with a sensing detector external to the container. In this section an MCNP analysis is presented which studied the gamma interaction rate from a 4 kg plutonium source centrally located inside a shipping container with a polyvinyltoluene (PVT) detector located outside the container with and without low atomic number cargo materials present. The results from this analysis are then used to extrapolate to the expected behavior of gamma monitoring system for a 1 kg HEU source.

PVT was chosen as the external detector material because it is commonly used in such applications. PVT is a scintillating plastic that is sensitive predominately to gammas and insensitive to other types of radiation. Scintillation detection systems are useful only for gross counting, and when combined with photodiodes can be used for imaging purposes.

The 4 kg plutonium source was modeled as a sphere composed of 93% Pu^{239} , 6.5% Pu^{240} , and a 0.5% Pu^{241} by mass, which is the isotopic composition of weapons grade plutonium (Kokoski 1995). This composition is nearly identical to reactor grade plutonium discussed in section 10.1. Plutonium's 155 discrete gamma energies between 100 KeV and 1057 KeV were modeled as 10 discrete emission bins in order to simplify the MCNP model (Brown, 1986). The initial MCNP runs showed that the plutonium would strongly self absorb the photons internally generated inside the sphere. To improve the MCNP run time and the resulting statistics with the output, the corresponding gamma spectrum emitted by the volume source was converted into a surface source with a thickness of 0.5 mm. Figure 10-5 shows the gamma spectra for plutonium, modeled both as a spherical and a surface source. The difference in these spectra is the preferential self absorption of the lower energy gammas by the plutonium. The y-axis in figure 10-5 is the rate the gammas are emitted from each bin from 4 kg of plutonium. This rate was determined by multiplying the gammas per second produced by this mass of plutonium (i.e. 2.14×10^9 gammas/sec) by the probability the gamma would be emitted into that bin. The probability a gamma would be emitted into a particular bin

was determined from the output of MCNP based a run of 4×10^9 particles.

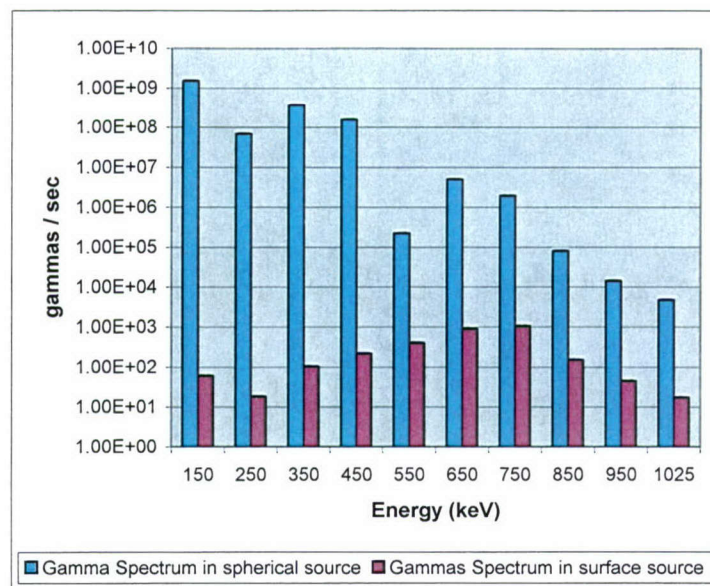


Figure 10-5. 4 kg plutonium gamma spectrum for volume and surface source modeled as 10 bins between 100 and 1057 KeV.

The discrete spectra shown in figure 10-5 compared satisfactorily with published data (Sampson, 1991).

The container was modeled as a 20 foot long Seabox, Inc. cargo container whose dimensions were 243.8 cm x 605.8 cm x 259.1 cm box with a 2 mm thick aluminum wall. These container dimensions are almost identical with the benchmark facility. The only significant difference is that container wall material in this analysis is aluminum, while in the benchmark facility it was iron. Below the container, the model had a 100 cm deep box of silicon oxide, which represented dry sand. Ten PVT plastic scintillators, which represented a portal monitoring system, were each represented as a rectangular box of dimensions, 3 cm x 30 cm x 260 cm, and were located 0.5 m from the outer wall of the container. Thus the PVT detectors extended along the entire height of the container, were each 30 cm (1 foot) wide, and had a thickness of 3 cm. The first detector was located on the container midplane with each successive detector places 30 cm to the right. Figure 10-6 is a 3-D depiction of the model showing only the midplane PVT detector. In this model, the PVT detector system extends over one half the container length on one side of the container when all 10 PVT detectors are modeled. Since the plutonium source was located in the center of the container, the gamma/detector interaction results of the model could be extrapolated to the case where a PVT detector system extended along both sides of the container, simply by multiplying these results by a factor of 4.

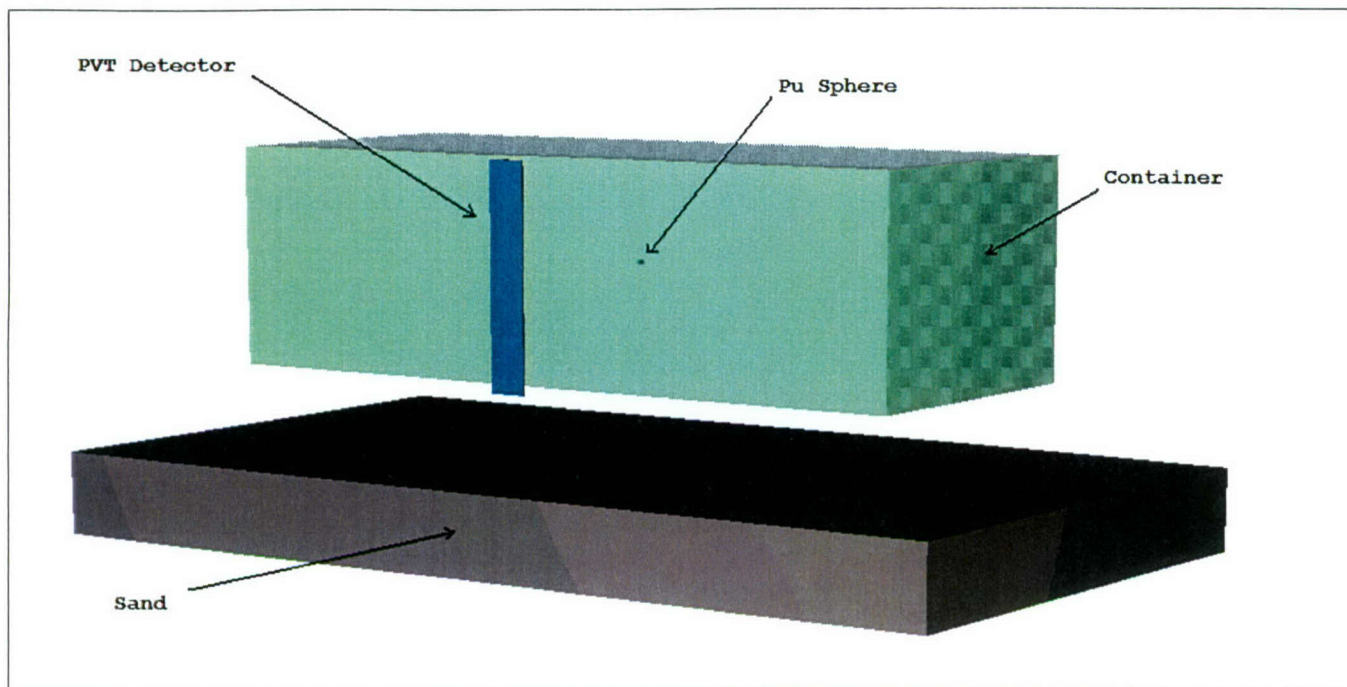


Figure 10-6. MCNP model of container with plutonium source and single PVT detector located at the container midplane.

The MCNP input file for this model with air as cargo is given in appendix A.

The model was examined for three cases: (1) empty container with only air inside; (2) container filled with water; and (3) container filled with aluminum. Water was chosen, because gamma transport through it would correspond to many food items. Both water and aluminum were given a density of $.73 \text{ grams/cm}^3$ so that the cargo weight would be a payload of 28,000 kg, which is the maximum payload of this size Seabox container. Water's actual density is 1 gram/cm^3 , while aluminum's real density is 2.7 grams/cm^3 . So this assumption would result in an underestimation of both material's effect on the gamma interaction rate in the external detector.

Figure 10-7 shows the gamma interaction rate in the PVT detector as a function of distance the PVT detector is from the midplane of the container when the container is empty. The figure was obtained by taking the MCNP output, which is given in interactions per source particle, and multiplying this result by the source emission rate ($2.14 \times 10^9 \text{ gammas/sec}$). As can be seen, if the PVT detector is in the center (lined up with the source and zero distance from the midplane), the interactions are a maximum with 56 gamma interactions occurring per second. The detector near the end of the container (270 cm from the container midplane), the interaction rate will be a minimum and was found to decrease to 18 interactions per second.

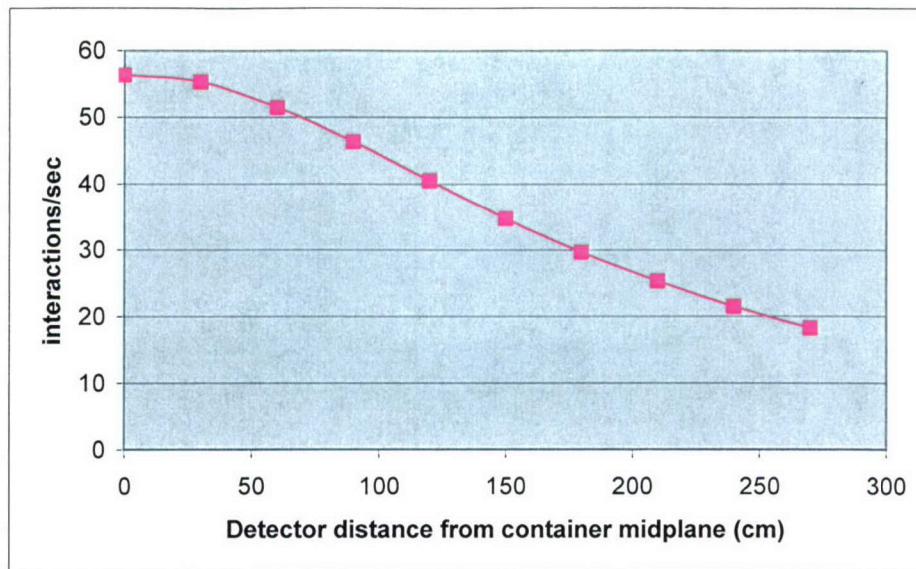


Figure 10-7. PVT detector gamma interaction rate as a function of its distance from container midplane with no cargo.

The data from figure 10-7 also shows that 10 one foot wide gamma detectors located from the midplane to the end of the container would have approximately 6.4 times the interaction rate as a single one foot wide PVT detector located in the center. Hence, if both entire lengthwise sides of the container had PVT detection systems, then the gamma interaction rate would be increased by a factor of 25.5 over that of a single centrally located PVT detector.

These calculations were repeated with the container filled with aluminum and water. Table 10-5 summarizes the results obtained for the midplane PVT detector. They were obtained by multiplying the MCNP output by the source strength. The second column gives the interaction if the entire lengthwise container sides were surrounded by PVT detectors. Also the number of MCNP case histories run is given for each material in the third column.

Table 10-5. Gamma interactions/sec with single midplane PVT detector and with entire container (243.8 cm x 605.8 cm x 259.1 cm) surrounded by PVT detector with 4 kg plutonium source located in container center.

Cargo material	Interactions/sec with single midplane PVT detector	Interactions/sec with entire container sides surrounded by PVT detector	MCNP case histories run
Air	56.30	1435.6	1×10^8
Aluminum	1.08	27.5	5×10^8
Water	0.75	19.1	5×10^8

As can be seen a significant attenuation in the number of interactions occurred with the presence of either cargo material. Since both aluminum and water have low atomic numbers relative to a material like lead, they are not considered effective gamma absorbers. However, the results of this analysis show that all cargo materials will greatly attenuate the gamma from the source. If the cargo was a higher atomic material, the expected gamma interaction would be very low, making it essentially indistinguishable from background.

The other problem with a gamma measurement system would be the likely high number of false positives from certain cargo materials. As mentioned in table 10-6, many food items contain a large quantity of potassium, which results in gamma emissions from K^{40} . Table 10-6 is a list of common foods, along with their potassium concentrations.

Table 10-6. Potassium-40 concentration in food.

Food	K-40 Concentration (pCi/g)
Dried Fruits	10.2 - 2.5
Fresh Fruit	2.5 - 0.7
Fruit Juice	1.8 - 1.0
Cereals	8.8 - 2.5
Dairy Products	1.5 - 1.3
Vegetables	4.3 - 0.9
Meat & Fish	4.3 - 2.1

Thus containers on trucks containing such items as milk, bananas, etc., would pose a problem if the system threshold was set low enough to detect elevated radiation levels associated with 4 kg of plutonium or 1 kg of HEU.

10.4 CONCLUSIONS.

This section has drawn several major conclusions. First is that gamma spectroscopy can distinguish between either HEU or reactor grade plutonium and singly natural occurring radioisotope that would be present in cargo materials. Gamma spectroscopy would also be successful in distinguishing HEU and plutonium from thorium and its daughter products. However, gamma spectroscopy would fail (i.e. produce false positives) for those cargo materials that contain isotopes in the uranium and actinium series. The principle cargo materials that contain the isotopes would be fertilizers and stones/rocks used for building material stones, such as granite.

Another conclusion of the section is that low Z materials, such as many common food items, will strongly attenuate the gamma signature from plutonium in a large shipping container. Since the isotopes of HEU have much shorter half-lives than the isotopes in reactor grade plutonium, while their gamma energies are not that much different, this problem also occurs in HEU. Thus portal monitoring systems, which rely on gross counting techniques, will yield many false positives if their thresholds are set to defeat the presence of a few kilograms of either HEU or Pu²³⁹.

SECTION 11

CONCLUSIONS AND RECOMMENDATIONS

11.1 CONCLUSIONS

The study started by reviewing three existing technologies that are being considered for use within the container security initiative (CSI) program. These technologies are as follows: (1) VACIS; (2) Portal Monitoring System; and (3) Radiation Isotope Detection system. It was concluded that each of these technologies has vulnerabilities which prevent them from successfully detecting the presence or absence of 1 kg of HEU within a large shipping container (i.e. 20' x 8' x 8') in a relatively short period of time without entering the container. Hence it was concluded that there is a need for an improved technology approach, such as external neutron stimulation, and that this technology could be successfully integrated into the current CSI program.

A number of conclusions were drawn with regard to the use of the neutron stimulation technology. The most important conclusion is that this approach should be successful even if the source/detector are configured in a relatively simple manner. The study reached the conclusion that this approach would not be defeated by the presence of most different types of cargoes, and in some cases such as lead, the detection of HEU would actually be enhanced. In order for the approach to succeed in an optimal manner, a single 14 MeV neutron source with a strength of 10^{12} neutrons/sec would need to be cycled 48 times during an examination period of approximately 300 seconds. This study found that counting prompt neutrons is futile, but instead one needs to count the neutrons after the prompt neutrons have dissipated and the neutron environment is dominated by HEU delayed neutrons (if it is present in the container) as well as background neutrons. The neutron detector employed must have high efficiency. In this study, the neutron detector chosen was the ONDAC for modeling purposes. The ONDAC detector is composed of nine commercially available He^3 tubes filled to pressure of 10 atmospheres with each tube surrounded by polyethylene. The ONDAC dimensions are very small compared to the container as they are only (.34' x .66' x .66'). The study chose the 10^{12} neutron/sec source strength, as this appears to be technically achievable with current technology.

The study investigated the limits of this approach staying within the single source/detector configuration. It found that the density of the material and the atom fraction of hydrogen were the most important parameters in affecting the neutrons that would be detected in the ONDAC with and without HEU present per source particle. The study concluded that if the cargo had a density equal to that of water (i.e. 1 gram/cm³) and a hydrogen atom fraction of 15% or less, then the HEU could still be detected. In order for the technique to

succeed when the above conditions don't exist, several options were suggested. First, one could increase the source pulse rate above 10^{12} neutrons/sec, although this may not be technically feasible given the state of current technology without a major research and development effort. Second, one could employ a multiple source/detector configuration. Third, if no high atomic materials were present in the cargo, one could employ gamma detection methods. Fourth, an internal inspection could be made of the cargo contents.

The study also concluded that the dose rate to facility personnel would be brought far below current radiation protection standards if an eight foot concrete shield was used behind the neutron source.

The study analyzed the effect of moving the 14 MeV stimulation source to greater distances away from the side of the container. As expected, as the distance the source was positioned farther from the side of the cargo container, the more difficult the system was in being successful. However, increasing the pulsed neutron source could compensate for this distance effect. It was concluded that if the 14 MeV source strength were increased to 10^{14} n/sec, then this technology would be successful to detect 1 kg of HEU with the source 24 feet from the container.

The cargo within the container would be activated by this technology. Current government regulations would require that the container be at background radiation levels before being released from the port. The study performed both an empirical and experimental analysis of this activation problem. For the wide range of materials examined, all were found to return to background radiation levels within several days. Based on a review of the Port of Baltimore operations, it was concluded that such a holding time would not have a significant impact on the flow of commerce, assuming the containers were immediately examined by this technology following their unloading from the ship.

A feasibility study was conducted on important regulatory and engineering aspects that would arise in the construction of a stimulation facility at a port site. It was concluded that a controlled area would be needed that enclosed the facility and provided for a storage area for the activated containers until they reached background radiation levels. Based on the Port of Baltimore data, the size of this area was determined to be 601' by 826'. The port workers in this area would need to be treated as radiation workers and have a radiation monitoring program. Second, the cost to build and operate a neutron stimulation facility for the first year would be slightly less than \$2 million. Less than half this amount would be required for subsequent years of operation. Third, the facility would have a capacity to examine 720 containers per week, which is 36% of the containers entering the Port of Baltimore each week. This capacity should comfortably meet the inspection needs of

the port. Also four different facility design layouts were developed for the facility, two of which would locate the facility on the port's surface, while the other two were subterranean designs.

The study compared gamma signatures of common cargo materials to that of HEU and reactor grade plutonium drawing several major conclusions. First, gamma spectroscopy can distinguish between either HEU or reactor grade plutonium and singly natural occurring radioisotopes that would be present in cargo materials. Gamma spectroscopy would also be successful in distinguishing HEU and plutonium from thorium and its daughter products. However, gamma spectroscopy would fail (i.e. produce false positives) for those cargo materials that contain isotopes in the uranium and actinium series. The principle cargo materials that contain the isotopes would be fertilizers and stones/rocks used for building material stones, such as granite.

Another conclusion of the section is that low Z materials, such as many common food items, will attenuate the gamma signature from plutonium making short count times in technologies such as portal monitoring system or radioisotope detector impractical. Since the isotopes of HEU have much longer half-lives than the isotopes in reactor grade plutonium, while their gamma energies are not that much different, this problem would also occur in HEU.

After evaluating the current methods and technologies used to prevent the passage of SNM through cargo containers, the study has concluded that a system using neutron stimulation is effective and necessary for better detection of HEU in U.S. ports. This new facility will have a place in the current inspection matrix used by U.S. Customs, and the use of this system should have a minimal effect on the flow of commerce into the United States.

11.2 RECOMMENDATIONS FOR FUTURE WORK.

The key to this technology is the availability of a pulsed 14 MeV, 10^{12} neutron/sec source. Neutron generators with long operating lifetimes must be developed with this capability before this technology can be practically implemented. Therefore, an updated assessment should be performed on the state of this technology, which would be needed to support the operation of the neutron stimulation facility.

As mentioned in section 4.3, the largest commercially available pulsed 14 MeV neutron generator has an output of only 3×10^8 n/sec, which is nearly 3300 times smaller than the neutron source of 10^{12} n/sec used in the benchmark facility design. A next step in the development of this technology would be the development of a detailed design and cost estimate of a facility, scaled in dimensions in order to replicate the neutron environment during the examination process in the benchmark facility. This facility would then be used to

collect data with different cargo materials in order to demonstrate the validity of the predictions made in this report and to gain experience in the design of a full scale facility.

In order to estimate the characteristics of this scaled facility, the following assumptions were made:

- (1) HEU located in the center of the scaled and benchmark facility;
- (2) Stimulation source and the monitoring detector positioned at both facility walls;
- (3) Counts per minute in monitoring detector same in scaled facility and benchmark facility.

Consequently, by using equation (4.14) and canceling out identical terms, the ratio of the dimensions of the benchmark to the scaled facility can be estimated by the equation:

$$\frac{CPM_{BMF}}{CPM_{SF}} = \frac{\dot{Q}_{BMF} / r_{BMF}^4}{\dot{Q}_{SF} / r_{SF}^4} = 1 \quad (11.1)$$

where

CPM_{BMF}	=	counts per minute benchmark facility
CPM_{SF}	=	counts per minute scaled facility
\dot{Q}	=	benchmark facility neutron source output, 1×10^{12} n/sec
\dot{Q}	=	scaled facility neutron source output, 3×10^8 n/sec
r_{BMF}	=	distance neutrons travel in benchmark facility to reach ONDAC detector
r_{SF}	=	distance neutrons travel in scaled facility to reach ONDAC detector

Rearranging equation 11.1 gives the following result:

$$\frac{r_{BMF}}{r_{SF}} = \left(\frac{\dot{Q}_{BMF}}{\dot{Q}_{SF}} \right)^{\frac{1}{4}} = 7.59 \quad (11.2)$$

Equation (11.2) can also be used to scale the facility with a different source output other than 3×10^8 n/sec. The scaled facility could also operate with less HEU since the external neutron detector detection efficiency would be much larger in this smaller size facility. Table 11-1 give a comparison of some estimated characteristics between these two facilities.

Table 11-1. Comparison of basic parameters in both benchmark and scale neutron stimulation facility assuming a pulsed source strength of 3×10^8 n/sec.

Item	Benchmark Stimulation Facility	Scaled Neutron Stimulation Facility
Container Dimensions	20' x 8' x 8'	2.63' x 1.05' x 1.05'
HEU Requirement	1.00 kg	0.11 kg
Detector Requirement	1 ONDAC (9 He-3 detectors)	1 He-3 detector
Neutron Source Requirement	10^{12} n/sec	3×10^8 n/sec
Estimated CPM at detector during pulsing	800	800

Included in this scaled facility design would be electronic hardware needed to pulse the generator and make the neutron measurements.

It is further recommended that a more advanced engineering design be performed, which integrates the stimulation technology with other current inspection technologies in order to more efficiently utilize US Customs resources at ports during the inspection process. In this integrated design, one would have available at least three different systems each having different monitoring capabilities. The three systems would include a commercial x-ray based cargo imaging system, the neutron stimulation system, and a radioisotope detection system. The radioisotope detecting system could look at the container's gamma signature before as well as after the container was exposed to the neutron stimulation in order to determine the presence of any undesirable materials (i.e. nuclear materials, chemicals, or illegal drugs). The integrated system would be spatially efficient as the x-ray imaging systems are based on the use of backscattered radiation, while the neutron stimulation and radioisotope detection systems make measurements after the radiation has been transmitted through the container. Thus the x-ray imaging systems and both the radioisotope and the neutron stimulation detection systems would be located on opposite sides of the container. Finally, the container could be scanned in a portal monitoring system such as that described in section 1.9 prior to leaving the port. Such an integrated system would almost be impossible to defeat, because its response would rely on widely different physical principles for different materials.

The analysis performed in this report could be expanded in several other areas. First, the activation study presented in this report while extensive is not complete. It is also recommended that this

study be expanded to a wider range of cargo materials to determine the decay time of such materials not covered in this report. Table 1-2 contains a comprehensive list of imported products that could be examined.

Secondly, an analysis could be performed, which considers the potential to count prompt gammas (i.e. gammas emitted from fissioning) following neutron stimulation. This approach has the potential to be high effective for HEU detection in systems with a large hydrogen content.

The final recommendation is to use a calibrated thermal neutron detector such as that developed by Dirk (Dirk, 2002) to perform thermal neutron background measurements at various US ports of entry. This new data is very important in order to properly estimate the magnitude of the ONDAC detector response that is due solely to background counts. In section 4.7, the ONDAC background response was assumed to be approximately 100 CPM based on data from LANL (Murphy, 1998). This background count rate was the basis of the 10^{12} n/sec source strength because at this magnitude the 1 kg delayed neutron HEU CPM in the ONDAC would be approximately 1000 CPM or ten times that due to background.

Undertaking these recommendations will ensure that when the stimulation facility is built, it will be a useful technology tool for the Department of Defense and the US Customs service in the US war against nuclear terrorism at defense bases or commercial shipping ports.

SECTION 12

REFERENCES

- 10CFR20.1003 Definitions, U.S. Nuclear Regulatory Commission, 2002.
- 10CFR20.1201 Occupational Dose Limits for Adults, U.S. Nuclear Regulatory Commission, 2002.
- 10CFR20.1206 Planned Special Exposures, U.S. Nuclear Regulatory Commission, 2002.
- 10CFR20.1301 Dose Limits for Individual Members of the Public, U.S. Nuclear Regulatory Commission, 2002.
- 10CFR20.1601 Control of Access to High Radiation Areas, U.S. Nuclear Regulatory Commission, 2002.
- 10CFR20.1902 Posting Requirements, U.S. Nuclear Regulatory Commission, 2002.
- 10CFR35.92 Decay-in-Storage, U.S. Nuclear Regulatory Commission, 2002.
- 10CFR36.25 Shielding, U.S. Nuclear Regulatory Commission, 2002.
- Abkemeirer, E.J. RASO Radiation Project Manager, Private Communication, March 28, 2003.
- Alfassi, Z.B., "Activation Analysis," Volume II, CRC Press, Boca raton, Florida, 1990.
- Americana Impex Consulting Co., "Mobile Vehicle and Cargo Inspection System," www.americanaimpex.com/cargo.htm, 2003.
- Anzelon, G., Hammond, W., Nicholas, M., "IAEA Illicit Trafficking Database Programme", IAEA Bulletin, issue 43, p.15, April, 2001.
- AS&E website. www.as-e.com/index.html.
- Austin, D.J., U.S. Customs Service, Baltimore, Maryland, Port of Baltimore Interview, February 5, 2003.
- Batchelor, R. Hyder, H.R. McK., no title, Journal of Nuclear Engineering, v. 3, 1956.
- Beckwith, Thomas G., Marangoni, Roy D., and Lienhard, John H.V. "Mechanical Measurements", 5th ed. Reading, MA: Addison-Wesley, 1993.

- Berger, H., "Neutron Radiography," Elsevier Press, Amsterdam, The Netherlands, 1965.
- Berger, J.D., Watson, E.E., Cloutier, R.J., "Health Physics Aspects of Low-Energy Accelerators", Proceedings on Conference on the Use of Small Accelerators for Teaching and Research, Oak Ridge Associated Universities, Oak Ridge Tennessee, April, 1968.
- Boerse, J.J., no title available, Kerntechnik, v. 9, 1967.
- Bonner, T.W. Bame, S.J., Evans, J.E., no title available, Physical Review, v. 101, 1956.
- Brown, D., Gozani, T., Stevenson, J., Ryge, P., Sivakumar, M., Loveman, R., Liu, F., "Pulse Fast Neutron Cargo Inspection System", Ancore Corporation, Santa Clara, Cal., www.whitehousedrugpolicy.gov/ctac/ctac01/pdfs/12/PULSEDFASTNEUTRON.pdf, 2001
- Browne, E., Firestone, R.B., "Table of Radioactive Isotopes", John Wiley and Sons, New York, New York, 1986.
- Bunn, G., Bunn, M., "Nuclear Theft and Sabotage", IAEA Bulletin, issue 43, p.20-29, April, 2001.
- Burgy, Pardue, Willard, Wollan, no title available, Physical Review, v. 70, 1946.
- Caldwell, J.T., Hastings, R.D., Herrera, G.C., Kunz, W.E., "The Los Alamos Second-Generation System for Passive and Active Neutron Assays of Drum Size Containers", LANL report LA-10774-MS, September, 1986.
- Chen, G., Lanza, R., "Fast Neutron Resonance Radiography for Elemental Mapping", Massachusetts Institute of Technology, Cambridge, Massachusetts, www.whitehousedrugpolicy.gov/ctac/ctac01/pdfs/12/FASTNEUTRONRESONANERADIOGRAPHY.pdf, 2001.
- Cloutier, R.G., no title available, American Industrial Hygiene Association, vol. 24, 1963.
- Costello, R., Baltimore Port Authority, Baltimore, Maryland, Port of Baltimore Interview, February 5, 2003.
- Csikai, G., Lantos, Z., Buchzo, C. "Investigations on the properties of D & D and D & T neutron sources", Proceedings at the Advisory Group meeting on Properties of Neutron Sources, Leningrad, USSR, June 9-13, 1986, Vienna IAEA (IAEA-TEC(DOC)-410), 1987.

Czapek, E.L., et al. "Reactor Shielding Design Manual". Edited by T. Rockwell III. New York: McGraw-Hill, 1956.

Czubek, J. A., "Pulsed Neutron Method of Uranium Well Logging", Geophysics, v. 37, p.160-173, February, 1972.

Dirk, J.D., Nelson, M.E., Ziegler, J.F., "Electronic Reliability and the Environmental Thermal Neutron Flux", Trident Scholar project report, no. 291, 2002.

Eisenbud, M., "Environmental Radioactivity", 3rd Ed., Academic Press, 1987.

Erdtmann, G., "Neutron Activation Tables", v. 6, 1976.

Exploranium AT-900 Brochure, Exploranium website
http://www.exploranium.com/pdf_files/AT-900.pdf, 2002

Fehlau, P.E., Garcia, Jr., C., Payne, R.A., Shunk, E.R., "Vehicle Monitors for Domestic Perimeter Safeguards", LA-9633-MS, January, 1983.

Fehlau, Paul E. Interview by author. Los Alamos National Laboratory, 25 June 2002.

Gillet, J. "Risques spécifiques à l'uranium." Rayonnements Ionisants, no. 1, 1992, pp. 31-36.

Givens, W.W., Mills, W.R., Dennis, C.L., Caldwell, R.L., Uranium Assaying Using a Pulsed 14-Mev Neutron Source", Paper V, SPWLA 17th Annual Logging Symposium Transactions, 1976.

Gozani, T., Elsalim, M., Strellis, D., Brown, D.R., "SEAVEDS-Nonintrusive Inspection of Maritime Vessels for Concealed Drugs", Ancore Corporation, Santa Clara, Cal.,

Haliburton website: www.halliburton.com/perl/Search.cgi, search: neutron, Houston, Texas, 2002.

Hanford website:
www.hanford.gov/techmgmt/factsheets/deploy/ipan.htm, 2002.

Hansen, L.F., Wong, C., Komoto, T.T., Pohl, B., Goldberg, E., Howerton, R.J., Webster, W.M., "Neutron and Gamma-ray Spectra from ²³²Th, ²³⁵U, ²³⁸U, and ²³⁹Pu After Bombardment with 14-MeV Neutrons", Nuclear Science and Engineering, Vol. 72, p.35-51, 1972.

International Commission on Radiation Units and Measurements,
 "Microdosimetry", ICRU Report no. 36, p. 72-73, December, 1983.

ICRP, "Radionuclide Transformations - Energy and Intensity of
 Emissions", ICRP Publication 38, 1983.

KAERI website: hpngp01.kaeri.re.kr/CoN/endfplot.shtml, 2002.

Ka-Ngo Leung, Lawrence Berkley National Laboratory, Berkeley,
 California, private communication.

Keepin, G., "Physics of Nuclear Kinetics", Addison Wesley, Reading,
 Massachusetts, 1965.

Knoll, G.F., "Radiation Detection and Measurement", 3rd ed., John
 Wiley and Sons, 2000.

Kokoski, R., "Technology and the Proliferation of Nuclear Weapons".
 New York: Oxford University for SIPRI, 1995.

L-3 communications website. www.dsxray.com/Linescan.asp, 2003.

LaMarsh, J., "Introduction to Nuclear Engineering", AddisonWesley,
 Reading, Massachusetts, 1982.

LaMarsh, J.R., Baratta, A.J., "Introduction to Nuclear Engineering,"
 Prentice Hall, Uppersaddle River, New Jersey, 2001.

Lindquist, P.E., "Considerations for U.S. Customs Service Use of
 Seaport Cargo Container Inspection Systems", US Customs service,
 Washington DC,
www.whitehousedrugpolicy.gov/ctac/ctac01/pdfs/23/CONSIDERATIONSfortheUSCustomsService.pdf, 2001.

Los Alamos National Laboratory, "MCNP4C2 Monte Carlo N-Particle
 Transport Code System", RSICC Computer Code collection, CCC-701,
 June, 2001.

Lux, I., "Monte Carlo Particle Transport Methods", CRC press, Boston,
 Massachusetts, 1991.

MacMurdo, R.W. and Bowman, W.W., "Assay of fissile materials by a
 cyclic method of neutron activation and delayed neutron
 counting", Nucl. Inst. And Methods, 144, p299, 1977.

MAXX Company website. www.maxx.bc/library, 2003.

Melton, S., Estep, R., Hollas, C., "Implementation of Advanced Matrix
 Corrections for Active Interrogation of Waste Drums Using the CTEN

Instrument", 6th NDA Waste Characterization Conference, Salt Lake city, Utah, November, 1998.

Millett, M. G., "Development of an Optimized Neutron Proportional Counter for Fission Spectra", University of Maryland, PhD Dissertation, 1997.

Millett, M.G., "Weight and Count Efficiency Optimization in a Moderated Neutron Detection System", Nuclear Instruments and methods in Physics Research A, v. 417, p. 332-341, April, 1998.

Moore, J.F., Chandran, V.C.R. Reiter, R.F., "Better Imaging: The Key to Better Cargo Inspection", Bio-imaging Research, Lincolnshire, Illinois, www.bio-imaging.com/news/better_imaging.html, 2002.

Murphy, L., Roxo, K., Nelson, M., Johnson, W., "Field Test Comparison of the Optimized Neutron Detector for Arms Control (ONDAC) and the INF Detector", DSWA-TR-97-65, April, 1998.

Nachtigall, D., Heinzelman, M., no title available, University of California Radiation Laboratory Report, UCRL-Trans-10128, 1966.

Nargolwalla, S.S., Przybylowicz, E.P., "Activation Analysis with Neutron Generators", John Wiley and Sons, New York, New York, 1973.

Naval Sea Systems Command, "Radiological Affairs Support Program Manual, NAVSEA S04020-AA-RAD010 (RAD-010), 1991.

Nelson, M. E., "Optimized Neutron Detector for Arms Control (ONDAC) Operation and Maintenance Manual", prepared for Defense Special Weapons Agency (DSWA), December, 1997.

Nelson, M. E., personal communication, 2003.

Orphan, V.J., Richardson, R.D., Bowlin, D.W., "VACIS - A Safe, Reliable and Cost-Effective Cargo Inspection Technology," SAIC website, Technical Paper IV, <http://www.saic.com/products/security/pdf/pt16.pdf>, 2001.

Radiation Safety Information Computational Center. "RSICC Computer Code Collection MCNP4C2". Oak Ridge National Laboratory: RSICC, 2001.

Richardson, R.D., Verbinski, V.V., Orphan, V.J., "New Cargo Inspection and Transportation Technology Applications," SAIC website, Technical Paper III, <http://www.saic.com/products/security/pdf/pt15-13.pdf>, 2001.

Rooney, B.D., York, R.L., Close, D.A., Williams III, H.E., "Active Neutron Interrogation Package Monitor", Los Alamos National Laboratory, 2002.

Saeger, Kevin J. Email to author. 25 June 2002.

SAIC Mobile Vehicle & Inspection System (Mobile VACIS™) website, <http://www.saic.com/products/security/mobile-vacis/>, 2003.

Sampson, T.E., "Plutonium Isotopic Composition by Gamma-Ray Spectroscopy." In *Passive Nondestructive Assay of Nuclear Material*. Edited by D. Reilly, N. Ensslin, H. Smith, and S. Kreiner. Washington, DC: GPO, 1991. (NUREG/CR-550 and LA-UR-90-732)

Scslumberger website:
www.connect.slb/brochure..._Gamma_Ray_Spectrometry, Houston, Texas, 2002.

Sea Box, Inc. drawing 20' x 8' x 8'6" General Arrangement.

Smith, H.D., "Pulsed Neutron Logging Systems", (Welex) Haliburton Report, unnumbered, January, 1979.

Sowby, F.D., "Annals of the ICRP", Pergamon Press, 1983.

Spyrov, N., Adessanmi, C., Kidd, M., Stephens-Newshang, I.G., Ortavol, A.Z., Ozch, F., "Use of thermal and epithermal cyclic actuation analysis with a reactor system". J. Radioanal. Chem., 72, 155, 1982.

St. John, J., SARA Internship Report, 2002 (unpublished).

St. John, J., Capstone Design Project, System Engineering Department, US Naval Academy, 2003 (unpublished).

Taylor, R., "High Tech Inspection System Hit Ports this Year," U.S. Customs Today, www.customs.gov/custody/mar2000/hitec.htm, March 2000.

Thermo MF Physics website: www.thermoMFphysics.com, 2002.

U.S. Customs Service, "Frequently Asked Questions, 24-Hour Advance Manifest Rule," [http://europa.eu.int/comm/taxation_customs/customs/information notes/infofiches/faq_24h_january03.pdf](http://europa.eu.int/comm/taxation_customs/customs/information_notes/infofiches/faq_24h_january03.pdf), January, 2003.

- U.S. Customs Service, "U.S. Customs Container Security Initiative Guards America, Global Commerce from Terrorist Threat," www.customs.gov/xp/cgov/newsroom/press_releases/112002/110120024.xml, November, 2002.
- U.S. Customs Service. "U.S. Customs Container Security Initiative Forging Ahead," *U.S. Customs News*. [cited 08 October 2002]. Available from <http://www.customs.ustreas.gov/cisf.htm>; INTERNET.
- U.S. Office of Personnel website:
<http://www.opm.gov/oca/payrates/index.asp>, 2002.
- Van Riper, K.A., "SABRINA User Manual", White Rock Science, White Rock, New Mexico, 2002.
- www.whitehousedrugpolicy.gov/ctac/ctac01/pdfs/12/NonintrusiveINSPECTIOnofMARITIMEVESSELS.pdf, 2001.

APPENDIX A

SAMPLE MCNP INPUT FILES

Sample 1: MCNP Input file to Study Delayed Neutrons emitted by HEU within a 20' by 8' by 8' iron-walled cargo container.

```

c      ONDAC detector model
1  3  -0.00122 -21 -4 5  $det 1 $(10 atm He-3)
2  3  -0.00122 -22 -4 5  $det 2
3  3  -0.00122 -23 -4 5  $det 3
4  3  -0.00122 -24 -4 5  $det 4
5  3  -0.00122 -25 -4 5  $det 5
6  3  -0.00122 -26 -4 5  $det 6
7  3  -0.00122 -27 -4 5  $det 7
8  3  -0.00122 -28 -4 5  $det 8
9  3  -0.00122 -29 -4 5  $det 9
10 1  -0.00118 6 -64 62 -54 57 -58 473  $air behind detector
11 1  -0.00118 -9 50 -64 62 -54 57 -58 470  $air in front of det
12 1  -0.00118 9 -6 4 -64 -54 57 -58  $top air slice
13 1  -0.00118 9 -6 -5 -64 -54 57 62  $bottom air slice
14 1  -0.00118 20 -310 9 -6 5 -4 -64 -54 471 $side air channel
15 1  -0.00118 -10 220 9 -6 5 -4 -64 57 472 $side air channel
16 2  -0.95 10 -12 7 -6 21 -4 5 -30  $back poly pieces
17 2  -0.95 12 -14 7 -6 21 22 -4 5
18 2  -0.95 14 -16 7 -6 22 23 -4 5
19 2  -0.95 16 -18 7 -6 23 24 -4 5
20 2  -0.95 18 -20 7 -6 24 -4 5 -31
21 2  -0.95 10 -20 8 -7 -4 5  $middle slab
22 2  -0.95 10 -11 9 -8 25 -4 5  $front poly pieces
23 2  -0.95 11 -13 9 -8 25 26 -4 5
24 2  -0.95 13 -15 9 -8 26 27 -4 5
25 2  -0.95 15 -17 9 -8 27 28 -4 5
26 2  -0.95 17 -19 9 -8 28 29 -4 5
27 2  -0.95 19 -20 9 -8 29 -4 5
28 1  -0.00118 10 -12 7 -6 30 -4 5  $rear corner air slice
29 1  -0.00118 18 -20 7 -6 31 -4 5  $rear corner air slice
30 1  -0.00118 -435 54 -437 63 -64  $air outside container positive x
31 1  -0.00118 436 -57 -437 63 -64  $air outside container negative x
32 1  -0.00118 57 -54 58 -437 -64  $air on top of container
    (positive z)
33 0  64:435:-436:437:-63  $outer space
c  *****
c  *  end of basic cell cards, put extended cells
c  *  for specific problems here
c  *****
c  *  the following cells were added for shipping cont, dirt & HEU
40 1  -0.00118 62 -58 -53 -54 57 -64 $air on source side of container
41 6  -1.5 63 -62 57 -54 -64  $dirt (SiO2) under container
42 4  -7.86 59 -58 -50 53 -54 57  $container top

```

```

43 4  -7.86 62 -61 -50 53 -54 57      $container bottom
44 4  -7.86 -59 61 -50 53 55 -54      $container +x side
45 4  -7.86 -59 61 -50 53 57 -56      $container -x side
46 4  -7.86 56 -55 61 -59 -50 51      $container +y side
47 4  -7.86 56 -55 61 -59 -52 53      $container -y side
c  * Container air is not used; replaced with drums, etc.
c  * 48 1  -0.00118 65 -55 56 -51 52 -59 61 $air in container
c  *
49 1 -0.00118 -65      $HEU placeholder (air in delayed neutron model)
c  *the following cells are drums in the container
100 9 -7.87 -100 -59 60      $stop drums, first row
101 9 -7.87 -101 -59 60
102 9 -7.87 -102 -59 60
103 9 -7.87 -103 -59 60
104 9 -7.87 -104 -59 60
105 9 -7.87 -105 -59 60
106 9 -7.87 -106 -59 60
107 9 -7.87 -107 -59 60
108 9 -7.87 -108 -59 60
109 9 -7.87 -109 -59 60
110 9 -7.87 -110 -59 60      $stop drums, second row
111 9 -7.87 -111 -59 60
112 9 -7.87 -112 -59 60
113 9 -7.87 -113 -59 60
114 9 -7.87 -114 -59 60
115 9 -7.87 -115 -59 60
116 9 -7.87 -116 -59 60
117 9 -7.87 -117 -59 60
118 9 -7.87 -118 -59 60
119 9 -7.87 -119 -59 60
120 9 -7.87 -120 -59 60      $stop drums, third row
121 9 -7.87 -121 -59 60
122 9 -7.87 -122 -59 60
123 9 -7.87 -123 -59 60
124 9 -7.87 -124 -59 60
125 9 -7.87 -125 -59 60
126 9 -7.87 -126 -59 60
127 9 -7.87 -127 -59 60
128 9 -7.87 -128 -59 60
129 9 -7.87 -129 -59 60
130 9 -7.87 -130 -59 60      $stop drums, fourth row
131 9 -7.87 -131 -59 60
132 9 -7.87 -132 -59 60
133 9 -7.87 -133 -59 60
134 9 -7.87 -134 -59 60
135 9 -7.87 -135 -59 60
136 9 -7.87 -136 -59 60
137 9 -7.87 -137 -59 60
138 9 -7.87 -138 -59 60
139 9 -7.87 -139 -59 60

```


140	9	-7.87	-100	61	-60					\$bottom drums, first row
141	9	-7.87	-101	61	-60					
142	9	-7.87	-102	61	-60					
143	9	-7.87	-103	61	-60					
144	9	-7.87	-104	61	-60					
145	9	-7.87	-105	61	-60					
146	9	-7.87	-106	61	-60					
147	9	-7.87	-107	61	-60					
148	9	-7.87	-108	61	-60					
149	9	-7.87	-109	61	-60					
150	9	-7.87	-110	61	-60					\$bottom drums, second row
151	9	-7.87	-111	61	-60					
152	9	-7.87	-112	61	-60					
153	9	-7.87	-113	61	-60					
154	9	-7.87	-114	61	-60					
155	9	-7.87	-115	61	-60					
156	9	-7.87	-116	61	-60					
157	9	-7.87	-117	61	-60					
158	9	-7.87	-118	61	-60					
159	9	-7.87	-119	61	-60					
160	9	-7.87	-120	61	-60					\$bottom drums, third row
161	9	-7.87	-121	61	-60					
162	9	-7.87	-122	61	-60					
163	9	-7.87	-123	61	-60					
164	9	-7.87	-124	61	-60					
165	9	-7.87	-125	61	-60					
166	9	-7.87	-126	61	-60					
167	9	-7.87	-127	61	-60					
168	9	-7.87	-128	61	-60					
169	9	-7.87	-129	61	-60					
170	9	-7.87	-130	61	-60					\$bottom drums, fourth row
171	9	-7.87	-131	61	-60					
172	9	-7.87	-132	61	-60					
173	9	-7.87	-133	61	-60					
174	9	-7.87	-134	61	-60					
175	9	-7.87	-135	61	-60					
176	9	-7.87	-136	61	-60					
177	9	-7.87	-137	61	-60					
178	9	-7.87	-138	61	-60					
179	9	-7.87	-139	61	-60					
c										*these cells are air columns in the container between the drums
200	1	-0.00118	61	-59	-51	70	100	56	-80	\$first half row of air columns
201	1	-0.00118	61	-59	-51	70	100	101	80	-81
202	1	-0.00118	61	-59	-51	70	101	102	81	-82
203	1	-0.00118	61	-59	-51	70	102	103	82	-83
204	1	-0.00118	61	-59	-51	70	103	104	83	-84
205	1	-0.00118	61	-59	-51	70	104	105	84	-85
206	1	-0.00118	61	-59	-51	70	105	106	85	-86
207	1	-0.00118	61	-59	-51	70	106	107	86	-87

208	1	-0.00118	61	-59	-51	70	107	108	87	-88	
209	1	-0.00118	61	-59	-51	70	108	109	88	-89	
210	1	-0.00118	61	-59	-51	70	109	89	-55		
211	1	-0.00118	61	-59	-70	71	100	110	56	-80	\$second row of air
columns											
212	1	-0.00118	61	-59	-70	71	100	110	101	111	80 -81
213	1	-0.00118	61	-59	-70	71	101	111	102	112	81 -82
214	1	-0.00118	61	-59	-70	71	102	112	103	113	82 -83
215	1	-0.00118	61	-59	-70	71	103	113	104	114	83 -84
216	1	-0.00118	61	-59	-70	71	104	114	105	115	84 -85
217	1	-0.00118	61	-59	-70	71	105	115	106	116	85 -86
218	1	-0.00118	61	-59	-70	71	106	116	107	117	86 -87
219	1	-0.00118	61	-59	-70	71	107	117	108	118	87 -88
220	1	-0.00118	61	-59	-70	71	108	118	109	119	88 -89
221	1	-0.00118	61	-59	-70	71	109	119	89	-55	
222	1	-0.00118	61	-59	-71	72	110	120	56	-80	\$third row of air
columns											
223	1	-0.00118	61	-59	-71	72	110	120	111	121	80 -81
224	1	-0.00118	61	-59	-71	72	111	121	112	122	81 -82
225	1	-0.00118	61	-59	-71	72	112	122	113	123	82 -83
226	1	-0.00118	61	-59	-71	72	113	123	114	124	83 -84
227	1	-0.00118	61	-59	-71	72	114	124	115	125	84 -85 65 \$no HEU in
Cell											
228	1	-0.00118	61	-59	-71	72	115	125	116	126	85 -86
229	1	-0.00118	61	-59	-71	72	116	126	117	127	86 -87
230	1	-0.00118	61	-59	-71	72	117	127	118	128	87 -88
231	1	-0.00118	61	-59	-71	72	118	128	119	129	88 -89
232	1	-0.00118	61	-59	-71	72	119	129	89	-55	
233	1	-0.00118	61	-59	-72	73	120	130	56	-80	\$fourth row of air
columns											
234	1	-0.00118	61	-59	-72	73	120	130	121	131	80 -81
235	1	-0.00118	61	-59	-72	73	121	131	122	132	81 -82
236	1	-0.00118	61	-59	-72	73	122	132	123	133	82 -83
237	1	-0.00118	61	-59	-72	73	123	133	124	134	83 -84
238	1	-0.00118	61	-59	-72	73	124	134	125	135	84 -85
239	1	-0.00118	61	-59	-72	73	125	135	126	136	85 -86
240	1	-0.00118	61	-59	-72	73	126	136	127	137	86 -87
241	1	-0.00118	61	-59	-72	73	127	137	128	138	87 -88
242	1	-0.00118	61	-59	-72	73	128	138	129	139	88 -89
243	1	-0.00118	61	-59	-72	73	129	139	89	-55	
244	1	-0.00118	61	-59	-73	52	130	56	-80		\$fifth half row of air
columns											
245	1	-0.00118	61	-59	-73	52	130	131	80	-81	
246	1	-0.00118	61	-59	-73	52	131	132	81	-82	
247	1	-0.00118	61	-59	-73	52	132	133	82	-83	
248	1	-0.00118	61	-59	-73	52	133	134	83	-84	
249	1	-0.00118	61	-59	-73	52	134	135	84	-85	
250	1	-0.00118	61	-59	-73	52	135	136	85	-86	
251	1	-0.00118	61	-59	-73	52	136	137	86	-87	
252	1	-0.00118	61	-59	-73	52	137	138	87	-88	


```

253 1 -0.00118 61 -59 -73 52 138 139 88 -89
254 1 -0.00118 61 -59 -73 52 139 89 -55
c * additional detectors
c *
c * second detector
301 3 -0.00122 -221 -4 5 $det 1 $(10 atm He-3)
302 3 -0.00122 -222 -4 5 $det 2
303 3 -0.00122 -223 -4 5 $det 3
304 3 -0.00122 -224 -4 5 $det 4
305 3 -0.00122 -225 -4 5 $det 5
306 3 -0.00122 -226 -4 5 $det 6
307 3 -0.00122 -227 -4 5 $det 7
308 3 -0.00122 -228 -4 5 $det 8
309 3 -0.00122 -229 -4 5 $det 9
310 1 -0.00118 -210 9 -6 5 -4 -64 57 $side air channel (-x)
311 2 -0.95 210 -212 7 -6 221 -4 5 -230 $back poly pieces
312 2 -0.95 212 -214 7 -6 221 222 -4 5
313 2 -0.95 214 -216 7 -6 222 223 -4 5
314 2 -0.95 216 -218 7 -6 223 224 -4 5
315 2 -0.95 218 -220 7 -6 224 -4 5 -231
316 2 -0.95 210 -220 8 -7 -4 5 $middle slab
317 2 -0.95 210 -211 9 -8 225 -4 5 $front poly pieces
318 2 -0.95 211 -213 9 -8 225 226 -4 5
319 2 -0.95 213 -215 9 -8 226 227 -4 5
320 2 -0.95 215 -217 9 -8 227 228 -4 5
321 2 -0.95 217 -219 9 -8 228 229 -4 5
322 2 -0.95 219 -220 9 -8 229 -4 5
323 1 -0.00118 210 -212 7 -6 230 -4 5 $rear corner air slice
324 1 -0.00118 218 -220 7 -6 231 -4 5 $rear corner air slice
c * third detector
401 3 -0.00122 -321 -4 5 $det 1 $(10 atm He-3)
402 3 -0.00122 -322 -4 5 $det 2
403 3 -0.00122 -323 -4 5 $det 3
404 3 -0.00122 -324 -4 5 $det 4
405 3 -0.00122 -325 -4 5 $det 5
406 3 -0.00122 -326 -4 5 $det 6
407 3 -0.00122 -327 -4 5 $det 7
408 3 -0.00122 -328 -4 5 $det 8
409 3 -0.00122 -329 -4 5 $det 9
410 1 -0.00118 320 9 -6 5 -4 -64 -54 $side air channel (+x)
411 2 -0.95 310 -312 7 -6 321 -4 5 -330 $back poly pieces
412 2 -0.95 312 -314 7 -6 321 322 -4 5
413 2 -0.95 314 -316 7 -6 322 323 -4 5
414 2 -0.95 316 -318 7 -6 323 324 -4 5
415 2 -0.95 318 -320 7 -6 324 -4 5 -331
416 2 -0.95 310 -320 8 -7 -4 5 $middle slab
417 2 -0.95 310 -311 9 -8 325 -4 5 $front poly pieces
418 2 -0.95 311 -313 9 -8 325 326 -4 5
419 2 -0.95 313 -315 9 -8 326 327 -4 5
420 2 -0.95 315 -317 9 -8 327 328 -4 5

```

```

421 2 -0.95 317 -319 9 -8 328 329 -4 5
422 2 -0.95 319 -320 9 -8 329 -4 5
423 1 -0.00118 310 -312 7 -6 330 -4 5 $rear corner air slice
424 1 -0.00118 318 -320 7 -6 331 -4 5 $rear corner air slice
c *** Borated Poly around source ***
c 426 7 -1.19 -460 $Block of borated poly using RPP command
430 1 -0.00118 -470 $Front Cd Shield
431 1 -0.00118 -471 $Left Side Cd Shield
432 1 -0.00118 -472 $Right Side Cd Shield
433 1 -0.00118 -473 $Back Cd Shield
c * end of cell cards
c *****

c *****
c * beginning of surfaces
c *
c * surfaces #1-31 are the detector alone
c * (originally contained within surfaces 1,2, and 3)
c *****
c * 1 cy 20 $horizontal pipe, detector in the middle
c * 2 py 10 $back of pipe
c * 3 py -110 $front of pipe
4 pz 10 $stop of detector
5 pz -10 $bottom of detector
6 py 4 $detector back face
7 py -0.5 $back of center poly region
8 py -3.0 $front of center poly region
9 py -6.5 $detector front face
10 px -10 $left side of detector
11 px -8 $2 cm regions
12 px -6
13 px -4
14 px -2
15 px 0
16 px 2
17 px 4
18 px 6
19 px 8
20 px 10 $right side of detector
21 c/z -7 1 1.27 $back 4 detectors, L to R
22 c/z -2.5 2 1.27
23 c/z 2.5 2 1.27
24 c/z 7 1 1.27
25 c/z -8 -4.5 1.27 $front 5 detectors L to R
26 c/z -4 -4.5 1.27
27 c/z 0 -4.5 1.27
28 c/z 4 -4.5 1.27
29 c/z 8 -4.5 1.27
30 c/z -6 0 4
31 c/z 6 0 4

```



```

c *****
c * add extended surfaces for specific problems here
c *****
c * following surfaces added for shipping cont & surrounds
50 py -37          $+y outer surface
51 py -37.64       $+y inner surface
52 py -281.64      $-y inner surface
53 py -282.28      $-y outer surface
54 px 305.64       $+x outer surface
55 px 305          $+x inner surface
56 px -305         $-x inner surface
57 px -305.64      $-x outer surface
58 pz 122.64       $+z outer surface
59 pz 122          $+z inner surface
60 pz 0            $half-height divider for shipping barrels
61 pz -122         $-z inner surface
62 pz -122.64      $-z outer surface-top of dirt
63 pz -127.64      $bottom of dirt
64 sy -159.64 452  $sphere surrounding problem
65 sy -159.64 2.32  $HEU sphere
c * following surfaces added for cylinders inside shipping container
70 py -68.14       $perpendicular dividing surfaces -
71 py -129.14      $to help define air gaps
72 py -190.14
73 py -251.14
80 px -274.5
81 px -213.5
82 px -152.5
83 px -91.5
84 px -30.5
85 px 30.5
86 px 91.5
87 px 152.5
88 px 213.5
89 px 274.5
100 c/z -274.5 -68.14 30.5 $first row of 10 drums
101 c/z -213.5 -68.14 30.5
102 c/z -152.5 -68.14 30.5
103 c/z -91.5 -68.14 30.5
104 c/z -30.5 -68.14 30.5
105 c/z 30.5 -68.14 30.5
106 c/z 91.5 -68.14 30.5
107 c/z 152.5 -68.14 30.5
108 c/z 213.5 -68.14 30.5
109 c/z 274.5 -68.14 30.5
110 c/z -274.5 -129.14 30.5 $second row of 10 drums
111 c/z -213.5 -129.14 30.5
112 c/z -152.5 -129.14 30.5
113 c/z -91.5 -129.14 30.5
114 c/z -30.5 -129.14 30.5

```

```

115 c/z 30.5 -129.14 30.5
116 c/z 91.5 -129.14 30.5
117 c/z 152.5 -129.14 30.5
118 c/z 213.5 -129.14 30.5
119 c/z 274.5 -129.14 30.5
120 c/z -274.5 -190.14 30.5 $third row of 10 drums
121 c/z -213.5 -190.14 30.5
122 c/z -152.5 -190.14 30.5
123 c/z -91.5 -190.14 30.5
124 c/z -30.5 -190.14 30.5
125 c/z 30.5 -190.14 30.5
126 c/z 91.5 -190.14 30.5
127 c/z 152.5 -190.14 30.5
128 c/z 213.5 -190.14 30.5
129 c/z 274.5 -190.14 30.5
130 c/z -274.5 -251.14 30.5 $fourth row of 10 drums
131 c/z -213.5 -251.14 30.5
132 c/z -152.5 -251.14 30.5
133 c/z -91.5 -251.14 30.5
134 c/z -30.5 -251.14 30.5
135 c/z 30.5 -251.14 30.5
136 c/z 91.5 -251.14 30.5
137 c/z 152.5 -251.14 30.5
138 c/z 213.5 -251.14 30.5
139 c/z 274.5 -251.14 30.5
c *
c * additional detectors
c *
c * second detector
210 px -210 $left side of detector
211 px -208 $2 cm regions
212 px -206
213 px -204
214 px -202
215 px -200
216 px -198
217 px -196
218 px -194
219 px -192
220 px -190 $right side of detector
221 c/z -207 1 1.27 $back 4 detectors, L to R
222 c/z -202.5 2 1.27
223 c/z -197.5 2 1.27
224 c/z -193 1 1.27
225 c/z -208 -4.5 1.27 $front 5 detectors L to R
226 c/z -204 -4.5 1.27
227 c/z -200 -4.5 1.27
228 c/z -196 -4.5 1.27
229 c/z -192 -4.5 1.27
230 c/z -206 0 4 $rear corners

```



```

231 c/z -194 0 4
c *
c * third detector
c *
310 px 190          $left side of detector
311 px 192          $2 cm regions
312 px 194
313 px 196
314 px 198
315 px 200
316 px 202
317 px 204
318 px 206
319 px 208
320 px 210          $right side of detector
321 c/z 193 1 1.27    $back 4 detectors, L to R
322 c/z 197.5 2 1.27
323 c/z 202.5 2 1.27
324 c/z 207 1 1.27
325 c/z 192 -4.5 1.27  $front 5 detectors L to R
326 c/z 196 -4.5 1.27
327 c/z 200 -4.5 1.27
328 c/z 204 -4.5 1.27
329 c/z 208 -4.5 1.27
330 c/z 194 0 4        $rear corners
331 c/z 206 0 4
435 px 320
436 px -320
437 pz 140
c 460 RPP -115 -85 -35 -10 -15 15 $Borated Poly Box (Unused)
470 RPP -10.3 10.3 -6.8 -6.5 -10 10 $Front Cd Shield
471 RPP 10 10.3 -6.5 4 -10 10 $RHS Cd Shield
472 RPP -10.3 -10 -6.5 4 -10 10 $LHS Cd Shield
473 RPP -10.3 10.3 4 4.3 -10 10 $Rear Cd Shield
c * end of surface cards
c *****

c *****
c * neutron importance (ensure all cells included)
c *****
IMP:N 1 31R 0 1 147R 48R
c *****
c * source definition
c * Cf-252 point source, one foot from container
c *****
SDEF ERG=.713 POS=0 -159.64 0    $ .713 MeV delayed neutron source
c SP1 -3 1.025 2.926    $ Cf 252 SF neutron source
c *****
c * special tallies
c *

```

```

c * The following F4 tally gives neutron interactions
c * per cm^3 in each of the 9 tubes.
c * Multiply by tube volume for total interactions
c * (should agree with collisions (wgt) in each cell)
c *****
F4:N 1 2 3 4 5 6 7 8 9 & $ ave detector neut flux (det#1)
      301 302 303 304 305 306 307 308 309 & $det #2
      401 402 403 404 405 406 407 408 409 $ det #3
FM4 0.000244 3 1 $ mult for collisions
c * energy bins for special tallies (NOT USED)
c * E4 1E-6 10M 10M 10M 10M .025 2M 2M .2 13I 3 10I 14 $ E bins
c *****
c *
c *****
c * material definitions
c *****
M1 7014 0.806 8016 0.19 18000 0.004 $ air
M2 6000 .333 1001 .667 $ poly
M3 2003 1.0 $ detector gas
M4 26000 0.98 6000 0.01 14000 0.01 $ low carbon steel
M5 92235 0.93 92238 0.07 $ HEU
M6 14000 0.33 8016 0.67 $ SiO2 (dirt)
M7 1001 .652 6000 .326 5010 0.0044 5011 0.0176 $ Borated Poly
M8 48000 1 $Cd
M9 26000 1 $Cargo Material - As of 6SEP = Iron
c *
c *****
c * MCNP stops when 30 lost particles
c * number of source neutrons launched
c *****
LOST 30
NPS 60000000
c *****
c * special output requests
c *****
PRINT 40 50 140

```


Sample 2: (St. John, 2003)

aircargol8PVTsMODEL - MCNP input for a surface source corresponding to 4kg weapons grade plutonium surrounded by air cargo with 18 PVT sensors external to the container.

```
1 1 -0.001225 -1 17 $cargo in container- currently air
2 2 -2.6989 1 -2 $aluminum container wall
3 1 -19.84 -3 $plutonium sphere
4 1 -0.001225 2 -4 6 8 9 10 11 12 13 14 15 16 $surrounding
atmosphere
5 4 -1.76 -5 $soil beneath container
6 5 -1.02 -6 $PVT sensor 1
7 1 -0.001225 3 -7 $source shell
8 5 -1.02 -8 $PVT sensor 2
9 5 -1.02 -9 $PVT sensor 3
10 5 -1.02 -10 $PVT sensor 4
11 5 -1.02 -11 $PVT sensor 5
12 5 -1.02 -12 $PVT sensor 6
13 5 -1.02 -13 $PVT sensor 7
14 5 -1.02 -14 $PVT sensor 8
15 5 -1.02 -15 $PVT sensor 9
16 5 -1.02 -16 $PVT sensor 10
17 1 -0.001225 7 -17 $differential sensor shell
18 0 4 5 $outside universe
c * end of cell cards
c *****

c *****
c * begin surface cards
1 BOX 0 0 0 243.4 0 0 0 605.4 0 0 0 258.7 $interior wall
2 BOX -0.2 -0.2 -0.2 243.8 0 0 0 605.8 0 0 0 259.1 $exterior wall
3 SPH 121.7 302.7 129.35 3.63756 $source sphere
4 BOX -100 -100 -100 450 0 0 0 805.8 0 0 0 459.1 $ surrounding air
5 RPP -100 350 -100 705.8 -200 -100 $ soil
6 RPP 293.8 295.8 287.7 317.7 0 260 $ PVT sensor 1
7 SPH 121.7 302.7 129.35 3.73756 $surface source cell (1mm)
8 RPP 293.8 295.8 257.7 287.7 0 260 $PVT sensor 2 (1 left of sensor
1)
9 RPP 293.8 295.8 227.7 257.7 0 260 $PVT sensor 3 (2 left of sensor
1)
10 RPP 293.8 295.8 197.7 227.7 0 260 $PVT sensor 4 (3 left of sensor
1)
11 RPP 293.8 295.8 167.7 197.7 0 260 $PVT sensor 5 (4 left of sensor
1)
12 RPP 293.8 295.8 137.7 167.7 0 260 $PVT sensor 6 (5 left of sensor
1)
13 RPP 293.8 295.8 107.7 137.7 0 260 $PVT sensor 7 (6 left of sensor
1)
14 RPP 293.8 295.8 77.7 107.7 0 260 $PVT sensor 8 (7 left of sensor
1)
```

```

15 RPP 293.8 295.8 47.7 77.7 0 260    $PVT sensor 9 (8 left of sensor
1)
16 RPP 293.8 295.8 17.7 47.7 0 260    $PVT sensor 10 (9 left of
sensor 1)
17 SPH 121.7 302.7 129.35 3.83756 $differentially thin sensor
c  * end of surface cards
c  *****

```

MODE P

```

IMP:P 1 1 1 1 1 1 1 1 1 1 1 1 1 1 1 0
SDEF POS=121.7 302.7 129.35 RAD=3.68756 ERG=D1
SI1 L 0.1 .15 .25 .35 .45 .55 .65 .75 .85 .95 1.025
SP1 .00983 .02024 .00612 .03486 .07291 .13428 .30174 .34730 .05178 &
.01512 .00582
F4:P 3 $interior of sphere
F14:P 6 $PVT 1
F24:P 17 $differential (shell) sensor
F34:P 8 $PVT 2
F44:P 9 $PVT 3
F54:P 10 $PVT 4
F64:P 11 $PVT 5
F74:P 12 $PVT 6
F84:P 13 $PVT 7
F94:P 14 $PVT 8
F104:P 15 $PVT 9
F114:P 16 $PVT 10
E0 0.1 0.2 0.3 0.4 0.5 0.6 0.7 0.8 0.9 1 1.05
c  *****
c  * begin material cards
M1 7014 0.78118 8016 0.20948 18000 0.00934  $air
M2 13000 1 $aluminum
M3 94239 0.93 94240 0.065 94241 0.005 $weapons grade plutonium
UNCLASSIFIED
M4 14000 0.33 8016 0.67 $ soil (silicon dioxide)
M5 1000 0.525 6000 0.475 $polyvinyltoluene scintillator material
c  * end material cards
c  *****
LOST 30
DBCN 345783 $random seed number
NPS 1E8
PRINT

```

```

c  *****
c  * 18APR03 Pu spectral surface source, air cargo, Al wall
c  * atmosphere, ground, 10 PVT detectors, differential detector
c  *****

```


Sample 3: MCNP File to calculate neutron dose across concrete slab shield from 14 MeV source

```
1 1 -2.4 -1 $concrete
2 2 -0.00118 -2 $Cell where dose is to be calculated
3 2 -0.00118 -3 2 1 $Air sphere around problem
4 0 3 $Void around problem
c End of Cell Cards

c Beginning of Surface Cards
1 RPP -600 600 -122 122 -600 600 $Concrete Slab surface
c (xmin xmax) (ymin ymax) (zmin zmax)
2 SY 125 2 $Dose sphere
3 SO 1200 $Containment sphere
c End of surface cards

MODE N P
IMP:N,P 1 1 1 0
SDEF ERG=14 POS=0 -124.0 0
F4:N 2 $Avg neutron flux through target cell
c F4:P 2 $Avg photon flux through target cell
DE4 2.5E-8 1.0E-7 1.0E-6 1.0E-5 1.0E-4 1.0E-3 1.0E-2 1.0E-1
      5.0E-1 1.0 2.5 5.0 7.0 10.0 14.0
DF4 3.67E-6 3.67E-6 4.46E-6 4.54E-6 4.18E-6 3.76E-6 3.56E-6
      2.17E-5 9.26E-5 1.32E-4 1.25E-4 1.56E-4 1.47E-4 1.47E-4
      2.08E-4
M1 1001 -.004532 8016 -.512597 11023 -.011553 &
12000 -.003866 13027 -.035548 14000 -.360364 &
19000 -.014219 20000 -.043546 26056 -.013775
M2 7014 0.806 8016 0.19 18000 0.004 $Air
C *****
LOST 30
DBCN 363111 $random number seed
NPS 400000000
PRINT
```

APPENDIX B

CALCULATION OF AVERAGE DISTANCE FROM THE SOURCE TO CARGO DRUMS

In order to find the flux, a single distance from the source to the cargo drums was calculated. This appendix describes the details of this procedure.

Using the geometrical layout as used in the MCNP code that is included in Appendix A, the exact location of the source was taken to be located at $x = 0$, $y = -312.78$ cm, $z = 0$. As a reminder, the x -direction is lengthwise along the container's 20 ft length, the y -direction moves along the 8 ft container width, and the z -direction follows the 8 ft container height. Also, the origin of the coordinate system is at the center of the ONDAC detector ($x = y = z = 0$). Physically the ONDAC position is located lengthwise in the center of the container (10 ft from each end), 37 cm (14.6 inches) in the y -direction from the leftmost container wall, and 122 cm (4 ft) off the ground. The distance between the source and each of the four cargo drum rows was determined also from this model, and this information is summarized in table B-1.

Table B-1. Source location and width position of cargo drum rows used in the USNA MCNP cargo container model.

Position	x (cm)	y (cm)	z (cm)	Y Distance Between Row and Source (cm)
Source location	0	-312.78	0	N/A
row 1 of cargo drums	0	-251.14	0	61.64
row 2 of cargo drums	0	-190.14	0	122.64
row 3 of cargo drums	0	-129.14	0	183.64
row 4 of cargo drums	0	-68.14	0	244.64

The final column of table B-1 shows the distance between the source and each row. Since neither the source nor the rows differed in the x or z directions, the distance was obtained by subtracting the row position in the y -direction from the source position in the y -position.

There were 10 drums in each row, five on each side of the source. Since the source is external to the cargo container and the ten drums are symmetric about the source, there were really only five different lengthwise distances of the drums to the source that differed only in the x -direction (lengthwise). Since there were a top set and bottom set of drums, stacked directly on top of each other, the five lengthwise distances of the drums to the source also represented both the top and bottom drums. Table B-2 shows the x -position for each of these five lengthwise distances. The lengthwise distances are

labeled alphabetically as "a" through "e" with "a" being the cargo drums furthest away from the source.

Table B-2. X-position of each of the five container lengthwise distances. The defined distances are labeled alphabetically as "a" through "e" with "a" being the cargo drums furthest away from the source.

Lengthwise Distances	x (cm)
A	274.5
b	213.5
c	152.5
d	91.5
e	30.5

Since there are four y distances and five x distances, a total of 20 positions were used to find the average distance neutrons traveled from the source to the drums in the container. The straight line distance of each of these 20 positions was found by applying Pythagorean's Theorem which says,

$$d = \sqrt{x^2 + y^2} \quad (B.1)$$

where

- d = Straight line distance from source to drum location, cm
- x = Lengthwise distance from source as given in table B-2, cm
- y = Width distance from source as given in table B-1, cm

These 20 cargo drum positions are listed in table B-3 along with their straight line distances from the source.

Since there are 80 drums in the container, each of the 20 distances corresponds to 4 drums. The average distance (\bar{r}) for use in equation (3.4) was then found by averaging the 20 straight line distances given in table B-3. The result of this calculation was:

$$\bar{r} = 230 \text{ cm} \quad (B.2)$$

Table B-3. Twenty straight-line distances between the source and the cargo drums, used to calculate the average distance neutrons travel in the container.

Cargo Drum Position	Straight-Line Distance Between Source and Cargo Drum (cm)
1a	281.3
1b	222.2
1c	164.5
1d	110.3
1e	68.8
2a	300.7
2b	246.2
2c	195.7
2d	153.0
2e	126.4
3a	330.3
3b	281.6
3c	238.7
3d	205.2
3e	186.2
4a	367.7
4b	324.7
4c	288.3
4d	261.2
4e	246.5

APPENDIX C

PORT OF BALTIMORE AND MOBILE VACIS INFORMATION QUESTIONS AND ANSWERS (BASED OFF AN INTERVIEW WITH A PORT OF BALTIMORE (COSTELLO, 2003) & U.S. CUSTOMS AGENT (AUSTIN, 2003), FEB. 5, 2003)

PORT OF BALTIMORE

Q: How many containers are typically carried per ship?

A: There are around 3000 containers per ship, although the size of an average container ship has been steadily increasing. There are 2-3 cranes per ship. Not all of the containers will be off-loaded though. Last week for instance, only 2000 new containers entered the port of Baltimore.

Q: How many containers (or ships) typically enter port each day?

A: 5-6 ships per day. Last week 2000 containers were off-loaded into Baltimore.

Q: How much money is lost if the ships sit dormant in the port?

A: The cost of a ship per day is roughly \$60,000 to \$65,000. Specifically the cost of each crane gang is \$2300 per hour. This would pay 17 people.

Q: Is there a particular place where all containers go?

A: NO. There are containers stored throughout the port of Baltimore; most of the containers are taken from the pier to a holding area, but the location of this area can vary at any time. If the contents inside the container need to be unpacked, the contents are held in a warehouse.

Q: How long does it take to off-load a container?

A: For standard cargo, a ship is in port for 8-10 hours then it leaves again. If it has to off-load sand, cement, or sugar, it can be up to 2-3 days.

Q: How long do the containers stay in the port before being shipped out?

A: They can stay for up to 2 weeks. The average time is 5 days.

Q: By what means do the containers exit the Baltimore port?

A: 80% leave by truck and a small percentage leave by barge or rail.

Q: Is Baltimore's port set-up similar to many others in the US?

A: Yes, but it has more waterline than most, so it's a little larger, and has a bit more activity.

Q: How much interaction is there with the ships crew and Captain?

A: There is very little. The captain can become involved if there is hazardous material on board, but even then, there is still little interaction.

Q: What methods are currently in place to account for incoming cargo containers?

A: There is a CONTAINER SECURITY INITIATIVE that is in place right now. Part of this initiative is directed by the SEA AUTOMATED MANIFEST SYSTEM (AMS). This mandates that all companies wanting to land in a US port must first electronically fill out a manifest 24 hours before the cargo is laden on a vessel that specifies:

Their company

The country they are sending from

The exact materials that will be shipped; vague answers will not be tolerated, for example "Toys" would be unacceptable. It would need to say "micro-racing cars."

Date of arrival

What company is carrying their cargo

This system is enforced 100% of the time. If a company fails to comply with every step, the cargo ship is issued a "Do Not Load Order" and is sent home.

Q: Does the port authority and other personnel present know what is supposed to be inside the cargo container?

A: Yes, from the AMS described above in the above answer.

Q: Are visual inspections ever completed on the cargo containers?

A: Yes, there is an inspection process named LANDED QUANTITY VERIFICATION (LQV). In this process, each container number is recorded, and at the very least, each container will be opened. Here they look for tampered seals. They are looking for 100% accuracy in the manifest information they provided. 20% of this cargo will be completely taken out to be inspected. These visual inspections do not disqualify an X-Ray examination if the manifest info raised an alarm, or for random purposes.

Q: If yes, what qualifies a visual inspection?

A: If the manifest info provided raises an alarm a LQV can be conducted. It can also be random.

Q: Is there a schematic of the port layout (to include major port facilities)?

A: There is a map included with these questions and answers.

MOBILE VACIS

Q: What is the voltage potential (kVp) and current in amps that the machine normally operates at?

A: One 220 V, 20 Amp circuit supplied by onboard generator, and 12 V rechargeable truck batteries.

Q: Is the current and machine voltage controllable? If not controllable, are there discrete settings?

A: Information not needed.

Q: Is the image produced either like a film in a dental x-ray or a video image such as used in airports?

A: Similar to a highly detailed x-ray image.

Q: What is the resolution of the image created? How small of object can be seen? Note: 1 kg of HEU could be a sphere of radius 2.32 cm (0.913 inches), can this system detect an object this small?

A: Spatial resolution is claimed to be 6 to 25 mm. For the Mobile VACIS, the resolution is approximately 9mm (0.354 inches). 256 NaI photo-multiplier scintillation counters used for detection. 1.125 in² in size, established in an array. The use of many small detectors helps increase the spatial resolution. The large array also helps reduce noise levels and improve the image quality.

Penetrating distances for Mobile VACIS

6.5 inches (165mm) through steel - Co-60 (average gamma ray energy = 1.253 MeV)

4.5 inches (114mm) through steel - Cs-137 (gamma ray energy = 0.662 MeV)

Can no longer get an accurate reading when the signal-to-noise ratio is less than one. Slowing down the scan time to less than 1 foot per second is required to achieve maximum penetration.

Q: How wide an area can it scan in a single shot? What percentage of the cargo container does this relate to?

A: Target scan size is 13 ft high x 8 ft wide. No restriction on length of target. Can scan up to maximum size of standard semi-truck.

Q: How much radiation leakage is there from the machine when it operates - i.e. how do they collimate the beam?

A: Source activity of Cs¹³⁷ is 1.6 Ci and Co⁶⁰ is 0.75 Ci (used in the Mobile VACIS). The source is contained within a steel and tungsten housing. When in use, a motorized actuator rotates a tungsten-slot shutter 90 degrees. The radiograph image is constructed by counting the gamma interactions with the detectors. The scanning speed is monitored and the image is corrected for any change in speed. The correction is intended to minimize any distortions in the image

geometry. Working scan speed of 1 km/hr (0.911 ft/sec) on the Mobile VACIS.

Q: What is the effect on the x-ray image if the beam intensity (i.e. the machine's current is decreased). Will a decrease by a factor of 10 result in significantly lower image quality?

A: Uses Co⁶⁰ or Cs¹³⁷ sources so the beam intensity is constant. The initial beam intensity is known (the activity of the source), and the detectors measure the decrease in intensity as the gammas travel through the container.

Q: Assuming you get a positive answer to the above question, calculate the thickness of either lead or platinum that will decrease the intensity by a factor of 10 (may have a different factor other than 10).

A: See Table C-1 below:

Table C-1. Penetration distances for Cs¹³⁷ and Co⁶⁰ in lead and platinum.

Material	Penetration Distance (cm)	
	Cs-137 (0.662 MeV)	Co-60 (1.253 MeV)
Lead (Pb)	1.94	3.57
Platinum (Pt)	1.09	1.94

Q: How do they use the system to determine the density consistency? Is this done by human study of the video image or automated?

A: The number of counts detected determines the density of the material being scanned. Materials of different densities show up as different scales of gray. However, materials of similar densities are not easy to distinguish. A program called pseudo-color does show small density differences. Humans operate the program and study the monitor output. The operator must adjust the output to show either the nonlinear contrast or pseudo color image.

Other VACIS Information

1. First developed and used to detect narcotics concealed within commercial cargo containers. Since September 11, 2001, the containers are also used to detect weapons of mass destruction.
2. Developed because manual searches are costly and time consuming (unloading of cargo).
3. Vendor - The gamma-ray imaging system was developed by SAIC. The company can be contacted by phone (1-800-962-1632), fax (1-858-826-9009), or email securityproducts@saic.com.
4. When detecting, only a very narrow beam of radiation is emitted. A personnel exclusion area is established behind the detectors.

5. Radiation dose level is about 5 microRem for any worker that happens to be scanned.
6. Three operators can set up the Mobile VACIS to be ready for inspecting in 10-15 minutes.
7. Cost is around \$1,000,000 per vehicle, while the competing x-ray machine (called the Heimen) costs \$5,000,000.

The information above was found at the SAIC Mobile VACIS website (www.saic.com/products/security/mobile-vacis) and from Americana Impex Consulting Co. website. The Americana Impex website provided general information about the VACIS applications, features, benefits, and performance characteristics (www.americanaimpex.com/cargo.htm).

DEPARTMENT OF DEFENSE

DEFENSE TECHNICAL
INFORMATION CENTER
8725 JOHN J. KINGMAN ROAD,
SUITE 0944
FT. BELVOIR, VA 22060-6201
2 CYS ATTN: DTIC/OCA

DEFENSE THREAT REDUCTION
AGENCY
8725 JOHN J. KINGMAN ROAD
STOP 6201
FT. BELVOIR, VA 22060-6218
2 CYS ATTN: CSC/G.
SAMPOLL-RAMIREZ

**DEPARTMENT OF DEFENSE
CONTRACTORS**

ITT INDUSTRIES
ITT SYSTEMS CORPORATION
1680 TEXAS STREET, SE
KIRTLAND AFB, NM 87117-5669
2 CYS ATTN: DTRIAC
ATTN: DARE

UNITED STATES NAVAL
ACADEMY
MECHANICAL ENGINEERING
DEPARTMENT
590 HOLLOWAY RD.
ANNAPOLIS, MD 21402
ATTN: M. E. NELSON